



Publicly Accessible Penn Dissertations


1-1-2013

The Impact of Mild Traumatic Brain injury on Neuronal Networks and Neurobehavior

Tapan P. Patel

University of Pennsylvania, tapan.p.patel@gmail.com

Follow this and additional works at: <http://repository.upenn.edu/edissertations>

 Part of the [Biomedical Commons](#), [Neuroscience and Neurobiology Commons](#), and the [Social and Behavioral Sciences Commons](#)

Recommended Citation

Patel, Tapan P., "The Impact of Mild Traumatic Brain injury on Neuronal Networks and Neurobehavior" (2013). *Publicly Accessible Penn Dissertations*. 788.

<http://repository.upenn.edu/edissertations/788>

This paper is posted at ScholarlyCommons. <http://repository.upenn.edu/edissertations/788>

For more information, please contact libraryrepository@pobox.upenn.edu.

The Impact of Mild Traumatic Brain Injury on Neuronal Networks and Neurobehavior

Abstract

Despite its enormous incidence, mild traumatic brain injury is not well understood. One aspect that needs more definition is how the mechanical energy during injury affects neural circuit function. Recent developments in cellular imaging probes provide an opportunity to assess the dynamic state of neural networks with single-cell resolution. In this dissertation, we developed imaging methods to assess the state of dissociated cortical networks exposed to mild injury. We probed the microarchitecture of an injured cortical circuit subject to two different injury levels, mild stretch (10% peak) and mild/moderate (35%). We found that mild injury produced a transient increase in calcium activity that dissipated within 1 h after injury. Alternatively, mild/moderate mechanical injury produced immediate disruption in network synchrony, loss in excitatory tone, and increased modular topology, suggesting a threshold for repair and degradation. The more significant changes in network behavior at moderate stretch are influenced by NMDA receptor activation and subsequent proteolytic changes in the neuronal populations. With the ability to analyze individual neurons in a circuit before and after injury, we identified several biomarkers that confer increased risk or protection from mechanical injury. We found that pre-injury connectivity and NMDA receptor subtype composition (NR2A and NR2B content) are important predictors of node loss and remodeling. Mechanistically, stretch injury caused a reduction in voltage-dependent Mg²⁺ block of the NR2B-containing NMDA receptors, resulting in increased uncorrelated activity both at the single channel and network level. The reduced coincidence detection of the NMDA receptor and overactivation of these receptors further impaired network function and plasticity. Given the demonstrated link between NR2B-NMDARs and mitochondrial dysfunction, we discovered that neuronal de-integration from the network is mediated through mitochondrial signaling. Finally, we bridged these network level studies with an investigation of changes in neurobehavior following blast-induced traumatic brain injury (bTBI), a form of mild TBI. We first developed and validated an open-source toolbox for automating the scoring of several common behavior tasks to study the deficits that occur following bTBI. We then specifically evaluated the role of neuronal transcription factor Elk-1 in mediating deficits following blast by exposing Elk-1 knockout mouse to equivalent blast pressure loading. Our systems-level behavior analysis showed that bTBI creates a complex change in behavior, with an increase in anxiety and loss of habituation in object recognition. Moreover, we found these behavioral deficits were eliminated in Elk-1 knockout animals exposed to blast loading. Together, we merged information from different perspectives (in silico, in vitro, and in vivo) and length scales (single channels, single-cells, networks, and animals) to study the impact of mild traumatic brain injury on neuronal networks and neurobehavior.

Degree Type

Dissertation

Degree Name

Doctor of Philosophy (PhD)

Graduate Group

Bioengineering

First Advisor

David F. Meaney

Keywords

automated behavior, blast induced traumatic brain injury, calcium imaging, concussions, neuronal networks, transcription factors

Subject Categories

Biomedical | Neuroscience and Neurobiology | Social and Behavioral Sciences

THE IMPACT OF MILD TRAUMATIC BRAIN INJURY ON
NEURONAL NETWORKS AND NEUROBEHAVIOR

Tapan P. Patel

A DISSERTATION

in

Bioengineering

Presented to the Faculties of the University of Pennsylvania

in

Partial Fulfillment of the Requirements for the

Degree of Doctor of Philosophy

2013

Supervisor of Dissertation

David F. Meaney, PhD

Solomon R. Pollack Professor and Chair, Dept. of Bioengineering

Graduate Group Chairperson

Daniel A. Hammer, PhD, Professor, Dept. of Bioengineering

Dissertation Committee

Diego Contreras, MD, PhD, Associate Professor, Dept. of Neuroscience

Ravi Radhakrishnan, PhD, Associate Professor, Dept. of Bioengineering

Beth Winklestein, PhD, Professor, Dept. of Bioengineering

THE IMPACT OF MILD TRAUMATIC BRAIN INJURY ON
NEURONAL NETWORKS AND NEUROBEHAVIOR

COPYRIGHT

2013

Tapan P. Patel

*"To my parents and my sister whose unconditional love and incredible sacrifices
have led me to this point."*

ACKNOWLEDGMENT

Over the past many years, I have had the good fortune to be mentored and taught by incredibly dedicated teachers and professors who fostered an attitude of learning, resilience, and independence. My interest in research began as an undergraduate at the University of Delaware in the developmental biology lab of Dr. Melinda Duncan. She fostered my curiosity for discovering new knowledge and set me on a path of lifelong student. My parents, Pinakin and Jayshree, on the other hand, helped me identify my true passion for medicine. I am forever grateful to these two individuals for setting me on a track of becoming a physician-scientist. Additionally, my sister, Shweta, has been the driving force behind each of my personal and academic milestones in life and I cannot be more grateful to have the support of such a talented and compassionate sibling.

Of the many mentors, one stands out from the rest. My true intellectual and scientific transformation began during graduate education, under the guidance of Dr. Dave Meaney. Dave let me explore my interests in science, while keeping me focused on the perusing the most relevant questions. He created an atmosphere of academic creativity, curiosity, and above all, a trusting relationship. These are the elements that would make any graduate student thrive and succeed. I am also grateful for the support of my thesis committee, Drs. Winklestein, Radhakrishan and Contreras, who helped define the focus of my project and provided instrumental insight for its direction. I would also like to acknowledge the bright and dedicated members of the Meaney Lab, who have all contributed to the success of my work in more ways than one.

Lastly, of all my discoveries throughout graduate school, my most important discovery will always be my best friend and partner in life, Alison Pouch. Those that know me well will agree that she has already made me a better person and I look forward to continued academic and personal growth with her by my side.

ABSTRACT

THE EFFECTS OF TRAUMATIC BRAIN INJURY ON NEURONAL NETWORKS AND NEUROBEHAVIOR

Tapan P. Patel

David F. Meaney, PhD

Despite its enormous incidence, mild traumatic brain injury is not well understood. One aspect that needs more definition is how the mechanical energy during injury affects neural circuit function. Recent developments in cellular imaging probes provide an opportunity to assess the dynamic state of neural networks with single-cell resolution. In this dissertation, we developed imaging methods to assess the state of dissociated cortical networks exposed to mild injury. We probed the microarchitecture of an injured cortical circuit subject to two different injury levels, mild stretch (10% peak) and mild/moderate (35%). We found that mild injury produced a transient increase in calcium activity that dissipated within 1 h after injury. Alternatively, mild/moderate mechanical injury produced immediate disruption in network synchrony, loss in excitatory tone, and increased modular topology, suggesting a threshold for repair and degradation. The more significant changes in network behavior at moderate stretch are influenced by NMDA receptor activation and subsequent proteolytic changes in the neuronal populations. With the ability to analyze individual neurons in a circuit before and after injury, we identified several biomarkers that confer increased risk or protection from mechanical injury. We found that pre-injury connectivity and NMDA receptor subtype composition (NR2A and

NR2B content) are important predictors of node loss and remodeling. Mechanistically, stretch injury caused a reduction in voltage-dependent Mg^{2+} block of the NR2B-containing NMDA receptors, resulting in increased uncorrelated activity both at the single channel and network level. The reduced coincidence detection of the NMDA receptor and overactivation of these receptors further impaired network function and plasticity. Given the demonstrated link between NR2B-NMDARs and mitochondrial dysfunction, we discovered that neuronal de-integration from the network is mediated through mitochondrial signaling. Finally, we bridged these network level studies with an investigation of changes in neurobehavior following blast-induced traumatic brain injury (bTBI), a form of mild TBI. We first developed and validated an open-source toolbox for automating the scoring of several common behavior tasks to study the deficits that occur following bTBI. We then specifically evaluated the role of neuronal transcription factor Elk-1 in mediating deficits following blast by exposing Elk-1 knockout mouse to equivalent blast pressure loading. Our systems-level behavior analysis showed that bTBI creates a complex change in behavior, with an increase in anxiety and loss of habituation in object recognition. Moreover, we found these behavioral deficits were eliminated in Elk-1 knockout animals exposed to blast loading. Together, we merged information from different perspectives (*in silico*, *in vitro*, and *in vivo*) and length scales (single channels, single-cells, networks, and animals) to study the impact of mild traumatic brain injury on neuronal networks and neurobehavior.

TABLE OF CONTENTS

ACKNOWLEDGMENT	IV
ABSTRACT	VI
CHAPTER 1: DISSERTATION OVERVIEW	1
BACKGROUND AND SIGNIFICANCE.....	1
Mild traumatic brain injury is a major health problem	1
The effect of mTBI on information flow through neuronal networks is unknown	2
Synchronization of neuronal activity is key for information flow over long-distances	3
THESIS OUTLINE	4
CHAPTER 2: AUTOMATED QUANTIFICATION OF NEURONAL NETWORK DYNAMICS WITH SINGLE-CELL RESOLUTION USING CALCIUM IMAGING.....	7
ABSTRACT	7
INTRODUCTION	8
METHODS	11
Cell culture:.....	11
Induction of Lewy body pathology	12
In silico simulation of network behavior	12

Defining the connectivity of the in silico network	14
Simulating calcium dynamics	14
Calcium imaging and data acquisition:	16
Immunocytochemistry	17
Data analysis	18
Segmentation	20
Single neuron temporal fluorescence intensity and spike-detection:	21
Single-cell calcium dynamics (SCCD) phenotyping module.....	27
Network analysis module:.....	30
Synchrony	30
Functional connectivity.....	34
Statistical Analysis:.....	35
RESULTS.....	35
In silico neural network yields estimates of optimal imaging parameters necessary to achieve accurate spike detection	35
Optical imaging of network activity in vitro reveals modules and minimum acquisition requirements ...	39
Knowledge-based automated detection of calcium transients is the most accurate spike detection algorithm	41
Single-cell calcium dynamics and network connectivity revealed through calcium imaging.....	43
Developmental changes in the frequency and coordination of neuronal network activity.....	49
Lewy body pathology impairs network synchrony and connectivity.....	52
Expression of human mutant variant of tau is associated with altered calcium homeostasis.....	59
Discussion.....	64

**CHAPTER 3: SINGLE NEURON NMDA RECEPTOR PHENOTYPE DICTATES
NEURONAL REWIRING AND RE-INTEGRATION FOLLOWING TRAUMATIC
INJURY 74**

ABSTRACT:..... 74

INTRODUCTION:..... 75

METHODS: 79

 Mechanical injury of cortical neurons: 79

 Drug Treatments 81

 Single cell phenotyping of the relative contribution of NMDAR subtypes to synaptically-evoked rise in
 intracellular calcium..... 82

 Statistical Analysis:..... 83

 Calcium imaging and data analysis:..... 83

RESULTS..... 83

 Integration of neurons within an injured network is influenced by pre-stretch connectivity. 83

 Neuronal NMDAR subunit composition influences functional rewiring following injury. 88

 NR2B-NMDA receptor, not NR2A, undergoes stretch induced reduction in Mg²⁺ block. 96

 Stretch-induced reduction in NR2B-NMDAR Mg²⁺ block causes asynchronous circuit activity..... 100

 Activation of NR2B-NMDARs in injured neurons reduces networks augmentation induced with
 synchronization. 107

DISCUSSION 112

 Differential roles for NR2A- and NR2B-NMDARs in shaping synchrony, functional recovery, and
 plasticity following injury 115

Network plasticity	117
Significance of synchronization	118
CHAPTER 4: NMDA-INDUCED MITOCHONDRIAL DYSFUNCTION CONTRIBUTES TO NEURONAL NETWORK IMPAIRMENT THAT IS MITIGATED BY NIM811 ...	121
ABSTRACT	121
INTRODUCTION	122
METHODS	124
Cell culture and calcium imaging:	124
Drug treatments.....	125
Measuring mitochondrial morphology.....	125
Measurement of $\Delta\psi_m$	126
Cell viability	127
Cytoskeletal disruption and mitochondria motility	127
Statistics	128
RESULTS.....	129
Brief, high dose NMDA stimulus increases synchronized network activity and leads to activity- dependent preconditioning.....	129
NIM811 reduces mitochondrial dysfunction following excitotoxic injury.....	132
Inhibition of mitochondrial permeability transition pore reduces NMDA-induced AMPA receptor internalization.....	135
Network impairments following excitotoxicity injury are reduced with NIM811.....	138
Mitochondrial motility influences NMDA-induced changes in morphology	141

DISCUSSION	145
CHAPTER 5: AUTOMATED ANALYSIS OF RODENT BEHAVIOR TASKS REVEALS A NEW MECHANISM FOR NEUROPSYCHIATRIC DEFICITS FOLLOWING BLAST- INDUCED MILD TRAUMATIC BRAIN INJURY	149
ABSTRACT	149
INTRODUCTION	149
METHODS	153
Subjects.....	153
Blast-induced traumatic brain injury (TBI).....	153
Neurobehavior assay development	154
Mathematical Approaches for Automating Behavior Scoring	156
Validation and Optimization of Automated Approaches:	164
Sensitivity analysis:	164
Statistical Analysis:.....	165
Behavior pattern analysis:	166
RESULTS.....	166
Comparison of automated and manual analysis of behavior tasks.....	167
Autotyping as a method to assess the influence of blast-injury and Elk-1 deletion	171
Blast-injury increases generalized anxiety in wildtype animals while Elk-1 knockout mice are resistant to post-blast anxiety.	172
Blast-injury to wildtype mice impairs object habituation but Elk-1 deletion recovers normal behavior	177
Blast injury impairment spatial and associative memory only in Elk-1 knockout mice.	178

Blast-injury impairs motor coordination and motor learning.....	179
Multivariate analysis reveals the relative effects of genotype, injury and genotype*injury on behavior outcome.....	180
DISCUSSION:	184
CHAPTER 6: CONCLUSIONS AND FUTURE DIRECTIONS.....	187
Dissertation summary	187
Chapter 2.....	187
Chapter 3.....	187
Chapter 4.....	189
Chapter 5.....	190
Limitations and future directions	192
CNS tissue preparation: in vitro to in vivo.....	192
In vivo multi-cell bolus loading.....	193
Calcium imaging is a proxy for electrical activity	198
NR2B receptor activation following stretch.....	199
Recovery of injured circuits over time	200
Na ⁺ channels and network recovery.....	202
Tau and traumatic brain injury.....	203
Repairing an injured circuit.....	207
Glial modulation of neuronal networks.....	210
BIBLIOGRAPHY	216

LIST OF TABLES

Table 2.1: Properties of two commonly used calcium indicator dyes	15
Table 5.1: Automated behavior tasks.....	163
Table 5. 2: Summary of behavior alterations relative to wildtype littermate (WTLM) sham	180

LIST OF ILLUSTRATIONS

Figure 2. 1: Overview of image analysis. A: Workflow for the analysis of time-lapse calcium imaging.....	19
Figure 2. 2: Automated spike detection methodology.....	26
Figure 2. 3: Classifiers for single cell calcium dynamics of neurons in the network.....	30
Figure 2. 4: Multi-scale computational model of neuronal network activity.. ..	37
Figure 2. 5: <i>In silico</i> predictions of fluorescent probe sensitivity.. ..	39
Figure 2. 6: Comparison of in vitro calcium imaging with fura-2 and fluo-4 at varying frame rates.....	40
Figure 2. 7: Estimate of functional connectivity.....	44
Figure 2. 8: Mapping functional connectivity of neural circuits <i>in vitro</i>	46
Figure 2. 9: Excitatory tone measurement.	48
Figure 2. 10: Developmental changes in network activity patterns.....	51
Figure 2. 11: α -syn pffs recruit endogeneous α -syn to form pathologic, insoluble aggregates.. ..	54
Figure 2. 12: Effect of aggregate formation on neural network activity. Calcium imaging on hippocampal neurons loaded with the calcium-sensitive fluorescent dye, Fluo4-AM, was performed.....	56
Figure 2. 13: Single-cell phenotypes revealed by calcium imaging.. ..	63
Figure 3. 1: Schematic of stretch injury device.. ..	81
Figure 3.2: Mechanical injury to a cortical network <i>in vitro</i> causes acute reduction in functional connectivity through NMDA receptor activation.. ..	85
Figure 3. 3: Profiling the contributions of NMDA receptors (NR2A and NR2B subtypes) and voltage-gated calcium channels to intracellular calcium oscillations.....	90
Figure 3. 4: Functional rewiring following injury is influenced by NMDA receptor composition.....	96
Figure 3. 5: Injury results in a reduction of NR2B-NMDAR Mg^{2+} block.....	99
Figure 3. 6: Computational model predicts the effects of reduced NR2B Mg^{2+} block on dendritic spine and network activation.. ..	103

Figure 3. 7: Activation of NR2B-containing NMDARs disrupt the coordinated activity of an injured neuronal network..	106
Figure 3. 8: Enhanced NR2B activation prevents task-learning in an injured network..	111
Figure 4. 1: Brief exposure to high dose NMDA enhances network activity and offers neuroprotection.	131
Figure 4. 2: Mitochondria dysfunction following NMDA stimulus is attenuated with NIM811 pretreatment.....	134
Figure 4. 3: Mitochondrial permeability transition pore inhibitor blocks NMDA-induced AMPA receptor internalization.....	137
Figure 4. 4: Excitotoxic NMDA stimulus results in network dysfunction.	139
Figure 4. 5: Activity-induced mitochondrial motility reduces NMDA-induced swelling..	144
Figure 5. 1: Overview of automated analysis of neurobehavior.	159
Figure 5. 2: Sensitivity of automated approach..	168
Figure 5. 3: Comparison of automated and manual scoring.	169
Figure 5. 4: Behavior deficits following bTBI in wildtype littermate and Elk-1 knockout mice.....	175
Figure 5. 5 : Multivariate analysis reveals the relative effects of genotype, injury and genotype*injury on behavior outcome.....	182
Figure 6. 1: Epidural SR-101 (100 μ M) was used to highlight cortical surface and to create contrast between blood vessels and brain parenchyma.	194
Figure 6. 2: Injection of fluo-4 and SR101 in an anaesthetized mouse..	196
Figure 6. 3: Multi-cell bolus loading of fluo-4 <i>in vivo</i>	197
Figure 6. 4: Changes in the immunoreactivity of Na _v 1.2 at 1, 3, and 5 days following stretch injury..	203
Figure 6. 5: Increased tau phosphorylation following stretch injury appears as early as 5 hr and is persist for 7 days.	205
Figure 6. 6: Selective silencing of calcium activity with ArchT <i>in vitro</i>	209
Figure 6. 7: Injury causes long-lasting increase in astrocytic calcium activity in the mechanical penumbra..	213
Figure 6. 8: The activity of <i>in vitro</i> neuronal networks in the mechanical penumbra is influenced by intercellular waves in astrocytes and purinergic signaling..	213

CHAPTER 1: Dissertation Overview

BACKGROUND AND SIGNIFICANCE

Mild traumatic brain injury is a major health problem

Concussions are a form of mild traumatic brain injury (mTBI) that represent at least 80% of the traumatic brain injuries occurring each year in the United States (Kraus and Nourjah, 1988). Although often associated with sports, the majorities of concussions occur outside of sporting activities and include motor vehicle accidents, falls, and any situation involving sudden acceleration or deceleration of the head. Despite its name, the consequences of mild TBI are not "mild"; 30%-80% of patients diagnosed with mTBI experience disabling problems, such as persistent headaches, fatigue, changes in sleep patterns, sensory problems (post-concussion syndrome), and mood changes (Alexander, 1995; Hall and Chapman, 2005; Kushner, 1998). In addition, repetitive mTBI is correlated to delayed neurodegenerative changes, often accompanied by severe decline in cognitive and psychiatric health (Stern et al., 2011).

Long considered an injury that was 'inevitable' with little recourse, the growing awareness of the long-term effects of concussion led to a renewed focus on understanding, preventing, and treating concussions. New technology to assess the mechanical circumstances of concussions is leading to a new perspective on effective protective equipment. Alongside the advances in basic science understanding of concussions, new diagnostic imaging methods are also becoming available to better

evaluate and assist clinicians in the care of patients with a concussion (Difiori and Giza, 2010). At the mechanistic level, our knowledge in the past decade increased considerably about the early events following traumatic axonal injury – e.g., the relative vulnerability of unmyelinated axons to trauma, the early and progressive cytoskeletal changes, the appearance of new surface channels or the loss of existing channels, and the acute mechanisms of injury both *in vivo* and *in vitro* (Buki and Povlishock, 2006; Farkas and Povlishock, 2007; Johnson et al., 2012).

The effect of mTBI on information flow through neuronal networks is unknown

Despite this progress, we know little about one potentially important aspect of mTBI: how do the cellular, subcellular and molecular perturbations following injury affect the structure and organization, or "information flow", through neuronal networks? Partly, this is because the cellular substrate of concussion is largely unknown (Meaney and Smith, 2011). One theory on the mechanical origin of concussions proposes that the cortical strains appearing in the gray matter at the moment of injury are the most likely reason for the impairments that occur in a concussion. Alternatively, others pose that deformation of the axonal tracts, termed diffuse axonal injury, are key in producing the cognitive and behavioral deficits associated with severe concussions (Andriessen et al., 2010; Biasca and Maxwell, 2007; Sharp and Ham, 2011). A common theme among these concussion theories is that the mechanical energy during rapid head motions will deform brain tissue and, ultimately, the cellular ensembles that form these tissues. However, at the multicellular scale, it is not clear if these transient mechanical events will cause

permanent changes in the neuronal morphology or, alternatively, the wiring of neural circuits within brain regions associated with concussion. These changes in both the neuronal connections and, alternatively, the wiring of neural networks can play a key role in the recovery of the brain following a concussion.

Synchronization of neuronal activity is key for information flow over long-distances

Synchronization of neuronal activity is fundamental in the operation of cortical networks. Neurons in cortical networks engage in synchronous activity in a wide range of frequencies bands, influenced by the central state of the brain (e.g. sleeping, awake), the presence of sensory stimuli (e.g. visual perception, attention demanding tasks), or motor acts. Functionally, synchronization is an integrated mechanism that brings a widely distributed set of neurons together into a coherent ensemble that underlies a cognitive act. In other words, the dynamic modulation of synchrony recruits specific brain regions that are required for executing a task, whereas de-synchronization resets the circuit for the next task.

Interestingly, alterations of oscillation patterns occur in several neurological disorders (Hammond et al., 2007; Isomura et al., 2008; Uhlhaas et al., 2008; Uhlhaas and Singer, 2006). Several recent reports also suggest that mTBI is a disease of network dysfunction. The changes in physical connections among brain regions, revealed through diffusion tensor imaging (DTI), and alterations in coordinated brain activity, revealed through a combination of EEG and functional magnetic resonance imaging (fMRI), suggest that the cognitive impairments and decline in task-related performance after

mTBI are likely a result of network dysfunctions. Although these aggregate measures have important diagnostic implications, it is difficult to extend these studies into therapeutic application because the mechanisms for network dysfunction following mTBI remain elusive and potential strategies to repair an injured circuit have not yet been explored.

THESIS OUTLINE

This dissertation aims to study the function of microcircuits in real-time, with single-cell resolution to understand how mTBI appears and evolves at the circuit level. Based on past work, it is likely that mechanical injury can disrupt both the timing and coordination of information transfer through a neural circuit. Of the available technologies for mapping neural circuits, functional multi-neuron calcium imaging by far is the best compromise between single-cell spatial resolution and near single action-potential temporal resolution.

Single-cell measures of electrophysiological function are important to determine how components of injured circuits can change following mTBI. Similarly, EEG, fMRI and DTI techniques provide valuable information about the macroscopic brain regions most affected by mTBI but they do not have the spatial or temporal resolution to probe the cellular mechanisms leading to network dysfunction. Although recording extracellular field potential using high-density electrode arrays can help reconstruct the wiring of a neuronal network in vivo, it is difficult to mechanically injure the brain and simultaneously record network activity with these rigid arrays. Alternatively, mapping

the connectivity of microcircuit either in vitro or in vivo can also be approximated with high speed imaging methods and is less invasive than electrode arrays. Voltage sensitive dyes are widely available and provide direct recording of the field potential changes that occur within in vitro networks and acute slice preparations. Developing an exact map of the functional connectivity among neurons within these preparations is difficult because the speed required for detecting action potential events requires ultrasensitive CCD cameras with poor spatial resolution, making it difficult to detect single neurons in the network.

In **Chapter 2**, we develop the tools to map the functional connectivity of hundreds of distinct neurons within a field of view using high speed calcium imaging. We then validate and test the sensitivity of these tools under physiologic and pathologic conditions with known network functions.

In **Chapter 3**, we explore the topology and function of an injured network subject to different injury severities and at different time points following the injury. The single-cell spatial resolution of our technique and the ability to image the same microcircuit before and after injury allows us to probe the mechanisms of dynamic changes in network topology. Specifically, we identify a few common features of the network prior to injury that are linked to increased susceptibility and greater network degradation following mechanical injury. Additionally, we identify a strategy to repair and regain plasticity in a post-traumatic circuit.

In **Chapter 4**, we explore the common and distinguishing features of mechanical and excitotoxic injuries. Specifically, we focus on the role of mitochondria morphology and motility on network patterns following overactivation of NMDA receptors. Additionally, we test whether targeted repair of mitochondria function improves post-injury network function.

In **Chapter 5**, we move the *in vitro* findings to an *in vivo* setting. We first create the tools necessary for automated high-throughput phenotyping of mouse neurobehavior, which are key outcome measures used in rodent models of neurological injury, disease, and degeneration. The behaviors tested span multiple neuroanatomic substrates, including tests of cortical, hippocampal, amygdala, and cerebellar circuitry. We applied the automated algorithms and used a systems-level analysis to study the alterations in behavior that occur following a new model of mild TBI and to examine the impact of mTBI in a transgenic mouse.

We conclude in **Chapter 6** with a brief discussion of few limitations of our studies and a set of future directions for this project. We present preliminary data for some of these future studies and highlight the importance of single-cell biomarkers for targeted repair of an injured network. Additionally, we point out a potentially broad role of astrocytes in disrupting neuronal networks surrounding the mechanical injury focus. Further studies on the astrocyte-neuron networks may open a new class of glio-centric targets for treating mild traumatic brain injuries.

CHAPTER 2: Automated quantification of neuronal network dynamics with single-cell resolution using calcium imaging

ABSTRACT

Neuronal networks exhibit a rich repertoire of context-dependent activity patterns that subserve numerous cognitive and behavioral tasks, including information processing, learning and memory, and interfacing with the external environment. Understanding the dynamics of spontaneous and/or stimulus-evoked network activity in health and in models of neurological, psychiatric and neurodevelopmental disorders is critical for understanding pathophysiology and guiding treatment. Recent advances in fluorescent calcium indicator technology and microscopy provide an opportunity to assess the dynamic state of neural networks with single-cell and single action potential resolution. However, a fully-integrated automated workflow for the analysis and visualization of these rich microcircuits is lacking. Here we estimated the imaging conditions needed to achieve accurate measures of network properties and developed an open-source, interactive software for automated quantification of numerous biologically relevant features of both the calcium dynamics of single-cells and the activity patterns of networks. Our software integrates and improves upon existing tools for spike detection, synchronization analysis, and inference of functional connectivity, making it most useful to experimentalists with little or no programming knowledge. We apply this software in several conditions of known network function. We first characterize the activity patterns

of neuronal microcircuits undergoing developmental maturation *in vitro*. We used an *in vitro* model of Lewy body pathology, known to cause selective decreases in synaptic proteins, to examine whether calcium imaging-based estimates of neuronal network excitability and connectivity are impaired. Separately, we highlight the utility of single-cell analysis of calcium dynamics for phenotyping a mixed population of neurons expressing a human mutant variant of the microtubule associated protein tau and wild-type tau. We expect the use of these tools will provide a comprehensive analysis of neuronal networks, promoting the rapid interrogation of circuits in health and disease.

INTRODUCTION

Understanding how the brain carries out the vastly diverse and complex tasks is arguably the greatest scientific problem of our time. This is inherently a multi-scale problem. Over the past decades, our knowledge of the microscopic properties of single ion channels and neurons increased tremendously through the use of electrophysiology. Similarly, recent advances in medical imaging allow researchers to study the macroscopic structural and functional organization of the brain with astonishing detail (Matthews et al., 2006; Sorbara et al., 2012; Toga et al., 2006). Despite this progress, the mechanisms of neurobehavior remain elusive, partly because we know little about how groups of interconnected neurons, or microcircuits, communicate and dynamically regulate their activity patterns to produce a seemingly effortless behavioral response. The ultimate goal of systems neuroscience is to record every spike from every neuron, at rest, during

sensory input, and during ensuing behavioral output to unravel the rules that govern behavior and to understand how these rules are broken in disease states.

Towards this goal, there has been a concerted effort to start mapping the connections among neurons within the brain for both small and large organisms. In parallel, a substantial new set of tools appeared for formulating principles of information flow among neural networks, measuring their relative connectivity map, and understanding key points of control for complex networks (Bullmore and Sporns, 2009; Cao and Slobounov, 2010; Garofalo et al., 2009; Liu et al., 2011; Rubinov and Sporns, 2010; Stam and Reijneveld, 2007). Key in this progress is a new emerging set of fluorescent reagents that provide stable, long term optically-based recording of dissociated neurons, ensembles of neurons within acute brain slices, and the living cortex (Dombeck et al., 2010; Mittmann et al., 2011; Tian et al., 2009). Collectively, these new tools allow for the direct visualization of the nervous system at an unprecedented scale – it allows one to estimate the input/output connectivity maps among neurons, assess the relative strength of connections among neurons in a network, and to define the network scaling principles used in the design of the network. However, quite often these tools are developed for a specific application, by different groups, in different locations, in different programming languages, and have limited integration into a workflow. As a consequence, the activation energy for experimentalists, who may not be well-versed in programming, to quickly go from raw time-lapse images of calcium fluorescence to quantifiable measures of activity, coordination and functional integration of the imaged

microcircuit is quite large.

In this study, we first critically analyze fluorescence based imaging methods for mapping neural network properties. We then created a comprehensive, consolidated and an interactive framework to aid in the analysis of calcium imaging data. We adapted and improved on existing tools for automatically computing numerous biologically relevant features of neuronal network activity. In addition, we created a graphical user interface (GUI) to streamline the processing and visualization of both single-cell and network parameters. Our calcium analysis software does not require any programming knowledge and will be especially useful to neuroscientists who want to use calcium imaging as a functional readout following an experimental manipulation. It can be used for the most basis application of visualizing a particular neuron's calcium fluorescence trace or for more complex analysis of synchronization, identifying different patterns of network activity and interactively exploring the functional connectivity of a microcircuit.

We applied our software in two separate contexts of known underlying pathology to determine the sensitivity and biological interpretation of calcium-imaging based estimates of network and single-cell parameters. First, we used a network-level analysis to study how developmental maturation of neurons grown in culture influence patterns of spontaneous activity. Then, we used a model of Lewy body pathology to determine if pathological inclusions of α -synuclein and its associated decrease in synaptic proteins alter the network excitability and connectivity. Separately, we used neurons expressing a human mutant variant of tau, suspected to alter calcium homeostasis, to determine if

automatically derived measures of single-cell calcium dynamics can be used to phenotype a mixed population of wild-type and transgenic neurons.

METHODS

Cell culture: All animal procedures were approved by the University of Pennsylvania Institutional Animal Care and User Committee. Embryos at day E18 were surgically removed from a timed pregnant Sprague-Dawley rat anesthetized with 5% CO₂ and sacrificed via cervical dislocation. Neocortical tissue was dissected from the embryos and dissociated for 15 minutes at 37C in trypsin (1.4 mg/mL) and DNase (0.6 mg/mL, Roche Applied Science, Indianapolis, IN). After trituration and filtration through Nitex mesh (Crosswire Cloth, Bellmawr, NJ), cells were resuspended in MEM with Earl's salts and GlutaMAX supplemented with 0.6% D-glucose (Sigma-Aldrich, St. Louis, MO), 1% Pen-Strep, and 10% Horse Serum and plated on poly-D-lysine (0.08 mg/mL, Sigma-Aldrich) and laminin (0.001 mg/mL BD Biosciences, San Jose, CA) coated glass bottom dishes (MatTek, Ashland, MA). Cell were plated at a density of 200,000 cells/mL, roughly 10,000 cells/mm². After overnight adhesion, media was replaced with Neurobasal media supplemented with B-27 and 0.4mM GlutaMAX and grown in a humidified 37C 5% CO₂ incubator.

For experiments involving mixed neuronal populations containing the expression of human mutant variant of the microtubule-associated protein tau (P301S) and wild-type

tau, we crossed a PS19 monogenic female mouse expressing P301S mutant tau (Yoshiyama et al., 2007) to a wild-type male and isolated hippocampal neurons from the embryonic litter. Hippocampi of 7 - 10 embryos from the same litter were dissociated together and plated onto MatTek dishes as described above, which yielded a mixed population of neurons that contained either 0 or 1 copy of P301S tau.

Induction of Lewy body pathology:

To induce the recruitment of endogenously expressed mouse α -syn into insoluble Lewy body-like and fibrillar aggregates, we added α -syn pre-formed fibrils (pffs) generated from full-length recombinant α -syn-hWT to primary hippocampal neurons derived from WT C57BL6 mice after culturing them for 5-6 days in vitro (DIV). PFF were a gift from Virginia Lee, University of Pennsylvania (Volpicelli-Daley et al., 2011). Pffs were diluted in PBS at 0.1 mg/mL, sonicated several times, and diluted in neuronal media. 5 ug/mL of α -syn pffs were added to a 35-mm MatTek dish.

In silico simulation of network behavior: We used a stochastic integrate and fire model to evaluate network dynamics, predict alterations in cytosolic calcium, and use these estimates of cytosolic calcium to predict measurements derived from fluorescent indicator dyes and genetically encoded calcium indicators (see next section). Each neuron within the model is designated as either an inhibitory (I) or excitatory (E) neuron. We base this model on previous models for network behavior, which contain neurons that show either a regular spiking (RS) or intrinsic bursting (IB) behavior (French and

Gruenstein, 2006). When modeled as a regular spiking neuron, the membrane potential of a single neuron will receive a spiking input, followed by a refractory period defined by a monoexponential decay. To monitor changes in membrane potential $v(t)$, we also include a leak current, a calcium sensitive hyperpolarizing current for potassium channels ($I_{K(Ca)}$), a noise component, and a generalized formulation of the synaptic current:

$$C \frac{dv}{dt} = I_{leak} + I_{spike} + I_{K(Ca)} + I_{noise} + I_{syn},$$

where C is the overall capacitance of neuronal membrane. The synaptic current has contributions from both the AMPA and NMDA receptors,

$$I_{syn} = d_j(I_{AMPA} + I_{NMDA}),$$

where d_j is a synaptic depression factor that accounts for the loss of vesicles from the j pre-synaptic terminals. AMPA and NMDA currents are computed from previous *Smoldyn* simulations that give a temporal profile of the number of open receptors (*AMPA* and *NNMDA*), following synaptic vesicular release (Singh et al., 2011):

$$I_{AMPA} = g_{AMPA} * (V_m - E) * N_{AMPA},$$

$$I_{NMDA} = g_{NMDA} * (V_m - E) * N_{NMDA},$$

where $g_{AMPA} = 12\text{pS}$, $g_{NMDA} = 45\text{pS}$ and the reversal potential $E = 0$. The remainder of model parameters are consistent with (French and Gruenstein, 2006).

For an intrinsic bursting neuron, we follow French et al. and add a low threshold calcium channel to augment the existing components incorporated for a bursting neuron. By incorporating the stochastic nature of AMPA and NMDA receptor opening, we enhance the previous model and account for the observed variability in activity patterns.

Defining the connectivity of the in silico network: The connectivity of our *in silico* model was prescribed to match *in vitro* neural network development. Past work using dissociated cortical neurons indicate that the input and output degree distribution is Poisson (Amit and Brunel, 1997; van Vreeswijk and Sompolinsky, 1996). In selecting targets for neuron i 's outputs, we utilized a weighted random sampling function, where neurons closest to, and in the direction of i 's axonal growth cone are preferentially connected. The number, or degree, of inputs (K_i) and outputs (K_o), and the relative distribution of the degree among an ensemble of neurons, defines the overall degree of connectivity in the neural circuit. Models of cortical neural networks were developed and executed using a custom MATLAB script (Mathworks, Inc.). We simulated the activity of 100 neurons for 10s, with 2-ms time steps, and average $K_i = K_o = 20$, where each connection was further divided into 20-50 synapses for a total of ~10,000 synapses. Synapses were populated with 80 AMPARs and 20 NMDARs. Simulations ran for 3 hours in simulation time to correspond with 10 seconds of imaging data.

Simulating calcium dynamics: Calcium influx is simulated by incorporating a step in free cytosolic calcium with each action potential, followed by an exponential decay. Calcium traces were used to predict changes in the fluorescence of two commonly used calcium

indicator dyes, fura-2 and fluo-4. Predicted fluorescence is dependent on a combination of the buffering property of the indicator (see Table 1), the acquisition rate of the imaging camera (0.4-20 frames per second; see methods below), and the sensitivity of the detector. The fluorescence, R , was determined from:

$$[Ca^{2+}] = \frac{R - R_{min}}{R_{max} - R} * K_d$$

and then down sampled to match experimental imaging speeds. R_{min} was determined by imaging neurons in a calcium free saline solution and R_{max} was determined by imaging neurons in normal saline solution, exposed to 5 μ M ionomycin (Sigma-Aldrich). The fraction of action potentials that were resolved by the calcium indicator dye was used to compare different imaging conditions.

Table 2.1: Properties of two commonly used calcium indicator dyes

	Fura-2	Fluo-4
K_d	145nM	345nM
R_{min}	.3982	121
R_{max}	2.7021	549
Frame rate	.4 Hz	.4-20Hz

Calcium imaging and data acquisition:

We measured calcium activity with the synthetic calcium indicator, fluo4-AM for short-term imaging, or a genetically engineered calcium indicator (GECI) for repeated long-term imaging.

For calcium imaging with fluo-4, a vial of 50 μ g Fluo4-AM (Invitrogen F-14201) was solubilized with the non-ionic surfactant Pluronic F-127 in 20% DMSO (Invitrogen, P-3000MP) to yield a 1mM stock solution. The stock solution was further diluted in controlled saline solution (CSS) to 2 μ M (CSS: in mM, NaCl 126, KCl, 5.4, MgCl₂*6H₂O, 1, CaCl₂*2H₂O, 1.8, HEPES, 10, glucose, 25). Osmolarity of CSS adjusted to 290mOsm and pH to 7.4. Culture media was exchanged with 2mL CSS and the cultures were loaded with Fluo-4AM for 30 minutes. Cultures were rinsed gently in CSS before imaging.

For calcium imaging with GECI, neurons were transduced at least 7 days prior to planned imaging study with an adeno-associated virus expressing GCaMP3, 5 or 6f under the control of the synapsin-1 promoter (GECI of Janelia Farm and Penn Vector Core, GC 5x10⁹/mL).

Images of spontaneous calcium activity were acquired with a Nikon Eclipse TE2000U microscope fitted with a spinning disk confocal (CSU-10b, Solamere Technologies), a CCD camera (Photometric Cool-Snap HQ2, BioVision, Exton PA), 488-nm excitation laser (Prairie SFC) and a Nikon 10X Plan Apo objective (N.A. = 0.4).

Exposure time was set to 50-ms and images streamed at 20Hz frame rate for at least 5 minutes. Each image frame was 520x696 pixels which corresponded to 0.3 mm² rectangular area.

A subset of cultures comparing Fluo-4 and Fura-2 indicator dyes were tested on a TE300 microscope. For Fura-2 imaging, cells were alternately excited at 340nm and 380nm using an excitation shutter filter wheel (Sutter Instruments, Novato, CA) and the corresponding emission images (510 nm) were collected using a 14-bit Hamamatsu camera (model- c4742-98; Optical Apparatus, Ardmore, PA) at a rate of one ratio image approximately every 2 seconds. Fluo-4 images were also collected at the same acquisition rate (.4 Hz), and higher rates (1Hz and 10Hz) for comparison purposes.

Excitatory tone in the network was determined using a modified approach of disintegrating the giant component (Breskin et al., 2006). Rather than using field stimulus and exposing neurons to large currents, we applied bicuculline and relied on the native excitatory circuitry to drive synchronous oscillations. By slowly adding increasing concentrations of AMPA receptor antagonist NBQX, we were able to stop synchronous oscillations and arrive at a critical value of $[NBQX]/K_d$ that disintegrates the excitatory network ($K_d = 47\text{nm}$, (Dev et al., 1996)).

Immunocytochemistry

Following calcium imaging experiments, neurons were fixed with 4% paraformaldehyde and probed for the presence of human P301S tau using rabbit polyclonal 17025 antibody per standard protocol (17025 gift from Virginia Lee, University of Pennsylvania). Briefly, cells were permeabilized with 0.2% Triton X for 10 minutes, blocked in 5% normal goat serum (NGS) for 30 minutes, incubated with 17025 primary antibody in NGS overnight and stained with Alexa Fluor goat anti-rabbit 594 secondary. Images were acquired on an upright Leica SP5 confocal microscope with a 25X objective (N.A. 0.95) and rotated 90⁰ to match the coordinate system of calcium images. Markers placed on the bottom of the glass cover slip prior to calcium imaging helped navigate to the same field of view. We manually co-registered the immunofluorescence image of fixed neurons to a fluo-4 image of the same field of view to retrospectively identify neurons that expressed the transgene.

Data analysis:

We used custom-coded MATLAB scripts to analyze the image stacks and created an interactive graphic user interface to facilitate broad use of our workflow. The general workflow is outlined in Figure 2. 1 and detailed below. Briefly, the steps are: 1) to identify cell bodies in an image (segmentation), 2) compute a time-varying fluorescence trace for each neuron across the image stack, 3) detect the onset of calcium transients, 4) quantify the shape and characteristics of calcium events for each neuron, and 5) compute the synchronization and functional connectivity of the network. We minimized user

interaction by automating each step in the workflow but allowed user flexibility to interactively explore the raw and processed data and make manual corrections if needed.

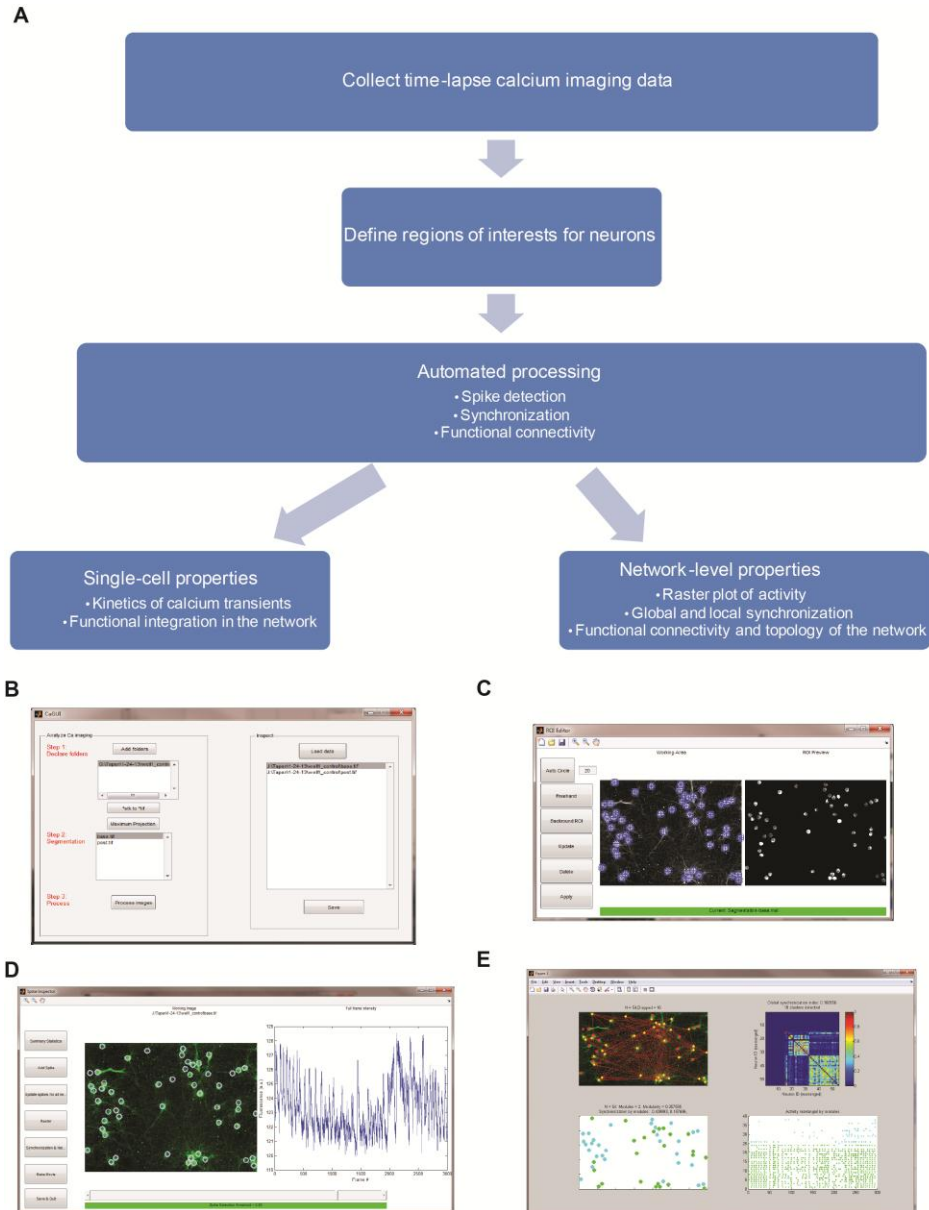


Figure 2. 1: Overview of image analysis. A: Workflow for the analysis of time-lapse calcium imaging. After acquiring images, pseudo-automated segmentation is performed to define regions

of interest (ROIs), delineating neuronal cell bodies from background. Fluorescence versus time is computed for each ROI and the onsets of calcium transients are automatically determined. Single-cell features of calcium transients and network-level measures of synchrony and functional connectivity are then derived. A graphical user interface was created to facilitate batch processing **(B)**, segmentation **(C)**, inspecting the fluorescence trace and spikes of individual neurons **(D)** and properties of the network **(E)**.

Segmentation:

A key first step in analysis is to identify cell bodies or regions of interest (ROIs) in an image frame. Often, it is difficult to manually draw ROIs around individual neurons because cell bodies *in vivo* are packed together and the expression of genetically encoded calcium indicators is restricted to the cytoplasm, necessitating careful delineation of cell edges. Rather, we integrated an automated cell identification method based on spatiotemporal independent component analysis into our workflow (Mukamel et al., 2009). Briefly, the algorithm uses spatial similarity of the fluorescence of groups of pixels and their temporal co-variation to identify "independent" sources of calcium signals. However, it cannot detect cells that do not spike or differentiate cells that fire synchronously. Further, it performs poorly if the signal-to-noise ratio is low (<0.1) or if there are too many cells (>200). We overcome these limitations with two key modifications. First, we subdivided the field of view into multiple smaller regions, performed ICA-based segmentation on each sub-region and then merged the results. This improved the fidelity of the algorithm by having fewer cells per sub-region and reduced

possible synchrony between sub-regions. To offset the increase in computation time associated with multiple segmentations, we transported the algorithms to a GPU and parallelized its execution to achieve similar computation time while increasing segmentation fidelity. To identify cells that do not spike or have low SNR, we generated a maximum projection image across the time series to improve image contrast and used K-means clustering algorithm to detect groups of spatially related pixels with similar intensities. To further improve segmentation quality, we built an interface that allowed users to interact with each automatically defined ROI and either delete falsely labeled ROIs, or add new ROIs simply by clicking on the interior of a cell. This greatly speeds up manual correction of an automatically generated segmentation and makes manual segmentation from scratch feasible by eliminating the need to carefully freehand cell contours.

Single neuron temporal fluorescence intensity and spike-detection:

Given a stack of .tiff images containing time-lapse images of calcium fluorescence and an accompanying segmentation file that delineates neurons (ROIs) from background, we first computed a fluorescence versus time trace for each neuron. The raw fluorescence trace was background subtracted to eliminate fluctuations in light source intensity or stage drift and then converted to a $\Delta F/F_0$ trace. This trace was characterized by a baseline that was periodically interrupted by calcium transients with varying amplitude and duration, consistent with a difference in the number and frequency of underlying action potentials (Dombeck et al., 2007; Greenberg et al., 2008; Kerr et al.,

2005; Tian et al., 2009). Past techniques show that the firing rate of neurons can be extracted by deconvolution if the waveform describing the rise and decay of calcium fluorescence following a single action potential is known (Yaksi and Friedrich, 2006). However, this requires a specialized combined electrophysiology and live cell microscopy setup. Instead, we directly used these traces as a surrogate measure of spiking activity and referred to them as the temporal activity pattern of the neurons.

We automatically identified the onsets of calcium transients for each neuron. Automated spike detection is generally a difficult problem, and especially more difficult for neuronal calcium fluorescence data because a given neuron may contain variable number of spikes. Moreover, individual spikes may have different amplitudes, different durations, occur at irregular intervals, and may be buried in significant noise. We explored three different methodologies for spike detection, providing each of these to the user in the software package. First method used a percentile based threshold (e.g., mean + 2*standard deviation of fluorescence) to detect peak events, but we discovered this methodology was not robust enough to correctly identify both small and large amplitude spikes (**Figure 2. 2 A, B**). Our second option employed a more sophisticated method inspired by an automated spike detection of EEG dataset using the continuous wavelet transform (Nenadic and Burdick, 2005). Wavelet transform decomposes a time-varying signal into its frequency and time components. Since spikes in EEG or calcium imaging experiments are restricted to a certain range of frequencies, the wavelet transform can identify *when* these frequencies occur. Although this is conceptually simple, we realized

that it requires setting a number of empirical parameters to achieve good accuracy in practice. Often, it falsely identified spikes that were part of background noise and, more importantly, does not correctly identify the exact time of a transient, often identifying a spike shifted in time relative to the true onset (**Figure 2. 2 C, D**). This is a result of limited temporal resolution of the wavelet transform but it is problematic because the precise timing of firing of neurons is an important feature of a microcircuit.

To overcome these limitations, our third option for spike detection developed a novel supervised spike detection algorithm using a database of known spike waveforms. We generalized the decisions that an observer makes when identifying spikes in a time series. Typically, a user has some prior knowledge on the characteristics of calcium spike, i.e. its fast onset, exponential decay, short duration, and timing. In practice, a user is constantly comparing their mental database with epochs of a times series to look for similarities. Algorithmically, we constructed a database of spike waveforms by asking several observers to manually identify the onset and duration of calcium spikes across multiple datasets. We eliminated entries that were too similar to each other, yielding a database containing 20 spike waveforms (**Figure 2. 2 E,F**). To detect spikes in a time series, we computed the time-varying correlation coefficient between a true spike waveform and target fluorescence trace (**Figure 2. 2 G, H**). We chose the correlation coefficient as our similarity metric because it is independent of amplitude, allowing us to identify a range of large and small transients. Local maxima in the correlation-coefficient domain correspond to onset of calcium transients (**Figure 2. 2 I, J**). A threshold

correlation coefficient > 0.85 was used since it maximized the true positive rate and minimized false positive rate.

Recognizing that the human observer is still the gold standard, we built a "Spike Inspector" module where users can click on individual neurons in the field of view and inspect the raw fluorescence trace, overlaid with automatically identified spikes. The user can interactively delete falsely identified spikes or add spikes with simple mouse clicks.

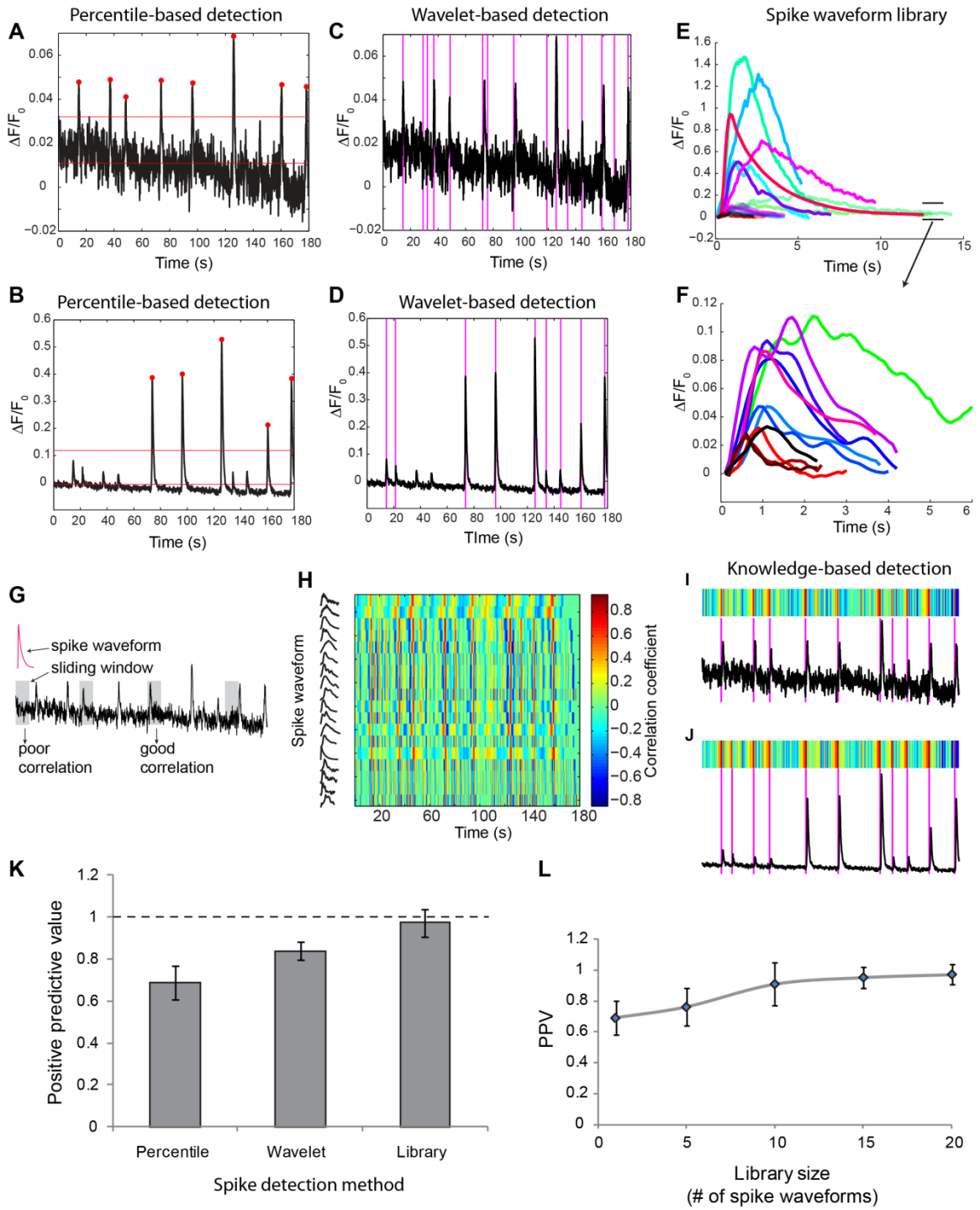


Figure 2. 2: Automated spike detection methodology. Percentile-based thresholding based on average fluorescence intensity for each ROI works well (positive predictive value = 86%) for spike detection if spike amplitude is nearly constant (**A**, example of an individual neuron's fluorescence trace) but fails to detect low amplitude spikes (PPV= 63%) when there are amplitude variations from spike-to-spike (**B**). Spike detection using continuous-wavelet transform is an alternative, more sophisticated method. However, it suffers from high false positive rate when the signal to noise ratio is low (**C**, 34% false positives) and the wavelet transform can introduce small phase-shifts in spike times (**D**). A third method for spike detection used a supervised algorithm by first building a database of unique calcium transient waveforms (**E**, **F** expanded view, note the different y-axes). Each waveform was used to derive a time-varying correlation trace that indicated the level of similarity between a true calcium transient and epochs of fluorescence trace (**G**; correlation value computed over 5 second windows, 100-ms displacement), generating a similarity matrix (**H**). Local maxima in the correlation matrix corresponded to the onset of calcium transients, providing a robust method for automated spike detection for a noisy trace (**I**, heat map shows the maximum correlation coefficient across all spike waveforms) and a trace with varying amplitude (**J**). Across these three methodologies, the average fraction of true spikes that were correctly identified (PPV) was significantly higher for the supervised spike detection method when compared to either the percentile or wavelet transform based methods (**K**). The accuracy of supervised

spike detection was relatively insensitive to the number of true spike waveforms beyond $n=10$ (**L**).

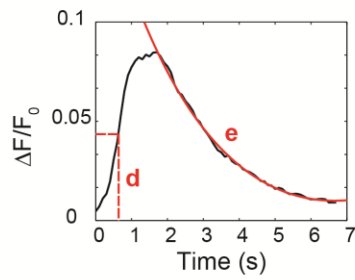
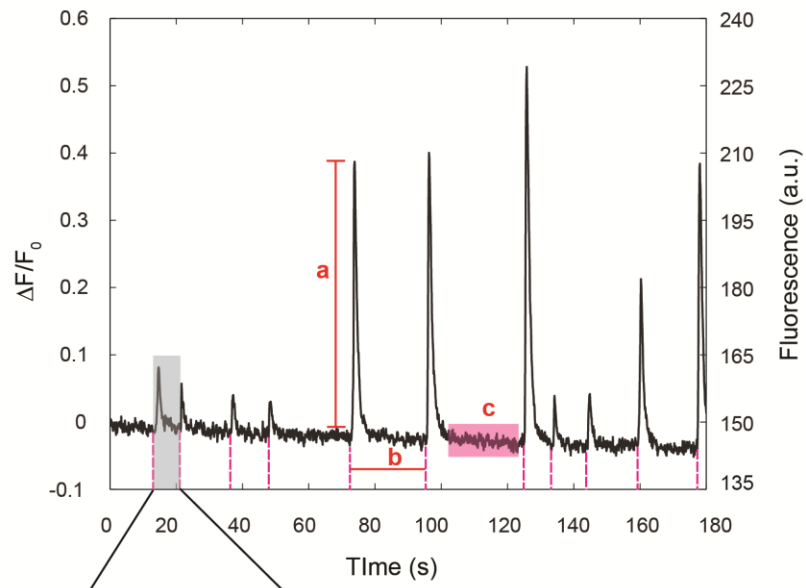
Single-cell calcium dynamics (SCCD) phenotyping module

We implemented several measurements to phenotype the temporal dynamics of calcium influx occurring within individual neurons. Overall, these measurements describe the spatiotemporal profile of calcium transients on a neuron basis and can be a useful adjunct to identify how alterations in calcium physiology correspond to the number or frequency of underlying action potential events measured with the spike detection algorithm (**Figure 2.3**). For example, past work shows the relative amplitude of a detected calcium spike can reveal differences in the number of action potentials generated over time within an individual neuron (Tian et al., 2009). In addition, the time to peak calcium can indicate the frequency of action potential firing within an individual neuron over time (Dombeck et al., 2007; Greenberg et al., 2008; Kerr et al., 2005; Tian et al., 2009).

Baseline fluorescence: The baseline calcium fluorescence of a neuron is an indication of the intracellular free calcium concentration, $[Ca^{2+}]_i$ and is related to resting membrane potential, V_m . For example, removing tonic inhibitory drive with bicuculline raises V_m and increase $[Ca^{2+}]_i$ whereas sodium channel blocker (TTX) slightly decreases V_m and $[Ca^{2+}]_i$. We computed the baseline fluorescence of each neuron by averaging parts of the fluorescence trace that are at least 2-seconds before and 10 seconds after the onset of a calcium transient.

Distribution of transients: The number of calcium events per neuron and the distribution of inter-event-interval (IEI) are important measures of the level of activity and rhythmicity. We report the mean and standard deviation of the IEI distribution for each neuron.

Kinetics of transients: The shape of a calcium transient is influenced by many factors, including the number and frequency of action potentials, the activation of synaptic sources of calcium entry, and the neuronal buffering capacity. We measured the amplitude, rise time, and fall time of each calcium event and their coefficient of variation. The amplitude was defined as the maximum change in fluorescence over baseline following the onset of a calcium transient. Rise time was defined as the time required to reach half maximum amplitude. Similarly, fall time was determined by fitting an exponentially decaying curve to the calcium transient. An $R^2 > 0.9$ indicated acceptable regression fit. When regression failed ($R^2 < 0.9$), we interpolated the time to reach half-max amplitude during the decay part of the calcium transient. We also computed the coefficient of variation of the amplitudes of calcium transient as a measure of peak-to-peak variability, indicative of variable AP firing rates.

A

a: amplitude
 b: inter-event-interval
 c: resting fluorescence
 d: rise time
 e: fall time

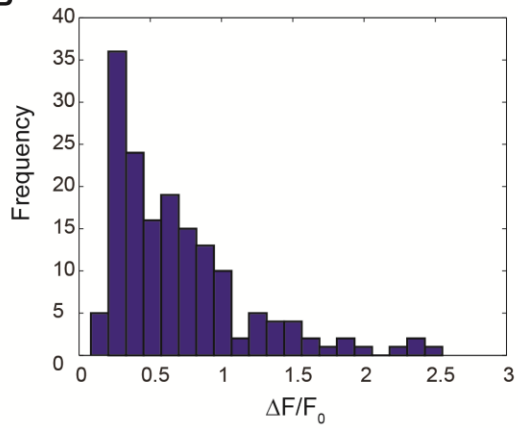
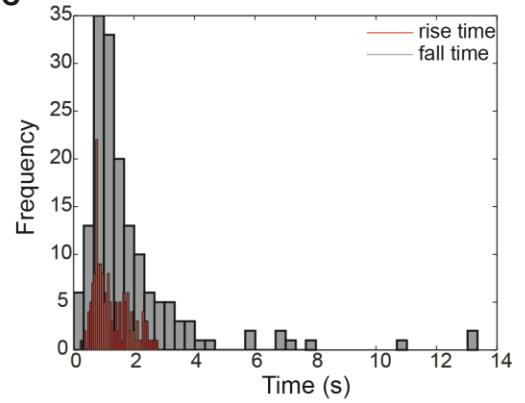
B**C**

Figure 2. 3: Classifiers for single cell calcium dynamics of neurons in the network. A:

Fluorescence versus time trace depicts automated detection of calcium transients (pink dashed lines). For each transient, the peak amplitude (a), rise time (d) and fall time (e) are determined. The resting fluorescence of each cell (c) and mean inter-event-interval (b) are also automatically computed. The resulting normalized peak intensity for an individual neuron shows a distribution of values across a network (**B**), while the rise and fall times show a more uniform range of values (**C**, red bars - rise time; gray bars - fall time).

Network analysis module:

Neural circuits display complex spontaneous and stimulus-evoked temporal activity patterns. Changes in the circuit wiring or neuronal physiology will manifest as a change in the pattern of network activity. Therefore methods to estimate the functional connectivity of the network, defined as the estimated connections a neuron forms with its neighboring neurons in the network, can be a powerful and sensitive functional output measure of an experimental manipulation. Additionally, many neurodegenerative and neuropsychiatric disorders are associated with changes in the pattern of resting state activity, and therefore methods for estimating network connectivity can provide new insights into the mechanisms and progressive changes that occur in these diseases.

Synchrony: A prominent feature of dynamic interconnected systems is their ability to synchronize. *In vivo*, synchronization serves a more general role by binding groups of distributed neuronal assemblies into functional units so that these assemblies can transfer information more easily. In essence, synchronized activity provides the necessary syntax

for neuronal communication. To identify groups neurons with similar pattern of activity and to quantify their synchrony, we use an approach based on the instantaneous phase of the raw fluorescence time series. Separating a time-varying signal into its amplitude and phase components allow us to focus on the *timing* of events, regardless of its amplitude (we measured the amplitude of calcium transients separately above). Phase synchronization has many features that make it attractive to the analysis of neuronal signals: a) it can capture non-linear dependencies between two or more time series (overcoming limitations of cross-correlation), b) it is time-resolved (overcoming limitations of coherence), c) it does not rely on estimating probability distributions which is often a limiting step for synchronization methods based on mutual information or transfer entropy, and d) the analysis can be restricted to specific frequency ranges, reflecting brain rhythms.

To quantify the phase synchronization of two time series, $x(t)$ and $y(t)$, we first compute their instantaneous phase $\phi_x(t)$ and $\phi_y(t)$. The Hilbert transform or a Morlet wavelet transform have been used in the past for obtaining instantaneous phase, however, these techniques are sensitive to noise and require filtering the signal, which can potentially introduce unwanted phase shifts. Instead, we numerically compute instantaneous phase using calcium spike times where a neuron undergoes a full oscillatory cycle (phase angle = 0 to 2π) from one spike event to the next. Mathematically, the unwrapped instantaneous phase is given by:

$$\phi(t) = 2\pi * \frac{t - t^{(k)}}{t^{(k+1)} - t^{(k)}} + 2\pi k$$

where $t^{(k)}$ is the spike time of the k^{th} spike.

If $x(t)$ and $y(t)$ are completely synchronized, their absolute phase difference $\psi_{x,y}(t) = \text{mod}(|\phi_x(t) - \phi_y(t)|, 2\pi)$ would be a constant. Alternatively, if $x(t)$ and $y(t)$ are completely independent, $\psi_{x,y}(t)$ will take on all values in the interval $[0, 2\pi]$. The distribution of $\psi_{x,y}(t)$ will be peaked at some phase-locked value in the former case and uniform in the latter case. The "peakiness" of a distribution can be quantified by its entropy and has been used as a measure of synchrony in some reports, however, this method requires normalizing and is sensitive to sample size and choice of bins. Instead, we use a definition of pair-wise phase synchronization index, $\gamma_{x,y}$, based on circular

variance of $\psi_{x,y}(t)$ give by $\gamma_{x,y} = \sqrt{(\langle \cos \psi_{x,y}(t) \rangle^2 + \langle \sin \psi_{x,y}(t) \rangle^2)}$, where

brackets denote average over time.

Geometrically, $\gamma_{x,y}$ measures the variability in the distribution of $\psi_{x,y}(t)$ when projected onto a unit circle. By definition, $\gamma_{x,y}$ takes on values in the interval $[0,1]$; $\gamma_{x,y} = 1$ if $x(t)$ and $y(t)$ are perfectly synchronized and 0 if they are completely independent. $\gamma_{x,y}$ is also a proper distance metric, i.e. it is positive definite and satisfies the triangle inequality.

This will be an important feature for cluster analysis described below.

To identify patterns of network activity, we compute pair-wise synchronization index of each neuron and populate a synchronization matrix S of size $M \times M$, where M = number of neurons in the network. $S(i,j)$ is the pair-wise synchronization index for the i -th and j -th neuron time series. Matrix formulation allows us to use linear algebra tools, namely Eigen decomposition, to cluster groups of neurons that display similar activity patterns and to quantify the level of synchronization in each cluster. For complete mathematical details, see (Allefeld C, 2007; Bialonski and Lehnertz, 2006; Li et al., 2010a). Briefly, clustering algorithm relies on examining the distribution of the eigenvalues of the matrix S . Given that S is symmetric and positive-definite, we are guaranteed to have M real eigenvalues, $\lambda^{(M)}$. If all neurons are completely synchronized and there is only 1 pattern of activity, all elements of the $S = 1$. In this case, there is only 1 eigenvalue that is disproportionately larger than the rest, $\lambda_1 = \lambda_2 = \lambda_{M-1} = 0$, $\lambda_M = M$. Alternatively, if all neurons fire independently and there are no patterns of activity, all elements of $S = 0$, and all eigenvalues are identical, $\lambda_1 = \lambda_2 = \lambda_M = 0$. The number of disproportionately large eigenvalues correspond to the number of unique activity patterns, and their corresponding eigenvectors contain information about which sets of neurons contribute to the creation of distinct patterns of activity. The largest eigenvalue is also proportional to the global synchronization index. We automatically compute pair-wise synchronization matrix and perform a synchronization cluster analysis as part of the workflow. The synchronization matrix and the raster plot of activity are rearranged based on their participation in a cluster and displayed for quick visual inspection of unique patterns of activity.

Functional connectivity: Key utility of calcium imaging is the inference of functional connectivity. Given the calcium fluorescence time series of two neurons, $x(t)$ and $y(t)$, the goal is to determine if x and y are functionally connected. The simplest method to assess temporal relationship is through Pearson's correlation or cross-correlation, however, these operations are limited to linear interactions and require the use of an arbitrary threshold to determine functional connectivity. Instead, we make use of surrogate data and statistical inference to determine functional connectivity. Given $x(t)$, $y(t)$, and their instantaneous phase $\phi_x(t)$, $\phi_y(t)$, our goal is to determine if the distribution of the instantaneous phase difference $\psi_{x,y}(t)$ is statistically significant. Since we do not know the null distribution H_0 a priori, we use amplitude adjusted Fourier transform (AAFT) of $y(t)$ to generate surrogate time series, $\hat{y}(t)$ and derive $\widehat{\phi}_y(t)$ and $\widehat{\psi}_{x,y}(t)$. $\hat{y}(t)$ has the same linear correlation structure, power spectrum and the marginal distribution as $y(t)$ but is otherwise random. In contrast to random permutation, which destroys any possible correlations in the time series, AAFT is autoregressive and is used to test H_0 that the time series is generated by a Gaussian process undergoing a monotonic static transform, i.e. the changes in fluorescence of $y(t)$ are a result of spontaneous presynaptic release events and not influenced by the activity of $x(t)$. We used the Kolmogorov-Smirnov test to determine statistical departure of $\psi_{x,y}(t)$ from the H_0 $\widehat{\psi}_{x,y}(t)$ and chose $\alpha=0.05$ and $p<0.001$ to define a functional connection between neurons x and y .

Our toolbox automatically computes functional connectivity of the network. We use routines from the Brain Connectivity Toolbox to describe the topology of the network

such as modularity, clustering coefficient and path length. We also created an interactive interface to aid in data exploration and data mining. Clicking on any neuron raises the focus of its functional targets, highlights their connections and provides detailed information about that neuron's single-cell and network properties, including the mean amplitude, inter-event-interval, rise and fall time, functional connectivity index, synchronization participation index, and nodal clustering coefficient.

Statistical Analysis:

Statistical differences in single-cell properties (peak amplitude, resting fluorescence, characteristic rise and fall time) and network properties (synchronization and frequency of calcium events) were assessed via student's t-test and/or one-way ANOVA and Tukey's post-hoc test. Shapiro-Wilk test was used to assess normality and nonparametric tests (Kruskal-Wallis and Mann-Whitney U) were employed when needed. At least $n=8$ wells from 3 different isolations were used to study developmental changes in spontaneous network function. alpha-level 0.05, $*p<0.05$ and $**p<0.01$ indicated significance. All values reported are mean \pm s.e.m. unless otherwise noted.

RESULTS

In silico neural network yields estimates of optimal imaging parameters necessary to achieve accurate spike detection

We first developed an *in silico* model of neural network activity, conducting a parametric analysis to understand advantages and drawbacks of choices that are commonly used in optical imaging of neural activity. Our multi-scale network model used a weighted pseudo-randomized network connection topology, and individual synapses, populated with AMPA and NMDA receptors, were assumed to follow a stochastic activation pattern per a recent report (Singh et al., 2011) (Figure 2. 4).

Integration of current from individual synaptic release events, which could include a random vesicular release event (i.e., synaptic noise), showed development of spontaneous network activity that would vary temporally (Figure 2. 4 F). Within individual neurons, these periodic bursts of activity would slightly precede or follow neighboring neurons, would show some modest diversity in the spontaneous timing of bursts. Repeat simulations of the same network topology yielded slightly different patterns of activity, owing to the stochastic synaptic activation scheme. Inhibitory neurons in the network provided modulation of the activity pattern, as reducing the relative strength of the inhibitory neuronal tone led to a progressive synchronization of network activity, resembling a common technique to synchronize the electrical activity of cortical neuron cultures *in vitro*.

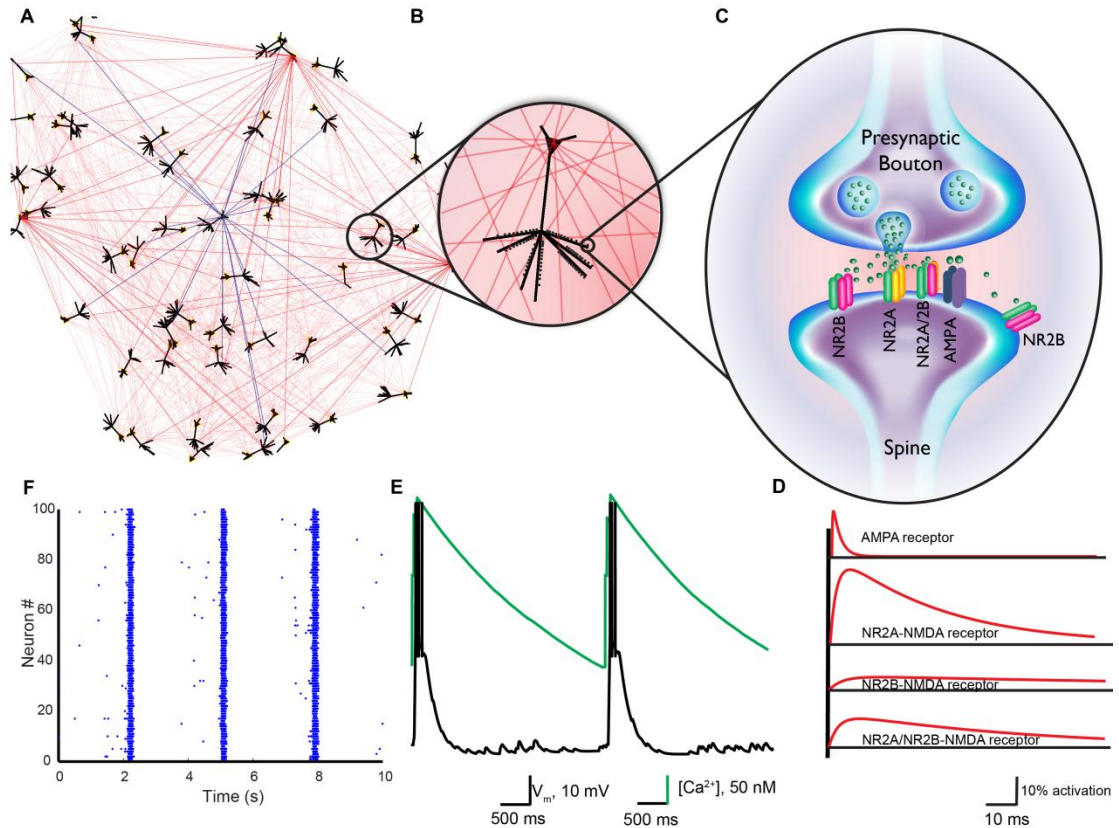


Figure 2. 4: Multi-scale computational model of neuronal network activity. **A:** We built an *in silico* network composed of 100 pyramidal-like neurons whose connectivity matched *in vitro* neural network development. **B:** The dendrites of each neuron were populated with spines, sites of synaptic contact. **C:** Synapses were populated with AMPA and different subunit compositions of NMDAR receptors. **D:** The temporal profile of activation of synaptic receptors in response to vesicular release of glutamate was used to update the cell membrane potential, following scaling by spine and somatic membrane capacitance. **E:** The variations in single-neuron membrane potential (black trace) and somatic calcium (green trace) were modeled and used to generate a temporal pattern of network activity (**F**, dots represent action potentials).

Using estimates of calcium binding for different calcium indicator dyes, we investigated how well fura-2 and fluo-4 capture underlying electrical activity. Under the most ideal conditions, without hardware noise, we found neither Fura-2 nor Fluo-4 provided accurate estimates of precise timing of action potential firing when sampled at relatively low rates. Although Fura-2 offers approximately double the accuracy in detecting action potentials within networks under very low framing rate conditions (.4 frames per second), the predicted accuracy was still less than 10% (Figure 2. 5). Fluo-4 offers the ability, with its single emission wavelength, to capture fluorescence imaging data at a much faster rate limited only by the imaging hardware (Takahashi et al., 2007). Across typical imaging rates available in commercial interline CCD and EMCCD camera, we find that image acquisition rate will substantially improve the fidelity between increases in calcium indicator fluorescence changes and action potential activity (Figure 2. 5). Optimal image acquisition rates with the Fluo-4 indicator exceed 80% accuracy in capturing action potentials ($85\% \pm 7.8\%$) at reasonable framing rates, and approach 60% ($58\% \pm 8.52$) even at 10 frames per second.

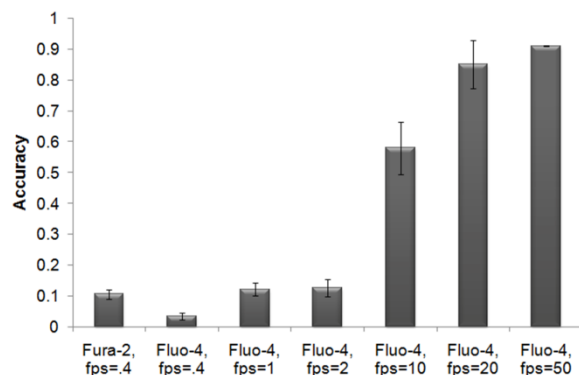


Figure 2. 5: *In silico* predictions of fluorescent probe sensitivity. Calcium transients predicted from underlying action potentials were converted to fluorescence traces for fura-2 and fluo-4, taking into account their unique buffering properties and down sampled to match imaging frame rates of most CCD cameras. The accuracy of resolving action potentials using fluorescent dye is greater for fluo-4 and increases with imaging acquisition speed.

Optical imaging of network activity in vitro reveals modules and minimum acquisition requirements

We tested these *in silico* predictions directly on our imaging system, assessing both the relative performance of different indicator dyes at low framing rates and the performance of the Fluo-4 indicator at higher framing rates. Several algorithms are available to detect spike patterns from optical imaging data, and our knowledge-based algorithm yielded consistent, repeatable measures of activity on a single neuron basis that was not complicated by altering or changing threshold conditions and baseline shifts that are often challenging experimental factors (**Figure 2. 2**). Applying this detection

algorithm to neuronal network cultures (n=10), we found no discernable difference between Fluo-4 and Fura-2 at framing rates typically used in time lapse imaging applications (.4 Hz) (Figure 2. 6 A,B). In the same culture, we progressively increased framing acquisition rates using the Fluo-4 indicator dye. Acquiring images at 1 Hz and 20 Hz, rather than .4 Hz, revealed a much more dynamic activity pattern, picking up many short lived calcium transients (Figure 2. 6 C,D). At higher imaging rates, we could no longer detect activity patterns clearly evident at lower framing rates, presumably due to the aggregate detection limits of the objective, filters, camera and other optical elements in the light path. We observed no significant difference in the activity patterns measured with either Fluo-4 or GCaMP6f, a recently introduced genetically engineered calcium sensor (Tian et al., 2009).

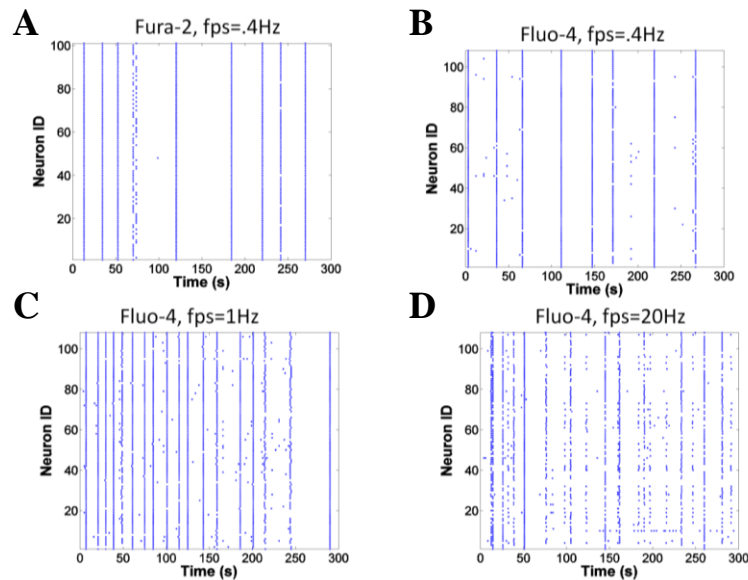


Figure 2. 6: Comparison of in vitro calcium imaging with fura-2 and fluo-4 at varying frame rates. A,B: Representative examples of spontaneous activity of a mature culture (DIV 18),

captured with fura-2 and fluo-4 at the same acquisition speed. The fluo-4 loaded culture was imaged at higher speed (**C**, 1Hz) and (**D**, 20 Hz), revealing richer temporal activity patterns.

After establishing the necessary acquisition speeds to accurately detect activity, we next considered both the number of neurons and length of imaging time necessary to accurately estimate network synchronization, a key parameter often used to determine network modules (Bialonski and Lehnertz, 2006). Across multiple cultures (n=8), we found that the phase difference in the calcium transients was not spatially sensitive, suggesting a randomized network topology often associated with dissociated cortical networks (Kamioka et al., 1996). The periodic bursting behavior observed with neural networks, when acquired at high framing rates (20 Hz), yielded a synchronization index for the entire culture. We divided the imaging field of view into regions of varying sizes and computed the synchronization index of neurons within the subregion. The percent difference in synchronization of a smaller neuronal network compared to the full-frame network was < 5% for networks consisting of > 40 neurons. Similarly, we found that at least 2.5 minutes of imaging spontaneous calcium activity in the dissociated cultures was necessary to achieve reasonably stable estimates of the synchronization index.

Knowledge-based automated detection of calcium transients is the most accurate spike detection algorithm

A crucial first step in the analysis of calcium fluorescence data is delineating calcium transients from resting fluctuations in fluorescence (noise). Several methods exist for spike detection. A common approach selects a threshold value based on some

predefined percentile (mean + 2* standard deviation) and identifies spikes that cross the threshold. This approach was not robust enough to detect both small and large amplitude transients (**Figure 2. 2 A,B**), yielding an optimum positive predictive value (PPV, the fraction of automatically detected spikes that are true positives) of 0.688 ± 0.08 across 22 randomly selected calcium traces, which contained 158 manually verified true spikes (**Figure 2. 2 K**). In comparison, the continuous wavelet transform to identify spike events either falsely detected spikes in noisy calcium fluorescence traces (average signal to noise ratio of < 5) or introduced small phase shifts when calcium transients are too broad or too narrow (**Figure 2. 2 C,D**). As a result, the average PPV for the wavelet transform method was $0.8395 \pm .041$ across the same imaging experiments analyzed with the threshold spike detection algorithm. Finally, a customized database of expert labeled calcium transient waveforms provided the necessary input for our knowledge-based spike detection algorithm, (**Figure 2. 2 E,F**). Given a fluorescence trace, $F_i(t)$, we compared the instantaneous similarity of $F_i(t)$ to known spike waveforms (**Figure 2. 2 G**), generating a time-varying similarity trace for each spike waveform (**Figure 2. 2 H**). Local maxima in the similarity matrix correctly identified the onset of calcium transients (**Figure 2. 2 I, J**), yielding a significantly better PPV 0.972 ± 0.065 compared to the other two methods (**Figure 2. 2 K**). For these tests, we had used a library of 20 unique spike waveforms. We next tested the sensitivity of our algorithm to the choice of spike waveforms in the library by using either 1, 5, 10, 15 or all 20 spike waveforms, chosen at random. We found that a

library of just 10 spike waveforms achieved a PPV of 0.91 ± 0.14 and correctly detected $89\% \pm 5\%$ of the total 158 calcium transients (**Figure 2. 2 L**).

Single-cell calcium dynamics and network connectivity revealed through calcium imaging

We implemented several quantitative descriptors of calcium dynamics of single-cells (**Figure 2. 3**) and networks (Figure 2. 7). Interestingly, we found large variability in the distribution of peak $[Ca^{2+}]_i$ amplitudes, ranging from $\Delta F/F_0 = 0.1$ to 3.0, in spontaneously active neurons (**Figure 2. 3 B**). Despite this large range, the variance in rise time and fall time of individual calcium transients was smaller, with a median rise time of $0.67s \pm 0.3s$ and a median fall time $1.7s \pm 0.6s$ (**Figure 2. 3 C**).

We inferred the functional connectivity of pair-wise neurons within a microcircuit by testing for statistical dependencies in their calcium activity (Figure 2. 7). We compared the similarity of the distribution of instantaneous phase difference of pair-wise neurons to the distribution generated by surrogate resampling. Amplitude adjusted Fourier transform was used to generate surrogate instantaneous phase because, rather than simple permutation, AAFT preserves the frequency content and power of the original signal but destroys phase relationship, mimicking the activity of an "unconnected" neuron. We used the Kolmogorov-Smirnov test and chose a p -value < 0.01 to infer a functional connection between the two neurons because we found that the total number of functional connections in the network were relatively insensitive to the choice of threshold beyond $p < 0.01$ (Figure 2. 7 F).

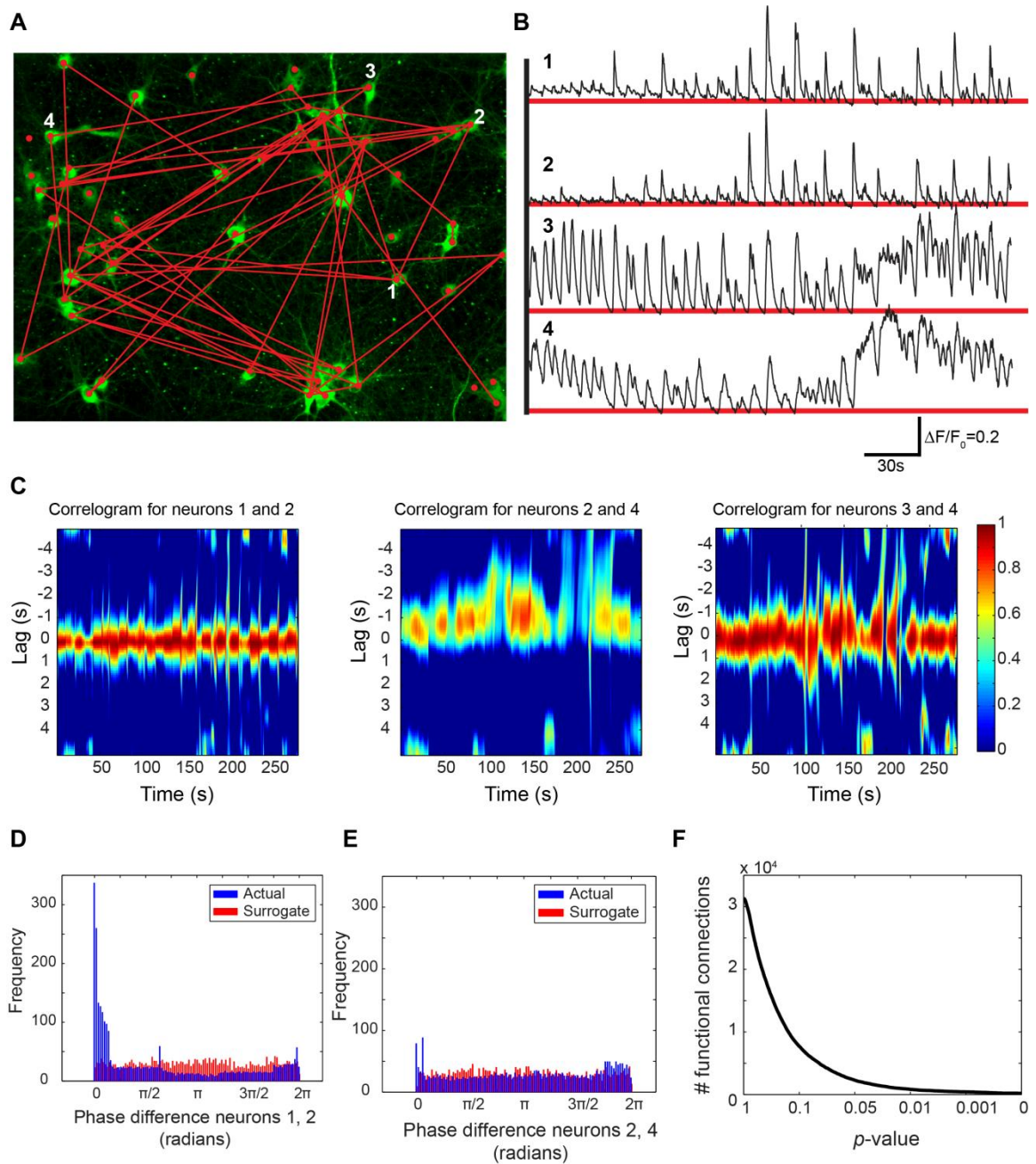


Figure 2. 7: Estimate of functional connectivity. The functional connectivity of pair-wise neurons (**A**) was determined by testing for statistical dependencies in their calcium activity. Visual inspection (**B**) and correlogram (**C**) of the fluorescence trace of 4 neurons indicated in **A**

shows temporal similarity between neuronal pairs (1,2) and (3,4) but not between the pair (2,4). The distribution of instantaneous phase difference of pair-wise neurons was compared to the distribution generated by resampling the fluorescence trace of one of neuron pairs (**D,E**). An overlap in the distributions of actual and surrogate samples is indicative of a lack of functional dependency. Kolmogorov-Smirnov test was used to test statistical similarity of the two distributions. A p -value < 0.01 was used as a threshold to infer functional connection since the total number of functional connections were relatively insensitive beyond this point (**F**).

The complete workflow for mapping functional connectivity of neuronal networks in vitro is illustrated in **Figure 2. 8**, where we quickly go from time-lapse images of calcium fluorescence to the detection of somatic calcium spikes, to temporal pattern of network activity, and functional connectivity and synchrony. Using graph theory, we identified groups of neurons with high-degree of functional connections within the groups and sparse connections between groups, i.e. communities or modules (Newman, 2006; Rubinov and Sporns, 2010), and grouped the activity map into modules. Interestingly, neuronal networks in vitro, thought to have random *structural* connectivity, show a *functional* modular organization (**Figure 2. 8 H**).

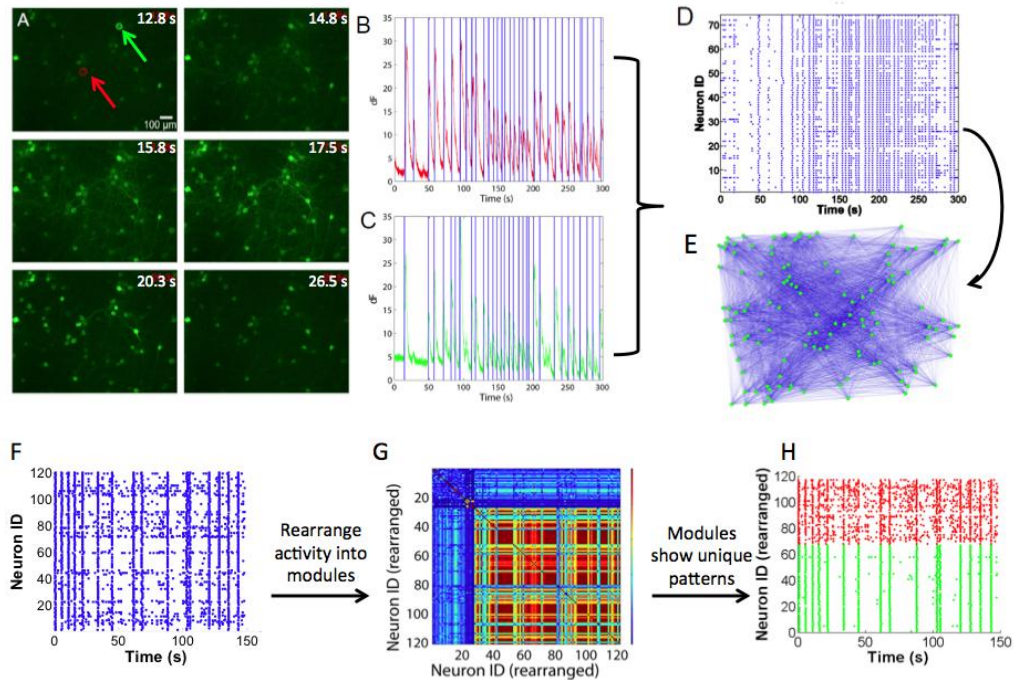


Figure 2. 8: Mapping functional connectivity of neural circuits *in vitro*. (A) Neurons are labeled with a calcium-sensitive fluorescent indicator dye. Time lapse images (time shown in each image) are analyzed, yielding the fluorescence intensity of individual neurons (B: red neuron highlighted in A; C: green neuron highlighted in A) is analyzed for peak detection, where each peak corresponds to neuronal activation. A raster plot of the activity for neurons within the entire circuit (D) is analyzed to develop the functional connectivity map of the neural circuit (E) using algorithms described above. Further analysis of an activity raster plot (F) will re-arrange subgroups of into synchronized modules (G) that show unique patterns (H; different patterns denoted by red vs. green pattern).

A final parameter that we investigated experimentally is the excitatory tone of the network. Network disinhibition with bicuculline caused synchronized calcium oscillations (Figure 2. 9 A) whose frequency was systematically reduced with increasing dose of AMPA receptor antagonist NBQX (Figure 2. 9 B-C), until oscillations abruptly stopped at certain threshold $[NBQX]$ (Figure 2. 9 D). The $[NBQX]_{\text{threshold}}/K_d$ was recorded as the excitatory tone. Similar to network synchronization, sampling from a large neuronal population may not be necessary to achieve accurate estimates of this parameter. Using a progressive inhibition of AMPA receptors in dissociated culture, we found that the measured excitatory tone would require recording activity from at least 30 neurons to achieve a stable measure with less than 5% variation. Using this as a guide, we verified that excitatory tone was modulated across development time in the dissociated cultures. Several studies indicate a progressive increase in AMPA receptor number indicated with immunoblotting and immunocytochemistry (Lin et al., 2002), and we found a similar increase in the excitatory tone that progressed and stabilized at later DIV (Figure 2. 9 E).

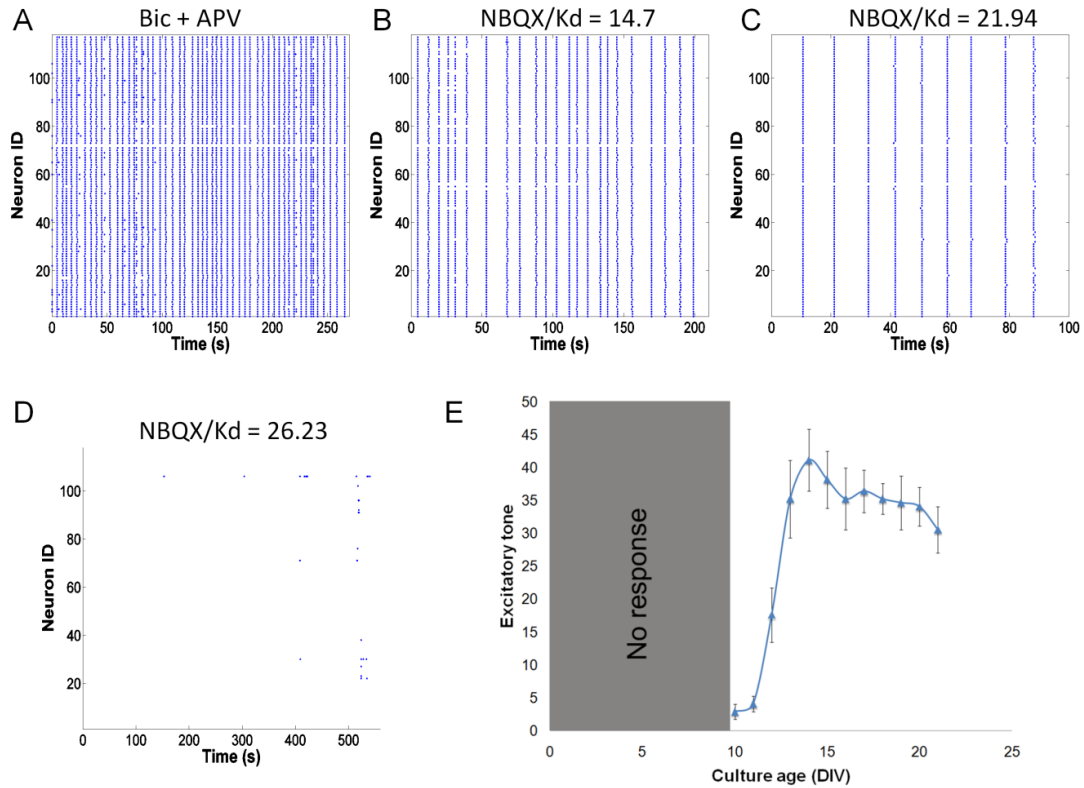


Figure 2. 9: Excitatory tone measurement. Forced oscillations were induced by network disinhibition with bicuculline (A). Progressive application of increasing [NBQX] decreased the frequency of oscillations until a critical threshold was reached when synchronous activity abruptly stopped (B-D). The excitatory tone increases as neurons mature in culture (E).

We applied the *network analysis module* of our software to better characterize the repertoire of spontaneously generated activity patterns at different stages during developmental maturation of embryonically derived cortical neurons in culture. Separately, we used the *single-cell phenotyping module* to investigate whether overexpression of a human mutant variant of the microtubule-associated protein tau disrupts the calcium homeostasis of neurons expressing the transgene and whether these

neurons can be distinguished from wild-type based solely on the dynamics of calcium activity.

Developmental changes in the frequency and coordination of neuronal network activity

Embryonic neurons in cultures form synaptic connections and undergo many similar developmental changes in receptor composition and phenotypic maturation that occur *in vivo* (Lesuisse and Martin, 2002). We imaged the spontaneous calcium activity of a population of neurons throughout this maturation process, beginning on day 8 *in vitro* (DIV 8) through day 21 (DIV 21). The activity of a microcircuit from each imaging session was time aligned using a network-wide burst event. The full raster plot of activity from DIV 8 - 21 is shown in **Figure 2. 10 A**, where each dot, color-coded by culture age, represents the onset of a calcium transient from a given neuron label assigned arbitrarily. Activity of a young network (DIV 8 -11) was sparse and uncoordinated, showing few rhythmic transitions between UP and DOWN states (**Figure 2. 10 B**). The frequency of spontaneous activity rapidly increased over DIV 12 - 14, reaching its peak at DIV 14 and subsequently reached a plateau over DIV 18-21 (**Figure 2. 10 A-B**). The pattern of coordinated activity followed a similar trend; the activity of young neurons was uncoordinated but became highly synchronized by DIV 14 and settled to a plateau by DIV 18 (**Figure 2. 10 C-D**). This evolution of network activity is consistent with the model that neurons in culture undergo a period of rapid synaptic growth and strengthening, followed by synaptic pruning, reaching the completion of developmental

synaptic modification at ~ 18 DIV (Nakanishi and Kukita, 1998; Nakayama et al., 2005; Passafaro et al., 2003; Tetzlaff et al., 2010; Voigt et al., 2005)

In addition to the structural remodeling associated with developmental maturation of neuronal networks, networks undergo a change in the balance of inhibition and excitation. In contrast to the mature brain, in which GABA is the major inhibitory neurotransmitter, in the developing brain GABA can be excitatory (Ben-Ari, 2002). We applied bicuculline, a GABA_A antagonist to neuronal cultures at different points in their development and measured the change in the frequency of calcium events and the synchronization of the network. In young cultures (DIV 8 - 11), bicuculline treatment significantly reduced excitatory activity and abolished synchrony. In contrast, exposure to bicuculline in older cultures (DIV 14+) significantly enhanced synchronized activity (**Figure 2. 10 D**), consistent with previous reports indicating that GABA_A receptor activation is a major route of excitation in young neurons, primarily from the altered expression of chloride transporters KCC2 and NKCC1 (Fukuda et al., 1998; Ganguly et al., 2001; Rivera et al., 1999; Yamada et al., 2004)

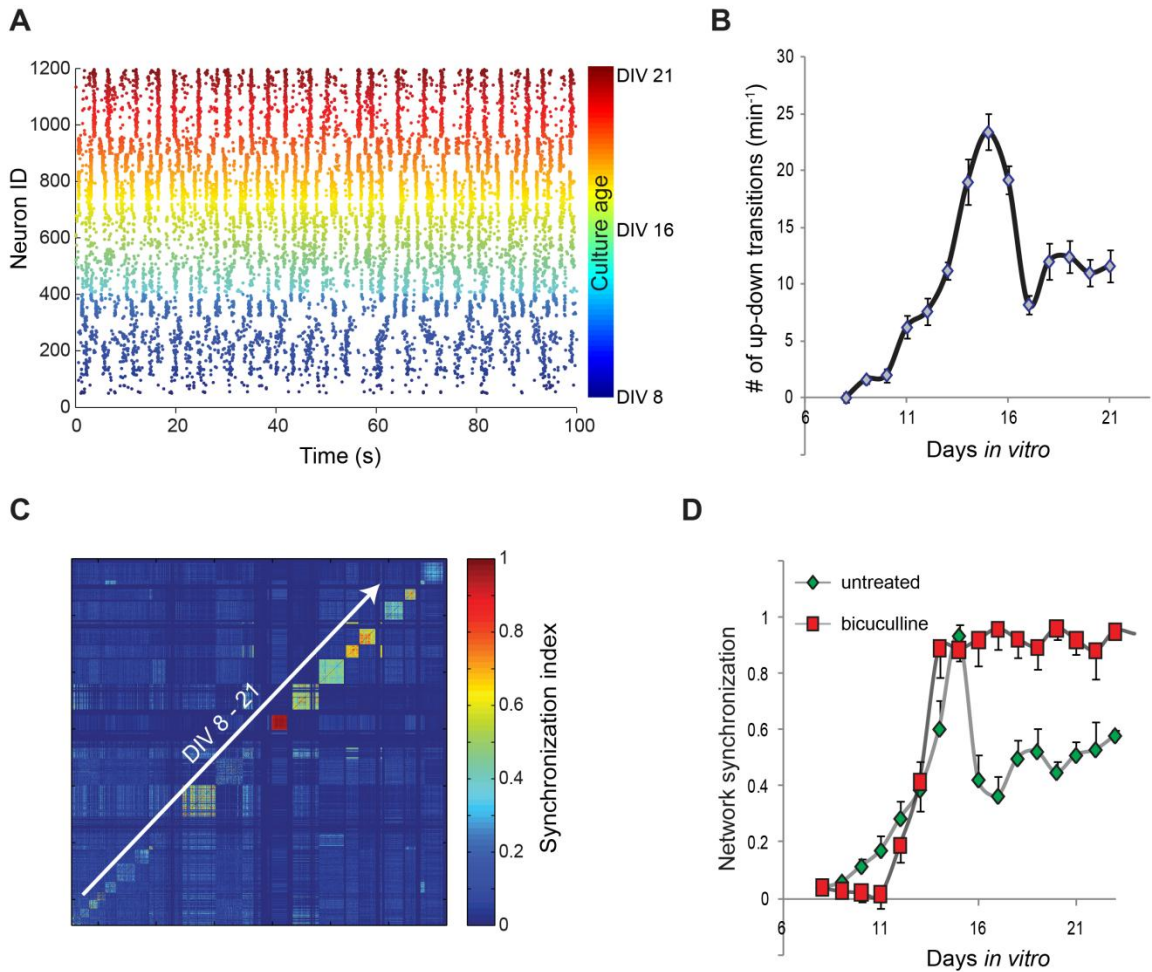


Figure 2. 10: Developmental changes in network activity patterns. **A:** Spontaneous activity patterns of neurons at different stages in development, colored-coded by age (days *in vitro*, DIV) and time-aligned for visual comparison, shows increasing frequency and greater complexity of activity as neurons mature. **B:** Network-bursts, recorded as simultaneous calcium spike in >90% of neurons in the imaging field of view, represent the transitions between depolarized (UP) and hyperpolarized (DOWN) states of the network. The number of UP-DOWN states per minutes gradually increased over

development and reached its peak at DIV 14, consistent with increased synaptic growth and strength. This was followed by a significant decrease in the frequency of network bursts over DIV 15-16, and a plateau DIV 18+. **C, D:** The pattern of activity became increasingly synchronized as neurons matured in culture and reached its peak at DIV 14 characterized by periodic synchronized calcium oscillations. Beyond DIV 14, spontaneous activity was moderately synchronized, characterized by a mix of synchronized network-wide bursts and intermittent flickering events. Antagonizing the GABA_A receptor with bicuculline forced synchronized calcium oscillations in mature (DIV 14+) cultures because of recurrent excitation and network disinhibition. In comparison, bicuculline greatly reduced the frequency and coordination of activity in immature cultures (DIV 8-12), likely due to the excitatory role of GABA in early development.

Lewy body pathology impairs network synchrony and connectivity

We used an *in vitro* model of Lewy body pathology to confirm that calcium imaging based estimates of network synchrony and functional connectivity show predictable changes under pathological conditions. Aggregates of amyloid proteins characterize many neurodegenerative disorders including Alzheimer's disease (AD) and Parkinson's disease (PD). Formation of pathological inclusions occurs in a multistep process including the misfolding of normal soluble proteins and their association into higher order oligomers, followed by their assembly into amyloid fibrils that form disease specific inclusions (Conway et al., 2000; Uversky et al., 2001). Proteinaceous aggregates

composed of tau and α -synuclein, characteristic lesions of AD and PD respectively, can induce pathology in health cells (Clavaguera et al., 2009; Desplats et al., 2009; Frost et al., 2009; Guo and Lee, 2011; Luk et al., 2009). Recently, our collaborators in Virginia Lee's research group found that the formation of PD-like Lewy bodies (LBs) and Lewy neurites (LNs) in cultured neurons can be facilitated under physiological conditions using pure WT α -syn pre-formed fibrils (pffs) and endogenous levels of α -syn expression (Figure 2. 11 A). LN-like accumulations were initially detected in axons and α -syn pathology then propagated to the cell body where LB-like inclusions developed (Figure 2. 11 B). They report that the Formation of these PD-like α -syn LNs and LBs caused selective reductions in synaptic vesicle-associated SNARE proteins, Snap25 and VAMP2, as well as proteins that participate in exo-endocytic synaptic vesicle cycle such as CSP α , and synapsin II (Volpicelli-Daley et al., 2011).

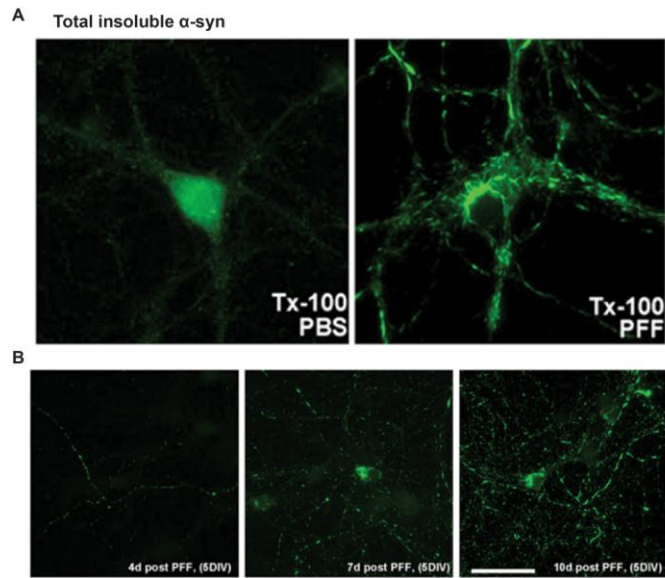


Figure 2. 11: α -syn pffs recruit endogenous α -syn to form pathologic, insoluble aggregates.

A: Two weeks after pff addition, neurons were fixed with paraformaldehyde with 1% Tx-100 to extract soluble proteins. Addition of α -syn pffs formed Tx-100 insoluble aggregates. **B:** Time dependence of aggregate formation. α -syn pffs were added to DIV 5 neurons and fixed either 4, 7, or 10 days later. Small puncta corresponding to neuritic p- α -syn were visible 4 days after pff addition, and by 7 days, neuritic p- α -syn levels increased, and accumulations were visible in some cell bodies. Ten days after addition of pffs, p- α -syn was seen throughout the neurites as small puncta, longer fibrous structures, and as somal inclusions. Image adapted from (Volpicelli-Daley et al., 2011) with permission.

The decreased levels of synaptic proteins and the presence of pathological inclusions in neurites suggest impairment in neural network activity. Calcium imaging of hippocampal neurons loaded with the calcium-sensitive fluorescent dye, Fluo-4 AM, was performed to investigate the effect of α -syn aggregates on the activity patterns of the in

vitro neural network established by these cultured neurons. The spontaneous activity of neurons treated with PBS was characterized by flickering events, intermixed with network-wide bursts when nearly all the neurons were simultaneously firing as reflected by a high synchronization index (Figure 2. 12 A). In contrast, neurons treated with α -syn pffs showed a significant decrease in synchronized activity as early as 4 days after treatment (Figure 2. 12 B). At this time point, low levels of α -syn aggregates were visualized exclusively in axons by immunofluorescence microscopy, and no pathological α -syn was detect biochemically. Yet, this level of axonal pathology was sufficient to impair coordinated network activity. This reduction in synchronized activity persisted at 7, 10, and 14 days after α -syn pff treatment (Figure 2. 12 B). In contrast, α -syn pff treated neurons from α -syn $-/-$ mice showed no impairments in synchronization index, indicating that these effects are selective for neurons harboring α -syn aggregates and do not result from exogenously added pffs.

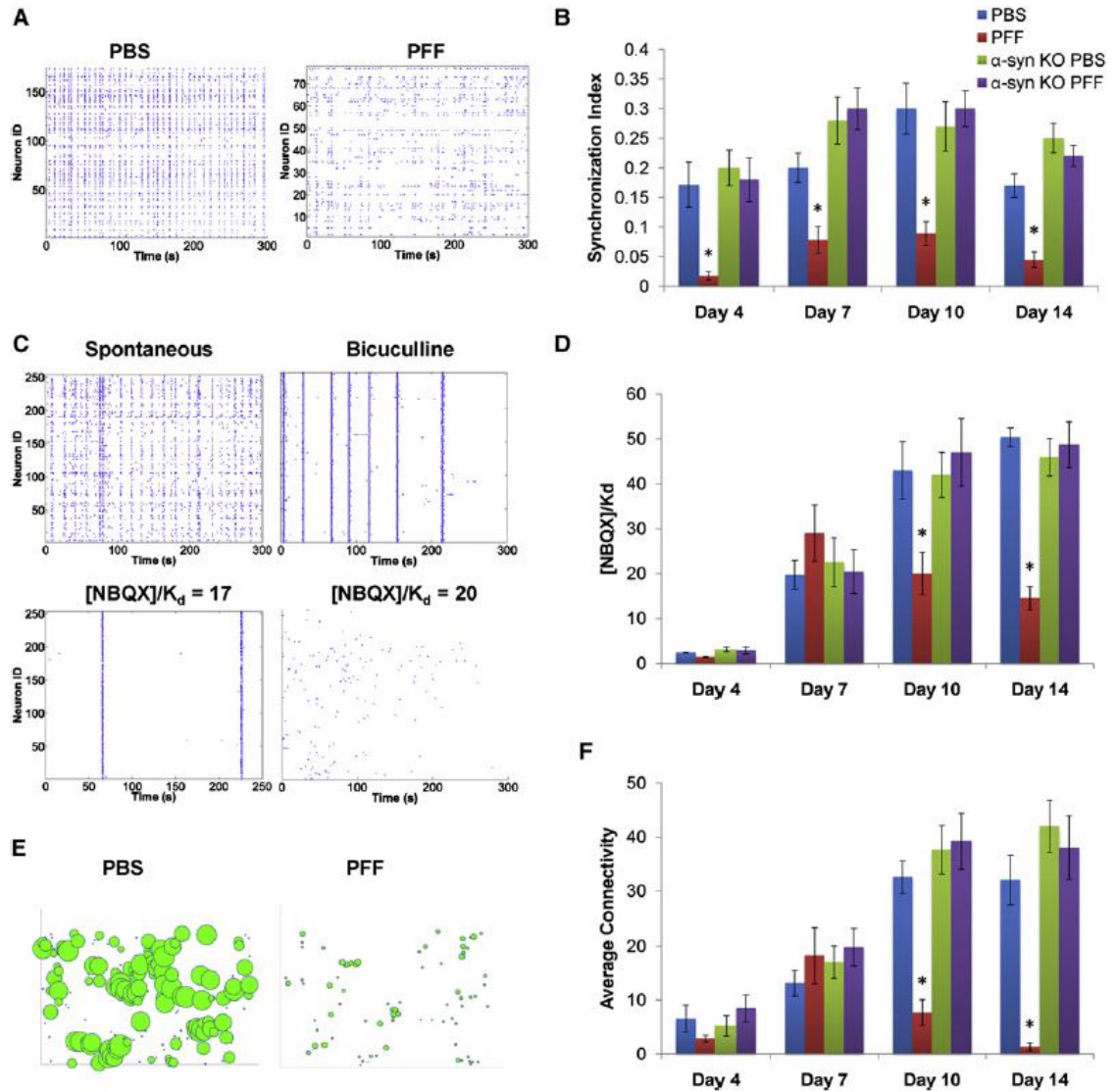


Figure 2. 12: Effect of aggregate formation on neural network activity. Calcium imaging on hippocampal neurons loaded with the calcium-sensitive fluorescent dye, Fluo4-AM, was performed. **A:** PBS-treated neurons showed flickering events and simultaneous bursting. The spontaneous activity in α -syn pff-treated WT neurons showed reduced coordination and frequency of oscillations. **B:** The level of coordinated spontaneous activity was quantified as the synchronization index. α -syn pff-treated neurons (red) showed a significant decrease in

synchronicity by day 4, relative to PBS-treated neurons (blue) and the deficit continued for longer treatment duration. Primary neurons from α -syn $-/-$ mice treated with α -syn pffs (purple) did not show reductions in the synchronization index relative to PBS-treated neurons (green). **C:** Excitatory tone in the network was determined by recording spontaneous activity and then by forcing synchronous oscillations via network disinhibition with bicuculline. Incremental concentrations of NBQX were added until coordinated activity stopped and the excitatory tone was reported as $[\text{NBQX}]/K_d$. **D:** Excitatory tone in PBS (blue) and α -syn pff (red)-treated neurons, showed significant decreases by 10 as well as 14 days after pff treatment. Addition of α -syn pffs to α -syn $-/-$ neurons did not affect excitatory tone. **E:** Functional network connectivity, derived from the rasters in **A**, is depicted as nodes (neurons) of varying sized, where the size of a given node is scaled to reflect the total number of connections to that particular node. **F:** The average number of connections per neuron was determined from functional connectivity map. Compared to PBS, α -syn pff-treated neurons has fewer numbers of functional connections. Connectivity of α -syn pff-treated α -syn $-/-$ neurons were similar to PBS-treated neurons. PBS-treated: day 4, n=9; day 7, n=11; day 10, n=10; day 14, n=9. PFF-treated: day 4, n=9; day 7, n=12; day 10, n=11; day 14, n=9.

We next determined whether the progressive recruitment of α -syn into pathologic aggregates and the decrease in synaptic SNARE proteins correlated with changes in the frequency of activity or the excitatory tone of the network. First, synchronous oscillations were forced using the GABA_A antagonist, bicuculline, to abolish inhibitory input, followed by increasing doses of the AMPA receptor antagonist, NBQX, until synchronous oscillations stopped. The final concentration of NBQX require to impair

activity within the excitatory network determined the excitatory tone (Figure 2. 12 C). No significant changes in excitatory tone was detected in cultures 4 or 7 days after α -syn pff treatment but by 10 and 14 days after treatment, when increasing accumulation of neuritic and perikaryal pathology was observed, there were significant reductions in excitatory tone, reflecting compromised synaptic activity (Figure 2. 12 D). Again, neurons from α -syn $-/-$ mice did not show impairments in excitatory tone at 10 and 14 days after pff treatment, confirming that the effects result from the accumulation of endogenous α -syn aggregates.

Since spatiotemporal patterns of activity are shaped by the underlying connectivity architecture and the relative balance of excitation and inhibition, we used network activity patterns to determine the functional connectivity in PBS and α -syn pff-treated neurons. As neurons matured *in vitro*, the number of functional connections increased and eventually plateau (Figure 2. 12 F). The timeframe for this correlated well with neurite sprouting and synapse stabilization. However, in α -syn pff-treated WT, but not α -syn $-/-$ neurons, the maturation of functional connections never reached the level achieved in PBS-treated cultures, as a significant reduction was observed 10 days after α -syn pff treatment. This functional connectivity was severely compromised 14 days after treatment and the network consisted of just a few sparse connections at this time point (Figure 2. 12 F). In summary, the formation of insoluble aggregates of endogenous α -syn results in early disruptions in coordinated network activity. Later, as more α -syn

inclusions develop and propagate throughout the neuron, excitatory tone is decreased and functional connectivity is greatly reduced.

Expression of human mutant variant of tau is associated with altered calcium homeostasis

As a separate application of our software, we investigated if the shape of calcium transients of individual cells can be used to develop functional neuron subgroups, or phenotypes, that can exist in a heterogeneous neuronal ensemble. To test, we cultured mouse embryonic hippocampal neurons that either contained human mutant tau variant (P301S) or wild-type tau protein, derived from cross of PS19 transgenic mouse line with wild-type mouse. We imaged the spontaneous calcium activity of this microcircuit using fluorescent calcium indicator, fluo-4 (**Figure 2. 13 A**). The cultures were fixed and probed for P301S tau using 12025 antibody to identify neurons within the same microcircuit that expressed the transgene (**Figure 2. 13 B**).

We extracted 4 relevant shape features from spontaneously generated calcium transients for a given neuron, which included fluorescence at the onset of a transient, F_0 , the peak amplitude of the transient, $\Delta F/F_0$, rise time, t_{rise} , and fall time, t_{fall} . Each calcium transient arose from a neuron expressing either transgenic or wt tau protein (**Figure 2. 13 C**). We projected the dataset into a lower dimensional space spanned by the first 2 principal components that were derived from a linear combination of the 4 shape-based features. Each dot in **Figure 2. 13 D** is the projection of quantifiable features of a single calcium transient. We found that two clusters readily emerged in the principal component

space. Given that a principal component analysis identifies the combination of the original variables that has the largest possible variation, the emergence of clusters or groups is highly suggestive of the presence of discriminating characteristics between calcium transients of P301S and wild-type neurons. We found that the resting free intracellular calcium, $[Ca^{2+}]_i$, and peak calcium amplitude of P301S tau expressing neurons undergoing spontaneous activity were significantly larger compared to neurons expressing wild-type tau (P301S tau $\Delta F/F_0$: 0.059 ± 0.004 vs. wild-type 0.043 ± 0.002 , $p < 0.001$, $n=54$; P301S tau $[Ca^{2+}]_i$: $128\text{nM} \pm 2.1\text{nM}$ vs. wild-type $95\text{ nm} \pm 2.8$, $p < 0.001$) (**Figure 2. 13 E**). Although spontaneously generated calcium transients of transgenic neurons reached a higher peak amplitude, these transients were significantly shorter-lived, resulting in equal calcium load (area under the curve of calcium transients) for transgenic and wild-type neurons (P301S t_{fall} : $0.92\text{s} \pm 0.15\text{s}$ vs. wild-type: $1.41\text{s} \pm 0.16\text{s}$, $p = 0.027$; P301S calcium load: 0.05 ± 0.009 vs. wild-type 0.063 ± 0.008 , $p > 0.05$) (**Figure 2. 13 E**). These alterations in the kinetics of calcium transients likely have an electrophysiological basis since expression of a different human mutant tau variant, P301L, has been shown to raise neuronal resting membrane potential, increase evoked action potential firing rate and decrease the duration of single action potentials (Rocher et al., 2010).

In addition to alterations in the kinetics of calcium transients, we used our software analysis module to identify if additional features separated neurons expressing mutant protein from other neurons expressing wildtype protein. We found that the

expression of P301S tau protein did not significantly change the pattern of network activity or the functional integration of these neurons in the network, likely because the fraction of neurons expressing the transgene was typically $< 10\%$. Together, these data demonstrate the utility of our calcium imaging software in two broad applications - monitoring the temporal evolution of network activity and single-cell phenotyping using features extracted from the shape of spontaneously generated calcium transients.

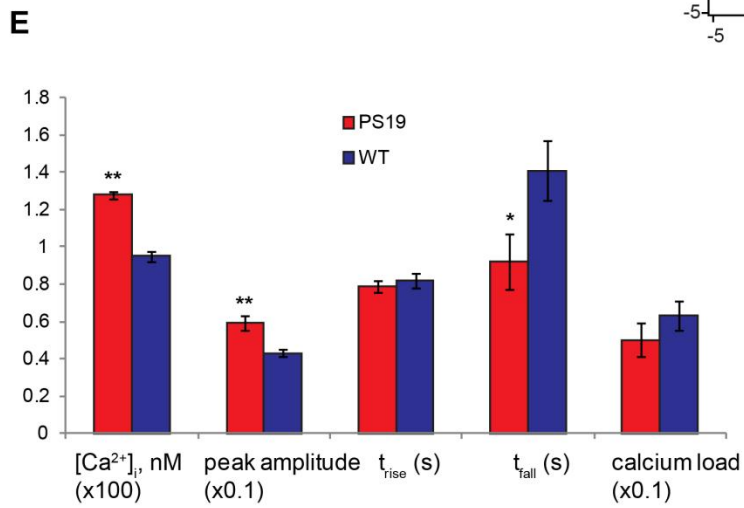
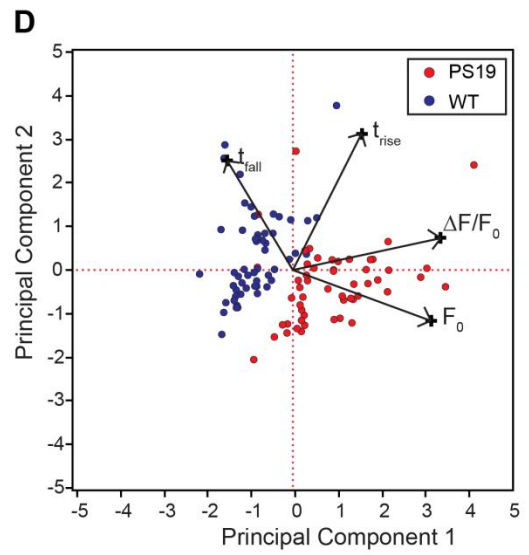
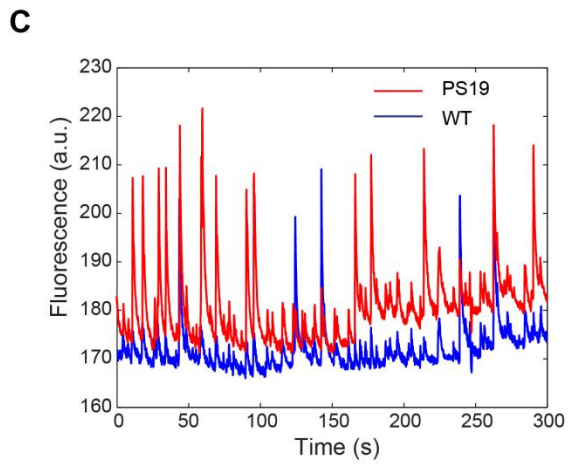
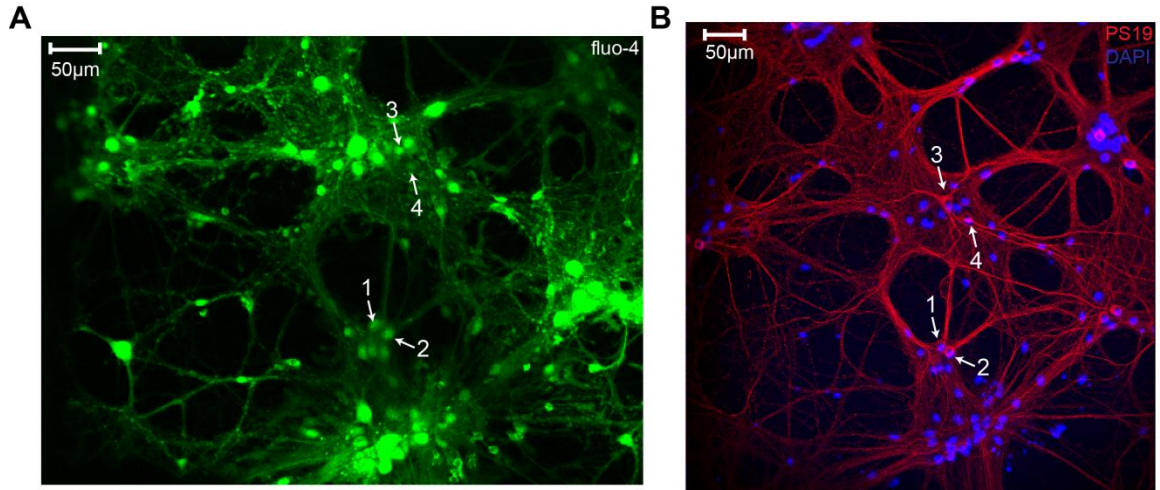


Figure 2. 13: Single-cell phenotypes revealed by calcium imaging. **A:** The spontaneous activity of mouse hippocampal neurons was recorded with the fluorescent calcium indicator, Fluo4-AM. **B:** Following calcium imaging, cells were fixed and probed for the expression of P301S tau protein with 12025 antibody (red - PS19, blue - DAPI). The same field of view used for calcium imaging was used during immunofluorescence microscopy to identify individual neurons that expressed the transgene (example of 4 co-registered neurons is indicated). **C:** Comparison of the average fluorescence trace of a representative neuron expressing the human mutant variant of tau (red) and wild-type neuron (blue) showed some obvious differences in the baseline fluorescence and amplitudes of calcium transients. **D:** Shape-based features of each calcium transient, including the fluorescence at the onset of a spike, peak amplitude, and characteristic rise and fall times, were computed and projected onto a 2-dimensional principal component space. Two clusters readily emerged in the principal component space, corresponding to neurons expressing mutant tau (red) or wild-type tau (blue). **E:** Resting $[Ca^{2+}]_i$ and peak amplitude were significantly larger in PS19 neurons and compared to wild-type. However, the duration of calcium transients was significantly shorter, resulting in similar calcium load between PS19 and WT neurons. PS19 n=54, WT, n=53. (** $p<0.01$, * $p<0.05$).

Discussion

In this chapter, we assessed fluorescence based imaging methods and created an automated workflow for mapping neural network properties *in vitro*. We used our analysis to design experiments to test the sensitivity of calcium imaging-based estimates of network properties in model systems with known physiological and pathological network alternations. We found that the pattern of network activity became more synchronized as neurons underwent developmental maturation *in vitro*, consistent with a period of synaptic growth and strengthening. As neurons continued to mature, activity pattern became more complex, characterized by few network-wide burst events intermixed with many flickering events, consistent with synaptic pruning. The degree distribution of functional connectivity of mature networks matched previous reports and showed a modular organization, consistent with a pseudo-random structural connectivity. Then, we used a novel, well-characterized model of Lewy body pathology to determine whether structural changes in the neurites and soma (α -syn inclusions) also result in functional impairments in the network. Surprisingly, we found evidence of decreased synchrony in α -syn pff-treated neurons at very early time points, when only low levels of α -syn aggregates were visualized exclusively in axons by immunofluorescence microscopy, and no pathological α -syn was detected biochemically. This suggests that estimates of network properties derived using functional calcium imaging can be sensitive indicators of even minor alterations in the physiology of neurons. In a separate study, we found that population calcium imaging can be nearly as sensitive as single-cell

electrophysiology in identifying phenotypic alterations of overexpression of human mutant variant of tau protein.

A number of recent efforts developed and characterized the ability of existing and new molecular probes to function as a surrogate indicator of single cell electrical activity. These efforts are now positioned to probe network dynamics and complement traditional microelectrode array technologies. Our predictions of probe sensitivity, accuracy, and minimum detection thresholds for network topology are supported by measurements in parallel on dissociated cortical neuron networks. Similar to past work (Fetcho et al., 1998; Stosiek et al., 2003), we find the relatively high speed imaging requirements restricts the use of probes to those with high efficiency and single emission capability – notably, Fluo-4 and some GCaMP variants. New contributions from our work include estimates for the number of neurons and the acquisition time period necessary to accurately capture descriptors of the network. These minimal imaging requirements will help set the framework for experiments where it may be useful to map the response of the network to any given stimulus. It is important to point out that our analysis assumed stability of the network topology during the imaging period. Certainly, any *in vitro* neural circuit exhibits the potential to change the strength, number, and degree of connections over time. The relatively short imaging periods needed to estimate network connectivity makes this approach ideal for studying changes in neural circuits that occur during development, in response to prolonged exposure to chemical treatment, or mechanical stimulus. Less ideal are conditions where the network changes in seconds; to

our knowledge, there is no optical imaging technology available to perform such a rapid examination of the network and microelectrode arrays may be a more appropriate approach.

In addition to identifying optimal imaging conditions, we created a comprehensive workflow for the automated analysis of calcium imaging. for the automated analysis of single-neuron and neuronal network properties using data acquired from *in vitro* or *in vivo* calcium imaging. Functional multineuron calcium imaging is becoming a more widely accessible and an important tool for measuring the effects of experimental manipulations on the activity of individual neurons and microcircuits. Many research groups use custom-coded algorithms for analyzing their data but these software routines are either not published or poorly documented, are in different programming languages, and the output from one algorithm is not always appropriately formatted as the input to the next step, limiting integration into a workflow. These restrictions create a technical barrier for biologists, who may not be well-versed in programming, to use many of these tools for interrogating microcircuit function. Our open-source software and the accompanying graphic user interface provide a comprehensive solution for the analysis of neuronal microcircuits.

Unlike other reports that focus on detection of cell bodies in an image frame (segmentation) (Mukamel et al., 2009; Ozden et al., 2008; Tomek et al., 2013), our software used a new segmentation method and also automated the measurement of additional biologically-relevant features describing the function of both single-neurons

and networks. At the single-neuron scale, we automatically detected the onset of $[Ca^{2+}]_i$ transients using a novel spike detection algorithm and measured the dynamics of each event, including peak amplitude, rise time, fall time, and resting fluorescence. We showed that these measurements of single-neuron calcium dynamics discriminated between two distinct neuronal populations within a dissociated culture of hippocampal neurons. Our measures of single neuron dynamics corresponded to measured differences in electrophysiological properties of individual PS19+ neurons compared to wildtype. At the network scale, we automatically compute the pair-wise synchronization of each neuron and quantify the level of global and local synchrony. We infer the functional connectivity of the microcircuit through a novel surrogate resampling method. Previous reports used temporal correlations between pair-wise time-series to determine functional connections (van den Heuvel et al., 2008), but this method is sensitive to noise fluctuations and requires the use of an arbitrary threshold to binarize correlation coefficients. Instead, we used the instantaneous phase of pair-wise neurons to determine statistically significant linear and non-linear dependencies through the use of surrogate resampling. We find that the activity patterns of groups of neurons from different functional modules also display distinct temporal patterns of activity. The patterns of activity evolve overtime as neurons undergo developmental maturation *in vitro*.

To increase usability, we created several routines that allow interactive exploration of the dataset. Users can inspect the raw fluorescence trace of any arbitrary neuron in the field of view with a simple mouse click and examine the functional

integration of the selected neuron to the rest of the network. Such level of exploration will be especially useful to investigate the role of particular neuronal subtypes or targeted gene manipulations on neuronal network function and dynamics of activity. We also anticipated shortcomings in automated segmentation of neurons and spike detection if image quality or SNR is extremely poor. To improve accuracy, we created GUI modules to remove falsely detected ROIs from the image series. Similarly, interactive adjustment of spike detection threshold or modifications to the spike waveform library could both improve accuracy. However, we found that knowledge-based spike detection is accurate, even with a few spike waveforms.

We used the calcium imaging software to analyze known behavior of circuits. The change in spontaneous patterns of activity over time as neurons mature *in vitro* is consistent with reports of synaptic growth and strengthening followed by synaptic pruning. Importantly, we identified subtle changes in network synchronization and the frequency of oscillations through calcium imaging that could not be possible with other modalities

We also investigated the sensitivity and biological interpretation of some of our network measurements using well-characterized disease models of known underlying etiology and pathology. Our research collaborators found that the recruitment of endogenously expressed α -syn into inclusions following treatment with α -syn pre-formed fibrils resulted in pathological aggregates in neurites and soma, accompanied by reduced levels of synaptic proteins. We used this model to investigate whether functional

measurements of network activity and excitability follow a similar timeframe as the progression of aggregate pathology. We found a diminished neuronal synchronization early after pff addition when only small aggregates are visible only in axons, suggesting that even minor burden of α -syn pathology can have a major impact on the coordinated activation of neuronal ensembles. By 10 days and 14 days after pff treatment, when pathology is extensive, neuronal excitability and connectivity is substantially reduced, which may be accounted for by the reductions in presynaptic proteins. Sequestration of α -syn away from the presynaptic terminal into insoluble inclusions may impair the homeostasis of presynaptic proteins and consequently, synaptic vesicle exocytosis since α -syn, in cooperation with CSP α , may act as a chaperone to maintain presynaptic SNARE complex assembly (Burre et al., 2010; Chandra et al., 2005).

Indeed, one major strength of our software is the analysis of calcium imaging at multiple length scales. We tested whether our single-cell measurements of the kinetics of calcium transients are informative in phenotyping a heterogeneous cell population, using immunofluorescence as gold standard. We could readily distinguish neurons from astrocytes based solely on the duration of calcium transients, since nearly all calcium activity in neurons was much shorter ($< 2s$) relative to astrocytic calcium waves, which could last for up to 5 - 10 seconds. Following calcium imaging, we co-labeled cultures with MAP-2 and GFAP to identify neurons and glia, respectively, and achieved $> 90\%$ classification accuracy. We could not accurately assign a neuron or astrocyte label to cells that did not exhibit spontaneous activity.

We next determined if we could distinguish excitatory neurons from inhibitory neurons, based solely on the characteristic of calcium transients. Inhibitory neurons express distinct phenotypic markers such as parvalbumin or cholecystinin and have exhibit fast-spiking activity that distinguish them from excitatory neurons. Given these differences, we expected that the spontaneous calcium activity of interneurons would be uniquely different from excitatory neurons. Indeed we found that some neurons had significantly more calcium transients than others, but we were not able to definitively identify interneurons with immunofluorescence using either parvalbumin, or GAD-67 antibodies. We found that nearly all neurons were diffusely labeled, possibly because interneurons in culture do not express parvalbumin and GAD67 immunoreactivity until very late in development (Kinney et al., 2006). Furthermore, previous attempts to use *in vivo* 2-photon calcium imaging failed to reveal significant differences among the spontaneous calcium transients (frequency, amplitude, or shape of transients) that would correspond to the post hoc classification of GABAergic or excitatory neurons with immunostaining (Langer and Helmchen, 2012).

Instead, we chose a different system to examine if differences in calcium transients appear in a heterogeneous population of neurons expressing a transgenic or wild-type tau protein. In the PS19 transgenic mouse model, monogenic expression of mutant human tau variant P301S leads to development of neurofibrillary tangles, memory impairment, and neuronal death, reminiscent of human tauopathies. Interestingly, cultured neurons from PS19 mice do not spontaneously develop NFTs. However,

alterations in the electrophysiology and morphology of individual neurons has been reported in cortical slices prepared from a P301L transgenic mouse and wild-type littermate. Thus, we prepared neuronal cultures from a cross between a heterozygous PS19 and a wild-type mouse, resulting in a heterogeneous cell population where neurons expressed either 0 or 1 copy of the mutant P301S tau. We found that although spontaneous patterns of network activity were not different between mutant and wild-type neurons, we consistently observed differences in the spontaneous calcium transients. Notably, we found that the resting intracellular $[Ca^{2+}]$ and peak transient amplitude were significantly elevated in neurons expressing P301S tau relative to wild-type but the duration of calcium transients was significantly reduced, resulting in the same amount of calcium load per event. These calcium-imaged based observations are consistent with an elevated resting membrane potential (+ 8 mV) and shorter duration of single APs in P301L transgenic cells recorded by electrophysiology. Single cell resolution of calcium imaging may provide a direct ability to compare a mixture of neurons in other transgenic or disease models.

Strictly speaking, a calcium transient only identifies an electrically active neuron and we are careful not to include an algorithm to extract either the number or action potentials contained within a transient or, in addition, the frequency of the bursts contained with a calcium transient event. Although new genetically encoded calcium indicators have near single action-potential resolution and a graded increase in fluorescence with firing rate (Akerboom et al., 2009; Tian et al., 2009), extracting more

detailed information on either spike rate or number requires a thorough calibration of each experimental system and would not be an easily generalizable feature of our open source software. Similarly, although calcium imaging has been used to infer functional connectivity, it is not demonstrable proof of structural connectivity. Functional connectivity is much more dynamic and dependent on the experimental context or the task (Friston, 2011), however consistent changes in functional connectivity are highly suggestive of differences in the flow of information through neuronal networks. As Ca^{2+} imaging methods improve (better indicators, fast microscopes), our ability to discern the functional connectivity of interconnected neurons will undoubtedly improve in parallel. To this end, our previous work investigated the relative improvement in connectivity of the actual network vs. the connectivity estimated from calcium imaging data and we showed that we approach the optimal limit of matching structural connectivity with functional connectivity estimates under the imaging conditions employed in this study (Patel et al., 2012). Using this previous work as background, we used surrogate resampling techniques to identify statistically significant temporal interactions between pair-wise neurons, thereby eliminating the use of empirical threshold parameters and standardizing the analysis between experiments or laboratory settings.

We believe the tools developed in this Chapter significantly extend the repertoire of image-derived quantitative metrics of network function. To our knowledge, no commercial software exists for automated analysis of calcium imaging and the only other publicly available software is limited to segmentation and measurement of fluorescence

versus time trace for each region of interest (Tomek et al., 2013). Several past reports use calcium imaging (and custom-coded analysis routines) to investigate the microarchitecture of local brain regions in anesthetized, awake and task-engaged animals (Dombeck et al., 2007; Greenberg et al., 2008; Kerr et al., 2007; Kerr et al., 2005; Petersen, 2007; Sato et al., 2007). Publically available tools have already had a clear benefit in the analysis of fMRI, EEG and electrophysiology data by offering research groups access to advanced routines and algorithms that go beyond the skills and expertise of an individual group (Cox, 1996; Cui et al., 2008; Delorme and Makeig, 2004; Duann et al., 2002; Meier et al., 2008; Quiroga et al., 2004; Spacek et al., 2008). Similar code sharing is only recently beginning to happen for calcium imaging datasets, partly because experimental tools for accurate interrogation of neuronal networks at sufficient spatial and temporal resolution are only recently becoming more widely available. We expect the continued use of functional multineuronal calcium imaging, combined with our framework for analysis will advance our understanding of how information flow within and across distributed brain networks drive behavior or contribute to disease.

CHAPTER 3: Single neuron NMDA receptor phenotype dictates neuronal rewiring and re-integration following traumatic injury

ABSTRACT:

Despite its enormous incidence, mild traumatic brain injury is not well understood. One aspect that needs more definition is how the mechanical energy during injury affects neural circuit function. Recent developments in cellular imaging probes provide an opportunity to assess the dynamic state of neural networks with single-cell resolution. In this Chapter, we applied the methodologies developed in the previous Chapter to evaluate if mild mechanical injury to cortical neurons produces graded changes to either spontaneous network activity or altered network topology. We found that modest injury produced a transient increase in calcium activity that dissipated within 1hr after injury. Alternatively, moderate mechanical injury produced immediate disruption in network synchrony, loss in excitatory tone, and increased modular topology. A calcium-activated neutral protease (calpain) was a key intermediary in these changes; blocking calpain activation restored the network nearly completely to its pre-injury state. With the ability to analyze individual neurons in a circuit before and after injury, we identified several nodal biomarkers that confer increased risk or protection from mechanical injury. We found that pre-injury connectivity and NMDA receptor subtype composition (NR2A and NR2B content) are important predictors of node loss and remodeling. Mechanistically, stretch injury caused a reduction in voltage-dependent Mg^{2+} block of the NR2B-cotaining

NMDA receptors, resulting in increased uncorrelated activity both at the single channel and network level. The reduced coincidence detection of the NMDA receptor further impaired network function by limiting plasticity, which was rescued by pairing an LTP stimulus with NR2B antagonists.

INTRODUCTION:

Mild traumatic brain injury (mTBI) is the most common form of head injury with an estimated incidence of 1.2 million cases per year. Concussions are a form of mild traumatic brain injury that represents at least 80% of the traumatic brain injuries occurring each year in the United States (Kraus and Nourjah, 1988). Although often associated with sports, the majorities of concussions occur outside of sporting activities and include motor vehicle accidents, falls, and any situation involving sudden acceleration or deceleration of the head. Long considered an injury that was ‘inevitable’ with little recourse, the growing awareness of the long-term effects of concussion led to a renewed focus on understanding, preventing, and treating concussions.

Despite its name, the consequences of mild TBI are not "mild"; 30%-80% of patients diagnosed with mTBI experience disabling problems, such as persistent headaches, fatigue, changes in sleep patterns, sensory problems (post-concussion syndrome), and mood changes (Alexander, 1995; Hall and Chapman, 2005; Kushner, 1998). In addition, repetitive mTBI is correlated to delayed neurodegenerative changes, often accompanied by severe decline in cognitive and psychiatric health (Stern et al., 2011). Advanced radiological and laboratory tests have led to better early diagnosis of

TBI (De Kruijk et al., 2001; Ingebrigtsen et al., 2000). However, treatment options are limited to reactive, rather than preventative, management of trauma-induced neurological and neuropsychiatric symptoms, partly because we do not yet fully understand the clinical and mechanistic progression of acute injury into long-term disability.

The cellular substrate of concussion is largely unknown (Meaney and Smith, 2011). One theory on the mechanical origin of concussions proposes that the cortical strains appearing in the gray matter at the moment of injury are the most likely reason for the impairments that occur in a concussion (Ommaya and Gennarelli, 1974). Alternatively, others pose that deformation of the brainstem structures are key in producing the brief periods of unconsciousness associated with severe concussion (Browne et al., 2011; Smith et al., 2000). A common theme among these concussion theories is that the mechanical energy during rapid head motions will deform brain tissue and, ultimately, the cellular ensembles that form these tissues.

At the mechanistic level, our knowledge in the past decade increased considerably about the early events following mTBI - e.g. the relative vulnerability of unmyelinated axons to trauma, the early and progressive cytoskeletal changes, the appearance of new surface channels or the loss of existing channels, and the acute mechanisms of injury both *in vivo* and *in vitro* (Buki and Povlishock, 2006; Farkas and Povlishock, 2007; Johnson et al., 2012). Despite this progress, we know little about one potentially important aspect of mTBI: how do the cellular, subcellular and molecular perturbations following injury affect the structure and organization, or "information flow", through neuronal networks?

In other words, it is not clear if transient mechanical events will cause permanent changes in the neuronal morphology or, alternatively, the wiring of neural circuits within brain regions associated with concussion. These changes in both the neuronal connections and, alternatively, the wiring of neural networks can play a key role in the recovery of the brain following a concussion.

Several recent studies highlight that mTBI is a disease of network dysfunction. Two network-based features are appearing as critical changes in the traumatically injured brain. First, the persisting loss of coordinated EEG brain activity after mTBI (Sponheim, 2011) suggests a potentially important alteration in cortical connectivity even after mTBI that can affect the processing of information, owing to the critical role of synchronization in relaying information throughout the brain (Buzsaki and Draguhn, 2004; Fries, 2005; Womelsdorf et al., 2007). Second, the change in the physical and functional connections among brain regions, revealed through a combination of diffusion tensor imaging (DTI) and functional magnetic resonance imaging (fMRI), is now thought to be a significant contributor to the cognitive impairment and decline in task-related performance after mild TBI (Bonnelle et al., 2012; Bonnelle et al., 2011; Hillary et al., 2011; Sharp et al., 2011; Witt et al., 2010).

Although we gain to learn valuable information about the brain regions most affected by mTBI through EEG and fMRI techniques, they do not provide sufficient resolution to examine the exact cellular mechanisms leading to network dysfunction after mTBI. Measuring changes in both the connection map and information flow

(synchronization) of the circuit with single cell resolution would provide key information on the functional consequences of mechanical injury and help identify novel therapeutic target. Additionally, probing network structure and function at this length scale provides an opportunity to identify whether certain injured neurons contribute disproportionately more to network dysfunction than other injured neurons or, alternatively, is a subset of neurons is critical for maintaining network functions after injury. Determining the relative contribution of neuronal subgroups to the overall changes in network dynamics and plasticity changes may provide new insight into the natural recovery of cortical microcircuits after injury, and if there are new therapeutic approaches that can target the recovery of a selective group of dysfunctional neurons to repair an injured circuit after TBI.

In this study, we measured and probed the mechanisms for changes in network behavior following mechanical stretch injury to cortical neurons *in vitro* at varying severities. Unlike higher injury levels (>80% stretch) that will cause neuronal death within 24h post-injury, we find that mild levels of mechanical injury (35% stretch) causes widespread changes in network topology, synchrony and excitatory transmission. The network that was once highly interconnected prior to injury breaks off into multiple, smaller clusters of locally connected modules. Long-range synaptic transmission is impaired. Functionally, there is a significant drop in network synchrony. Given recent work showing the unique mechanosensitivity of the N-Methyl-D-Aspartate (NMDA) receptor, we studied whether differential mechanical activation of NR2A- or NR2B-

containing NMDARs influences the coordinated activity of neurons and the functional connectivity of an injured circuit. We discovered that NR2B subtypes, but not NR2A, selectively impair network dynamics following mechanical stretch injury. Further, at these stretch levels, there is also delayed proteolysis of voltage gated sodium channels, mediated by the calcium sensitive protease, calpain (von Reyn et al., 2009). We show that pharmacological blockade of calpain improves network synchrony. Alternatively, even milder mechanical injury (10% stretch) produced very little changes in network topology or synchrony, however, there was a brief period of heightened spontaneous activity following injury, suggesting there is a mechanical threshold for permanent changes to the microcircuitry.

METHODS:

Mechanical injury of cortical neurons:

Cortical neurons at 18-21 days *in vitro* (DIV) were subjected to a strain-controlled stretch injury in CSS as described previously (Lusardi et al., 2004b). Briefly, cells plated on flexible membranes were placed on a stainless steel plate and covered with a top plate to form a sealed chamber. Increasing the chamber pressure to its peak level in 15 milliseconds caused the compliant silicone membrane to stretch, in turn applying a stretch to the cultured neurons. This pressurization phase was immediately followed by a release of the pressure, typically within 25 milliseconds of achieving the peak pressure. Although cells were cultured over a circular area (23 mm diameter), we designed the supporting stainless steel plate to expose only cells in a defined region (a 3mm x 18mm

rectangular region; approximately 1/3 of the culture surface area) to a stretch, designing the system to provide a uniform membrane stretch over 95% of the surface within that region (Lusardi et al., 2004a). The magnitude of the stretch injury was calibrated to the applied input pressure for each week of experiments, and a transducer recorded the applied output pressure of each test (Endevco, San Juan Capistrano, CA). The membrane in the injured region was stretched uniaxially, where the width was extended 10% (mild) or 35% (moderate) beyond its initial width before returning to its original dimension. These levels of strain magnitude and rates are typically observed in human and animal models of mild TBI (Meaney et al., 1995). At these levels of injury, we did not observe any obvious detachment of the cells from the membrane following stretch injury, nor did we observe any gross morphological changes in the cultures. This stretch level does not cause a significant increase in cell death compared to unstretched controls (Lusardi et al., 2004b). Naïve unstretched neurons served as reference conditions for statistical comparison.

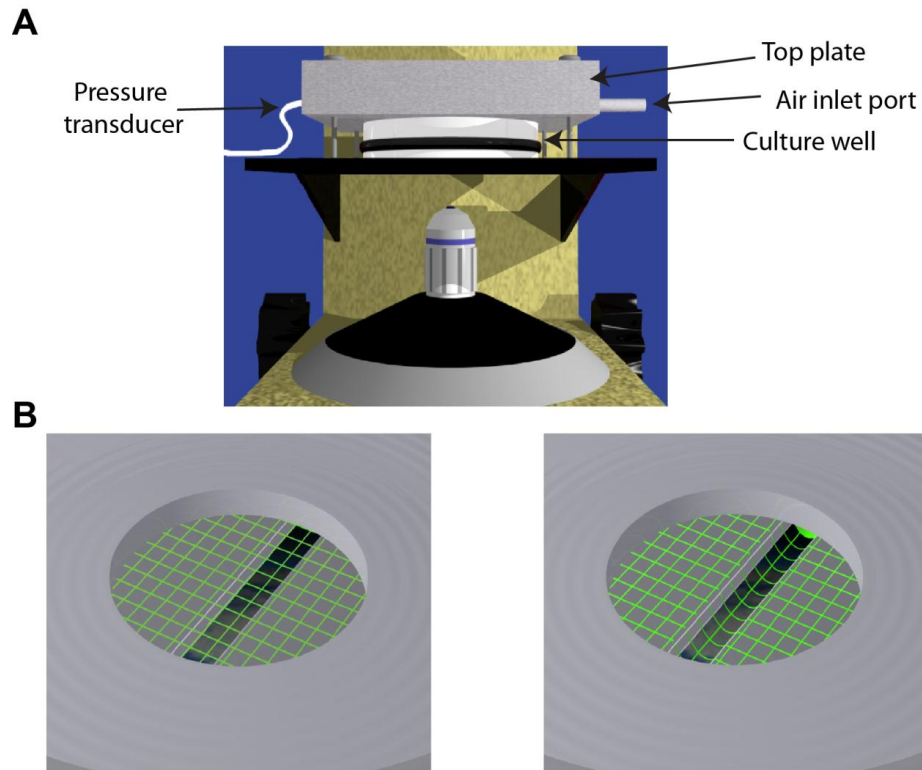


Figure 3. 1: Schematic of stretch injury device. **A:** Cells cultured on a silastic membrane and placed over a stainless steel plate with a 3" slit were secured to the microscope stage with a top plate, forming an air-sealed chamber. Rapid pressurization of the chamber through an air inlet port caused the membrane to deflect (**B**, right), producing a uniaxial strain deformation. The membrane returned to its original unstretched shape (**B**, left) following de-pressurization.

Drug Treatments: All compounds were solubilized in controlled saline solution (CSS; in mM: 120 NaCl, 5.4 KCl, 1 MgCl₂, 1.8 CaCl₂, 25 HEPES, 15 glucose, pH 7.3. Cortical neurons were incubated in bicuculline methobromide 50 μM (Tocris), APV 25μM (Tocris), Ro 25-6981 2μM (Sigma-Aldrich), NVP-AAM077 50nM (Novartis, CA) or MDL28170 50μM (Calbiochem) as needed.

Single cell phenotyping of the relative contribution of NMDAR subtypes to synaptically-evoked rise in intracellular calcium

We developed a rapid method to determine the relative fraction of NR2B and NR2A receptors of individual neurons within an intact network. We performed calcium imaging of neuronal networks and measured calcium fluorescence at the soma as described above. When a neuron fires a single or a train of APs, the rise in calcium indicator fluorescence is the product of influx through the NMDARs (all subtypes), calcium-permeable AMPARs, and the voltage gated calcium channels that are opened when the neuron is depolarized with AMPAR activation. We stimulated the excitatory network by blocking GABA_A receptors with bicuculline (50 μ M). This induced rhythmic oscillations with little variability in calcium amplitudes for a given neuron. The fractional drop in calcium-indicator fluorescence amplitude with the application of either NR2A-selective antagonist, NVP, or NR2B-selective antagonist, Ro 25, provided an estimate of the relative contribution of NR2B and NR2A subtypes to synaptically-evoked rise in intracellular calcium. Although not a direct estimate of the percent composition of NR2A or NR2B receptors at the synapse, this is a functional measure of the fraction of total somatic calcium load that is generated by the activation of NR2A and NR2B receptors at the synapse.

Statistical Analysis:

Data were analyzed using student's t-test or by ANOVA with Tukey's *post-hoc* test. At least $n = 10$ cultures, from three different isolations were tested for each experimental condition. All values are reported as mean \pm s.e.m.

Calcium imaging and data analysis:

We used the technology developed in past reports (Fetcho et al., 1998; Stosiek et al., 2003; Tian et al., 2009; Yuste et al., 1992) and methodology developed in Chapter 2 to measure neural circuit dynamics using fluorescent calcium indicator. The spontaneous activity of a mature culture (DIV 18-21) was measured prior to injury and at increasing time points post injury up to 5 days.

RESULTS

Integration of neurons within an injured network is influenced by pre-stretch connectivity.

Using newly developed methods to estimate the functional connectivity of neurons within a dissociated microcircuit (Figure 3.2A), we first measured the initial reduction and early recovery in the circuit connectivity after stretch injury. Neurons were cultured on a silastic membrane and a small region of the membrane was stretched uniaxially to $35\% \pm 5\%$ peak stretch within 15 ms duration, mimicking the strain magnitude and duration of human mTBI. Mechanically injured neurons showed an immediate transient increase in cytosolic calcium that returned to pre-stretch baseline

levels within 10 minutes of injury (Figure 3.2B). Consistent with previous reports, this calcium transient was eliminated completely by inhibiting the NMDA receptor population (APV, 25 μ M) prior to stretch insult. Although this level of mechanical injury did not produce significant cell death one day after injury, we did see both an immediate (10 minute) and more persisting impairment (1 hour) in functional connectivity of the microcircuit after injury (Figure 3.2C). Functional connectivity index of a neuron was defined as the ratio of the number of functional targets to the total number of neurons in the network (0 = neuron has no functional connections to the network, 1 = neuron is functionally connected to every other neuron in the network). The connectivity index of individual neurons did not vary spatially. The functional connectivity of the network, defined as the average of the connectivity index across all neurons, as well as the number of calcium events were significantly reduced 10 minutes and one hour following injury (Figure 3.2E-F). Consistent with the inhibition of stretch-induced transients, APV pretreatment restored the deficits in the connectivity and spontaneous activity following mechanical injury (Figure 3.2E-F).

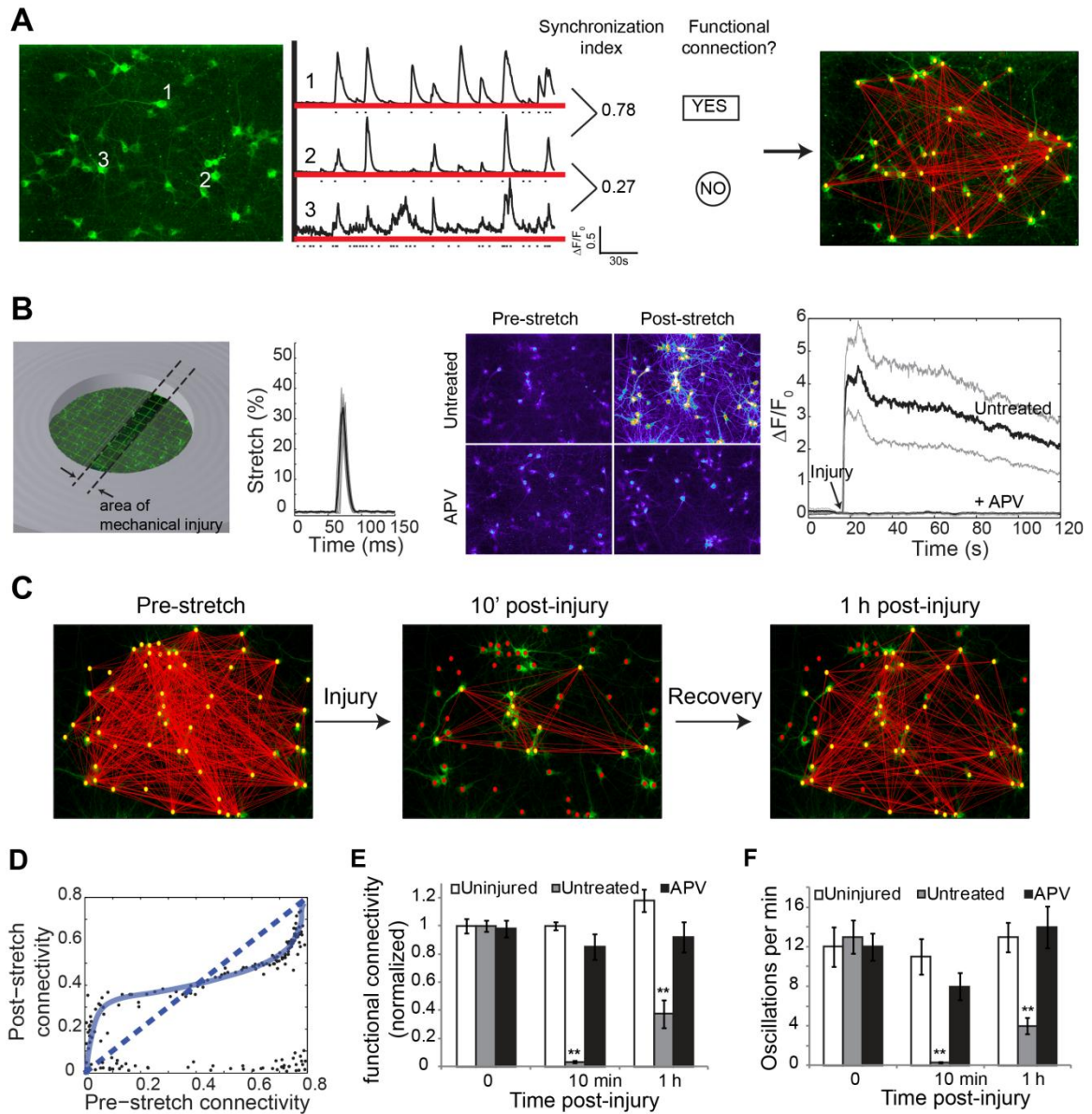


Figure 3.2: Mechanical injury to a cortical network *in vitro* causes acute reduction in functional connectivity through NMDA receptor activation. The calcium activity of a population of neurons was recorded with the genetically encoded calcium indicator, GCaMP5 (A). The temporal similarity in the fluorescence trace of each pair-wise neurons was quantified as the synchronization index and then binarized to yield a functional connectome. Example of 3

neuronal traces is depicted. Neuron pairs 1 and 2 have a similar temporal pattern of calcium fluorescence and hence are functionally connected whereas the activity of neuron pair 2 and 3 is not similar enough to be functionally connected. We measured the spontaneous activity of a population of neurons grown on a silastic membrane and applied stretch injury to a confined region of the well, yielding peak $35\% \pm 5\%$ uniaxial stretch in 15 ms duration (**B**). Stretch produced an immediate rise in $[Ca^{2+}]_i$ which could be completely blocked by pre-treatment with the NMDA receptor antagonist, APV (**B**). The functional connectivity of the network was significantly reduced immediately following stretch injury (10 min post-injury) but showed partial recovery by 1 h (**C,D**). The functional connectivity is overlaid on an image of the same set of neurons images pre and post-injury (**C**); yellow circles = neuronal cell bodies or nodes that are functionally integrated in the network, i.e. have at least 1 functional target, red circles = completely deintegrated nodes and red lines indicate functional connections or edges. Injury also significantly reduced network-wide calcium oscillations at 10 min and 1 h post-injury (**E**). The effect of injury on network functional connectivity and activity were completely blocked by APV pre-treatment (**D,E**). Although there was an overall decrease in the number of functional connections 1 h following stretch at the network scale, the pre-stretch connectivity of individual neurons within the network influenced their post-injury connectivity - a fraction of sparsely-connected neurons (connectivity index < 0.3) showed an increase in the number of functional connections following injury, whereas most highly connected neurons (connectivity index > 0.7) underwent a reduction (**F**, $n=221$ neurons from $N=5$ experiments, paired t-test $p<0.01$).

Although mechanical injury caused an overall reduction in synchronization, spontaneous activity, and the total number of functional connections, it was unlikely that every neuron showed the same level of de-integration after mechanical injury. With the

single cell resolution available in the calcium imaging methodology, we next examined if the initial connectivity of a neuron within the network influences their post-injury connectivity. We recorded the spontaneous calcium activity of the same microcircuit prior to and 1-hr following stretch injury and determined the number of functional connections, the node degree, of each neuron within the network at these two time points. Most neurons in our mature cultures were either fully integrated (connectivity index > 0.7) or sparsely connected (connectivity index < 0.3). In uninjured cultures, the connectivity index of individual neurons did not change over the 1-hr time interval (paired t-test $p > 0.1$). Using these broad groupings, we found a fraction of sparsely-connected neurons showed an increase in the number of functional connections following injury, whereas most highly connected neurons underwent a reduction (Figure 3.2F, $n=221$ cells from $N=5$ separate experiments, paired t-test $p < 0.01$, dotted line is the line of identify - neurons that fall above this line show an overall enhancement in connectivity whereas those that fall below the diagonal show a reduction in connectivity). Additionally, in the fully integrated group of neurons (connectivity index > 0.7), neurons with greater number of connections prior to stretch had a disproportionately lesser reduction in functional connectivity post-stretch, i.e. the slope and the change in slope of post vs. pre connectivity was > 0 .

Broadly, these data show that mechanical injury to cortical neurons will incur immediate and broad disruptions in network behavior. However, finite element models suggest a wide range of *in vivo* brain deformations occur during concussion. As such, we

also tested a less severe injury level ($10\% \pm 4\%$). Distinct from studies at the moderate injury level, we observed no change in functional connectivity. Interestingly, the frequency of network-wide spontaneous oscillations significantly increased acutely after injury and returned to pre-stretch levels by 1hr. The threshold for disrupting connectivity in the networks appears to be between these two levels of mechanical injury and we focused our efforts to understand the mechanisms of network degradation at 35% stretch.

Neuronal NMDAR subunit composition influences functional rewiring following injury.

In addition to examining the relative change of individual neuronal integration within a larger neural microcircuit, calcium imaging also provides the resolution to identify and group neuronal subpopulations with similar functional properties. Given that the source of calcium influx, as well as the potential secondary release from intracellular stores, can play a major role in the mechanisms that mediate changes in synaptic plasticity, neuronal remodeling, and network maintenance, we extended the calcium imaging methodology to functionally profile individual neurons within the microcircuit. We first blocked inhibitory GABA_A receptors with bicuculline, removing the contribution of fast inhibitory synaptic transmission from network activity. The contribution of NMDARs was assessed by comparing calcium oscillation amplitude in bicuculline vs. bicuculline + APV. Similarly, the contribution of CP-AMPARs and voltage-gated calcium channels was determined by the sensitivity to naspmm and nimodipine, respectively (two example traces in Figure 3.3 A, B). We further divided the contribution of NMDARs into NR2A and NR2B components by measuring the percent

reduction in amplitude with NVP and Ro-25, respectively (Figure 3.3D). Within individual neurons from the same microcircuit, single-cell calcium dynamics (SCCD) showed that the relative calcium influx profile could differ significantly. Consistent with past work showing a developmental change in the expression of AMPA and NMDA receptors over time *in vitro* (Ben-Ari et al., 1997), we also observed a shift in the average SCCD profile from influx primarily through the NMDA receptors (10 DIV) to a more significant influx associated with opening of voltage gated channels, presumably from an increase in AMPA receptor expression, at 21 DIV (Figure 3.3C, DIV 18-21 NMDAR contribution $62\% \pm 11\%$ vs. DIV 10 NMDAR contribution $80\% \pm 9\%$, $p < 0.05$, $n = 69$ cells). The relative composition in SCCD profile was examined further with subunit-selective antagonists of NMDA receptors, taking advantage of antagonists directed towards the glutamate binding site on either the NR2B subunit (Ro25-6981) or the NR2A subunit (NVP-AAM077). We found that the majority of synaptically evoked increase in cytoplasmic calcium during spontaneous activity in mature cortical neurons (DIV 18-21) arise from NMDARs ($65\% \pm 7.3\%$) and VSCCs ($32\% \pm 10.1\%$) (Figure 3.3C). Of the 65% NMDAR contribution to $[Ca^{2+}]_i$ oscillations in mature neurons, NR2A subtypes contributed $64\% \pm 7.3\%$ and NR2B contributed $28\% \pm 8.4\%$ to rise in $[Ca^{2+}]_i$, whereas, NR2B subtypes contributed significantly greater ($47\% \pm 5.9\%$) to Ca^{2+} oscillations in younger neurons, consistent with developmental turnover of NR2B subtypes and electrophysiological and Western blot-based estimates of subunit composition in cultured neurons (Liu et al., 2004; Stocca and Vicini, 1998; Tovar and Westbrook, 1999).

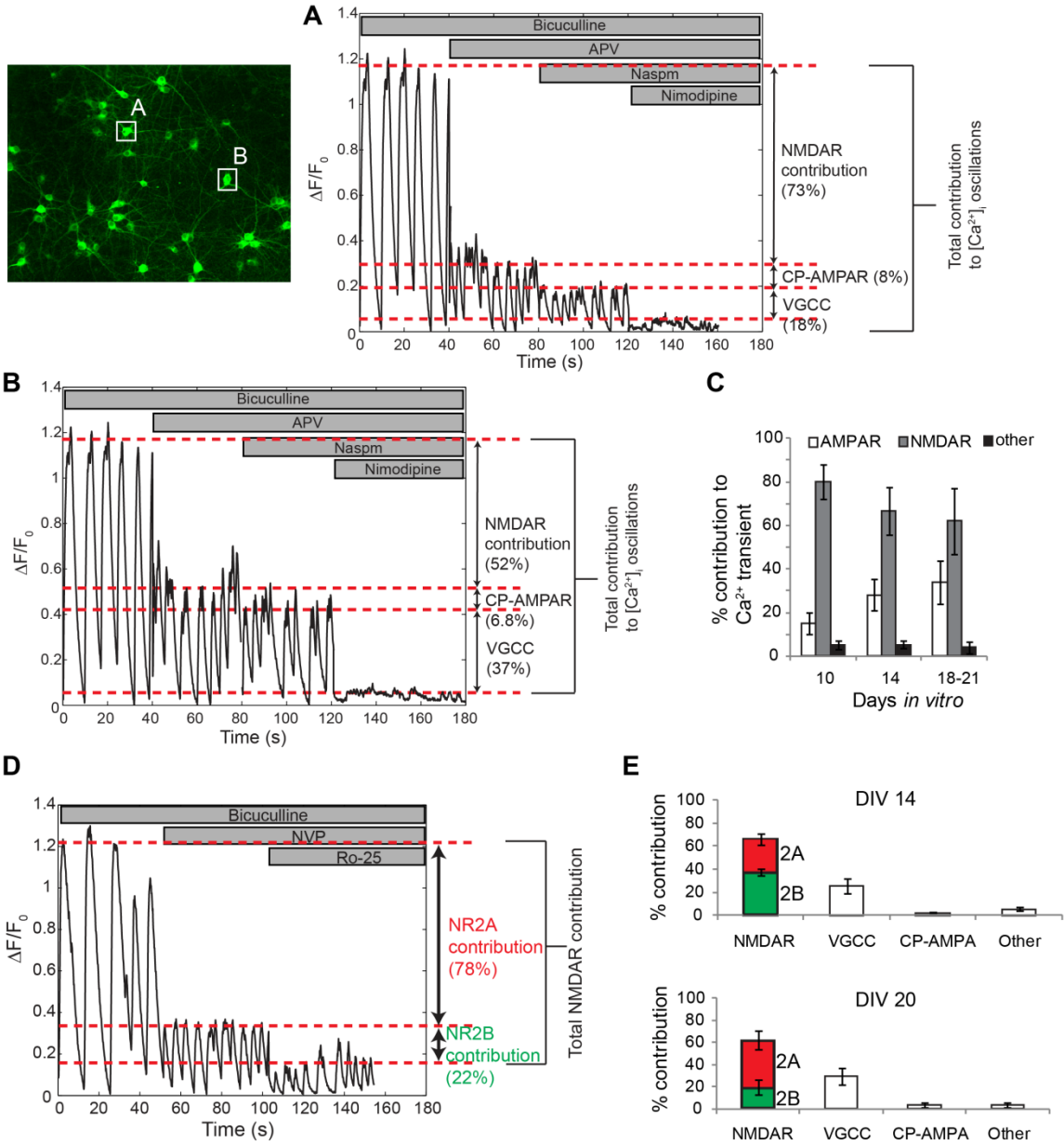


Figure 3. 3: Profiling the contributions of NMDA receptors (NR2A and NR2B subtypes) and voltage-gated calcium channels to intracellular calcium oscillations. Neuronal networks underwent rhythmic oscillations in $[Ca^{2+}]_i$ following the removal of fast inhibitory synaptic transmission with bicuculline. The contribution of synaptically-activated NMDA receptors to the

[Ca²⁺]_i oscillations was assessed by comparing calcium oscillation amplitude in bicuculline vs. bicuculline + APV. Similarly, the sensitivity to naspnm and nimodipine was used to assess the contributions of calcium-permeable AMPARs and voltage-gated calcium channels to [Ca²⁺]_i oscillations. The contributions of these channels to [Ca²⁺]_i oscillations varied from neuron-to-neuron (example of two neurons from the same network in **A** and **B**). The contribution NR2A and NR2B subtypes was assessed by the percent reduction in amplitude with NVP and Ro-25, respectively (**D**). As embryonic neurons matured *in vitro*, the contribution of NMDARs to [Ca²⁺]_i oscillations decreased (**C**) and showed greater sensitivity to NVP, indicative of turnover of NR2B subtypes with NR2A-containing NMDARs (**E**).

With an ability to estimate both the relative integration of a neuron within a microcircuit and its functional calcium influx profile, we tested directly if these two single cell-based features contributed to the individual neuronal response to traumatic mechanical injury. Previous study by our group investigated the mechanosensitivity of NMDAR subunits and found that majority of the immediate Ca²⁺ influx is through NR2B-containing NMDAR, and not NR2A-containing NMDARs (Singh et al., 2012). Based on this past work, we expected that neurons displaying a relatively large calcium influx through NR2B-containing NMDARS – indicative of a significant number of synaptic NR2B-containing NMDARs – would respond more robustly to traumatic mechanical injury. We used calcium imaging to quickly estimate the NR2A and NR2B contribution to [Ca²⁺]_i oscillations prior to stretch injury, yielding a biochemical phenotype for each neuron in the network. Although most neurons underwent a reduction in the total number of functional connections, we explored the relationship

between NMDAR subtype composition of a given neuron prior to injury and its functional connectivity following injury. The functional connectivity of a neuron, i.e. its functional neuronal targets, could undergo one of 3 changes: of the set of all functional targets, a fraction of connections may be lost as a result of injury, a fraction of connections may remain stable following injury or there maybe some newly formed functional connections following injury that were not present in the uninjured network. The "lost", "stable", and "new" fraction for a given neuron compactly describes its extent of functional rewiring in the injured network (Figure 3.4A,B).

In sham cultures, the *lost* and *new* fraction for nearly all neurons is $< 5\%$, indicating very little change in the functional connectivity over a 1 hour time period. In contrast, we found a large number of functional connections were lost and a smaller number of newly formed functional connections appeared 1-hr following stretch injury ($57\% \pm 9.6\%$ lost, $22\% \pm 8\%$ new, **Figure 3. 4**). Interestingly, the functional rewiring of single-cells fell into three clusters - a group of neurons that de-integrated from the circuit (i.e. lost many of their functional connections), a group of neurons that remained integrated and a group that re-integrated, forming new connections. Overlaying the pre-stretch NR2B and NR2A receptor "content" of each neuron onto its degree of functional rewiring following injury, we found a significant positive relationship between pre-stretch NR2B contribution and de-integration (**Figure 3. 4 C,D**, correlation coefficient 0.89 ± 0.12 $p < 0.01$). These data showed individual neurons whose $[Ca^{2+}]_i$ oscillations were most sensitive to Ro-25 prior to stretch *lost* many of its functional targets at 1-hr

following stretch, consistent with our earlier work showing that the sensitivity of the NMDA receptor to mechanical stretch injury is linked primarily to the NR2B subunit (Singh et al., 2012). There was no correlation between node degree and NR2A or NR2B contribution prior to stretch, indicating that NMDAR subtypes do not influence functional connectivity in an uninjured network.

If NR2B content is an injury-susceptibility marker, experimental manipulations that either reduce or enhance the relative NR2B:NR2A receptor content prior to stretch are expected to directly influence the functional integration of neurons following injury. We tested this hypothesis in two experimental conditions. During development, NR2B-containing receptors are expressed in immature neurons, whereas NR2A-containing receptors become the electrophysiologically predominant subunit at later stages of development (Carmignoto and Vicini, 1992; Hestrin, 1992; Kew et al., 1998; Monyer et al., 1994; Roberts and Ramoa, 1999). We confirmed that the NR2B contribution to $[Ca^{2+}]_i$ oscillations was greater in DIV 14 neurons compared to more mature neurons at DIV 20 (DIV 14 NR2B contribution $47\% \pm 3.9\%$ vs. DIV 20 $28\% \pm 3.8\%$, $p < 0.05$, Figure 3.2 E). Stretch injury to DIV 14 cultures caused a significantly greater reduction in functional connectivity relative to injury to DIV 20 cultures (DIV 14 $47\% \pm 5\%$ reduction vs. DIV 20 $35 \pm 6\%$, $p < 0.05$).

Separately, we altered the NR2B:NR2A ratio by chronic NMDA receptor blockade, which causes a preferential increase in the surface expression of NR2A subtypes (von Engelhardt et al., 2009). By blocking NMDARs, calcium activity was

reduced, but electrical activity was unaffected, resulting in a homeostatic increase in NR2A receptors. Following removal of APV, we noted an increase in calcium oscillation amplitude that was more sensitive to NVP relative to vehicle treated shams. The frequency of calcium oscillations and the functional connectivity were unaffected by chronic APV blockade (Figure 3.4E). However, cultures that were treated with 8 h APV, and hence had greater NR2A receptor content (lower NR2B:NR2A ratio) were protected against injury-induced loss in functional connections 1 h following injury (Figure 3.4 E), suggesting that the aggregate NR2B:NR2A ratio for a given neuron influences susceptibility to injury-induced functional rewiring.

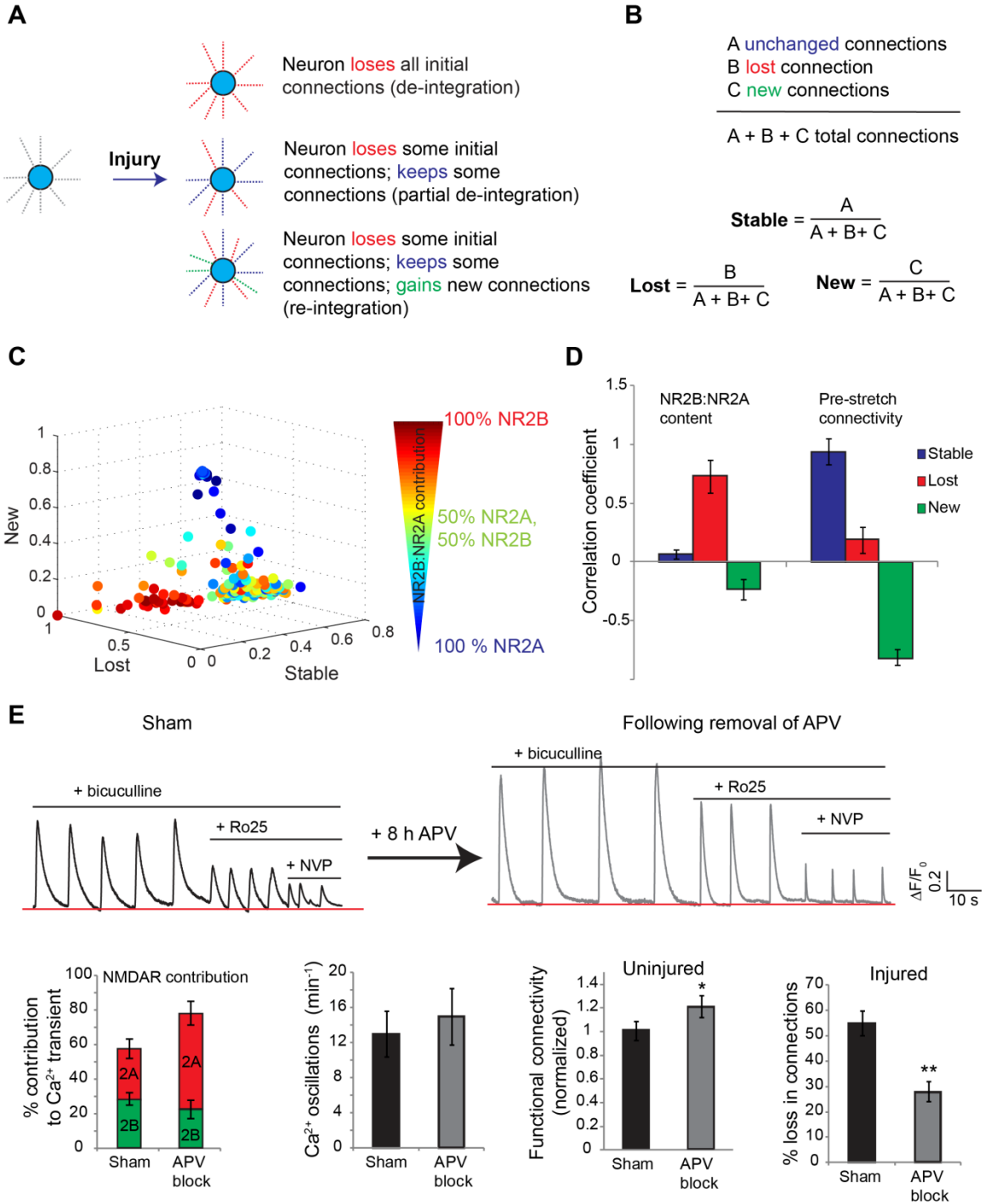


Figure 3. 4: Functional rewiring following injury is influenced by NMDA receptor

composition. As a result of injury, a neuron could undergo one of 3 changes in its functional connectivity. Of the set of all functional targets, a fraction of connections may be lost as a result of injury, a fraction of connections may remain stable following injury or there may be some newly formed functional connections following injury that were not present in the uninjured network. The "lost", "stable", and "new" fraction for a given neuron compactly describes its extent of functional rewiring in the injured network (**A, B**). Following injury, individual neurons fell into three clusters - a group of neurons that remained integrated, a group of neurons that de-integrated and a group of neurons that re-integrated. The pre-stretch NR2B and NR2A receptor contribution of $[Ca^{2+}]_i$ oscillations was a strong predictor of functional de-integration following injury (**C, D**). Experimentally increasing the NR2A contribution to $[Ca^{2+}]_i$ oscillations with a chronic APV blockade (**E**) abrogated loss in functional connectivity, indicating that the effects of injury on network connectivity are linked primarily to the NR2B subunit.

NR2B-NMDA receptor, not NR2A, undergoes stretch induced reduction in Mg^{2+} block.

To determine why neurons with high pre-stretch NR2B contribution to $[Ca^{2+}]_i$ oscillations are more adversely affected by stretch injury than NR2A dominant neurons, we investigated the mechanosensitive properties of these two subunits using whole-cell patch clamp to record agonist-activated currents. NMDA receptors have previously been shown to be mechanically activated (Paoletti and Ascher, 1994) and traumatic injury both *in vitro* and *in vivo* causes a reduction in the voltage-dependent Mg^{2+} block of the NMDARs (Furukawa et al., 2000; Zhang et al., 1996). NMDA-activated currents recorded from uninjured control neurons under voltage clamp in the presence of 2mM

extracellular Mg^{2+} showed a typical "J"-shape when plotted against membrane command potentials (Figure 3. 5A). The negative conductance below -40mV is due to Mg^{2+} block of NMDARs. Consistent with previous report (Zhang et al., 1996), the current-voltage (I-V) relationship was more linear in stretch injured neurons at 1-hour post-injury (Figure 3. 5A). Specifically, we noted significantly greater NMDA-activated currents at resting membrane potential (-62mV) in stretched neurons relative to unstretched (normalized current in stretched: -1.12 ± 0.16 vs. unstretched: -0.13 ± 0.17 , $n=16$, $p<0.001$).

We used the NR2A-selective antagonist, NVP-AAM077, and the NR2B-selective antagonist, Ro25-6981, to determine the effect of these two subtypes on the I-V relationship in uninjured and injured neurons. Cultures were injured as before (or uninjured for control) and the NMDAR antagonists were applied prior to patch clamp recording. NMDA-activated currents in uninjured neurons with either antagonist individually showed a "J" shape I-V relationship, suggesting that both NR2A and NR2B containing receptors are blocked by extracellular Mg^{2+} below -40mV (data not shown). In contrast, the I-V relationship of NVP-AAM077 treated injured neurons remained more linear but Ro-25 treatment rescued the "J" shape (normalized current in stretched: -1.12 ± 0.16 vs. stretched + Ro 25: -0.42 ± 0.21 , $p<0.01$), suggesting that the NR2B, not NR2A, containing NMDA receptors undergo a reduction in Mg^{2+} block following stretch (Figure 3.5A).

A selective reduction of voltage-dependent Mg^{+2} block of NR2B-containing NMDARs would suggest increased ionic fluxes, in particular Ca^{+2} flux through this

subpopulation of NMDARs following mechanical injury. Indeed, APV resulted in a greater reduction in Ca^{2+} oscillation amplitude in injured cultures relative to uninjured shams, suggesting a larger NMDAR component. Of the total Ca^{2+} influx through the NMDA receptors, the contribution of NR2B subtypes was significantly greater 1 h following injury relative to shams (Figure 3.5 B, injured NR2B contribution $54.3\% \pm 6\%$ vs. uninjured $32.3\% \pm 7\%$, $p < 0.01$).

We further measured NMDA-agonist induced rise in intracellular free calcium, ($[\text{Ca}^{2+}]_i$) in uninjured and stretch injured neurons using the fluorescent ratiometric Ca^{2+} indicator, fura-2 AM. Spontaneous activity and synaptic transmission were reduced with TTX (1 μM), bicuculline (10 μM) and nimodipine (10 μM). We observed that NMDA treatment (200 μM) increased $[\text{Ca}^{2+}]_i$ by 36% over basal levels in uninjured neurons (basal $[\text{Ca}^{2+}]_i$: $88\text{nM} \pm 13\text{nM}$, NMDA induced $[\text{Ca}^{2+}]_i$: $115\text{nM} \pm 9\text{nM}$), whereas $[\text{Ca}^{2+}]_i$ increased by 102% in injured neurons (basal $[\text{Ca}^{2+}]_i$: $93\text{nM} \pm 28\text{nM}$, NMDA-induced $[\text{Ca}^{2+}]_i$: $188\text{nM} \pm 19\text{nM}$). Moreover, blocking the NR2B, but not NR2A subtypes in injured neurons significantly attenuated NMDA induced rise in $[\text{Ca}^{2+}]_i$ (injured + Ro25 peak $[\text{Ca}^{2+}]_i$: $122\text{nM} \pm 19\text{nM}$, injured + NVP peak $[\text{Ca}^{2+}]_i$: $160\text{nM} \pm 14\text{nM}$, $p < 0.01$) (Figure 3.5 C-E). Together with electrophysiological recordings, these data strongly support an NR2B-selective reduction in voltage-dependent Mg^{2+} block following mechanical stretch injury. The selective vulnerability of NR2B-containing NMDAR subtypes supports our previous findings that neurons with high NR2B contribution to

$[Ca^{2+}]_i$ oscillations prior to stretch undergo more severe changes in functional connectivity.

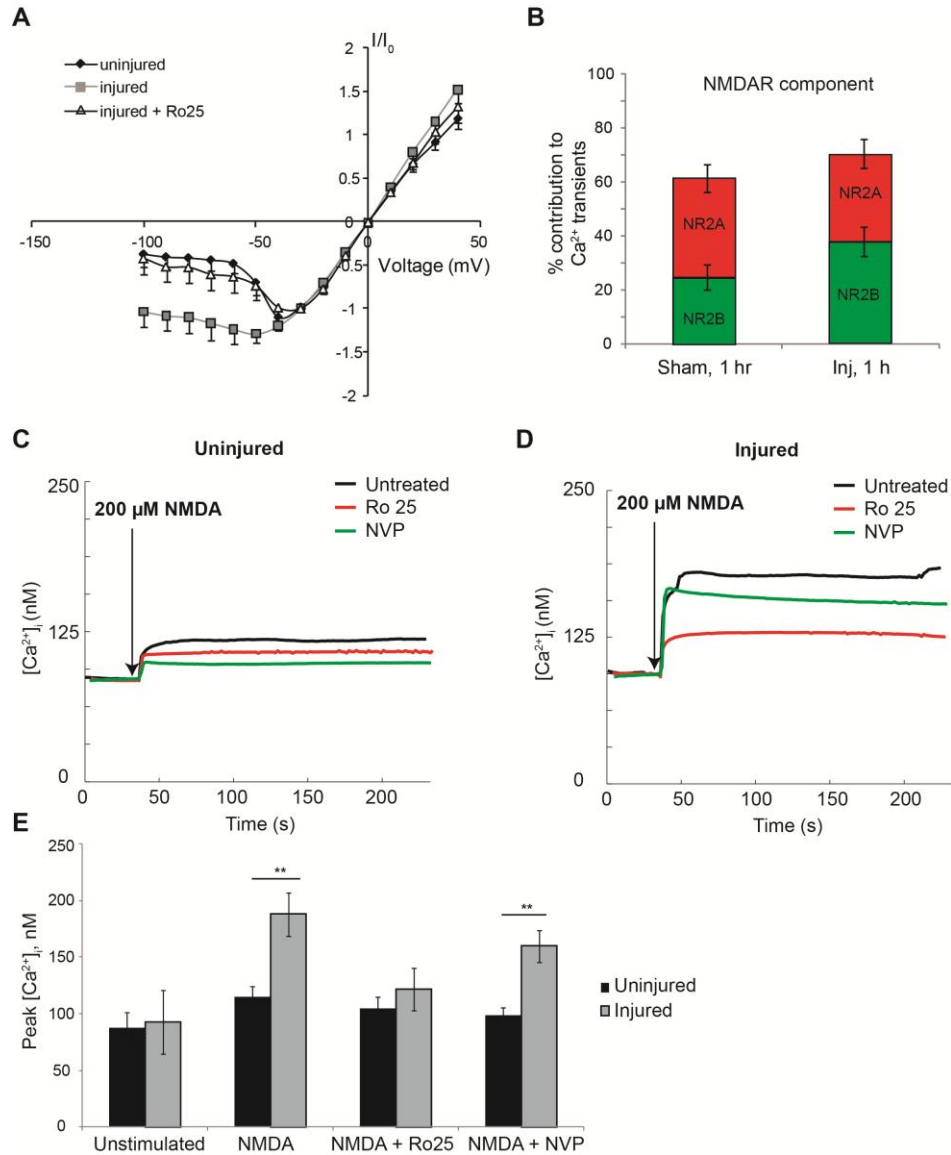


Figure 3. 5: Injury results in a reduction of NR2B-NMDAR Mg^{2+} block. A: Patch-clamp recording of NMDA-induced currents at different hold potentials showed a characteristic J-curve in uninjured neurons and uninjured neurons pre-treated with Ro-25, due to an intact voltage-

dependent Mg^{2+} block. Stretch injury caused a reduction in voltage-dependent Mg^{2+} block of NR2B-containing NMDARs as evidenced by a flattening of the I-V curve following injury but rescue of the J-shape when injured neurons were pre-treated with Ro-25. B: Consistent with a reduction in NR2B Mg^{2+} block, the contribution of NMDARs to spontaneously generated $[Ca^{2+}]_i$ oscillations was significantly greater following injury, along with a relative increase in NR2B component. C-D: Changes in $[Ca^{2+}]_i$ after NMDA application, measured with fura-2, show an enhanced response in injured neurons that is significantly attenuated by NR2B antagonist, Ro-25. Resting $[Ca^{2+}]_i$ in uninjured and injured neurons at 1-hr are not significantly different. Traces are representative of an individual uninjured and injured neuron. E: The peak $[Ca^{2+}]_i$ following NMDA stimulus was significantly greater in injured cultures relative to uninjured and could be attenuated with Ro-25 ($n=8$ uninjured and 7 injured cultures, $**p<0.01$).

Stretch-induced reduction in NR2B-NMDAR Mg^{2+} block causes asynchronous circuit activity

Ca^{2+} enters the cell through NMDA receptors only when presynaptic glutamate release and depolarization of the postsynaptic membrane occur simultaneously (correlated activity), whereas NMDAR-mediated Ca^{2+} influx is suppressed at voltages near the resting membrane potential due to Mg^{2+} block. This coincidence detection is a fundamental feature of neurons that allows signaling specificity in response to patterned synaptic input. Often, it allows temporal control over postsynaptic action potential initiation following an appropriate pattern of spatiotemporal afferent inputs. Following a vesicular release of glutamate, the NR2A and NR2B subtypes undergo multiple intermediate stages of activation before transitioning to a glutamate-bound and open state

(Erreger et al., 2005). The activation scheme and sensitivity to Mg^{2+} block are different for different subtypes (Kuner and Schoepfer, 1996). Given that injury selectively reduces NR2B-NMDAR Mg^{2+} block, little evidence exists to predict how this selective change to a NMDAR subpopulation would influence the temporal patterns of network activity.

To investigate the effects of reduced NR2B Mg^{2+} block on the calcium dynamics at the dendritic spine-, neuron-, and network-level, we built a multi-scale model of neuronal network spontaneous activity. We modeled the stochastic activation of NR2A, NR2B, and AMPA receptors at dendritic spines under physiologic glutamate release conditions. The resulting current from activation of these receptors was used to update the membrane potential of pyramidal neurons which were modeled as leaky integrate-and-fire. See Chapter 2 for methodological details.

Under physiologic Mg^{2+} block of the NR2A and NR2B subtypes, simulated release of a glutamate containing vesicle consistently activated AMPARs and NR2A subtypes, while NR2B activation was a rare event (3 out of 40 simulations showed NR2B activation). A raster plot of receptor activation for 40 independent simulations is shown in **Figure 3. 6 A**, where each dot represents glutamate-bound, open, and ion conducting state. Reducing NR2B Mg^{2+} block from extracellular $[Mg^{2+}]=0.8mM$ to $0mM$ resulted in significantly more activation of these receptors as expected, however, the model also predicted increased temporal jitter as a result of rapid transitions between glutamate-bound/open state and glutamate-bound/closed state (**Figure 3. 6 B**). In an otherwise physiologic spine, these flickering events contribute negligible calcium flux due to

voltage-dependent Mg^{2+} block; however, they become a significant source of calcium in an ‘injured’ spine. Interestingly, the total calcium load does not significantly increase until external $[Mg^{2+}]$ is lowered beyond 0.15mM, suggesting a level of resilience (**Figure 3.6 C**). Furthermore, the stochastic temporal activation of both AMPARs and NR2A subtypes was very similar across repeated simulations but varied greatly for the NR2B subtypes of a simulated injured spine as indicated by significantly greater variance across trials computed at each time point (**Figure 3.6 D**, red trace - variance in NR2A activation under physiologic $Mg^{2+} = 0.8mM$, black trace - variance in NR2B activation under $[Mg^{2+}] = 0mM$). This suggests that a reduction in NR2B Mg^{2+} block not only increases calcium flux, but the temporal pattern of activation becomes more irregular between trials and noisier within trials.

We expect that increased variability in NR2B activation will disrupt the timing of firing of neurons within the network. We used the computational model to examine the sensitivity of the pattern of spontaneous network activity to NR2B-specific reduction in Mg^{2+} block. Previous computational models have shown that the wiring of networks and the balance of inhibitory and excitatory connections are important features that influence the temporal patterns of spontaneous activity (Compte et al., 2003; Cossart et al., 2003; Parga and Abbott, 2007). In model simulations, a small fraction of synapses received a transient input in the form of glutamate-containing vesicles, triggering a burst of activity that was self-sustained by virtue of NMDAR-dependent recurrent excitation but limited to 1-2 second duration due to inhibitory potentials (Fig 3.6E). The pattern of activity was

synchronized in the excitatory network and matched *in vitro* recordings of mature cortical cultures.

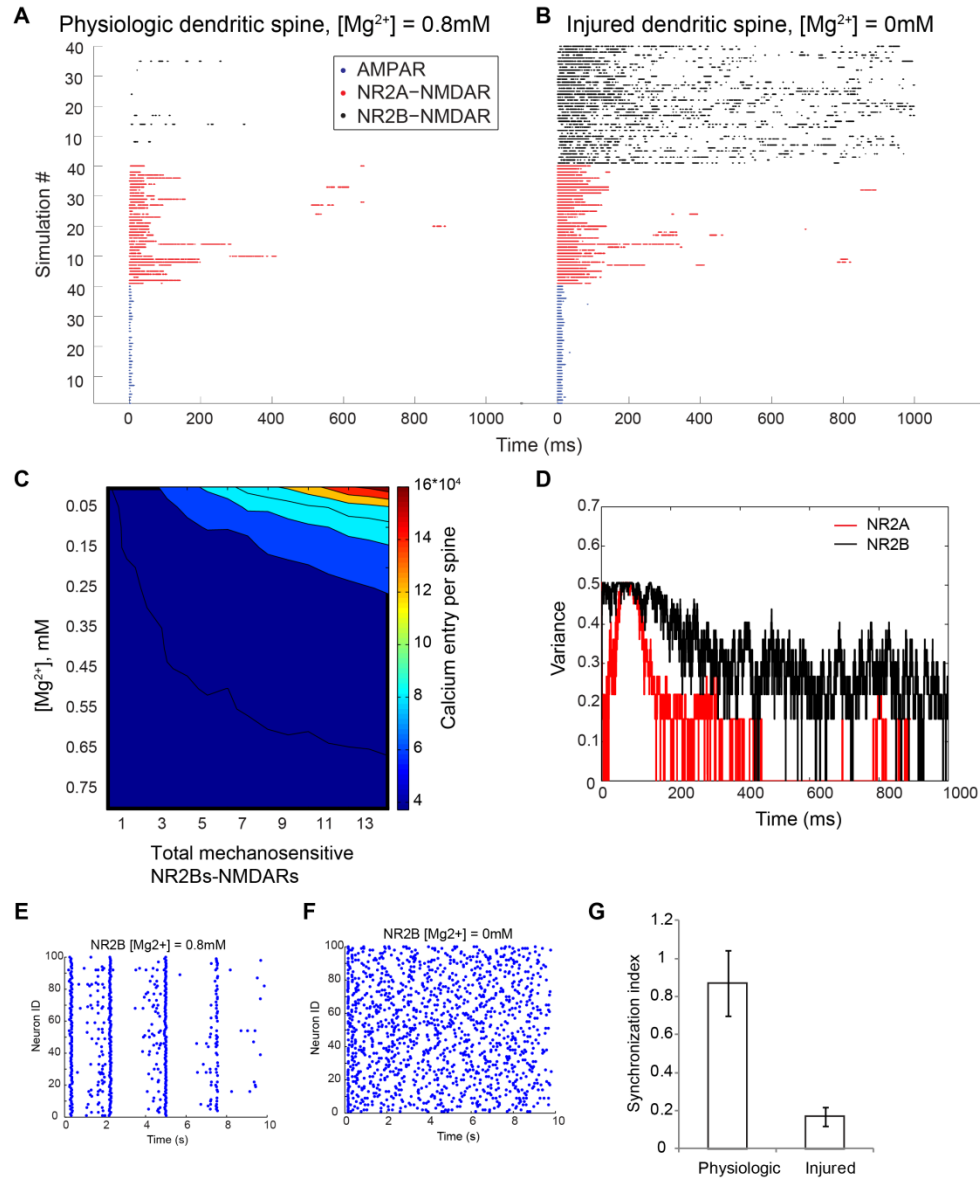


Figure 3. 6: Computational model predicts the effects of reduced NR2B Mg^{2+} block on dendritic spine and network activation. The activation of AMPA receptors, NR2A

and NR2B-containing NMDA receptors on a prototypical dendritic spine were simulated following vesicular release of glutamate (**A**, blue dots - active AMPA receptors, red dots - open and conducting NR2A, black dots - open and conducting NR2B receptors). AMPA receptors opened quickly and desensitized within 50 ms of vesicular release, whereas NR2A receptors were open for ~200 ms. Under these release conditions, activation of NR2B receptors was rare. Selective reduction in NR2B $[Mg^{2+}]$ greatly increased activation of these subtypes as expected, however, the temporal pattern of activation varied greatly from trial-to-trial (**B**, **D** - variance in receptor activation across 40 independent trials). Reduction in voltage-dependent Mg^{2+} block is expected to result in more calcium influx, however, the calcium load is relatively insensitive to reduction from physiologic 0.8mM to 0.15mM and dependent on the number of NR2B receptors at the spine (**C**). The receptor activation scheme under physiologic and simulated injury conditions were used to simulate the activity patterns of neuronal networks (**E**, **F**). A selective loss in NR2B Mg^{2+} block resulted in significant loss in synchrony (**G**, physiologic $[Mg^{2+}] = 0.8mM$ synchronization index: 0.87 ± 0.17 vs. $[Mg^{2+}] = 0mM$, 0.17 ± 0.08 , $p < 0.01$, $n = 20$ simulations).

In different simulation trials, we reduced the voltage-dependent Mg^{2+} block of NR2B subtypes by varying amounts while keeping the network connectivity and all other simulation parameters constant. Complete relief of Mg^{2+} block resulted in significantly increased level of spontaneous activity but a significant reduction in synchrony

(synchronization index with NR2B [Mg^{2+}] = 0.8mM: 0.87 ± 0.17 vs. NR2B [Mg^{2+}] = 0mM: 0.17 ± 0.08 , $p < 0.01$).

Experimentally, antagonizing either the NR2A-NMDAR or the NR2B-NMDAR subtypes did not alter the pattern of network activity in uninjured neurons (**Figure 3.7 A**). In contrast, the activity of a mechanically injured network was significantly desynchronized (SI uninjured 0.55 ± 0.13 vs. 0.14 ± 0.09 , paired t-test, $p < 0.01$, $n = 8$ cultures). Although the global synchronization of the network was reduced as a result of injury, several clusters of modestly synchronized oscillations within smaller neuronal ensembles emerged with the reduction of overall synchronization. These clusters encompass subpopulations of neurons whose activity pattern is different from neurons in other clusters. Antagonizing NR2A subtypes with NVP did not significantly alter the temporal pattern of activity or synchronization in an injured network (A). However, selective blockade of NR2B-subtypes with Ro-25 unmasked synchronization of injured neuronal networks (SI injured 0.14 ± 0.09 vs. injured + Ro-25 0.32 ± 0.18 , $p < 0.05$) (Figure 3.7 A, C). Interestingly, the cluster of neurons that were most desynchronized (SI < 0.1) remained desynchronized following Ro-25 treatment. In comparison, modestly synchronized clusters ($0.2 < \text{SI} < 0.4$) expanded in size. Consistent with increased contribution of NR2B subtypes to $[\text{Ca}^{2+}]_i$ oscillations following injury, Ro-25 caused a significant reduction in the frequency of calcium activity relative to uninjured controls or vehicle-treated injured cultures (Figure 3.7 B). Together, these data suggest that the underlying synchronous oscillations in an injured network are masked by the

uncorrelated activity of NR2B-NMDARs, and this synchronization can be recovered by selectively antagonizing NR2B-NMDARs.

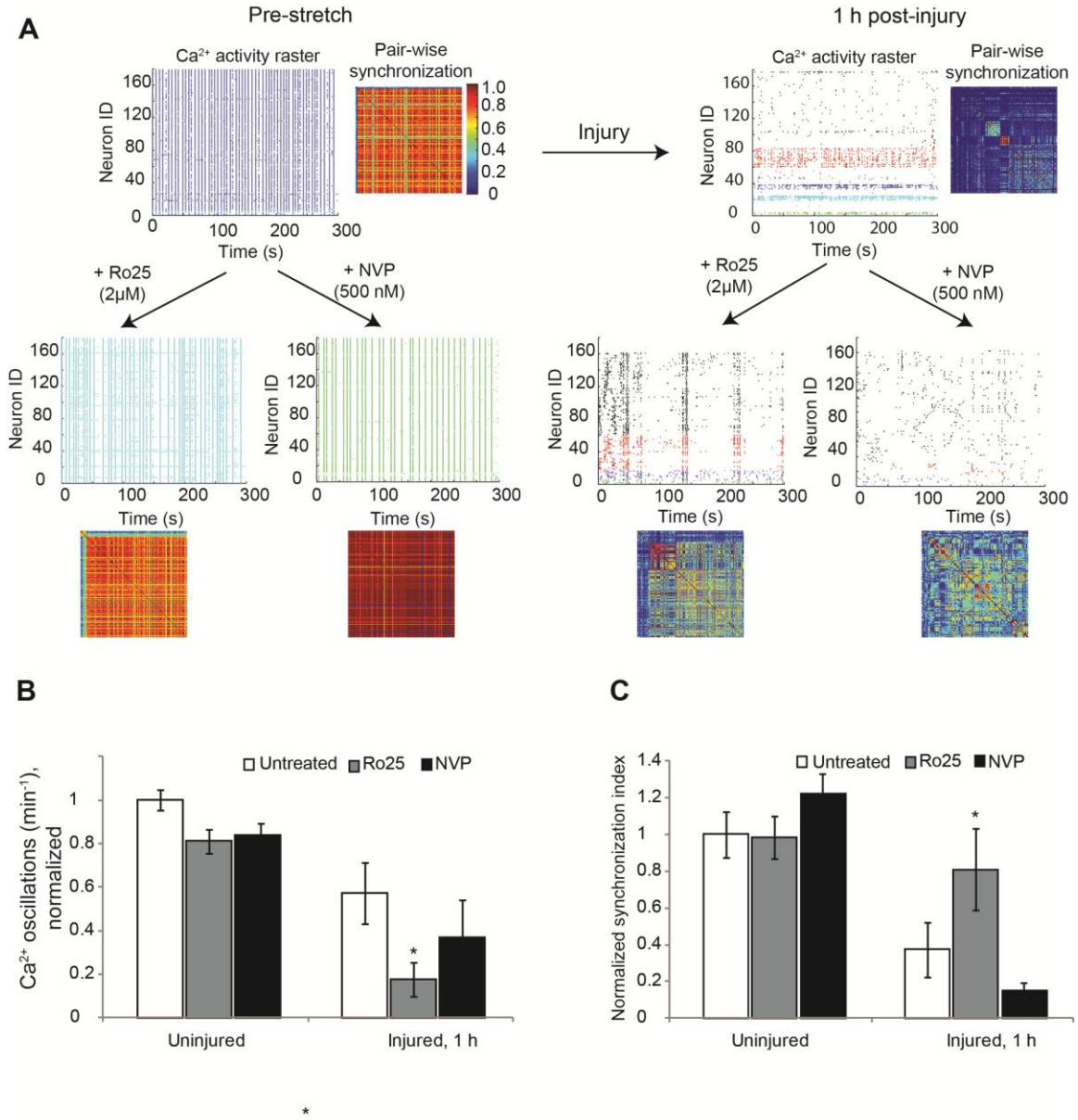


Figure 3. 7: Activation of NR2B-containing NMDARs disrupt the coordinated activity of an injured neuronal network. Injury caused a reduction in synchronization of calcium activity at 1

h (**A**, **C**). Frequency of spontaneous $[Ca^{2+}]_i$ activity (**B**) was also significantly reduced following injury. The amount and the pattern of activity were insensitive to selective NR2A or NR2B-NMDAR block in naive cultures, however, Ro-25 significantly rescued synchronization in injured networks. **A**: Representative raster plot of somatic calcium activity of a microcircuit prior to injury (left) and the same circuit following injury (right). Neurons with similar pattern of activity are grouped together and color-coded.

Activation of NR2B-NMDARs in injured neurons reduces networks augmentation induced with synchronization.

With evidence that both the initial functional connectivity and NR2B:NR2A NMDAR content of individual neurons strongly influence the post-injury network topology and synchronization of the neural circuit, we next explored how these factors influenced remodeling of the circuit following mechanical injury. Past work shows that a fixed period of induced synchronization by blocking inhibitory neurons permanently changes the activity pattern of *in vitro* networks and increases global functional connectivity (Arnold et al., 2005). We recognize this model of "recurrent network excitability" is not a classic model of long-term potentiation (LTP), but this adaptation response of the microcircuit shares many mechanisms with different models of LTP - the re-shaping of the microcircuit depends on protein translation, NMDA receptor activation, and the early transcriptional changes occurring during the induced synchronization (Arnold et al., 2005). Therefore, we selected this as a method to explore how the function of injured microcircuits can be recovered after injury.

We explored the plasticity of an injured circuit by measuring changes in global functional connectivity, single-cell somatic Ca^{2+} amplitudes, and nuclear c-fos localization two hours following an induced synchronization period (Figure 3.8A). To maintain consistency with prior experiments, we introduced this synchronization period one hour after injury and evaluated the network three hours after injury. In uninjured cultures, bicuculline-induced brief period of heightened synaptic activity resulted in persistent synchronous calcium oscillations and significantly increased global functional connectivity two hours post-stimulus (Figure 3.8B). This switch in network state was dependent on signaling through the NMDARs, and more specifically, relied on NR2A, but not NR2B receptor, activation (Figure 3.8C). Although we could induce synchronous oscillations in an injured network with bicuculline treatment, the network activity reverted to its pre-treatment state following bicuculline washout and there was no enhancement of functional connectivity two hours after injury (Figure 3.8C). Given a deficit in the induction of network plasticity following injury, we examined if we restored the deficit by targeting the blockade of either NR2A- or NR2B-containing NMDARs. To this end, we measured the amplitude of somatic calcium transients of unstretched and stretch injured neurons before and 2-hours after bicuculline stimulus as an indication of excitability (Frick et al., 2004). We found an enhancement in calcium signals from unstretched neurons post-stimulus, which was greatly diminished in injured neurons (Figure 3.8D). Finally, since the long-term changes in excitability following bicuculline stimulus are dependent on transcription, we measured the nuclear localization of the

activity-dependent transcription factor, c-fos, in uninjured and stretch injured neurons (3 hours post-injury and 2 hours post-bicuculline stimulus). Uninjured neurons showed significantly elevated nuclear c-fos following bicuculline stimulus compared to untreated cultures, whereas this response was greatly reduced in injured neurons (Figure 3.8E). Together, these data support an impairment in network plasticity following stretch injury, consistent with previous reports of altered excitability and impaired expression of LTP following TBI (Reeves et al., 1995; Schwarzbach et al., 2006; Sick et al., 1998).

Several reports highlight the importance of precise spatiotemporal pattern of synaptic activation for generating dendritic calcium influx and for the induction of plasticity (Spruston et al., 1995). We hypothesized that injury-induced reduction in voltage-dependent Mg^{+2} block of NR2B-containing NMDARs, resulting in uncorrelated activation of NR2B subtypes, is responsible for the inability of injured neurons to encode an external stimulus and change their functional integration within the microcircuit following bicuculline stimulus. To test, we stretch injured neurons as before and paired the 15-min bicuculline stimulus with either Ro-25 or NVP. All drugs were washed away and neurons incubated for additional 2 hours before calcium imaging. We compared the functional connectivity of an injured network 2-hrs following bicuculline + Ro-25 stimulus to the connectivity pre-stimulus and found a significant increase (Figure 3.8C). Other measures of synaptic scaling, somatic Ca^{2+} amplitude and c-fos nuclear localization, also increased. Task learning in injured networks still depended on signaling through NR2A-containing NMDARs since pairing bicuculline stimulus with either APV

or NVP did not increase functional connectivity. Together, these findings suggest that enhanced contribution of NR2B-subtypes to $[Ca^{2+}]_i$ activity reduces the stimulus encoding capacity of an injured network. At the single neuron scale, recovery of recurrent excitability requires a targeted inhibition of NR2B-containing NMDARs.

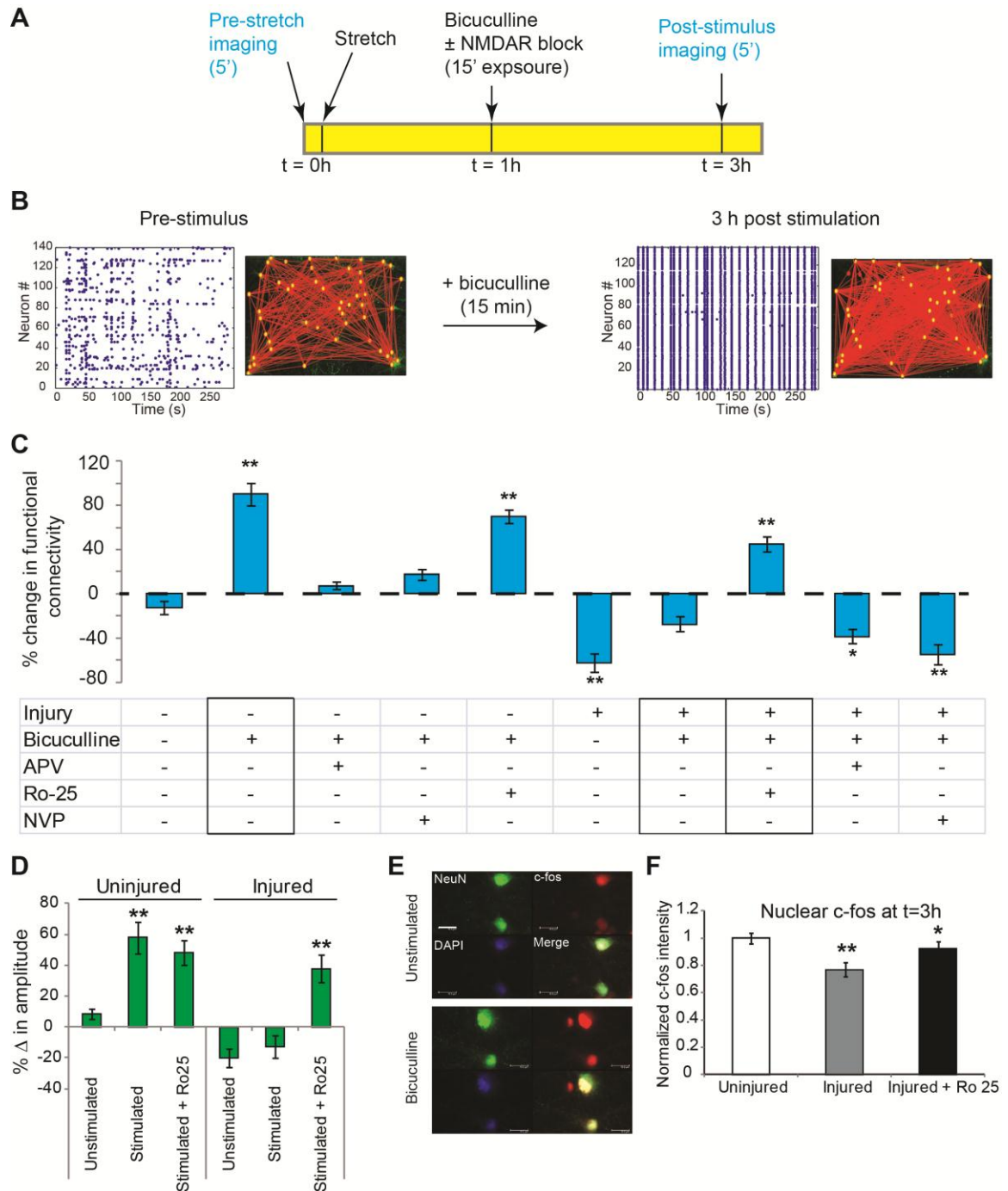


Figure 3. 8: Enhanced NR2B activation prevents task-learning in an injured network. A:

Neurons were stretch injured ($t=0$) and their spontaneous activity recorded at 1-hr ($t=1$ hr). A 15-

min exposure to bicuculline was used to induce a period of synchronized activity and the spontaneous activity measured 2-hr following washout (t=3hr). An increase in functional connectivity from t=1hr to t=3hr indicated acquisition and maintenance of task-learning or a memory of the bicuculline stimulus (**B**). Task-learning was dependent on signaling through the NR2A-containing NMDARs in uninjured cultures. Injury significantly abolished task-learning, but antagonizing NR2B subtypes during the acquisition phase significantly rescued the ability of injured neurons to change their integration in the network (**C**). The change in amplitude of somatic calcium transients before and 2 h after bicuculline stimulus was used as an indication of excitability. We found an enhancement in calcium amplitude from uninjured neurons which was greatly diminished in injured neurons but could be rescued by pairing Ro-25 with bicuculline (**D**). Since long-term changes in network activity patterns and enhancement in functional connectivity following bicuculline stimulus are dependent on transcription, we measured the nuclear localization of the activity-dependent transcription factor c-fos in uninjured and stretch injured neurons. Nuclear c-fos localization increased following bicuculline stimulus at t=3hr relative to no treatment in uninjured neurons. The normalized nuclear c-fos intensity was significantly reduced in injured neurons stimulated with bicuculline but was rescued by pairing bicuculline stimulus with Ro-25 (**E**). ** $p < 0.01$, * $p < 0.05$.

DISCUSSION

In this study we explored how properties of connectivity and calcium signaling at the single neuron scale relate to the disruption in network structure and function that occurs following mechanical injury. Our main finding was that individual neurons undergo complex functional rewiring following injury; this rewiring response is

influenced strongly by the initial neuronal connectivity within the microcircuit, the relative balance of NR2B- and NR2A-containing NMDARs in each neuron, and the subsequent synchronization of the circuit after injury. Together, these data point to dual roles for the NR2B-containing NMDARs in influencing outcome after injury. First, by acting as primary mechanosensors, the NR2B-NMDARs confer individual neuronal susceptibility to mechanical injury. Second, by contributing to uncorrelated activation after injury, of NR2B NMDAR subtypes contribute to impairments in network activity and a reduction in network plasticity.

An emerging set of studies show immediate disruptions in the network activity following mechanical trauma. Cullen et al. show that a rapidly applied fluid shear stress was capable of disrupting spontaneous action potential firing within selected neurons (LaPlaca et al., 2006), and similar changes were observed when three-dimensional constructs were injured in pure shear (Cullen et al., 2007). Using organotypic hippocampal slice cultures, Morrison et al. demonstrate that sublethal biaxial stretch causes electrophysiological dysfunction in the CA1, CA3, and dentate gyrus and results in changes in short-term plasticity (Yu and Morrison, 2010). Similarly, a suppression in broad periodic calcium oscillations appeared following injury to dissociated cortical neurons, and this suppression in activity persisted two days following the initial injury and was accompanied with a change in the composition of synaptic glutamate receptors (Goforth et al., 2011). The recent results from Goforth et al. are most directly comparable to our tests using a moderate level of mechanical injury, where our results

also show an immediate reduction in spontaneous activity. Moreover, we observed a similar reduction in the excitatory tone of the network post-injury, using a method distinct from the electrophysiological techniques employed by Goforth et al. By acquiring imaging information at higher imaging rates and performing individual cell-based analysis, our data also reveal new features of this response that included an emergence of numerous local modules within the network, reduction in the functional connectivity, and a broad loss in synchronization. These new data suggest that mechanical trauma can immediately change the topology of a network. The origin or functional consequence of this change in network wiring are in large part mediated by NR2B-containing NMDAR activation.

The NMDA receptor subserves many important processes in the central nervous system, including survival signaling, synaptic plasticity and memory. Many of its functions depend on the presence of voltage-dependent Mg^{2+} block which only allows Ca^{2+} influx when both pre-synaptic and post-synaptic cells are active and suppresses NMDAR activity when the post-synaptic cell is inactive. Although many reports highlight the detrimental effects of excessive Ca^{2+} influx through the NMDAR acutely following traumatic brain injuries, the effect of mechanical forces on the properties of the NMDAR have largely been ignored. NMDARs have previously been shown to be mechanically activated (Paoletti and Ascher, 1994) and both in vitro and in vivo traumatic injury causes a reduction in the voltage-dependent Mg^{2+} block of NMDARs (Furukawa et al., 2000; Zhang et al., 1996). Here we investigated the contributions of

NR2A and NR2B subunits of the NMDAR to mechanical injury mediated changes in functional rewiring of neurons within a microcircuit.

Differential roles for NR2A- and NR2B-NMDARs in shaping synchrony, functional recovery, and plasticity following injury

The NMDA receptor subunit composition differentially regulates several biochemical pathways in neurons. For example, the NR2A-containing NMDAR is required for LTP induction while the NR2B-type influences LTD, though the age of the animal, the region of the brain investigated, and the experimental protocol for induction of plasticity can also affect this distinction (Bartlett et al., 2007; Cui et al., 2013; Foster et al., 2010; Jin and Feig, 2010; Morishita et al., 2007). Additionally, the distribution of NR2A- and NR2B-subtypes at the synapse is different - the NR2B-subtypes are found at the post-synaptic, extrasynaptic and presynaptic regions while NR2A-subtypes are primarily localized to the synaptic surface (Kohr, 2006; Thomas et al., 2006). Many neurons express more than one of the modulatory NR2 subunits and the full spectrum of NMDAR signaling is critically dependent on the receptor composition, spatial distribution and association with intracellular binding partners. The distinct spatial distribution also has important consequences for survival signaling since activation of extrasynaptic NMDA receptors lead to activation of pro-apoptotic pathways while synaptic NMDAR activation is neuroprotective (Hardingham and Bading, 2010). Given the distinct roles for these subtypes in several important physiologic processes, it is not surprising that the NMDAR subtypes also differentially influence outcome in pathologic

states. However, to our knowledge, this is the first report that signaling through the NR2A and NR2B subtypes differentially affect patterns of spontaneous calcium activity and plasticity of injured neurons.

Neuronal networks are comprised of heterogeneous elements and have rich repertoire of structural and functional connectivity. The rules that determine how the functional connectivity of an individual neuron will change as a result of injury have so far been elusive. By studying the same neuronal networks in culture with single cell resolution before- and after-injury, we found that neurons that were highly connected prior to injury are more likely to keep their connection targets post-injury, whereas low degree nodes are more likely lose their targets or form new targets. Within the low degree group, the decision to lose connections or form new connections is in part influenced by the ratio of NR2B to NR2A content. From network controllability standpoint, nodes with high degree, or hub nodes, are essential for *maintaining* the rhythm or a particular state of the network, whereas, low degree nodes are required to *change* the network state (Liu et al., 2011). Our results suggest that NR2B subtypes influence susceptibility of individual neurons to mechanical injury and shed new light on how neurons change their integration into the network following injury. These findings provide new avenues for cell-based or network-based repair of an injured brain.

Network plasticity

Stretch-induced selective loss of voltage-sensitive Mg^{2+} block of the NR2B-type receptors eliminates a cardinal feature of the NMDAR. Calcium enters the cell through the NMDAR only when presynaptic glutamate release and postsynaptic depolarization occur simultaneously (correlated activity). At resting membrane potential, the pore of the NMDAR is blocked by external Mg^{2+} ions which prevents NMDAR-mediated Ca^{2+} influx and suppresses uncorrelated activity. One type of uncorrelated activity that is suppressed by Mg^{2+} block is spontaneous, action potential-independent, single vesicle release events ("minis"). Supporting this idea, we observed a significant increase in cytosolic Ca^{2+} with $1\mu M$ glutamate application to injured neurons that was nearly absent in uninjured neurons, which have an intact Mg^{2+} block mechanism. This concentration was chosen because the concentration of glutamate released by minis is on the order of $1\mu M$ at the synaptic cleft (Hertz, 1979).

Activity-dependent modulation of synaptic efficacy is an important aspect of brain function during learning and memory. Animal models of TBI show behavioral impairments in long-term memory, as well as reduced long-term potentiation in acute brain slices. We found that plasticity in an injured network could be recovered by blocking signaling through the NR2B-containing NMDARs during chemical-LTP stimulus. Our findings are consistent with previous reports of the importance of the NMDAR Mg^{2+} block for the induction of plasticity (Miyashita et al., 2012), but highlight an important distinction of NR2B-containing NMDARs. Many forms of LTP, including

bicuculline stimulus used in this study, are dependent on CREB signaling (Hardingham et al., 2001). Miyashita and colleagues used transgenic flies expressing NMDARs defective for Mg^{2+} block and found that these mutants have increased expression of CREB repressor genes and as a result, are defective for long-term memory formation (Miyashita et al., 2012). Activation of extrasynaptic NR2B receptors (by injured astrocytes) can further shut-off CREB signal and even override CREB-activating signal triggered by synaptic NR2A-NMDAR activation (Hardingham and Bading, 2002). In light of these reports, our data suggest that acute behavioral deficits and memory impairments following mild TBI may be reduced by pairing NR2B antagonists during memory acquisition task.

Significance of synchronization

Rhythmic, synchronized activity is a natural property of neuronal networks, conserved across CNS tissue preparations, from dissociated cultures to *in vivo*, and across species, from *C. elegans* to humans. Mounting evidence suggests that transient synchronization of neuronal discharges dynamically binds widely distributed sets of neurons into functionally coherent ensembles, allowing these networks to communicate effectively. (Singer, 1993; Womelsdorf et al., 2007). In mice and humans alike, synchronization in the β - and γ -band is involved in a variety cognitive functions, such as perceptual grouping, attention-dependent stimulus selection, routing of signals across distributed cortical networks, working memory, and perceptual awareness. Due to its pervasive role of in cognitive and executive processes, it is not surprising that disruptions

in neural synchrony are found in several pathological brain states, including schizophrenia, epilepsy, autism, Alzheimer's disease and Parkinson's disease. We believe that many of the cognitive deficits following TBI may be linked to changes in the coordinated firing of brain regions.

In contrast to the large number of studies that investigated the mechanisms for emerge of synchrony and its role in physiological cognitive processing, relatively few studies have identified the mechanisms that reduce or alter neuronal synchrony in pathological brain states. An obvious mechanism for desynchrony is any number of disorders that cause structural or functional damage to axons and thereby interfere with fast and precise electrical transmission needed for synchronization. Demyelination of axons in multiple sclerosis(Arrondo et al., 2009; Hardmeier et al., 2012), cytoskeletal damage to long-range axonal tracts in traumatic axonal injury(Marquez de la Plata et al., 2011), proteolysis of axonal Na⁺ channels after mechanical stretch injury (Patel et al., 2012), or the overabundance of misfolded pathological protein aggregates in the axons of α -synucleinopathies(Volpicelli-Daley et al., 2011) or tauopathies (Babiloni et al., 2004; Stam et al., 2003) are all correlated with abnormalities in neuronal synchronization. Alternatively, change in the excitatory vs. inhibitory balance can influence synchronization as evidenced by the impairment in γ -band synchronization when NMDA receptors in parvalbumin-positive interneurons are selectively ablated in mice (Korotkova et al., 2010). Here, we report an entirely new mechanism for network desynchronization:

the reduction in voltage-dependent blockade of NR2B-containing NMDARs following mechanical injury, leading to increased uncorrelated activity.

In closing, our work identifies new features embedded within neural circuitry that dictate whether individual neurons will de-integrate from a microcircuit following injury, how the structure of the network is re-shaped after injury, and how selective changes to the properties of individual NMDAR subtypes mediates the impairment of plasticity in networks after injury. Although the exact mechanisms to re-integrate neurons into the remaining microcircuit after injury are the focus of future studies, our current work identifies important properties of individual neurons that lead to the complex rewiring of circuitry that occurs following traumatic injury, and may provide insights into how the circuitry within different brain regions can change and recover following traumatic brain injury.

CHAPTER 4: NMDA-induced mitochondrial dysfunction contributes to neuronal network impairment that is mitigated by NIM811

ABSTRACT

NMDA receptor overactivation induced excitotoxicity is a common pathological mechanism of neurodegeneration. Given the central role of mitochondria in ATP production, Ca²⁺ buffering, oxidative stress, and apoptosis, there has been a concentrated effort on targeting the mitochondria for reducing excitotoxic burden that may lead to better behavioral and cognitive outcomes following stroke, epilepsy, or traumatic brain injury. Here we report that brief NMDA receptor overactivation increases the coordinated activity of the neuronal network resulting in activity- and transcription-dependent neuroprotection. In contrast, longer NMDA receptor overactivation increased the permeability of mitochondrial inner membrane resulting in depolarization of the mitochondrial membrane potential and mitochondria swelling. Neuronal activity and the functional integration of the neuronal microcircuit were both significantly impaired following an excitotoxic NMDA stimulus. Interestingly, acute functional de-integration of individual neurons from the network was predictive of delayed cell death. Inhibiting the mitochondrial permeability transition pore with NIM811 attenuated NMDA-induced mitochondria swelling and improved network connectivity, in part due to reduced AMPA receptor internalization. Separately, we found that mitochondrial motility is closely tied to morphology. Acute synaptic priming reduced NMDA-induced mitochondria swelling, however, this protection was lost when mitochondria movement was halted. Together,

these studies provide a better definition of the acute effects of excitotoxicity and mitochondria dysfunction on neuronal networks and point to two separate targets for repair.

INTRODUCTION

NMDA receptor activation plays a critical role in synaptic physiology and neuronal survival while overactivation of the same receptor can drive neuronal death (Cull-Candy and Leszkiewicz, 2004). NMDA-induced excitotoxicity is a shared feature of the pathophysiology of many neurological and neurodegenerative disorders (Arundine and Tymianski, 2003; Doble, 1999; Sattler and Tymianski, 2000). Over the past decade, our knowledge of the mechanisms of NMDA-induced excitotoxicity has increased tremendously: the relative contributions of synaptic vs. extrasynaptic receptor activation to excitotoxicity, the role of NR2A- vs. NR2B-containing NMDARs on Ca²⁺ load, and the effects of mitochondrial Ca²⁺ accumulation on cell viability (Arundine and Tymianski, 2003; Palmer et al., 1993; Rego and Oliveira, 2003; Sattler and Tymianski, 2000; Stanika et al., 2009). However, one potentially important aspect of excitotoxicity that needs more definition is how these molecular changes within individual neurons, especially mitochondria dysfunction, affect the dynamics of an interconnected microcircuit.

Mitochondria are key potential mediators in synaptic development and neuronal degeneration, and therefore are ideal candidates to play a significant role in reshaping a neural microcircuit after excitotoxic exposure. Certainly, the role that the

mitochondria play in the intrinsic apoptosis pathway is well recognized, and targeting this pathway is a frequent theme in neuroprotection strategies for traumatic injury, stroke, and other neurodegenerative disorders (Chen and Chan, 2006; Mbye et al., 2009; van Horssen et al., 2012; Wood-Kaczmar et al., 2013). Recent work shows that caspase-3 activation and release of cytochrome C from mitochondria are key intermediary steps in the induction of long term depression at hippocampal synapses, expanding the role of caspase-3 activation beyond the well recognized role in neuronal apoptosis (Li et al., 2010c). The movement and positioning of mitochondria near the base of synapses also seems to play a role in synaptic plasticity, given that synaptic activity will influence the relative residence time of synapses trafficking along dendrites in the vicinity of synapses and, more broadly, the association of mitochondria movement disorders with some neurological diseases. Finally, the mitochondria are also important regulators of axonogenesis (Mattson and Partin, 1999) and the formation of the dendritic arbor (Chihara et al., 2007). Together, these past studies indicate that mitochondria can serve to change three aspects of the network structure – the number of neurons (nodes) in the network through apoptosis, the strength of connections among nodes through modulation of synaptic strength, and the number of connections (i.e., network degree) that occur within a network through the regulation of neurite outgrowth.

In this report, we used calcium imaging to assess the changes in neuronal network firing patterns and functional connectivity following NMDA stimulus. Given the pervasive role of mitochondria in supporting the energy demands of ongoing neural

activity, as well as its central role in calcium buffering, LTD, and excitotoxic death (Chen and Chan, 2006; Li et al., 2010b; Stanika et al., 2009), we investigated the role of the mitochondria in mediating neurodegeneration and neural circuit adaptation.

We found that a toxic dose of NMDA (100 μ M + 10 μ M glycine), applied for as little as 30s, resulted in fast synchronized network activity and led to an activity-dependent tolerance against subsequent longer exposure to NMDA. The same toxic dose, applied for 10min or 20min, resulted in ballooning of the mitochondria, depolarization of the mitochondrial membrane potential and loss of activity in a fraction of the population. Pretreatment with the mitochondrial permeability transition pore inhibitor, NIM811, prevented the mitochondrial shape changes, improved network function and attenuated cell death. Interestingly, we found that NMDA-induced changes in mitochondria morphology are influenced by mitochondrial motility.

METHODS

Cell culture and calcium imaging:

Primary cortical neurons from E18 rats were isolated and cultured for DIV 18-21 as described in previous chapters. For calcium imaging, neurons were loaded with either fluo-4 or transduced with GCaMP3 for long-term imaging and the network activity analyzed as described in Chapter 2.

Drug treatments

For excitotoxic injuries, neurons were treated with NMDA (100 μ M) and glycine (10 μ M) in saline solution containing physiologic $[Mg^{2+}] = 0.8mM$ for various durations.

NIM811 (20 μ M, Novartis), bicuculline (100 μ M, Sigma-Aldrich), jasplakinolide (2 μ M)

Measuring mitochondrial morphology

Primary neurons were transfected with Mito eYFP protein overnight the day before imaging. The mitochondrially targeted eYFP construct (generously provided by Dr. Ian J Reynold, University of Pittsburgh, Pittsburgh, PA) consists of the gene for eYFP fused to subunit IV of cytochrome c oxidase, inserted into the mammalian expression vector pCDNA3 (Rintoul et al., 2003). The construct was complexed with Lipofectamine 2000 (Invitrogen) with a reagent-to-plasmid ratio of 3:2. The complex was incubated in Dulbecco's Modified Eagle Medium (BioWhittaker, Basel, Switzerland) at room temperature for 20 min before it was added to the cells. Transfected cells were then incubated in Neurobasal medium for 4 h at 37⁰C and 5% CO₂ before the media was replaced with feeding medium. Cells were ready for use the following day, and the eYFP tag allowed for a determination of mitochondrial morphology. On average, approximately 10% of the cells in a culture were successfully transfected. Images of the mitochondria were collected prior to and following NMDA stimulus every 10s for a total 1 hour.

Each mitochondrion in an image was identified manually, and the outline of the mitochondrion was automatically identified using an adaptive threshold algorithm which accommodates for variation in the local background fluorescence of each mitochondria.

An aspect ratio (AR) was computed for each mitochondrion as the ratio of the maximum length to width of the outlined mitochondrion. Since the same set of neurons were imaged prior to and following NMDA stimulus, we computed the difference in the aspect ratio each mitochondrion. Normally, mitochondria in dendrites assume a long tubular shape ($AR > 1$) that can change to nearly spherical following NMDA stimulation ($AR \sim 1$). Therefore, negative values for ΔAR indicate a contraction and swelling of mitochondria. Mitochondria were quantified from 8-11 cultures in each treatment group with an average of $N = 50$ ΔAR measurements per condition.

Measurement of $\Delta\psi_m$

The mitochondrial membrane potential, $\Delta\psi_m$, was estimated in individual neurons with the $\Delta\psi_m$ -sensitive fluorescent dye JC-1 per previous reports (Molecular Probes, Eugene, OR; (Hoyt et al., 2000; White and Reynolds, 1996). Briefly, neurons were loaded with JC-1 (3 μM) for 20 min at room temperature in CSS, rinsed with dye-free CSS for 10 min and then imaged on Leica SP5 confocal microscope using a 25X water-immersion objective (N.A. 0.95). Fields of neurons were illuminated with the 488-nm laser and emission at 530 and 590 nm was monitored. Once loaded into neurons, JC-1 exists in either aggregate or monomer forms, depending on $\Delta\psi_m$ (i.e. the more negative the $\Delta\psi_m$, the greater the aggregation). By monitoring JC-1 fluorescence at 590nm (red, aggregate) and 530 nm (green, monomer), one can assess relative changes in $\Delta\psi_m$. Mitochondrial depolarization is indicated by a decrease in the red to green fluorescence intensity ratio. Ratio values were obtained by dividing the signal at 590 nm by the signal at 530 nm on a

cell-by-cell basis and normalized to a starting value of 1 for comparison between cells. With this approach, a decrease in the normalized ratio represents mitochondrial depolarization.

Cell viability

Cell viability was assessed at six hours post-stimulus with a fluorescence based assay. Cells were incubated for thirty minutes with Hoechst 33342 (Invitrogen) and membrane impermeable ethidium homodimer (EtHD, Sigma-Aldrich) in order to stain total and dead/dying cells. Fluorescence images were taken at three wavelengths with FITC, TRIC, and DAPI filter sets to detect GCaMP, EtHD, and Hoechst, respectively.

Cytoskeletal disruption and mitochondria motility:

Prior to mitochondrial labeling, cortical neurons were treated with drugs to disrupt the cytoskeleton, in order to elucidate the mechanisms involved in mitochondrial transport. The actin cytoskeleton was stabilized with 2 μ M jasplakinolide (Molecular Probes) for 30 min.

For each experimental well, the percent of mitochondria moving within a 2.5 minute experimental period was determined. The total number of mitochondria within three representative regions at onset of imaging were counted. The mitochondria were then tracked for 2.5 minutes and any mitochondria that moved completely outside of the original region of interest were counted as moving. The number of moving mitochondria

in all three regions was then summed and normalized to the total number of mitochondria within the three regions.

The distance and velocity of moving mitochondria was also determined using the object tracking feature in MetaMorph (Universal Imaging, Inc., West Chester, Pa.). The tracking feature of MetaMorph was automated as much as possible but needed to be adjusted manually in regions of high mitochondrial density. Up to six mitochondria were tracked within each experiment. Mitochondria were chosen randomly as long as they moved at any time during the duration of the experiment, regardless of when they moved. Velocities of mitochondrial movement were only assessed when analysis was entirely automated. In this case, mitochondrial density was generally low and mitochondria never came in contact with other mitochondria.

Statistics

Shape change measurements developed from time lapse images of mitochondrial morphology and relative changes in $\Delta\Psi_m$ were analyzed using a one-way ANOVA, followed by Tukey posthoc testing. Changes in network properties are also analyzed using one-way ANOVA. Differences were considered significant at $p < 0.05$. All data are presented as mean \pm SEM.

RESULTS

Brief, high dose NMDA stimulus increases synchronized network activity and leads to activity-dependent preconditioning.

Despite the well-known neurotoxic effects of prolonged NMDAR overactivation, chronic low-dose NMDAR activation can offer neuroprotection against brain damage induced by ischemia, seizures, and closed-head injury (Damschroder-Williams et al., 1995; Jonas et al., 2001; Kitagawa et al., 1991; Pagliaro et al., 2001; Sasahira et al., 1995; Soriano et al., 2006). We investigated whether brief exposure (30 s) to a toxic dose of NMDA (100 μ M + 10 μ M glycine) offered the same level of neuroprotection and investigated the underlying network activity pattern signature of a preconditioned culture. The bath application of NMDA and glutamate induced an intracellular Ca^{2+} transient (Figure 4. 1 A). Following washout, $[\text{Ca}^{2+}]_i$ returned to pre-stimulus levels. However, we found that immediately following a brief NMDA stimulus, there was a significant increase in the frequency of Ca^{2+} transients in individual neurons (pre-stimulus frequency 0.08 ± 0.05 Hz vs. 15 min post-stimulus $.87 \pm 0.22$ Hz, $p < 0.01$) (Figure 4. 1 F). Furthermore, individual neurons in the network were oscillating synchronously and were sensitive to TTX + MK801, suggesting that Ca^{2+} oscillations were synaptically driven (Figure 4. 1 B-C). The frequency of oscillations and synchronization remained elevated up to 6 hr following the removal of the 30s NMDA stimulus (Figure 4. 1 F). This level of NMDA stimulus did not cause significant cell death at 6 hr or 24 hr (Figure 4. 1 G).

Given that synaptic NMDAR activity boosts intrinsic antioxidant defenses (Papadia et al., 2008) and suppresses intrinsic apoptosis pathways (Al-Mubarak et al., 2009), we hypothesized that the heightened synaptic activity following brief NMDA stimulus contributes to neuroprotection. To test, we applied an apoptotic stimulus (staurosporine) to cultured neurons that were exposed to NMDA for varying durations (30s - 30 min). Compared to no death stimulus, cultures that were previously stimulated with brief (30s - 2 min) NMDA exposure had a significantly lower cell death following staurosporine treatment (Figure 4. 1 G). In contrast, NMDA applied for longer durations (10 min or 30 min) resulted in significant cell death, which was exacerbated with staurosporine. Consistent with the neuroprotective effects of synaptic activity, TTX + MK801 applied immediately following brief exposure to NMDA resulted in significantly more cell death with staurosporine. Interestingly, the neuroprotective effects of NMDA_{brief} were dependent on transcription since pre-treatment with actinomycin D prevented the establishment of synchronous network-wide Ca²⁺ oscillations and resulted in significantly elevated cell death following staurosporine. Together, these results suggest that a toxic dose of NMDA (100 μM) applied for very brief duration (30 s - 2 min) promotes synchronized network activity and activates a transcriptional program, resulting in preconditioning and neuroprotection. In the absence of synchronized activity, the brief overactivation of NMDA receptors is unable to promote protection.

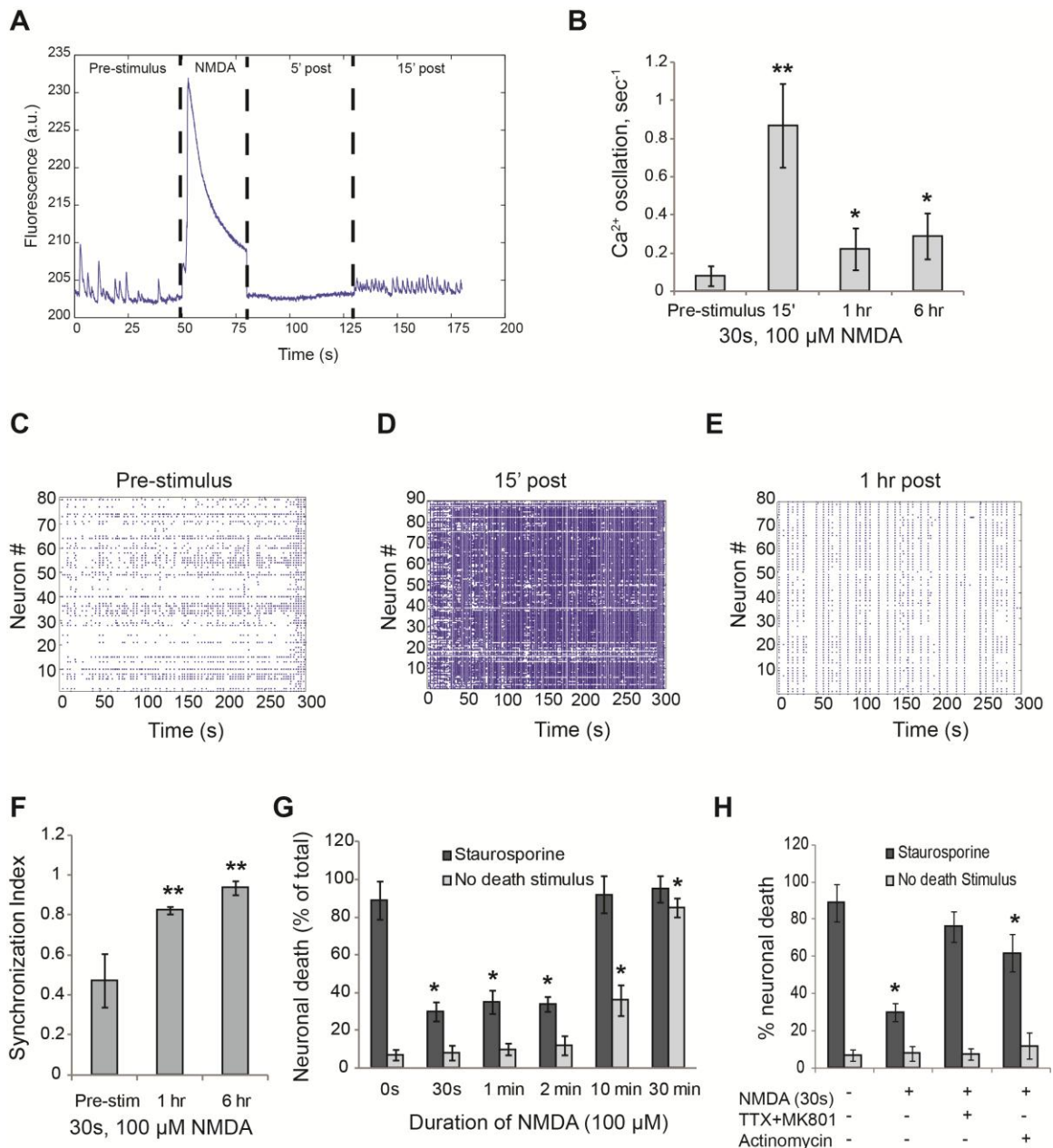


Figure 4. 1: Brief exposure to high dose NMDA enhances network activity and offers

neuroprotection. A: Intracellular Ca²⁺ fluorescence trace of an individual representative neuron shows a stable baseline interrupted by spontaneous elevations, calcium transients. A 30-s NMDA stimulus caused an immediate increase in [Ca²⁺]_i, which was quickly buffered. Following

washout, spontaneous activity was heightened at 15 min and remained elevated up to 6 hours (**B**). The temporal pattern of network activity showed a transition from sporadic activity (**C**) to higher frequency synchronized oscillations by 15 min (**D**) and remained synchronized up to 6 hr following the removal of the stimulus (**E**, **F**). Brief exposure (30s - 2 min) preconditioned neurons against the apoptotic stimulus, staurosporine. (**G**). This neuroprotection was activity-dependent and required transcription (**H**). * $p < 0.05$, ** $p < 0.01$

NIM811 reduces mitochondrial dysfunction following excitotoxic injury.

Brief exposure to toxic dose of NMDA resulted in neuroprotection that was dependent on enhanced synaptic activity and enhanced functional connectivity (Figure 4. 1). In contrast, longer exposure to NMDA (100 μ M NMDA + 10 μ M glycine for 10 min) resulted in significant cell death both at 6 hr and 24 hr (control 7% \pm 3% cell death; 10 min NMDA stimulus 36% \pm 8% death at 6 hr and 52% \pm 9% at 24 hr, ANOVA $p < 0.01$). Given the central role of mitochondria in mediating outcome after excitotoxic injuries, we investigated the effects of mitochondrial dysfunction on network dynamics.

Several past reports suggest that NMDA stimulation will lead to an accumulation of mitochondrial calcium and the rounding of mitochondrial shape (Choo et al., 2012; Peng and Greenamyre, 1998; Rintoul et al., 2003). Normally, mitochondria exist as long tubular organelles throughout the dendrites. Similar to previous reports, we found that 10 min NMDA stimulation caused a rapid change in mitochondria morphology throughout the dendrites, with these stimulated neurons showing a much more rounded mitochondria profile within 2 min of NMDA stimulation and lasting up to several hours following the

removal of the stimulus (Figure 4. 2 A, B, E). We confirmed that these changes in mitochondria shape parallel a functional impairment in mitochondrial membrane potential, $\Delta\psi_m$. The $\Delta\psi_m$ was monitored with a fluorescent probe JC-1, where a decrease in the ratio of JC-1 fluorescence emission at 590 nm relative to the emission at 530 nm indicates $\Delta\psi_m$ depolarization. Exposure of neurons to excitotoxic concentrations of NMDA (100 μ M, 10 min) caused a decrease in $\Delta\psi_m$ at 1 hr (Figure 4. 2 F, G, J). When NIM811, an mPTP inhibitor, was included during the NMDA exposure, there was a notable attenuation of the $\Delta\psi_m$ depolarization (Figure 4. 2 H, I, J) and a concomitant decrease in mitochondria swelling (Figure 4. 2 C, D, E), indicating that the mPTP is a critical regulator of mitochondria shape and function.

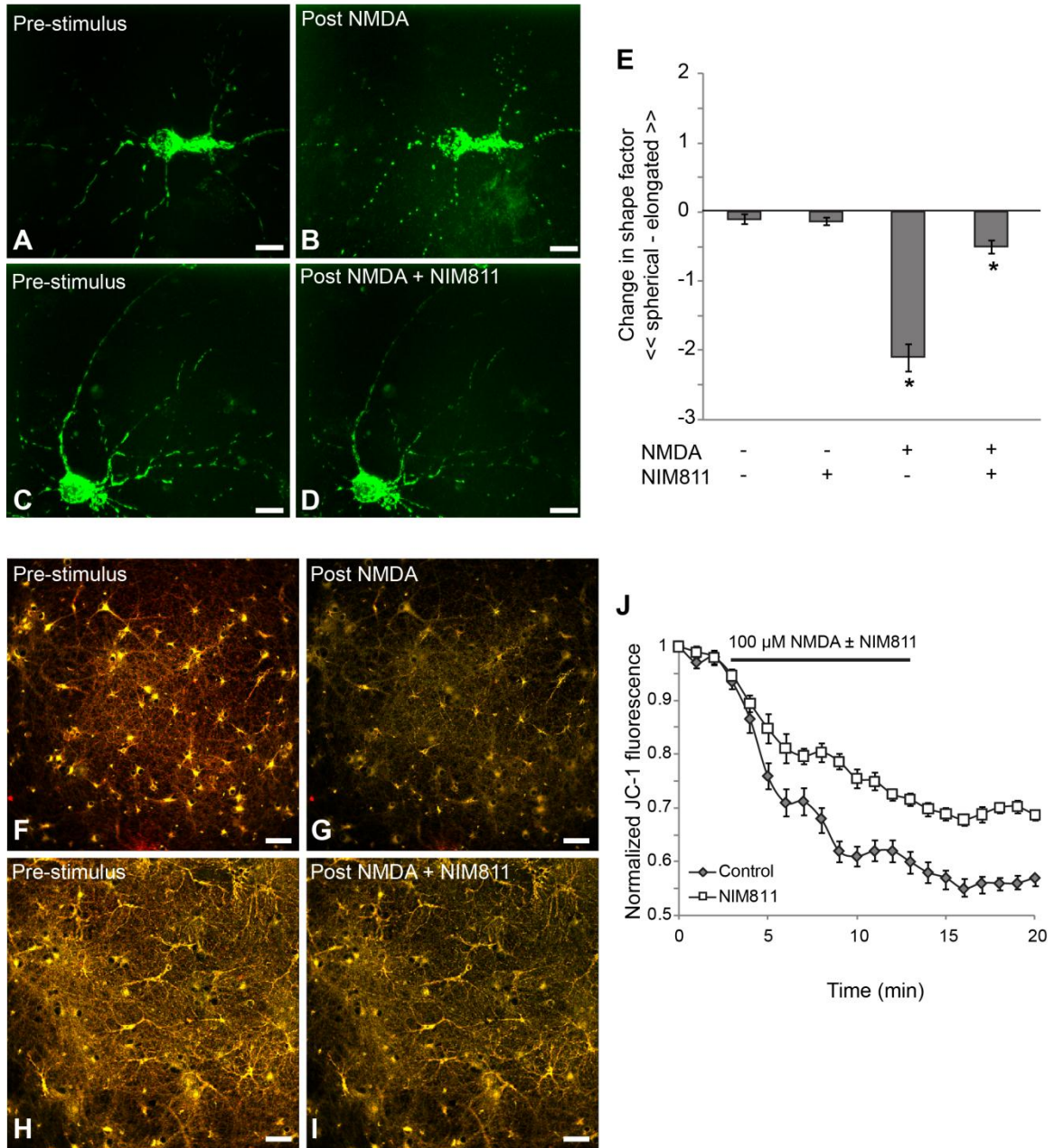


Figure 4. 2: Mitochondria dysfunction following NMDA stimulus is attenuated with NIM811 pretreatment. Individual mitochondria, tagged with eYFP, underwent a morphological change from elongated to spherical shape following 10-min NMDA stimulus (**A**, pre-stimulus, **B** - 1 hr following the removal of the NMDA stimulus). Pretreatment with the mitochondrial

permeability transition pore inhibitor, NIM811 significantly reduced mitochondria shape changes (representative images **C**, **D**; **E** summary statistics from $n=69$ mitochondria, $N = 5$ wells).

Mitochondria membrane potential, $\Delta\psi_m$, was measured with the fluorescent probe JC-1.

Following NMDA stimulus, there was a significant decrease in the fluorescence emission intensity at 590nm relative to 530nm, indicative of membrane depolarization (**F**, **G** representative images of overlay intensity of 590nm and 530nm; red indicates polarized $\Delta\psi_m$). Normalized JC-1 fluorescence ratio significantly decreased following NMDA stimulus, which was attenuated by NIM811 pre-treatment (**J**, $n = 142$ cells).

Inhibition of mitochondrial permeability transition pore reduces NMDA-induced AMPA receptor internalization.

Mitochondrial swelling is associated with the rupture of the outer mitochondrial membrane and the release of cytochrome c from the inter membrane space into the cytosol (Shalbuyeva et al., 2006). Once inside the cytosol, cytochrome c has been reported to activate caspase-3 and cause the internalization of AMPARs (Li et al., 2010b). Given that NIM811 reduced mitochondrial swelling following excitotoxic NMDA stimulus, we tested whether AMPA receptor internalization was also reduced by NIM811 treatment. AMPA receptor trafficking is a fast and dynamic process that can occur on the time scale of minutes. To identify the relative fraction of surface to internalized AMPA receptors, we used an antibody-feeding assay. Before NMDA treatment, surface AMPARs were labeled with a primary antibody recognizing an extracellular epitope of the rat GluR1 subunit. Following the NMDA stimulus \pm NIM811, cells were fixed and the previously labeled surface receptors were fluorescently tagged with a secondary

antibody. Cells were then permeabilized and the internalized AMPARs were tagged with a different fluorescent secondary antibody. To quantify, we computed the ratio of integrated fluorescence intensity of internalized GluR1 to the intensity of internalized + surface GluR1 and normalized to unstimulated untreated cells per (Lee et al., 2002). We found that an excitotoxic NMDA stimulus resulted in significantly greater internalization of AMPARs relative to untreated unstimulated cells (normalized GluR1 internalization 276 ± 29 following NMDA stimulus vs. 100 ± 21 unstimulated, $p < 0.05$, $n=18$ neurons). Antagonism of the mitochondrial permeability transition pore opening significantly significantly attenuated GluR1-containing AMPA receptor internalization (GluR1 internalization 167 ± 18 NMDA+NIM811, $p < 0.05$ relative to unstimulated and NMDA treated groups). This suggests that mPTP plays a significant role in synaptic receptor trafficking.

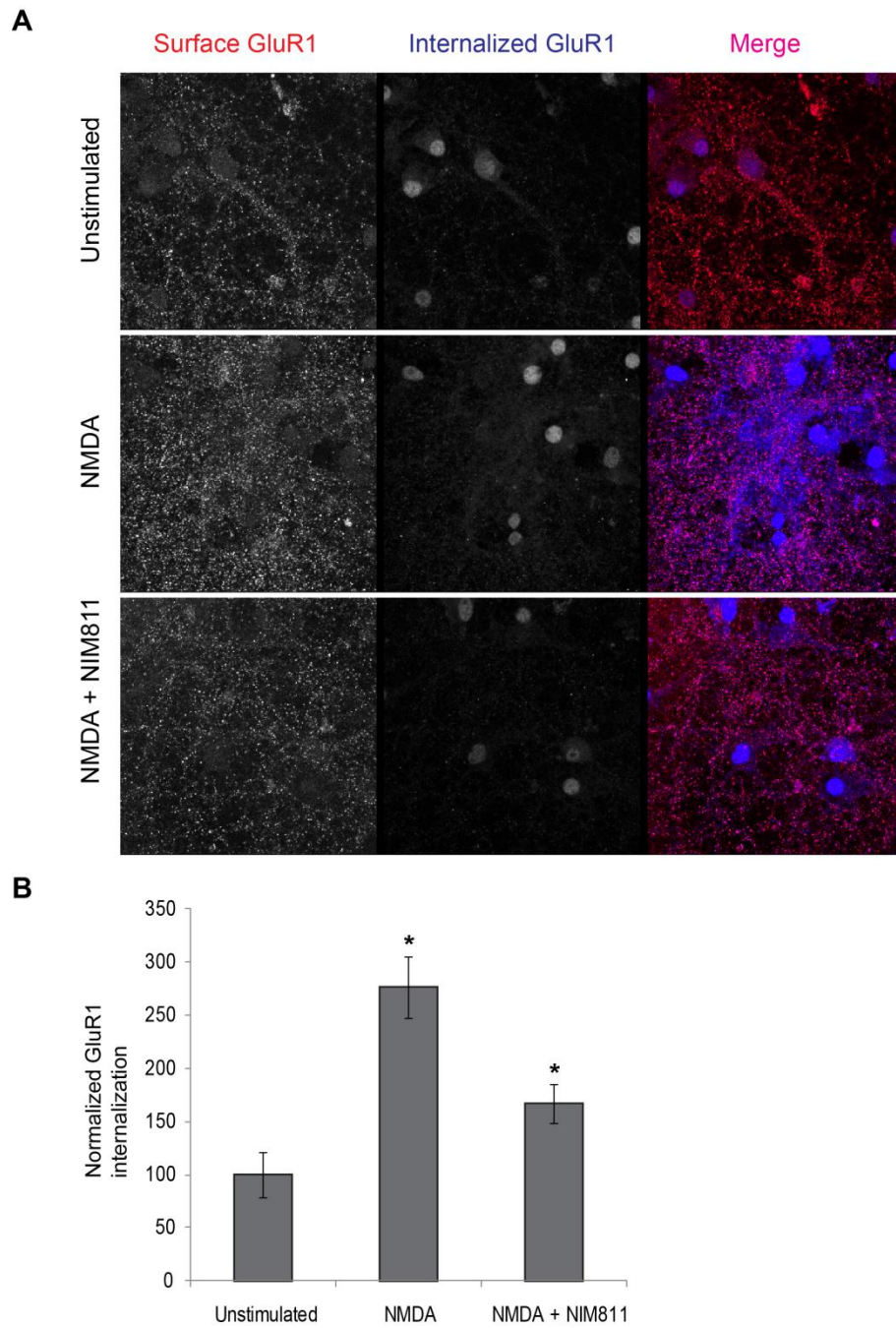


Figure 4. 3: Mitochondrial permeability transition pore inhibitor blocks NMDA-induced AMPA receptor internalization. The relative fraction of surface and internalized GluR1-containing AMPA receptors were determined using an antibody-feeding assay. **A:** Representative

images of double-label immunostaining for surface GluR1 (red, first column) and internalized GluR1 (blue, second column) and merge (third column) following either NMDA stimulus, NMDA + NIM811 or untreated. **B:** Normalized fraction of internalized GluR1 significantly increased following NMDA-stimulus relative to unstimulated untreated cells. NMDA-induced internalization was attenuated with NIM811 pretreatment. $n=18$ neurons. $*p<0.05$ compared to untreated unstimulated.

Network impairments following excitotoxicity injury are reduced with NIM811.

Given that the detrimental effects of NMDA receptor overactivation (i.e. mitochondria swelling and internalization of AMPA receptors) are attenuated by blocking mPTP, we investigated whether this improves the functional recovery of neuronal networks. In untreated cells, NMDA exposure elevated $[Ca^{2+}]_i$ throughout the duration of stimulus, which returned to pre-stimulus levels by 30 minutes following washout. Spontaneous activity of individual neurons and the coordination of Ca^{2+} oscillations between groups of neurons were both significantly reduced following excitotoxic NMDA exposure at 1 hr, Figure 4. 4 A, B (change in synchronization $-68\% \pm 23\%$ following NMDA stimulus relative to 10.6 ± 6.8 unstimulated controls, $p<0.01$). A large fraction of neurons either had no spontaneous calcium activity or their calcium activity had poor temporal correlation to other neurons, resulting in a significant decrease in functional connectivity (Figure 4. 4 C). Interestingly, we found a significant relationship between an individual neuron's functional integration in the network at 1 hr post stimulus and whether that neuron survived at 6 hr post-stimulus (logistic regression, $p<0.001$, $n=432$ cells from 8 independent trials). Network impairment was significantly attenuated with

NIM811, resulting in fewer percent of neuronal de-integration and reduced cell death (Figure 4. 4 D).

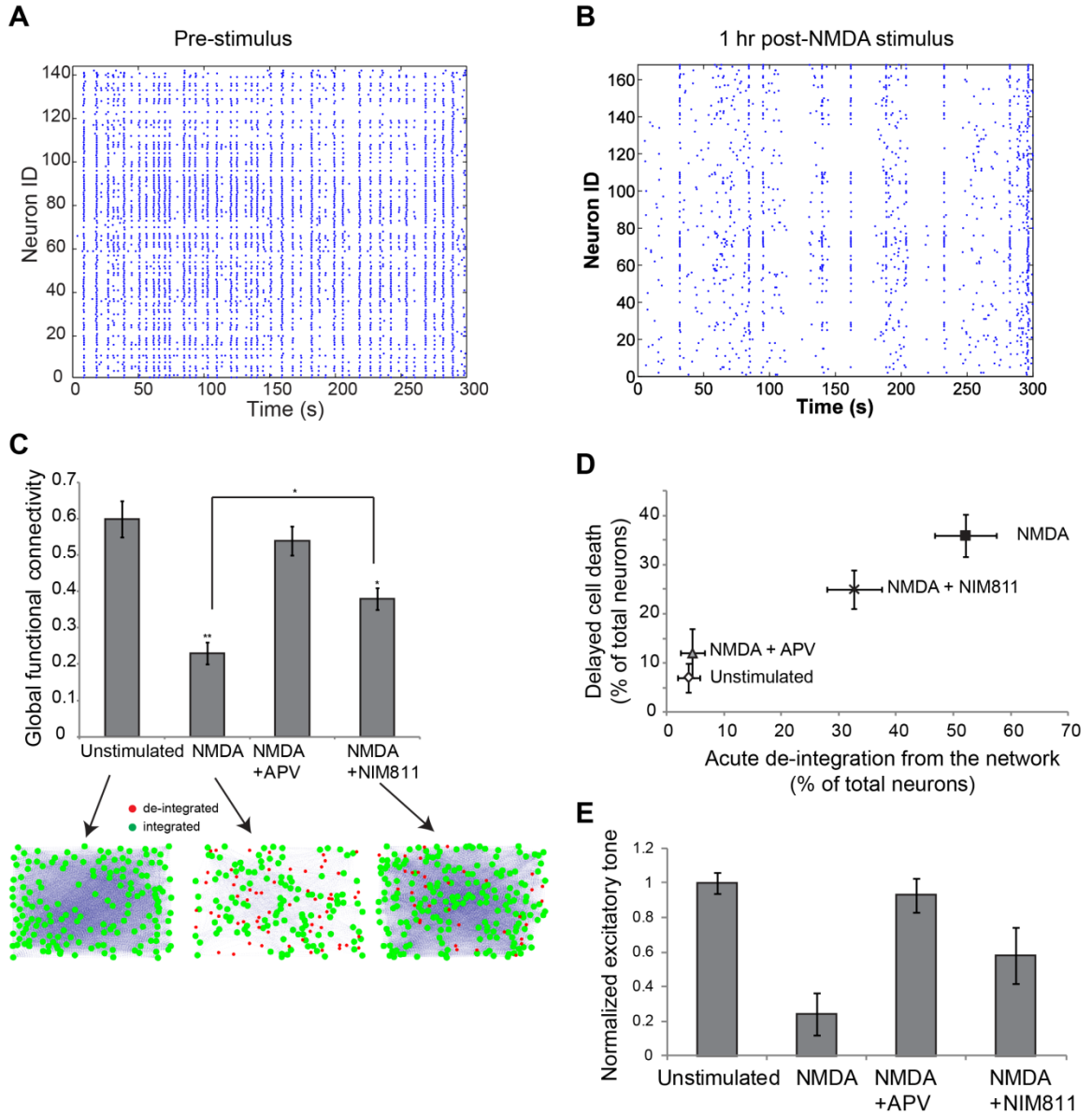


Figure 4. 4: Excitotoxic NMDA stimulus results in network dysfunction. The spontaneous activity of a mature neuronal culture (A) prior to NMDA stimulus showed many network-wide

simultaneous calcium oscillations. One hour following an excitotoxic NMDA stimulus, the activity was reduced and uncoordinated (**B**). The functional connectivity of the network, measured as the ratio of average number of functional connections per neuron to the total number of neurons, was significantly reduced following NMDA treatment, whereas NIM811 pretreatment attenuated the loss in functional connections (**C**). Representative functional connectivity maps are shown for unstimulated untreated network, following NMDA stimulus and NMDA + NIM811. Dots denote individual neurons (nodes) and blue lines indicate functional connections (edges). Red dots denote neurons that are functional disconnected from the rest of the network. **D**: The percent of neurons that de-integrated from the network acutely following injury (1 hr) correlated with percent cell death at 6 hr (logistic regression, $p < 0.01$). **E**: The excitatory tone of the network, defined as the concentration of AMPA receptor antagonist NBQX needed to stop oscillations normalized to control levels decreased following NMDA excitotoxicity. NIM811 pretreatment reduced the loss in excitatory tone.

We next determined whether NMDA receptor overactivation correlated with changes in the excitatory tone of the network. Synchronized oscillations were forced using the GABA(A) antagonist, bicuculline, to abolish inhibitory input, followed by increasing doses of the AMPA receptor antagonist, NBQX, until synchronous oscillations stopped. The final concentration of NBQX required to impair activity within the excitatory network determined the excitatory tone (Patel et al., 2012; Volpicelli-Daley et al., 2011). We found a significant decrease in normalized excitatory tone 1 hr following NMDA stimulus that was attenuated with NIM811 pretreatment (unstimulated $1.0 \pm .06$, NMDA stimulated 0.24 ± 0.12 , NMDA+NIM811 0.58 ± 0.16 , ANOVA $p < 0.05$, Figure 4.

4 E) . These functional estimates of excitatory tone are consistent our previous observation of increased AMPA receptor internalization following NMDA stimulus and the modulatory effects of NIM811. Together, these data suggest that mitochondrial swelling and mPTP opening contribute to network dysfunction following excitotoxic injury.

Mitochondrial motility influences NMDA-induced changes in morphology

The spatial distribution of mitochondria within neurites is closely tied to synaptic activity to match the energy demands at these sites. An excitotoxic injury, modeled here with a bath NMDA stimulus, causes overactivation of the NMDA receptors of all active, inactive and silent synapses. We hypothesized that the positioning of mitochondria, i.e. at the base of an synapse or away from an inactive synapse, may influence the dynamics of Ca^{2+} uptake and the ensuing morphological change following bath NMDA stimulus. Indeed, we observed that increasing synaptic activity via network disinhibition reduced NMDA-induced mitochondrial swelling (change in shape factor following NMDA stimulus -2.1 ± 0.2 vs. with bicuculline pre-treatment -1.7 ± 0.13 , $p < 0.05$). To determine whether this was due to activity-induced redistribution of mitochondria, we first tested various cytoskeletal-targeted drugs to modulate mitochondria motility. Since mitochondria use the motor proteins kinesin and dyenin for transport, we hypothesized that stabilizing or destabilizing the microtubules may influence their motility. We performed time-lapse imaging of mitochondria within mature neurons with the fluorescent MitoTracker dye and tracked their motion using the particle tracker feature of

MetaMorph. Majority of the imaged mitochondria were stationary for the duration of the experiment (2.5 min), though an average of $7.4 \pm 1.1\%$ of the total mitochondria were mobile (Figure 4. 5 A, sequence of images illustrating mitochondrial movement over a 7.5 minute period).

Depolymerizing actin filaments with latrunculin A did not alter the percent of moving mitochondria, whereas the percent moving mitochondria was significantly reduced (but not halted) when microtubules were depolymerized with nocodazole (Figure 4. 5 B). Mitochondrial movement was entirely halted when both microtubules and actin were depolymerized, indicating that mitochondria preferentially move along microtubules but can also move along actin when necessary. Intriguingly, stabilizing the actin network with jasplakinolide completely halted mitochondrial movement though stabilizing the microtubule network with taxol had no effect on mitochondrial movement (Figure 4. 5 B).

Since jasplakinolide had the biggest effect on mitochondria motility, we pre-treated cultures with jasplakinolide for 15 minutes and induced a brief period of heightened synaptic activity (bicuculline 5 min). These cultures were then stimulated with NMDA (100 μ M, 10 min). Following the removal of all drugs, we found a significant portion of mitochondria underwent morphological rounding. Importantly, the distribution of NMDA-induced mitochondria shape change in jasplakinolide + bicuculline group was no different than jasplakinolide alone or no treatment. However, as noted before, bicuculline pre-treatment rescued a small fraction of mitochondria from

swelling. These results suggest that part of synaptic activity-induced neuroprotection is due to repositioning of the mitochondria which reduces their dysfunction following an excitotoxic injury.

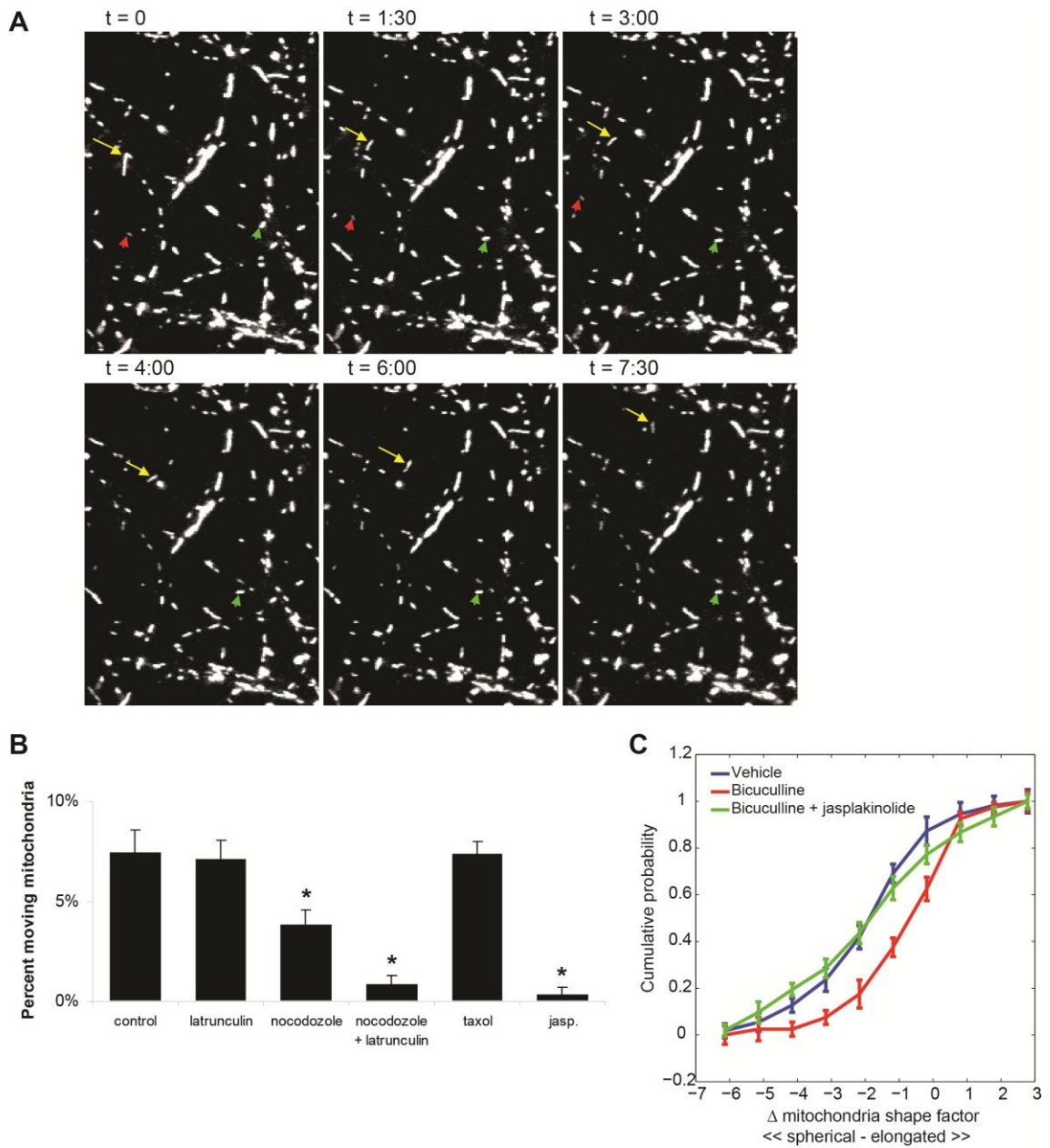


Figure 4. 5: Activity-induced mitochondrial motility reduces NMDA-induced swelling. A:

Representative time-lapse images of mitochondria movement recorded with the fluorescent dye MitoTracker. Binarized objects correspond to individual mitochondria are shown; red, green and yellow arrows track 3 mitochondria over a 7.5 min imaging session. **B:** Mitochondria motility

was significantly reduced with the actin stabilizing agent jasplakinolide (control $7.8\% \pm 1.2\%$ moving mitochondria vs. jasplakinolide $0.4\% \pm 0.2\%$, $p < 0.01$). **C:** Cumulative distribution of NMDA-induced changes in mitochondria shape. Negative values indicate mitochondrial swelling. Compared to untreated vehicle, heightened synaptic activity with bicuculline reduces mitochondria swelling (KS test, $p < 0.01$). Activity-induced protection is abolished with jasplakinolide compared to vehicle ($p > 0.05$).

DISCUSSION

In this report, we investigated the mechanisms of network dysfunction following excitotoxic NMDA stimulus. We found that NMDA receptor overactivation causes two different types of changes at the network scale. Cultured neurons exposed to a high dose of NMDA for brief duration (30s - 2 min) showed a stable increase in synaptic activity, synchronization and functional connectivity that persisted for up to several hours. This level of stimulation was neuroprotective and depended on synaptic activity and transcription. In contrast, prolonged overactivation of NMDA receptors significantly depressed spontaneous activity, reduced synchronization and functional connections. These effects were mitigated by blocking the mitochondrial permeability transition pore with NIM811, which also reduced alterations in mitochondria morphology and attenuated the internalization of AMPA receptors. Interestingly, the motility of mitochondria prior to NMDA stimulus influenced the extent of swelling following the removal of the NMDA stimulus.

The NMDA receptors have a recognized role in synaptic plasticity, pro-survival signaling, and excitotoxic death. Using high speed calcium imaging, we measured the network activity patterns that underlie survival and death signaling. Previous reports suggest chronic low level activation of the NMDA receptor results in heightened activity and protects against excitotoxic insults (Soriano et al., 2006). We found that brief overactivation of the NMDAR for as little as 30s caused long-lasting increase in the frequency and synchronicity of neuronal network activity that was dependent on transcription. These changes are reminiscent of long-term potentiation induced by brief (15 min) application of bicuculline, which causes an increase in recurrent excitability up to several hours following the removal of bicuculline (Arnold et al., 2005). Prolonged overactivation of the NMDAR, on the other hand, caused a significant desynchronization of spontaneous activity, and many neurons completely de-integrated from microcircuit. Once de-integrated, these neurons were more likely to die, possibly as a result of reduced pro-survival signaling. In support of this, we found that increasing synaptic activity via network disinhibition significantly reduced cell death in cultures that were stimulated with excitotoxic dose of NMDA.

The alterations in functional connectivity and decreased synchronization following excitotoxic stimulus may underlie cognitive impairments associated with stroke, seizures or traumatic brain injury. Many of these changes were mediated by mitochondria dysfunction. Mitochondria not only supply the ATP demands of ongoing electrical activity, they are also high capacity Ca^{2+} buffers. It is not surprising that

overactivation of NMDARs caused many intact mitochondria to accumulate excessive Ca^{2+} , resulting the opening of permeability transition pores. PTP opening causes an increase in the mitochondrial permeability to ions and solutes with molecular weight less than 1500 Da, matrix swelling and subsequent depolarization of the membrane potential. Swelling or ballooning of the mitochondria can cause rupture of the outer mitochondria membrane and release cytochrome c into the cytosol, where it has been shown cause internalization of AMPA receptors via caspse-3 activation (Li et al., 2010b). In support of this model, NIM811 pretreatment significantly reduced mitochondrial swelling, reduced AMPA receptor internalization, prevented the loss in excitatory tone, and improved the integration of individual neurons within the microcircuit. Similar improvement in network activity was seen when NIM811 treatment was initiated 30 min following the removal of the NMDA stimulus, suggesting a possible narrow therapeutic window. Indeed, the beneficial effects of NIM811 on neuronal network properties are consistent with a recent report of improved behavioral outcome following NIM811 treatment in a rodent model of severe traumatic brain injury (Readnower et al., 2011). Together, these studies prove a more clear mechanistic understanding of how mitochondria dysfunction cause network dysfunction and contribute to behavioral deficits.

A separate point of control is mitochondria motility, or more specifically, mitochondrial distribution within the cell. Mitochondria are dynamic organelles whose spatial distribution is closely tied to the energy demands of active synapses. Dysfunctions in mitochondria motility create an imbalance between energy supply-and-demand and are

thought to contribute to many neuromuscular disorders (Cho et al., 2010). Mitochondria, like many organelles, use the motor proteins kinesin and dynein for anterograde and retrograde transport respectively along the microtubules (Pilling et al., 2006). We found that stabilization of the actin cytoskeleton completely halted mitochondria as they became 'trapped' in stabilized actin nanodomains. As a consequence of reduced motility, mitochondria swelling was worsened following excitotoxic NMDA stimulus. Some researchers have proposed that microtubule stabilizing drugs may prevent neurite damage following mechanical injury. However, these studies point to one potentially important role that structural cytoskeletal filaments may play in the transport and localization of mitochondria within dendrites.

CHAPTER 5: Automated analysis of rodent behavior tasks reveals a new mechanism for neuropsychiatric deficits following blast-induced mild traumatic brain injury

ABSTRACT

Although the significance of blast-induced traumatic brain injury is well known, the contributing mechanisms for the complex behavioral deficits created by blast exposure is not currently defined. In this study, we test if behavioral deficits following blast exposure are mediated by Elk-1, a transcription factor linked to both neuronal plasticity and survival. To overcome the time-intensive and often subjective methodology used for completely characterizing behavioral tasks in rodents, we develop and used the first open-source toolbox for automating the scoring of several common behavior tasks used by the neuroscience community. Our systems-level analysis shows that bTBI creates a complex change in neuropsychiatric behavior, and that this change is significantly augmented following Elk-1 deletion. To our knowledge, this is the first report of a specific molecular pathway that mediates posttraumatic anxiety, made possible with our open-source software system. We expect the use of this open-source toolbox will provide a more consistent analysis of behavior across laboratories, promoting the rapid discovery of novel pathways mediating disease progression and treatment.

INTRODUCTION

Blast induced traumatic brain injury (bTBI) is a well-recognized injury occurring in the modern military environment, and determining bTBI etiology is a major focus

across many laboratories. Some contributing mechanisms for bTBI are shared with mechanisms for traumatic brain injuries in the civilian population, since some phases of bTBI include contact and inertial loading (acceleration) mechanisms (Bass et al., 2012). However, it is not yet clear if there are *unique* mechanisms associated with primary blast loading that contribute to the resulting neurological impairment of bTBI. There is some debate about the relative difference between blast and other types of TBI. Recently, our group examined common shock tube configurations used to study blast-induced brain injury in the laboratory, and concentrated on defining the optimal configuration to minimize the effect of torso overpressure and blast-induced head accelerations. We use this model to characterize the complex behavioral deficits of bTBI and investigate the possible role of Elk-1 in recovery from bTBI.

An increasing number of behavioral assays are available to the neuroscience community for identifying a phenotype in mouse behavioral studies. Many of these behavioral tasks are linked to one or more neuroanatomic substrates (Balderas et al., 2008; Barker and Warburton, 2011; Broadbent et al., 2004; Phillips and LeDoux, 1992). As such, rapidly defining a behavioral phenotype could bridge the gap between changes in brain structure and the advancement of new therapies for treating TBI treating neurological diseases.

Key bottlenecks limit the use of task-related experiments for behavioral phenotyping across laboratories. Many tests use time-intensive manual scoring techniques that limit the number of behavior tests performed and the extent of

quantitative analysis for each test. Moreover, manual scoring methods do not provide an opportunity to explore or “re-mine” data not collected during the initial scoring.

Scientifically, manual scoring techniques are susceptible to inter-operator variability and can lead to poor reproducibility between laboratories even though individual behavioral tests are standardized (Cryan and Holmes, 2005; Richter et al., 2009).

Recognizing the benefits of an automated system, the neuroscience community has developed many different methods to automate the phenotyping of animals in their home-cage (Bonasera et al., 2008; Casadesus et al., 2001; Chen et al., 2006; Goulding et al., 2008; Millecamps et al., 2005; Steele et al., 2007; Tamborini et al., 1989; Tang et al., 2002; Tang and Sanford, 2005). In contrast, automation of video recordings of *task-related* experiments has lagged behind. Existing home-cage software, including most recent machine learning (Kabra et al., 2013)- or computer vision (Jhuang et al., 2010)-based methods cannot be applied to score task-experiments, partly because these methods are primarily designed to classify the way in which a mouse's body deforms over small time intervals and assign behavioral labels such as rearing, grooming, or sitting. Scoring task-related experiments requires an entirely different approach based on the temporal evolution of an animal's *interactions* with the environment (e.g. exploration of objects in spatial object recognition or social interaction) or by the *choices* the animal makes (e.g. entry into different regions of an arena as in Y-Maze, place-preference, etc). Only recently have tools emerged to score some common tasks¹⁸ or, more generally, a more general purpose tools to develop automated scoring functions (JAABA).

We now significantly extend the repertoire of computerized methods for scoring video recordings of many behavior tasks that span tests of anxiety, cognition, learning and memory. These include fear conditioning, open field, zero-maze, Y-maze, plus-maze, T-maze, place preference, spatial/novel object recognition, and two- or three-chamber social interaction. We overcome the limitations of existing methods that either required inking part of the animal for automatically identifying body landmarks (Rutten et al., 2008) or required specialized equipment to monitor activity. For each behavior task, we use this new toolbox to automatically compute performance metrics that are commonly scored manually and achieved equal or better consistency compared to inter-observer variability. In addition, we introduce novel fine-grained measurements of task performance that are not available through manual scoring. We employ some of these tools and a systems-level analysis to evaluate how the aggregate behavior of animals changes with a genetic and/or experimental manipulation. This *automated phenotyping* of behavior, or autotyping, reveals a novel behavior pattern for a mouse model of blast-induced traumatic brain injury (bTBI). Some, but not all, behavior impairments of bTBI are ameliorated by the genetic deletion of a transcription factor (Elk-1), associated with neuronal survival and degeneration (Besnard et al., 2011; Morris et al., 2012; Sharma et al., 2010).

METHODS

Subjects

All animal studies were conducted according to NIH guidelines and were approved by the University of Pennsylvania's Institutional Animal Care and Use Committee (IACUC). We studied the behavioral effects of bTBI using an Elk-1 knockout mouse (C57/BL6N genetic background) (Cesari et al., 2004) and wildtype littermate (WTLM) mice. All mice were 12-14 week old males at the time of injury and behavior testing. Prior to blast-injury, each animal was either placed under isoflurane anesthesia and injured or simply placed under isoflurane (sham) and returned to its home-cage. Lights were maintained on a 12-hr light/dark cycle, and all experiments were performed during the light phase. Per previous experience, 10-12 male animals were used in each group for statistical power.

Blast-induced traumatic brain injury (TBI)

We used a shock-tube to generate a fully developed shock wave within an aluminum tube. The animal was placed 16-mm from the exit of the tube, and experienced a typical blast overpressure loading – a rapid rise in pressure (40 microseconds) followed by a slightly longer pressure decay (0.615 milliseconds) per previous reports (Effgen et al., 2012; Panzer et al., 2012). For all experiments, we used blast input conditions (peak overpressure: 215 kPa, duration: 0.65 milliseconds) that, when averaged across three pressure transducers placed along the periphery of the exit of the tube, varied less than 5% across all animals tested, and caused an immediate impairment in righting reflex.

Once animals recovered their righting reflex, they were returned to a warmed recovery cage.

Neurobehavior assay development

We developed a test battery to evaluate potential impairments in cortical, cerebellar, amygdala, and hippocampal function following blast exposure. We ordered tests to minimize potential confounding effects among the different tests that include: elevated zero-maze (day 1 post-blast), rotarod (days 1-3), open-field (day 4), spatial object recognition (days 4,5), and fear conditioning (days 8,9). Standard protocols were used to perform all tests.

Elevated Zero-Maze (Day 1)

The elevated zero maze was used to examine anxiety-related behavior. The apparatus comprised of an elevated annular platform with two opposite, enclosed quadrants and two open quadrants. Mice were placed in the walled region and left undisturbed for 5 minutes. The latency to first exit from the walled region and the cumulative time spent the open region were recorded. In addition, a risk assessment measure was calculated.

Rotarod performance (Days 1-3)

Motor coordination and motor learning was assessed on days 1,2, and 3 following blast injury. Animals were placed on a rotarod apparatus (model: ENV-577M, MedAssociates Inc., Georgia, VT) that accelerates linearly from 4 to 40 RPM over a five-minute session.

Three trials, separated by an hour each, were conducted each day. Two measures were recorded for each rotarod test: the time lapsed until first fault, and the total time the animal remained on the rotating rod before falling. Fault is defined as making a complete revolution around the rotarod. In the event that an animal did not fault, we used fall time for fault.

Open field test (Day 4)

Individual mice were released in the corner of a rectangular (30cmx40cm) open field arena. Mice were left undisturbed and videotaped with a camera mounted on the ceiling above the center of the open field arena for 30 minutes. At the end of testing, mice were returned to their home cage.

Spatial Object Recognition (SOR; Days 4, 5):

Spatial object recognition was used to determine the effects of blast loading on memory storage. On the day of training (d4), mice were placed in the training arena for a total of 10-minute session. The first session consisted of context habituation without objects in the arena. During the next 3 sessions, mice were allowed to explore the arena with two distinct objects (a glass bottle and a metal tower). Each session lasted 10 minutes. Testing occurred 24 hours after the four training sessions in which one of the two objects was displaced. The mouse's preference for the displaced object over the non-displaced object was measured for all sessions.

Fear Conditioning (Days 8, 9):

Contextual fear conditioning was performed to develop a complementary measure of hippocampal and amygdala function. On the training day (d8), the mouse was placed in the conditioning chamber for 2:28 minutes before the onset of a foot shock (2-sec 1.5 mA). Contextual conditioning was assessed 24 hours later by placing the mouse back in the same chamber for 5 minutes.

Mathematical Approaches for Automating Behavior Scoring

Movement detection, tracking, and orientation overview:

Several simple observations from the video record were automated: 1) determining whether the animal was moving and classifying the type of motion (goal-directed or exploratory), 2) determining the absolute location of the animal in an arena and relative to other objects, 3) identifying several landmarks on the animal's body, and 4) determining the animal's gaze direction and body curvature. These movement classifiers were key for determining an automated score for a given test. All algorithms described below are implemented in MATLAB (MathWorks) and available on www.seas.upenn.edu/~molneuro.

Motion detection and tracking:

Our first objective was to define periods where the animal stopped moving for at least 2 seconds, showing a 'freezing' behavior that is traditionally recorded in fear

conditioning tests. We used an image difference matrix, defined as the matrix created by subtracting an image at time t_i with the preceding image at t_{i-1} . Theoretically, no motion between consecutive frames would yield a difference image matrix of all zeros.

However, due to camera noise, a null image difference matrix rarely occurred. We estimated hardware noise by recording a 1-minute video of an empty chamber, using consecutive image pairs and assigning a threshold motion limit (ϵ) equal to the 95th percentile of the matrix magnitude for image difference pairs. Freezing was designated to occur when consecutive image difference matrices over 2-s or longer duration (15+ image frame pairs) showed a net difference magnitude $< \epsilon$ (**Figure 5. 1 A**). A resulting bar code of activity (**Figure 5. 1 A**) denotes the periods of motion and inactivity over the 5-minute monitoring period.

We next automated the process for determining the precise location of an animal and time spent interacting with an object or within a region of interest (ROI) (**Figure 5. 1 B**). To our knowledge, the only other open-source automated software for object interaction requires inking the mouse's tail to denote a starting point and iteratively searches for position of the nose via multiple line fittings (Rutten et al., 2008), a process that can easily create cumulative errors. In our experience, proprietary software (e.g. Clever Systems) often suffered from this limitation, restricting its utility. Our algorithm consisted of segmenting the mouse in the image; determining locations of head, tail, and centroid; determining the direction of gaze; extrapolating whether the mouse's line of site crosses an ROI; and assigning a label (interacting or not interacting) to each frame.

Segmentation was accomplished by background subtraction (**Figure 5. 1 C**). Many sophisticated techniques exist to estimate the background of a scene(Oliver et al., 2000; Qin and Yaonan, 2008; Stauffer and Grimson, 1999). We used frame averaging to yield the background scene in a fast and accurate manner(Cucchiara et al., 2003).

The centroid of the moving object (mouse) and the coordinates of the head and tail were determined via geodesic distance transform (tail is the farthest point from the centroid and head farthest from the tail, **Figure 5. 1 C**). To determine the direction of the mouse's gaze, we drew a vector from the centroid to the head coordinates.

Mouse trajectory was visualized by plotting its centroid coordinates (**Figure 5. 1 D**).

Changes in the total distance travelled in an arena or the amount of time spent interacting with the same object across multiple exposures are common measures of habituation(Vianna et al., 2000), one of the most elementary nonassociative learning tasks in rodents. Our automated tracking computes this directly in real-time, and also allows us to plot the angle of each exploratory bout of an object (**Figure 5. 1 E**).

Additionally, a heat-map plot of the mouse position during the test facilitates high-throughput characterization of behavior through novel pattern recognition or machine learning algorithms (**Figure 5. 1 F**). The algorithm for detecting interaction with an object is also useful for measuring social interactions (**Figure 5. 1 G-I**) and regions explored by an animal in an open-field test (**Figure 5. 1 J,K**). Finally, the automated tracking also facilitates defining periods when the animal is walking (straight and

relatively fast), exploring (slow, non-straight line paths), or sitting (no locomotion for at least 3 seconds) in the open field(Choleris et al., 2001) (**Figure 5. 1 L**).

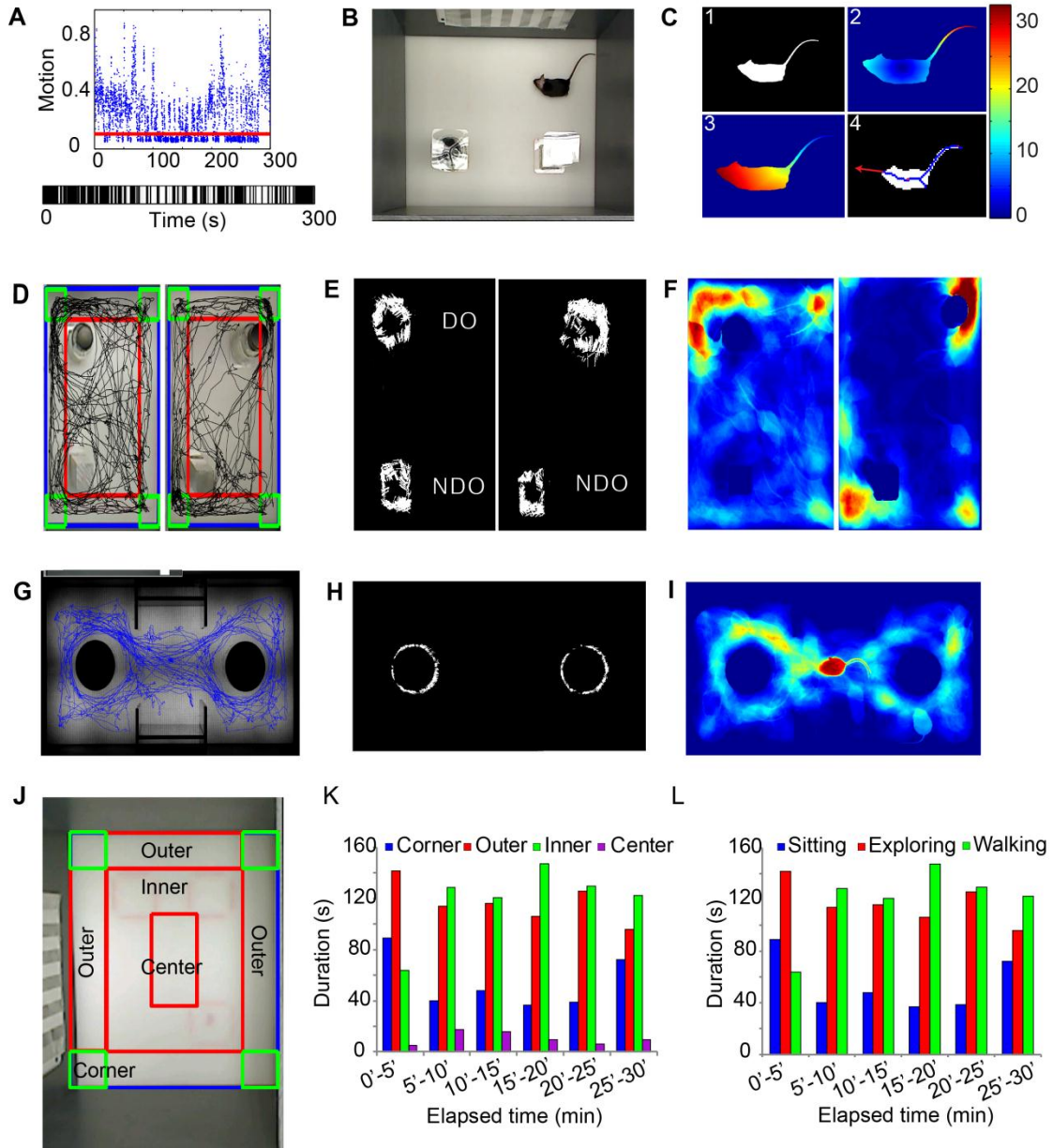


Figure 5. 1: Overview of automated analysis of neurobehavior. A: (Top) Discrimination of motion from freezing events using an estimate of camera noise (red line). (Bottom) Time strip

showing bout length of freezing behavior (white space) relative to movement bouts (black space) in fear conditioning. **B-C**: Overview of geometric algorithm to track the body and landmarks on a mouse. **B**, Example of a still frame image. The mouse was segmented by background subtraction (**C1**) and the centroid, tail (**C2**) and head (**C3**) coordinates determined. A vector from the centroid to head or extrapolation of the medial axis provided gaze direction (**C4**). **D-L**: Application of automated algorithm in neurobehavioral experiments. **D-F**: Response to novel objects and spatial novelty. **D**, The path traveled (black) by the mouse during the first exposure session to the objects (**left**) and during the second exposure where one of the objects is displaced (**right**). **E**, Exploration of the displaced and non-displaced objects represented by white lines that denote the angle of approach and the number of exploratory bouts. **F**, Heat-map representing the mouse position in the experimental arena, red = more time, blue = less time. **G-I**: Analysis of a social interaction experiment shows path traveled (**G**) and non-biased exploratory bouts (**H**) between the two non-social objects. Most time is spent in the neutral zone (**I**). **J-L**: Automated tracking (**J**) and measurement of the time spent in different regions of the open-field in any 5-minute interval (**K**), along with the time spent walking, exploring and sitting (**L**).

Application to automated scoring of tasks

In an **open-field experiment**, we automatically partitioned the arena into outer periphery, inner, and center region and 4 corner quadrants. Using the automated tracking of the mouse centroid, the software computed the amount of time spent and the distance travelled in these subdivisions, **Figure 5. 1 J,K**. The ambulation data was further categorized as exploring, walking, or sitting behaviors, **Figure 5. 1 L** (Choleris et al., 2001).

In **elevated zero-maze** experiments, a user initialized the videos by identifying walled and open regions of the maze. In each frame, the software automatically identified the mouse's centroid, area, and major axis length. We defined entry into the open regions when >95% of the mouse's area and its centroid were simultaneously in the open region. The amount of time spent in the open and walled regions was automatically recorded as a measure of anxiety-like behavior (Jacobson et al., 2007). Since experimentally altered locomotion can influence the time spent in open or walled regions, independent of anxiety, we also measured ambulation. Risk assessment includes a stretch-attend posture in which the head extends into the open area but the remainder of the body stays in the walled compartment (Karlsson et al., 2005). This behavior was automatically identified when several empirical conditions were met: centroid of the mouse was in the walled region, head was in the open region, and the mouse's body length (major axis length of the segmented image) exceeded mean + 2*standard deviation of body length throughout the experiment.

In **spatial object recognition** testing, we determined the location and visual field of the mouse during the test procedure. The user defined an ROI for each object in the arena, and the software computed the fraction time (% of total) the animal was interacting with the ROI. During each bout of interaction, the instantaneous direction of gaze was also recorded to determine whether there were direction-approach biases (**Figure 5. 1 E**). For example, the software permits measurement of the interaction time with different sides of the object facing the center, walls or corners of an arena. This level of analysis

can be informative for models of autism in which gaze aversion or avoidance is a prominent phenotype (Clifford et al., 2007; Defensor et al., 2011).

In **fear conditioning** experiments, we used the freezing detection algorithm to determine the total fractional time the animal displayed freezing behavior over a five minute testing period. Additionally, by recording these freezing events over time, we generated a bar code representation of the behavior that could be later analyzed for patterns of freezing over the different test conditions. Continuous scoring, rather than assessing freezing at arbitrary fixed time intervals, also permits analysis of cumulative freezing distributions.

In the **social interaction** task, we defined two separate ROIs that contain an inanimate and an animate object. Similar to spatial object recognition, we determined the interaction time for both ROIs, the approach angle during each bout of interaction, and distance travelled. Heat-map indicating cumulative time spent in different parts of the sociability apparatus is especially useful to visually inspect preferences between novel objects and novel mice.

A list of automated behavior tasks and commonly used performance metrics for each task are provided in Table 2. Modular implementation (object-oriented style) of these algorithms can facilitate automation of other behavior tasks not listed in Table 2.

Table 5. 1: Automated behavior tasks

Behavior test	Performance metric
Open field	Thigmotaxis Total distance traveled Time spent walking, sitting, exploring Entries into the center of the arena
Fear conditioning	Total freezing time (test session) Freezing time immediately after foot shock (training session)
Elevated zero maze	Latency to first exit Time in open/walled regions Total distance traveled Risk assessment
Y-maze, T-maze	Time spent and distance traveled in each of 3 arms Number of spontaneous transitions and total transitions Conditional probability of transitions between arms
Morris water maze	Latency to the platform Instantaneous speed
Barnes maze	Latency to escape Number of errors Path length to the escape box Strategy to escape - random, systematic or spatial
Spatial/Novel object recognition	Time spent interacting with each object Direction of approach for each interaction bout Spatial extent of object exploration - uniform or one-sided Distance, speed and exploratory tendencies
Social interaction	Interaction time with inanimate object vs. animate object Visual gaze (direction) of exploration

Validation and Optimization of Automated Approaches:

Comparison to manual scoring methods: We compared the results obtained from automated analysis to those obtained by manual scoring (visual inspection by an expert observer). In each task, we created a Bland-Altman plot to analyze the limits of agreement between the two methods (manual scoring being the gold standard). At least 20 videos each for fear conditioning, SOR, elevated-zero maze, and social interaction were manually scored. For each behavior task, we computed the mean and standard deviation of the difference between two values obtained by automated and manual scoring. Two expert observers scored the same videos to estimate inter-observer variability.

Sensitivity analysis:

Video quality: Videos were recorded in bright, even light conditions, using a high-definition camera. Segmentation by background subtraction was fast (< 2 minutes for a 10-minute video) and worked very well under these settings. To test its sensitivity to light conditions and video quality, we recorded a set of videos in lower resolution and in which the mouse was placed in an arena either dimly illuminated or not evenly illuminated.

Fear conditioning threshold: Assessment of freezing depends on estimating hardware noise; freezing was defined when the difference between successive frames drops below noise. Given a distribution of hardware noise obtained by recording a 1-minute video of an empty chamber, we selected threshold values at the 50th, 70th, 90th and 95th

percentile. We manually scored several experimental videos and compared the accuracy of the automated algorithm as a function of varying thresholds.

Interaction distance: In our implementation, interaction is scored by first defining a gaze vector originating from the nose and extending in the direction of vision with magnitude x . When this gaze vector crosses a user-defined ROI, it is scored as an interaction. To find the user-specific optimal magnitude of the gaze vector, users scored SOR videos frame-by-frame and annotated each frame with "interacting" or "not-interacting" labels. The same videos were processed with our algorithm. We swept through different magnitudes of the gaze vector (0" to 6", step-size 0.1") and for each vector length, we computed the total number of true positives and false positives. The user-specific interaction distance corresponds to the optimum point on the ROC curve, defined as the point on the ROC curve closest to the upper left corner (100% sensitivity and 100% specificity).

Statistical Analysis: Statistical differences in task-related performance of animals in four experimental groups (wildtype littermate sham, wildtype littermate blast injured, Elk-1 knockout sham, and Elk-1 knockout blast) were assessed via one-way ANOVA and Tukey's post-hoc test. Shapiro-Wilk test was used to assess normality and nonparametric tests (Kruskal-Wallis and Mann-Whitney U) were employed when needed. A repeated-measures (RM) ANOVA was performed when the same measurement was obtained for an animal over multiple trials as in rotarod or habituation. Group sizes were: WT sham $n= 13$, WT blast $n= 13$, Elk-1 KO sham $n= 11$, Elk-1 KO blast $n= 12$. alpha-level 0.05,

* $p < 0.05$ and ** $p < 0.01$ indicated significance. For a given level of analysis, a Bonferroni correction for multiple comparisons was used. All values reported are mean \pm s.e.m. unless otherwise noted. Significance of time in all RM-ANOVA, $p < 0.001$ unless otherwise noted.

Behavior pattern analysis: The standardization of test scoring also provides an opportunity for employing a statistical framework for analyzing behavior patterns across experimental groups. Each animal was subjected to a battery of behavior tasks and 14 performance metrics were computed. Principal component analysis (PCA) visualized the dataset in a lower dimensional space and identified a combination of the original variables that explained the largest possible variation. Following PCA, a MANOVA identified a linear combination of the original variables with the largest separation between groups. Relationships between group means were visualized in a distance dendrogram. Additionally, the ability to use a pattern of behavior to correctly identify group membership was assessed by multiclass support vector machine (SVMlight(Joachims, 1999)).

RESULTS

Our goal was to develop, assess, and apply an automated analysis of commonly used behavior tasks, including open field test, spatial object recognition (SOR), novel object recognition (NOR), social interaction, zero-maze, and fear conditioning (**Figure 5. 1**). We used this new toolbox and a systems-level analysis of behaviors tested to

characterize a new transgenic mouse line (Elk-1 knockout) and investigate the effects of bTBI on behavior.

Comparison of automated and manual analysis of behavior tasks

After confirming the robustness of our automated algorithms and calibrating them on a small subset of the recorded tests (**Figure 5. 2**), we tested the accuracy of the automated video analysis in 4 specific behavior tasks: fear conditioning, SOR, elevated zero-maze, and open field test. For each task, 20 videos were both manually analyzed by trained observers and scored using the automated approach, resulting in 2 data points for each video. The mean biases of the automated approach relative to manual measurements were 5.24% for freezing time in fear conditioning task (**Figure 5. 3 A**), 1.07-s for latency to first-exit in elevated zero maze (**Figure 5. 3 B**), -0.37s for amount of time spent in the open region in elevated zero maze (**Figure 5. 3 C**), 0.003 for thigmotaxis in open-field (**Figure 5. 3 D**), and 2.98% for object interaction time in SOR (**Figure 5. 3 E**).

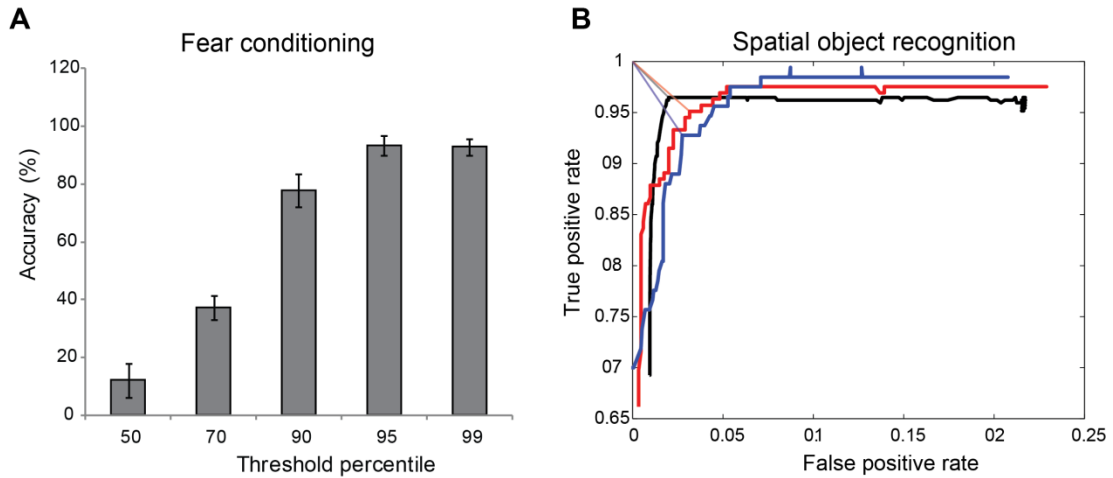


Figure 5. 2: Sensitivity of automated approach. **A:** Discriminating motion from freezing in automated scoring of fear conditioning experiments relies on choosing a threshold value for hardware noise. The accuracy of the automated approach compared to manual scoring approached >90% when point threshold value was at 95th percentile of hardware noise ($n=4$). **B:** Object interaction was defined when a gaze vector of magnitude u extending from the mouse’s nose crossed a user-defined region of interest. This allowed us to calibrate the software to user’s definition of interaction by determining the optimum u for each user. Three different users scored the same SOR video, annotating each frame in the video with “interacting” or “not-interacting” labels. An ROC curve generated by varying u identified the optimum interaction distance for each user as the point on the ROC curve closest to the upper left corner (true positive rate = 1, false positive rate = 0), denoted by straight lines.

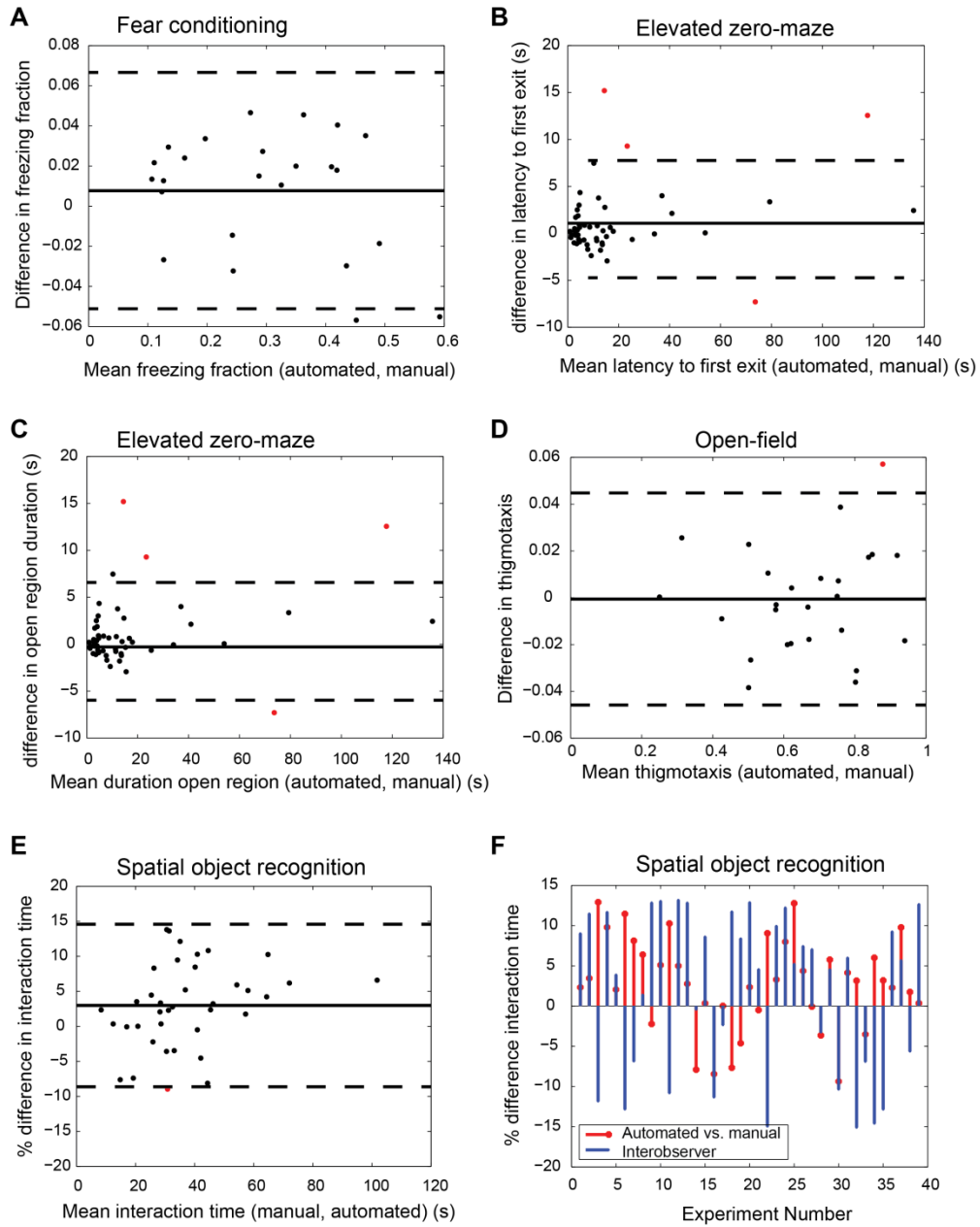


Figure 5. 3: Comparison of automated and manual scoring. Bland-Altman plots show excellent agreement between manual and automated scores for freeze fraction in fear conditioning (**A**, bias 5.24%, limits of agreement [-0.0511, 0.067] freeze fraction), latency to first exit (**B**, bias 1.07-s, limits of agreement [-5.97s, 8.11s]), time spent in open region of the elevated zero maze

(**C**, bias -0.37s, limits of agreement [-5.78s, 5.04s]), thigmotaxis in open-field experiment (**D**, bias 0.003, limits of agreement [-0.046, 0.045]), and interaction time in spatial object recognition task (**E**, bias 2.98%, limits of agreement [-8.62%, 14.6%]). Bias and limits of agreement between automated and manual methods are denoted by horizontal solid and dashed lines in A-E ($n \geq 20$ for each task). Red dots indicate measurements that fall outside limits of agreement. The difference in interaction time of automated and manual methods is comparable to inter-observer variability (**F**, limits of agreement between automated and User A [-8.6%, 14.6%] and agreement between Users A and B [-17%, 21.8%]).

Automated methods for assessing behavior not only increase throughput, but may potentially reduce user bias and variability. Forty SOR videos were manually scored for object interaction time in SOR experiments by two independent expert human observers, user A and user B. User A calibrated the automated approach using 3 videos chosen at random as described in Methods. All videos were then automatically processed using the definition of interaction provided by User A. We compared the percent difference in interaction time between automated and User A, and between User A and User B (Fig 3F). The limits of agreement (bias \pm 1.96*std) between automated and User A was [-8.62%, 14.6%], compared to [-17%, 21.8%] for User A vs. User B. The improved agreement between automated and User A is likely because User A calibrated the software to his/her own specification of interaction, yielding better agreement with the software than with another human observer.

Real-time tracking of the animal and scoring of object interaction is possible with our implementation. Our automated system consistently identified the correct coordinates of the nose and scored object interaction. There were few instances when the animal was sitting in a corner and in a curled posture where the algorithm did not correctly identify the head and tail coordinates. However, this did not pose a problem because objects are rarely placed in the corners and mislabeled events span less than 2-3 consecutive frames. Additionally, since each video frame is automatically annotated with "interacting" or "not-interacting" labels, we were able to quickly scroll through a set of interacting frames and remove false positives. In our experience, manual correction took less than 1 minute for a 10 minute video and improved the sensitivity to nearly 98%.

Autotyping as a method to assess the influence of blast-injury and Elk-1 deletion

With these validated algorithms for automating the analysis of individual behavioral tasks, we examined if blast-induced traumatic brain injury (bTBI) caused a significant change in the normal behavior of C57/BL6N wildtype mice. In addition, we explored if there were significant behavioral differences that appeared when a neuronal transcription factor, Elk-1, was deleted completely from a C57/BL6N animal background and whether behavioral impairments following bTBI can be ameliorated with Elk-1 deletion. Several recent reports implicate Elk-1 in neuronal loss and degeneration (Morris et al., 2012; Sharma et al., 2010), however it is unclear if a) Elk-1 is important for normal behavior and b) whether Elk-1 deletion improves outcome after bTBI. Studying a range of behavioral tasks, rather than a single task, is particularly important because of the

widespread changes that can occur throughout the brain following a gene deletion and bTBI alike (Davenport et al., 2012).

Blast-injury increases generalized anxiety in wildtype animals while Elk-1 knockout mice are resistant to post-blast anxiety.

Our collective results from open-field and elevated zero-maze tests show that bTBI significantly increases anxiety-like behavior. Uninjured animals placed in an open-field arena showed a typical spatiotemporal response to novel environment, spending most of their time along the periphery (thigmotaxis) during the first 5 minutes and gradually entering the central zone of the arena during the next two 5 minute intervals. We quantified thigmotaxis by determining the ratio of time spent along the periphery relative to time spent in the center over any five-minute interval as an index of anxiety (Simon et al., 1994). Following bTBI, wildtype animals show increased thigmotaxis during the second 5 minute interval compared to sham group (mean \pm SEM: 0.820 ± 0.033 blast vs. 0.588 ± 0.039 sham, $p = 0.0013$, **Figure 5. 4 A**). In addition, blast injured mice spent significantly more time sitting in an open-field arena compared to uninjured shams, another measure of anxiety (Prut and Belzung, 2003) ($95.81s \pm 9.19s$ blast vs. $62.56s \pm 8.83s$ sham, $p = 0.0484$, **Figure 5. 4 B**). The total distance traveled and time spent walking or exploring were not significantly different between sham and injured wildtype animals, suggesting that the spatial component important in thigmotactic behavior is being directly increased by blast.

In contrast to wildtype littermates, blast-injured Elk-1 KO animals did not show a significant difference in thigmotaxis or total time spent sitting compared to uninjured sham Elk-1 KO controls (thigmotaxis: 0.626 ± 0.028 blast vs. 0.638 ± 0.026 sham, $p > 0.05$; sitting: $82.3s \pm 9.69s$ blast vs. $73.4s \pm 9.82s$ sham, $p > 0.05$). Moreover, blast-injury in Elk-1 KO group resulted in significantly less thigmotaxis compared to blast injured WTLM, suggesting a possible role for Elk-1 in post-traumatic anxiety (0.626 ± 0.028 Elk+blast vs. 0.820 ± 0.033 WTLM+blast, $p = 0.0081$).

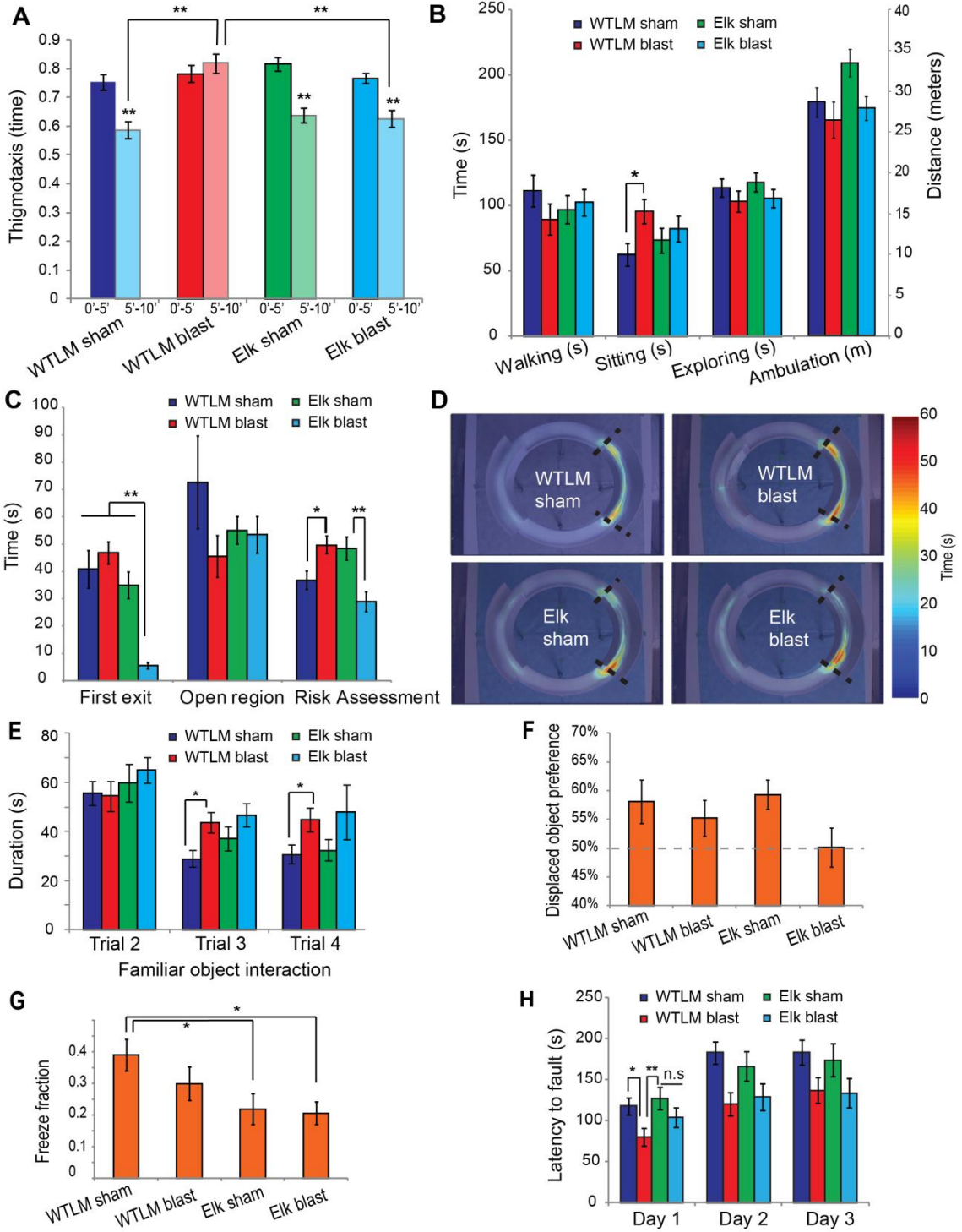


Figure 5. 4: Behavior deficits following bTBI in wildtype littermate and Elk-1 knockout mice. A-B: Open-field. **A**, Thigmotaxis decreased from the first five-minute interval to the second five-minute interval in wildtype sham (paired t-test $p < .001$, $n = 13$), Elk-1 KO sham ($p < .001$, $n = 11$) and Elk-1 KO blast injured animals ($p < .001$, $n = 12$) but was not significantly different in wildtype bTBI ($p = 0.194$, $n = 12$). **B**, Wildtype bTBI animals spent significantly more time sitting in the open-field compared to uninjured shams ($p = 0.0484$). Other open-field measures were not different across the 4 groups (ANOVA $p > 0.05$). **C-D:** Elevated zero-maze. **C**, Latency to first exit of walled regions and risk assessment was significantly lower in Elk-1 KO bTBI compared to Elk-1 KO sham ($p < 0.01$). However risk assessment was significantly elevated in wildtype bTBI relative to sham ($p = 0.0312$). **D**, Average heat-map showed an increased localization to the walled/open interface in wildtype bTBI group. **E-F:** Spatial object recognition. **E**, Object habituation was significantly impaired in wildtype bTBI compared to sham (RM-ANOVA $p < 0.005$) but was not different between Elk-1 KO sham and injured animals ($p = 0.181$) **F**, Preference for the displaced object was $> 50\%$ for wildtype sham, blast and Elk-1 KO sham groups suggesting acquisition of spatial memory. However, displaced object preference was reduced in blast injured Elk-1 KO ($50.1\% \pm 3.4\%$ Elk+blast vs. $59.3\% \pm 2.6\%$ Elk+sham, $p = 0.0531$). **G**, Elk-1 KO sham showed a deficit in fear conditioning compared to wildtype sham ($p = 0.0213$) and this impairment was not worsened by bTBI ($p > 0.05$). **H**, Motor coordination and motor memory was assessed by computing latency to fault on rotarod. On day 1, WTLM blast had significantly lower fault time compared to both WTLM sham and Elk-1 KO sham (WT blast $79.8s \pm 10.8s$ vs. sham $117.9s \pm 10.5s$, $p = 0.0145$; WT blast vs. Elk-1 sham $127.3s \pm 13.5s$, $p = 0.0074$). An improvement in fault was observed over days 1-3 for all four groups, however, the improvement was greater for uninjured shams than injured animals, regardless of genotype

(repeated-measures ANOVA within subjects time $p < 0.001$, between subjects sham vs. blast $p = 0.0037$, wildtype vs. KO $p = 0.8712$).

An alternative test for anxiety-like behavior is the elevated zero maze. Indicators of increased anxiety include a relative increase in latency to first exit, decreased time spent in the open unprotected region, and increased risk assessment behaviors. We found increased risk assessment activity in WTLM blast group relative to uninjured sham ($49.8s \pm 4.08s$ blast vs. $36.8s \pm 3.41s$ sham, $p = 0.0312$, **Figure 5. 4 C**). No significant difference was found between WTLM blast and WTLM sham groups in latency to first exit or time spent in unprotected open regions (**Figure 5. 4 C**). We observed a very significant decrease in latency to first exit in Elk-1 KO blast injured mice relative to 3 other groups ($5.63s \pm 1.14s$ Elk+blast vs. $40.82s \pm 6.87s$ WTLM sham, $46.8s \pm 4.08s$ WTLM blast, $35s \pm 4.9s$ Elk sham, $p < 0.001$, **Figure 5. 4 C**). Similar to decreased latencies to exit, a decrease in risk assessment behavior appeared in Elk-1 KO blast injured mice (**Figure 5. 4 C, D**). The cumulative distance traveled in the zero-maze, as well as the peak instantaneous speed, were not statistically different between the 4 groups (ANOVA, $p > 0.05$).

The behavioral alterations of animals using two anxiety-related assessments, open-field test and elevated zero-maze indicate heightened anxiety following blast-injury in WTLM. In contrast, blast-injury does not worsen anxiety-related behavior in Elk-1 KO mice relative to their sham counterparts.

Blast-injury to wildtype mice impairs object habituation but Elk-1 deletion recovers normal behavior

Habituation is one form of nonassociative learning that can be readily measured in the spatial object recognition test where exploration of the objects during consecutive training trials decreases as novelty decreases (i.e., before one of the objects is displaced). Therefore, we analyzed the duration of interaction with the non-displaced object in trials 2-4 of the spatial object recognition test in mice that received bTBI prior to training. Uninjured wildtype sham mice habituate to the SOR arena as the duration of interaction with the non-displaced object significantly decreased over time (RM-ANOVA, $p=0.0062$, **Figure 5. 4 E**). In contrast, blast injured wildtype animals failed to show a significant decline in object exploration from trial 2 to trials 3 and 4 (RM-ANOVA $p>0.05$). Direct comparison between sham and blast injured wildtype animals showed a significant deficit in object habituation during trial 3 (blast: $42.8s \pm 4.12s$, sham: $26.1s \pm 5.03s$, $p=0.0036$).

In contrast to WTLM, blast injured Elk-1 KO animals did not show a deficit in object habituation compared to sham (multivariate RM-ANOVA, $p>0.05$). Both sham and injured Elk-1 KO groups spent equally large amounts of time interacting with the non-displaced object in trial 2 (first exposure to objects in the arena) and significantly less time in trials 3 and 4 (Trial 3: Elk-1 KO sham, $37.1s \pm 2.36s$ compared to Elk-KO injured, $46.6s \pm 2.26s$, $p = 0.2366$).

Blast injury impairs spatial and associative memory only in Elk-1 knockout mice.

We assessed spatial memory by calculating the percent of total object interaction time that was devoted to the displaced object in the SOR test during trial 5. Typically, by trial 4, mice spend nearly equal time interacting with the two objects. Upon displacing an object in trial 5, both wildtype sham and blast injured animals spent significantly more time (>50%) interacting with the displaced object, consistent with acquisition of spatial memory. Preference for the displaced-object was not different between sham and injured wildtype animals (wildtype sham $58.1\% \pm 3.8\%$ vs. wildtype injured $55.2\% \pm 3.2\%$, $p > 0.05$). Similarly, Elk-1 KO sham animals showed a preference for the displaced object in trial 5. However, the preference for displaced object was abolished in blast injured Elk-1 KO group (Elk-1 KO sham $59.3\% \pm 2.6\%$ vs. Elk-1 KO injured $50.1\% \pm 3.4\%$, $p = 0.0034$) (**Figure 5. 4 F**).

Since blast injured WT animals still retained spatial memory, we next tested contextual fear memory, a distinct hippocampus-dependent form of associative memory. Pairing of an aversive foot shock to a novel environment resulted in freezing responses when mice were reintroduced to the same environment 24-hours following the shock. We found no statistical difference in total freeze fraction between sham and blast injured wildtype animals (sham: 0.390 ± 0.049 , 0.3 ± 0.053 , $p = 0.18$) suggesting that associative memory is not altered following blast-injury (**Figure 5. 4 G**).

Compared to wildtype mice, Elk-1 KO showed significantly less freezing behavior (wildtype sham freeze fraction: 0.3904 ± 0.0494 , Elk-1 KO sham: $0.2198 \pm$

0.0492, $p = 0.0213$). However, the impairment in associative memory was not made worse by blast-injury (Elk-1 KO blast: 0.2069 ± 0.035 , $p > 0.05$ compared to Elk-1 KO sham) (**Figure 5. 4 G**). A deficit in contextual fear conditioning in Elk-1 knockout mice suggests an important role for this transcription factor in associative memory.

Blast-injury impairs motor coordination and motor learning.

We assessed motor coordination and motor learning in rotarod task by measuring the latency to fault. Fault is defined when an animal makes a complete revolution around the rotarod and is a more sensitive measure of motor coordination than latency to fall. On first exposure to the rotarod (day 1), wildtype blast injured animals had significantly lower fault time compared to wildtype sham, suggesting a deficit in motor coordination as a result of blast (wildtype blast fault $79.8s \pm 10.8s$ vs. wildtype sham $117.9s \pm 10.5s$, $p=0.0145$) (**Figure 5. 4 H**). Interestingly, Elk-1 KO animals were resistant to blast-induced deficits in motor coordination (Elk sham fault: $127.3s \pm 13.5$ vs. Elk blast fault: 104.2 ± 12.2 , $p=0.2097$).

An improved performance on the rotarod during subsequent trials 2 and 3 is indicative of acquisition of motor memory. All four groups showed an improvement in latency to fault over days 1-3, but the increase in performance was greater for uninjured shams than blast-injured animals regardless of genotype (RM-ANOVA, within subjects time $p < 0.0001$, between subjects sham vs. blast $p = 0.0037$, wildtype vs. KO $p = 0.8712$). Together, blast-injury impairs the acquisition of motor memory in wildtype littermates and Elk-1 knockout mice equally.

*Multivariate analysis reveals the relative effects of genotype, injury and genotype*injury on behavior outcome.*

A summary of behavioral alterations in WT blast, Elk-1 knockout sham and Elk-1 knockout blast relative to WT sham animals are provided in Table 5.2.

Table 5. 2: Summary of behavior alterations relative to wildtype littermate (WTLM) sham

Task	Metric	Elk sham	WTLM blast	Elk blast
Open Field	Walking	n.s	n.s	n.s
	Sitting	n.s	↑	n.s
	Exploring	n.s.	n.s.	n.s.
	Total ambulation	n.s.	n.s.	n.s.
Elevated zero maze	Thigmotaxis	n.s.	↑	n.s.
	Latency to first exit	n.s.	n.s.	↓
	Time in open region	n.s.	n.s.	n.s.
	Risk assessment	n.s.	↑	n.s.
Spatial object recognition	Habituation	n.s.	↓	n.s.
	Displaced object preference	n.s.	n.s.	n.s.
Fear conditioning Rotarod	freeze fraction	↓	n.s.	↓
	Latency to fault, day1	n.s.	↓	n.s.
	Improvement over days 1-3	n.s.	↓	↓

Given the complex phenotypic spectrum, we applied principal component analysis (PCA) followed by MANOVA to identify a linear combination of the original behavior variables with the largest separation between groups (**Figure 5. 5 A**), followed by MANOVA to identify a linear combination of the original behavior variables with the largest separation between groups. We found a significant difference in overall group mean centroids,

Wilk's lambda $p = 0.0011$. Genotype alone did not have an effect on multivariate group mean differences (WTLM vs. Elk-1 KO, $p=0.0825$), however, injury severity (sham vs. blast, $p=0.0007$) and genotype*injury ($p=0.0018$) were both significant. We projected these multivariate behavior scores for each mouse onto a canonical subspace and color-coded each group (**Figure 5.5 B**). Inspection of the group mean centroids (+ marker) and 95% confidence bounds reveals intersecting groups with no significant difference from each other (WTLM sham vs. Elk sham), while non-intersecting domains represent groups that are significantly different from each other (e.g., Elk-1 KO sham vs. Elk-1 KO injured). Using this canonical representation, a dendrogram constructed from pair-wise Mahalanobis distances between each pair of group means identified the hierarchical similarity among groups - WTLM sham and Elk-1 KO sham were phenotypically most similar; blast-injury affects the two genotypes differently, - wildtype injured mice are

most affected while Elk-1 KO injured have milder phenotypic alterations (**Figure 5.5 C**).

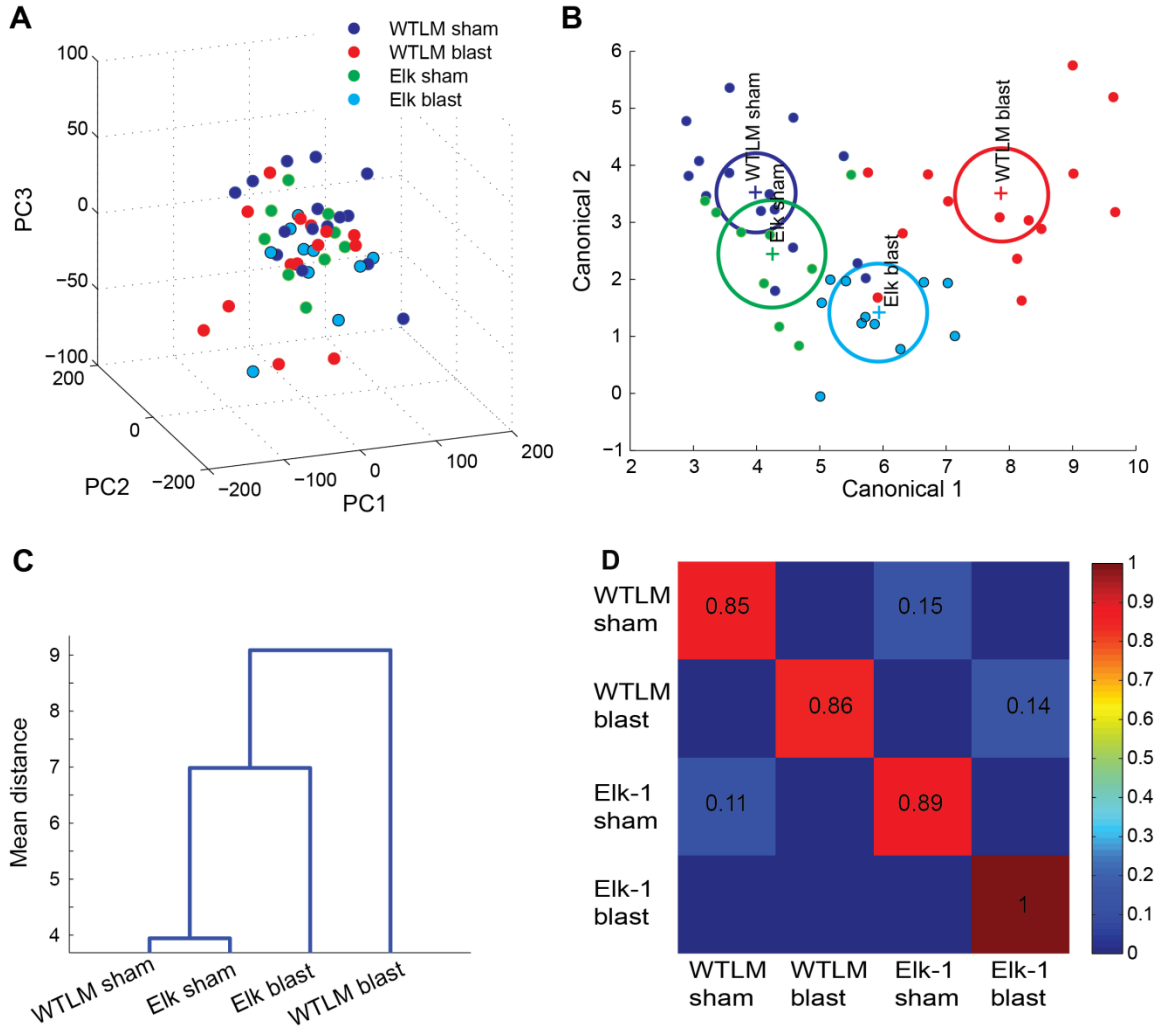


Figure 5.5 : Multivariate analysis reveals the relative effects of genotype, injury and

genotype*injury on behavior outcome. **A**, Projection of 14 behavior attributes for each animal onto the first 3 principal components did not reveal obvious groupings. **B**, Multivariate ANOVA identified differences in the population means of the 4 groups (Wilks' $\lambda = 0.0011$). The multivariate behavior scores are projected onto a MANOVA canonical subspace and color-coded by experimental groups (dots represent the aggregate neurobehavior of individual mice, + marker indicates group centroids with 95% confidence bounds shown in circles). **C**, Dendrogram of pair-

wise group centroids reveals the hierarchical similarity among groups. **D**, Confusion matrix. A multiclass support vector machine was trained using multivariate behaviors to determine whether a pattern of task-related behaviors can accurately predict injury severity or genotype. The fraction of a group of mice (along the rows) that were classified as each of the four alternative groups (along the columns) are indicated in the confusion matrix.

With the ability to quickly screen several tasks simultaneously, we then tested whether the patterns of task-related behaviors could accurately predict the injury severity or genotype of an animal. We trained and tested a linear multiclass support vector machine using the 14 behavior attributes. The results of a leave-one-animal-out cross validation are shown in a confusion matrix (**Figure 5. 5 D**). The confusion matrix indicates the fraction of a group of mice (along the rows) that were classified, on the basis of its pattern of behavior, as each of the four alternative groups (along the columns). Larger values along the diagonal indicate successful classification. As expected, the classification accuracy for wildtype sham and blast-injured groups is the largest, while there is some confusion in accurately classifying animals into WTLM sham and Elk-1 KO sham groups - 85% of true wildtype sham animals were correctly classified as wildtype sham, while 15% were falsely classified as Elk-1 KO. However, the overall classification accuracy was 90.2% suggesting that automated behavioral assessment can successfully phenotype animals.

DISCUSSION:

We identified and incorporated a number of automation algorithms to generate a new, open access software platform for scoring and analyzing several common behavioral tasks. Automated scoring can be done in real-time and the results matched manual measurements within the limits of inter-observer variability. We then applied automated tools to phenotype animals carrying a genetic manipulation (Elk-1 KO), experimental manipulation (blast TBI), and the combination of these two effects. Examining the behaviors separately, we discovered that blast-injury significantly increased the level of anxiety and impaired the ability to habituate to a novel environment. Elk-1 KO animals were resistant to these detrimental effects of blast-injury, but showed a deficit in associative memory after blast exposure. A multivariate analysis designed to identify differences in aggregate behavior showed that Elk-1 KO and wildtype animals were not significantly different prior to blast-injury. Following injury, wildtype animals showed more severe changes in behavior than Elk-1 KO animals.

Blast-injury is characterized by modest neuronal loss or pathologic remodeling that can disrupt both anatomic and functional connectivity throughout the brain (Levin et al., 2010; Mac Donald et al., 2013; Magnuson et al., 2012; Sponheim et al., 2011). Given this potential broad disruption of brain networks, our automated screening tool was an ideal method to scan across multiple behavior tasks and develop a behavioral phenotype for each animal. The early signs of anxiety observed in our wildtype mice are reminiscent of symptoms associated with post-traumatic stress disorder in human blast TBI, and is

consistent with some evidence from other rodent models of bTBI (Park et al., 2013). At the level of blast exposure studied, we saw no significant memory deficits using two independent measures of associative learning - contextual fear conditioning, and spatial object recognition. However, we found a significant reduction in motor memory following blast. The consistent appearance of a memory deficit is not a universal consequence of bTBI in rodents, and some of these deficits appear to be linked to the head accelerations induced by the blast exposure (Goldstein et al., 2012).

To our knowledge, this work presents the first evidence that Elk-1 plays an important role in the recovery of function after a neurological injury. One key modulatory point for controlling the function of Elk-1 is its multisite phosphorylation 'state'. The mitogen activated protein kinase ERK phosphorylates Elk-1 on multiple sites, and the ERK pathway is activated in several models of TBI (Carbonell and Mandell, 2003; Otani et al., 2002; Raghupathi et al., 2003). However, many of the controlling phosphatases and kinases that regulate the control of Elk-1 within its transactivation domain, as well as the domain that controls its neurodegenerative function are not known (Barrett et al., 2006; Sharma et al., 2010; Yang et al., 2002). Based on our current data, we cannot conclude if the behavioral differences between Elk-1 KO and wildtype littermates is simply because the knockout animals have lost the ability to prune dysfunctional neurons from hippocampal and cortical circuits, or if these changes are more linked to Elk-1 dependent changes in gene expression. Determining the key regulating mechanisms that mediate these Elk-1 dependent effects is particularly

important because we found that Elk-1 deletion can eliminate posttraumatic anxiety. Given that posttraumatic stress disorder is a condition commonly associated with soldiers exposed to blast, a more thorough exploration of these Elk-1 dependent mechanisms of anxiogenic behavior may yield important insights for a significant clinical condition.

From a broader perspective, the rapid scanning of several behaviors in parallel facilitates a new framework to assess the broad effects that can occur in a rodent model of neurological disease. Compared to manual scoring, our automated analysis can reduce user-to-user variability or observer bias. This leads to more consistent findings within and across laboratories. Further, an automated method greatly speeds up data analysis and lessens the time burden on researchers, making more complex behavior protocols possible. Our open-source algorithms are intuitive to use, provide biologically relevant information for each task and overcome limitations of existing proprietary systems. We expect the broader behavior spectrum that can be analyzed with our autotyping system will permit a more complete and rapid understanding of disease models in rodents, with the goal of using this same toolbox to test potential treatment strategies.

CHAPTER 6: Conclusions and future directions

Dissertation summary

The goal of this work was to examine how traumatic brain injury affects information flow within neuronal networks and to identify the mechanisms of acute network dysfunction that are thought to underlie cognitive and behavioral deficits associated with mild brain injuries. Previous reports have used calcium imaging to examine the microarchitecture of the brain, however, its use in TBI research has been limited.

Chapter 2

In Chapter 2 of this dissertation, we first carefully assessed fluorescence based imaging methods for mapping neural network properties. We then created an open-source, interactive software for automated quantification of numerous biologically relevant features of both the calcium dynamics of single-cells and network activity patterns, including automated spike detection, synchronization analysis, and inference of functional connectivity. We validated our method against physiological and pathological conditions known to cause a change in network function, including how the developmental maturation of neurons in cultures affects network activity and the effects of α -synuclein and tau pathology on neuronal networks.

Chapter 3

In Chapter 3 of this dissertation, we used calcium imaging to measure changes in network behavior following mild mechanical injury to cortical networks *in vitro*. First,

we found that a 35% stretch causes an acute loss in network synchrony, changes in the network topology, and a reduction in the excitatory tone that is not recovered up to 6 h following injury. In contrast, a milder level of injury (10% stretch) caused heightened activity, but the network returned to its pre-injury state within 1 h. Next we investigated the mechanisms for network impairment following 35% stretch. A more detailed analysis of the same neuronal network before and after injury revealed a highly nonlinear relationship between pre-stretch and post-stretch connectivity of individual neurons. Notably, highly connected neurons tended to lose less connections than sparsely connected neurons, however, some of these low degree neurons gained new functional connections post-injury. These changes in the functional connectivity were completely preventable by blocking the activation of NMDARs prior to injury, suggesting a key role for these receptors in network remodeling. Given the heterogeneous response of individual neurons to injury, we investigated whether there were biomarkers that predicted if individual neurons will de-integrate, remain integrated or re-integrate following injury. We used a novel method to phenotype the NMDAR subtype content for each neuron prior to injury and found that neurons with high NR2B content were most adversely affected by injury whereas neurons with high NR2A content were resistant to injury-induced alterations in functional connectivity. Mechanistically, we showed that the NR2B-containing NMDARs, not NR2A, lose voltage-dependent Mg^{2+} block following injury. A multi-scale computational model showed that the NR2B receptors undergo many irregular transitions between glutamate-bound/open and glutamate-bound/close

states. With a reduced Mg^{2+} block, these receptor "flickering" events contribute to temporally uncoordinated electrical and calcium activity at the network-scale. Indeed, we were able to unmask synchrony in an injured network by inhibiting NR2B receptor activation. Functionally, a voltage-dependent Mg^{2+} block is the crux of the "coincidence detection" property of the NMDA receptor which allows dendritic Ca^{2+} influx only during coordinated pre-synaptic release and post-synaptic depolarization. The precise spatiotemporal pattern of synaptic activation is key for the induction of plasticity. We found that neurons within an injured network lose their ability to change their functional connections with other neurons in the network. Pairing a chemical LTP stimulus with an NR2B receptor antagonist rescued plasticity in an injured network. These studies highlight a new role for the NR2A and NR2B subtypes in the modulation of network activity patterns and point to a new strategy for improving cognitive outcome following TBI.

Chapter 4

In Chapter 4 of this dissertation, we investigated how mechanical injury is different from excitotoxicity. We used a bath NMDA stimulus to overactivate the NMDA receptors for varying durations and recorded changes in the network properties. Brief NMDAR overactivation (both synaptic and extrasynaptic) heightened synaptic activity, similar to a 10% mechanical stretch. However, different from stretch injury, brief NMDA stimulus led to a persistent stabilization of the network activity and preconditioned neurons from further injuries. These effects were dependent on activity and transcription.

On the other hand, longer NMDAR overactivation caused significant decrease in network connectivity and synchrony, similar to 35% mechanical stretch. However, unlike mechanical stretch, the balance of NR2A or NR2B activation did not influence network activity patterns following bath NMDA stimulus. Instead, mitochondria played a key role in shaping network outcome following excitotoxic injury. Similar to previous observations, we found that NMDAR overactivation caused an increased permeability of the mitochondrial inner membrane resulting in depolarization of the mitochondrial membrane potential and mitochondria swelling. Our new studies showed that acute functional de-integration of individual neurons from the network was predictive of delayed cell death. Inhibiting the mitochondrial permeability transition pore with NIM811 attenuated NMDA-induced mitochondria swelling and improved network connectivity, in part due to reduced AMPA receptor internalization. Separately, we found that mitochondrial motility was closely tied to morphology. Acute synaptic priming reduced NMDA-induced mitochondria swelling, however, this protection was lost when mitochondria movement was halted.

Chapter 5

Neuronal circuits exhibit a rich repertoire of context-dependent activity patterns that subserve numerous cognitive and behavioral tasks. Understanding the dynamics of spontaneous network activity following TBI has been the focus of this dissertation. Ultimately, these research findings in vitro will have to be tested in vivo to determine the therapeutic potential of network repair on behavioral outcomes following TBI. However,

complete characterization of behavior is time-intensive, prone to subjective scoring, and often requires specialized equipment. In Chapter 5, to facilitate rapid discovery of disease causality and screen potential therapeutic agents, we created the first toolbox of its kind for automating the scoring of several common behavior tasks used by the neuroscience community. Our software requires minimal user interaction, is robust under different video recording conditions and computes accurate results that are within limits of inter-observer variability. Our automated tool also allowed us to identify novel behavioral patterns that are not accessible with manual scoring. We applied the automated algorithms and used a systems-level analysis to study the alterations in behavior that occur following blast-induced traumatic brain injury (bTBI) and to examine the impact of bTBI in an Elk-1 knockout mouse. Elk-1 is a neuronal transcription factor that has been implicated in both neuronal plasticity and neurodegeneration and cell death. Among other behavioral impairments following blast injury, notably we found that blast injured animals show increased generalized anxiety. Interestingly, deletion of Elk-1 prevented post-trauma anxiety. Given that posttraumatic stress disorder is a condition commonly associated with soldiers exposed to blast, a more thorough exploration of these Elk-1 dependent mechanisms of anxiogenic behavior may yield important insights for a potentially broadly significant clinical condition. To our knowledge, this work presents the first evidence that Elk-1 plays an important role in the recovery of function after a neurological injury.

In summary, we created novel tools for interrogating neuronal networks and for classifying phenotypic patterns of neurobehavior. These tools have broad applications in basic and translational neuroscience and will permit a more complete and rapid understanding of neurological, neurodevelopmental and psychiatric diseases, with the goal of using these same tools to test potential treatment strategies. We used these tools to study the microarchitecture of neuronal networks and changes in neurobehavior following mild TBI. We believe that mTBI is a disorder of network function. Our studies point to a new strategy for repairing injured networks by identifying and targeting unique nodal biomarkers that confer susceptibility to mechanical injuries.

Limitations and future directions

CNS tissue preparation: in vitro to in vivo

We choose *in vitro* approached, rather than *in vivo* or *in situ*, for two main reasons (a) the ability to measure changes at the single cell level, while also measuring the network connectivity, is best suited in *in vitro* systems; the same measures are far more technically challenging with *in vivo* or *in situ* imaging and (b) we can rapidly screen through different testing conditions (stretch level, drug treatments, targeted genetic manipulations) and identify the key circuit remodeling features. Dissociated cell cultures have robust and consistent spontaneous activity that is often lacking in organotypic or acute slice preparations. Further, dye loading in an acute slice is technically more challenging for the cortex and even more challenging when slices are prepared from adult animals. An acute slice is arguably the best experimental CNS tissue preparation as it

preserves the anatomical connectivity of different neurons and cell types.

Electrophysiology recordings allow one to measure the field potentials from the activation of different brain regions, however, this requires an external stimulus since spontaneous activity is nearly nonexistent. These studies preclude the investigation of how individual neurons change their integration in the network following injury and the mechanisms for network remodeling and/or repair.

In vivo multi-cell bolus loading

Recording the activity of individual neurons within an *in vivo* cortical circuit should be the next step for this project. Using a simpler *in vitro* system, we developed and validated the tools for interrogating network function and applied them to investigate neuronal phenotypes that confer mechanosensitivity. These conclusions should be tested *in vivo*. Due to technical limitations, we cannot record the activity of the same set of neurons before and after injury, but we may still learn whether the spontaneous cortical oscillations of an injured animal are different from controls. To make progress on this front, we already began to use multi-cell bolus loading of membrane-permeable fluorescent calcium indicators to record the activity from cells in the mouse cortex. (Garaschuk et al., 2006). Briefly, 10-12 week old C57BL6 mice were anaesthetized with an intraperitoneal injection of 1.5g/kg urethane. After achieving surgical plane, animals were fixed in the stereotactic device and the skin was removed giving access to the skull. Although optical imaging through a thinned skull preparation has been reported, which offers smaller motion artifacts from respiration and heart beat, we used an open-skull

preparation for better imaging quality. We gently created a small 2-mm craniotomy above the somatosensory cortex and a head plate with an imaging window was superglued onto the skull. The animal was positioned on a Leica SP5 confocal microscope and an optically transparent membrane placed over the opening of exposed brain to reduce motion artifacts. An epidural SR101 (100 μ M) was applied to label pial astrocytes and to create contrast for visual guidance of needle containing the calcium indicator (**Figure 6. 1**).

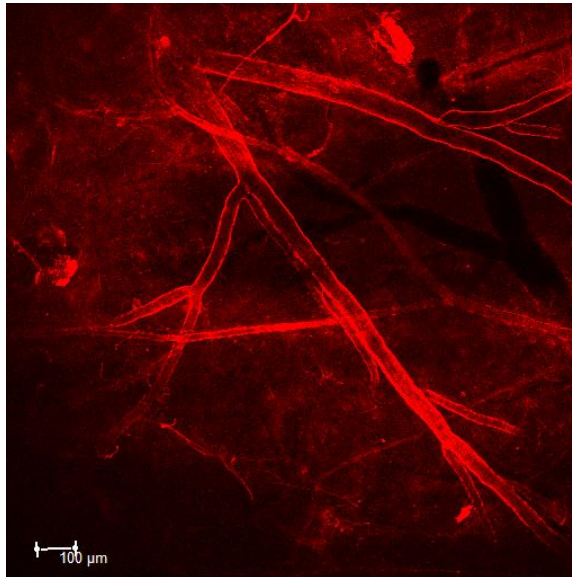


Figure 6. 1: Epidural SR-101 (100 μ M) was used to highlight cortical surface and to create contrast between blood vessels and brain parenchyma.

We filled a sterile finely pulled glass capillary (0.2 μ m opening diameter, Femtotip II, Eppendorf) with a solution of 1mM fluo-4 and 100 μ M SR101 in aCSF. A micromanipulator was used to position the needle above the dura and carefully guide it to

a depth of 150-200 μm below the cortical surface, at a 30° angle. Continuous imaging with 820nm IR laser was used to visualize needle placement and to avoid blood vessels. The dye was ejected from the needle with a pressure pulse (1 min, 70kPa) generated with a FemtoJet (see Figure 6. 2 for time-lapse images of dye injection at 200 μm depth). We estimated that ~400 femtoliters were delivered per injection. Multiple injections separated by 200 - 300 μm were performed to obtain a wide area of labeled cells.

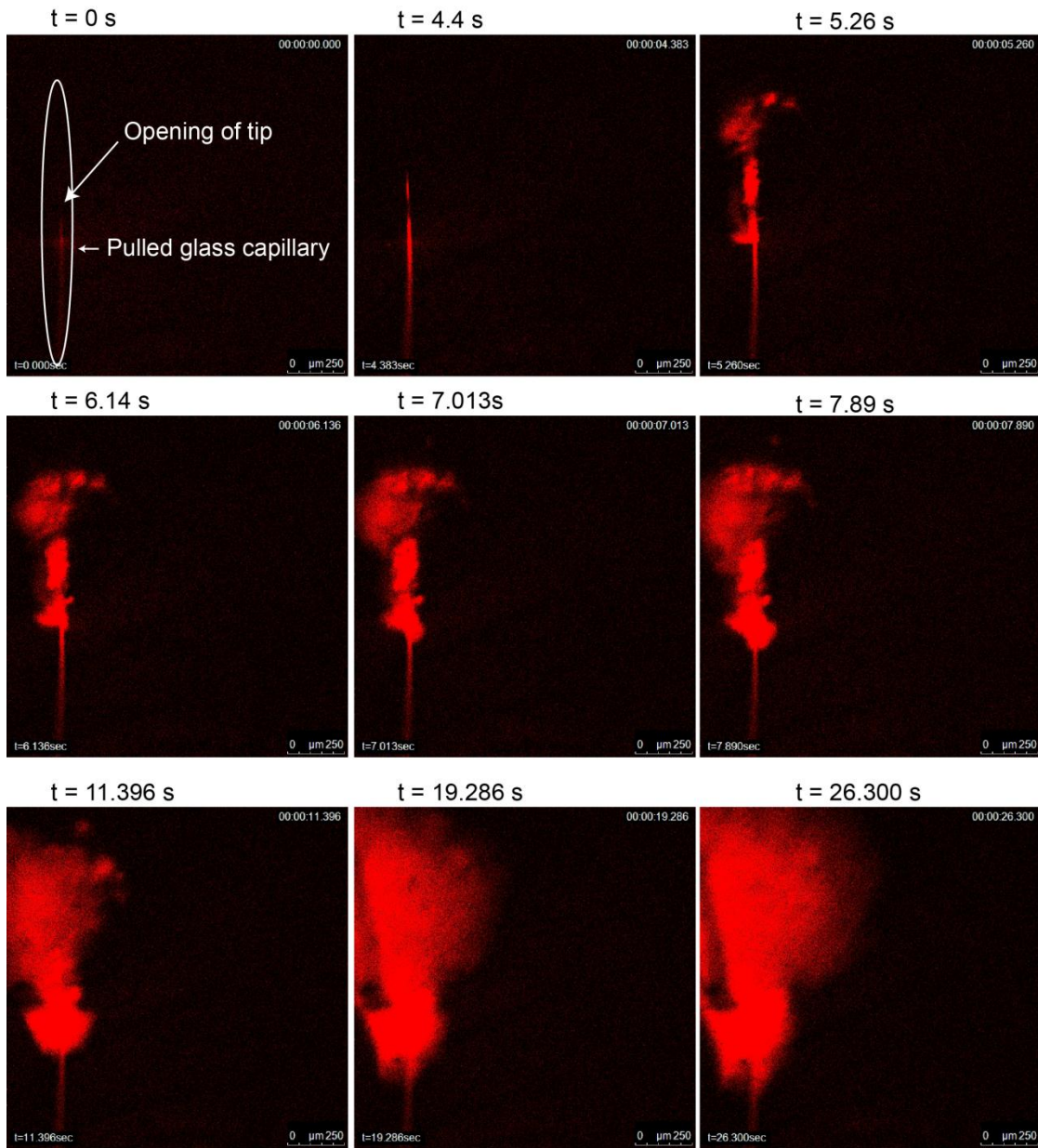


Figure 6. 2: Injection of fluo-4 and SR101 in an anaesthetized mouse. A pulled glass capillary needle was positioned 200 μm below the cortical surface with micromanipulator assist. Approximately 400 femtoliters of dye was ejected with a pressure pulse delivered through a FemtoJet injection system.

Following 1 hr incubation for dye loading, we imaged the calcium fluorescence of labeled cells, using SR101 to discriminate between neurons and astrocytes (**Figure 6. 3**).

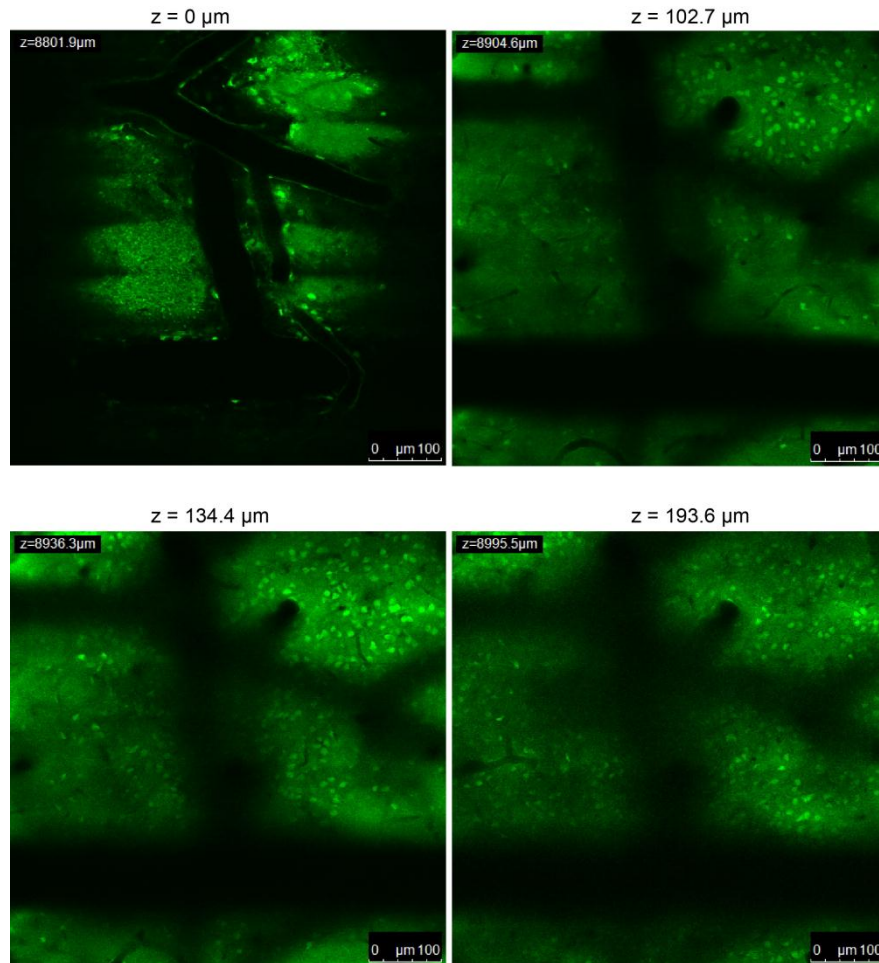


Figure 6. 3: Multi-cell bolus loading of fluo-4 *in vivo*. Images of cells loaded with the fluorescent calcium indicator, fluo-4 at increasing depths from the cortical surface. Approximately 300 - 400 cells are labeled at 150 μm depth.

Although we were able to load neurons with calcium indicator *in vivo*, we observed significant background and low levels of spontaneous activity. To capture both

long and short duration calcium events, we acquired images of a 1 mm² brain region at 20 Hz frame rate. However, we noted significant motion artifact. We did however induce synchronized oscillations with bicuculline. We believe that the level of spontaneous activity in an anaesthetized animal is critically dependent on the animal's heart rate, temperature, blood pressure, and the level of sedation. We did not have the equipment to track these vital signs, which could be a complicating factor for low level of activity. Troubleshooting motion artifact and loading conditions might allow us to perform in vivo measurements of network activity. The same network could then be injured with a micro-impactor as described previously by our lab (Choo et al., 2013) and would provide an in vivo correlate to the in vitro stretch injury experiments.

Calcium imaging is a proxy for electrical activity

We made extensive use of calcium imaging to understand the dynamics of neural activity within microcircuits. Strictly speaking, action potential induced rise in somatic $[Ca^{2+}]_i$ is only a proxy for electrical activity. Although majority of $[Ca^{2+}]_i$ fluctuations are related to APs, changes in Ca^{2+} homeostasis following injury, e.g. altered Ca^{2+} buffering capacity or de-coupling of synaptic receptor activation and the increase in intracellular Ca^{2+} , may manifest as alterations in calcium dynamics. Therefore, we were careful to make the distinction between electrical activity and inferred activity using Ca^{2+} imaging. Our estimates of synchronization and functional connectivity relate to the dynamics of intracellular Ca^{2+} only. Furthermore, measurements with different GCaMP indicators may be confounded by an overexpression of the protein, which could cause an enhanced

buffering of calcium within the cytosol and an apparently lower activity level. We performed several side-by-side experiments comparing the activity and network indices of age matched cultures using GCaMP3, 5, 6 and fluo-4. We found that activity measurements with fluo-4 were more comparable to GCaMP 5, 6 than GCaMP3.

To demonstrate that Ca^{2+} imaging results correlate with electrical activity, we had previously cultured neurons on microelectrode arrays (MEAs) and performed simultaneous measurements of extracellular field potentials and intracellular Ca^{2+} dynamics. Although we found a good correlation, interpretation of these results was complicated because we often detected an electrical spike that lagged the onset of Ca^{2+} transient. Also, since an MEA electrode recorded the changes in extracellular field potential from many neighboring neurons, it was difficult to pair changes in calcium activity with electrical activity, even after using sophisticated spike sorting algorithms.

Instead, we propose to measure the calcium activity of a population of neurons and simultaneously patch into individual neurons to measure changes in membrane potentials. Similarly, a combined Ca^{2+} imaging and mEPSC or mIPSC recording may provide useful information of the relative balance of excitatory and inhibitory input to individual neurons and how that affects network activity patterns.

NR2B receptor activation following stretch

We showed that following mechanical stretch injury, the NR2B-containing NMDA receptors preferentially undergo a loss in voltage-dependent Mg^{2+} block. We

used a stochastic diffusion-reaction scheme to simulate NMDA receptor activation following vesicular release of glutamate at a prototypical dendritic spine. These simulations showed that once bound to glutamate, the NR2B subtypes undergo many rapid transitions between glutamate-bound/open state and glutamate-bound/closed state. With a physiological $[Mg^{2+}] = 0.8\text{mM}$, these flickering events contribute very little calcium influx at the spine, however, a complete loss of Mg^{2+} block significantly increased the total Ca^{2+} influx and resulted in a noisier Ca^{2+} trace over time. We argued that the changes in synchrony at the network-scale are a manifestation of altered receptor kinetics of the NR2B subtypes. To validate these simulations, one could measure single channel characteristics of NR2B-subtypes at rest and following injury using an inside-out patch clamp. We expect greater current through these channels following injury, consistent with flattening of the current-voltage relationship of the NMDA receptor at the soma level. Single channel activity measurement may reveal changes in the transitions between closed and open states following injury. Alternatively, changes in open probability, frequency of opening or mean open time may also influence somatic membrane potential and the timing of firing of APs.

Recovery of injured circuits over time

In this work, we focused on the acute changes in network activity following mechanical injury to cultured neurons and identified the NR2B subtypes as one of the key regulators for network dysfunction. We showed that the NR2B contribution to $[Ca^{2+}]_i$ oscillations increased following injury, which reduced task learning in a model of chemical model of

long-term potentiation. Over time, NR2B receptors that underwent stretch-induced reduction in $[Mg^{2+}]$ block will likely be replaced with newly synthesized receptors that have an intact $[Mg^{2+}]$ sensitivity. Over the same timescale, however, stretch-induced calcium accumulation causes delayed activation of the neural protease calpain. Additionally, overactivation of the NMDAR receptor may lead to mitochondria dysfunction and further exacerbate the effects of primary mechanical stretch. It is unclear if the injured network will continue to degrade over the ensuing hours to days or whether there are compensatory/homeostatic mechanisms that rescue activity in an injured circuit. If the injured network repairs itself over a course of several days, we need to identify the mechanisms of recovery so that the recovery process could be hastened. Given that individual neurons responded differently to mechanical injury, it is likely that some neurons may recover faster than others. Some, but not all neurons may need to recover to fully restore network function. If so, it will be important to identify neuronal phenotypes associated with recovery versus demise. Alternatively, the injured network may never return to its pre-injured state, in which case we need to identify a therapeutic window where administration of either NR2B antagonists or mitochondria and cytoskeleton targeted agents prove most beneficial.

In order to perform these experiments, we need to monitor the activity of the same set of neurons over multiple days. *In vitro* cultures are ideal for this task. We have already begun preliminary set of experiments and recorded the activity of an injured network at 1 day, 3 day and 5 days post injury. However, due to technical limitations,

specifically the lack of an environmental chamber, we did not record the same set of neurons over this time period. Nonetheless, we found that the frequency of Ca^{2+} activity remained significantly reduced at 1 day post-injury however the amplitude of Ca^{2+} oscillations had returned to pre-injury state. By 5 days post-injury, the frequency and coordination of calcium oscillations were no different than age-matched controls.

Na⁺ channels and network recovery

Sodium channel proteolysis is a key early event after ischemia and traumatic brain injury. Previous reports show that calpain cleaves voltage gated sodium channel α -subunit following mechanical stretch injury, suggesting a mechanism for altered action potential initiation or propagation. In support of this, we found that preventing the activation of calpain (MDL-28170 pretreatment) rescued synchrony in mechanically injured networks (Patel et al., 2012). However, it is unclear if cleaved NaChs are replaced with functional NaChs over time and whether this coincides with network recovery. The experiments outlined above should be combined with $\text{Na}_v1.2$ immunocytochemistry to identify whether the recovery of networks or the integration of individual neurons is related to changes in NaCh expression. These studies are currently underway and show promising preliminary results. Alternatively, one could overexpress the endogenous calpain inhibitor, calpastatin, in a subset of neurons and investigate whether the functional integration of calpastatin + neurons is significantly improved. Such targeted genetic manipulation may allow one to determine the fraction of neurons that need to be "rescued" in order to repair the circuit.

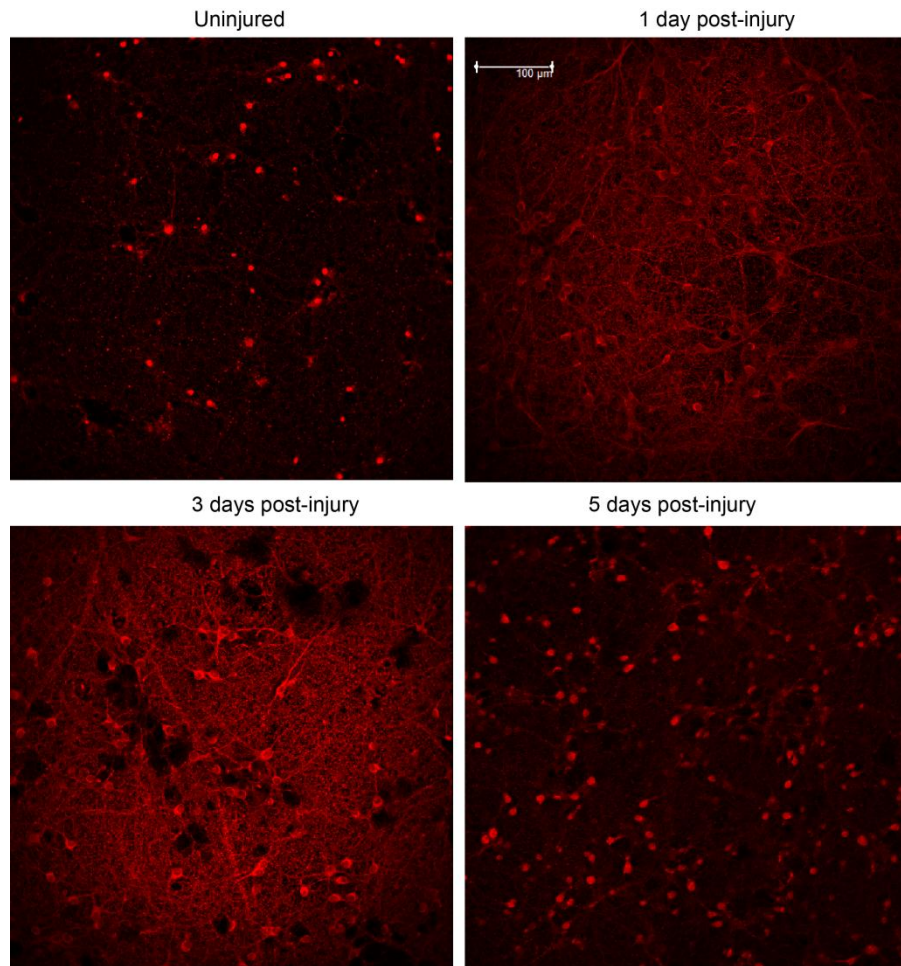


Figure 6. 4: Changes in the immunoreactivity of $Na_v1.2$ at 1, 3, and 5 days following stretch injury. Note the increased expression at 1 and 3 days and the prominent appearance of axonal fascicles.

Tau and traumatic brain injury

Repeated concussions are correlated with histopathological changes reminiscent of neurodegeneration of aging. Once described as *dementia pugilistica*, there is lot of debate over the causal role of repeated brain injuries in the pathogenesis of chronic

traumatic encephalopathy (CTE). A characteristic finding in CTE is the presence of hyperphosphorylated microtubule associated protein tau and deposition of pathological tau aggregates or fibrils in various brain regions. The spatial distribution of tauopathy of TBI, however, is distinct from other common tauopathies such as Alzheimer's disease or fronto-temporal dementia with Parkinson's disease. We investigated if mechanical stretch injury to cortical neurons in culture causes increase tau phosphorylation, tau aggregate formation and whether these changes in tau influence the activity of the neuronal network. We assessed tau phosphorylation with immunocytochemistry (AT8 antibody) at 5 hours, 1 day, and 7 days post-stretch injury and found significant increase at all time points relative to uninjured controls (Figure 6. 5). Under physiological conditions, tau associates with the microtubules and stabilizes the cytoskeleton. Tau phosphorylation reduces its association with the microtubules. We saw evidence of axonal bundling following injury with AT8 immunocytochemistry, suggesting possible changes in microtubule structure. Treatment with a microtubule stabilizing agent, such as taxol, may be effective in reducing structural remodeling associated with axonal injury.

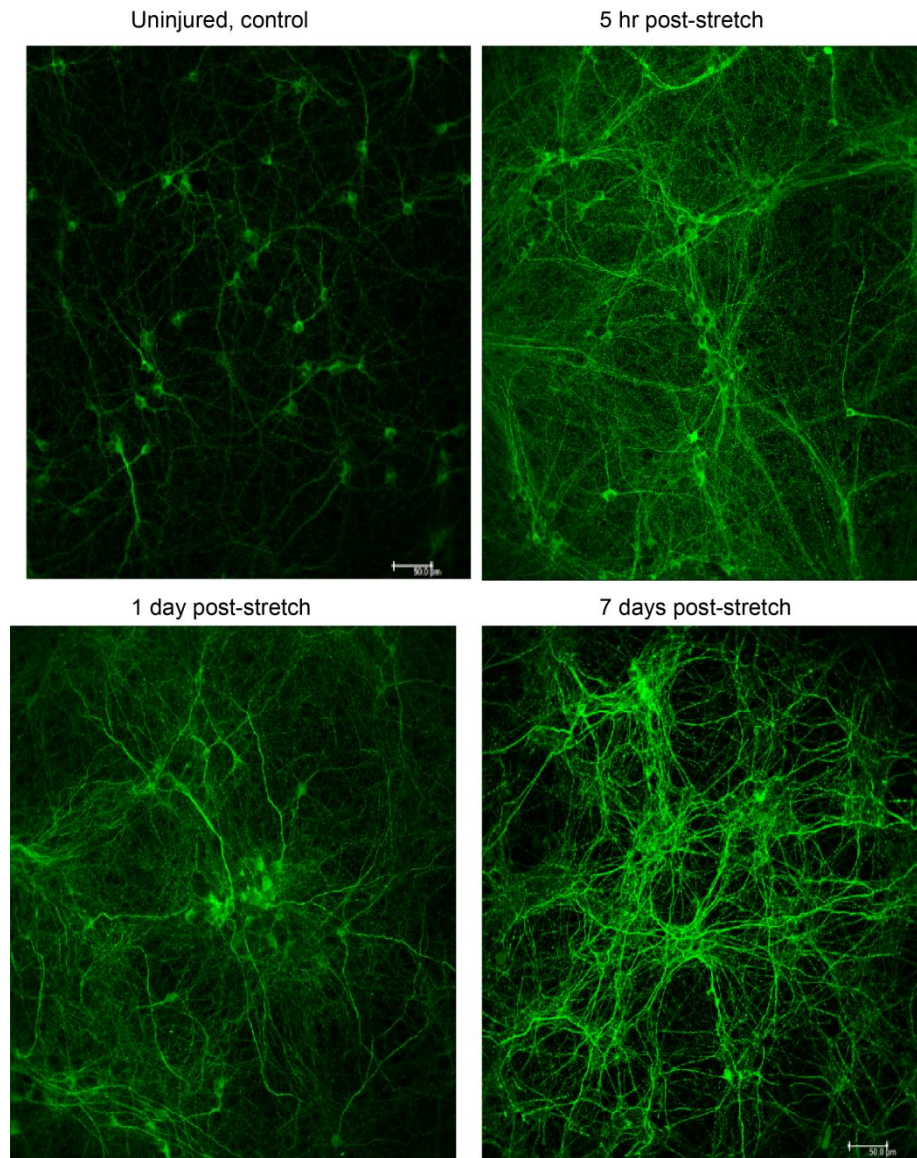


Figure 6. 5: Increased tau phosphorylation following stretch injury appears as early as 5 hr and is persist for 7 days.

Glycogen synthase kinase 3 (GSK3) is a known kinase of tau. We tested whether GSK3 inhibitors reduced tau phosphorylation following stretch. Indeed, both Li^+ and

AR-A014418 reduced tau phosphorylation, though neither drug or in combination completely return tau phosphorylation to control levels.

Since insoluble tau aggregates are thought to be pathogenic, we tested whether stretch injury caused the hyperphosphorylated tau protein to insolubilize. We used two separate methods to test for insoluble aggregates. First, we extracted the soluble fraction with 1% Triton and performed immunocytochemistry to detect remaining insoluble tau with AT8 antibody. Alternatively, we used the MC-1 antibody which specifically recognizes the pathological tau conformers. Neither approach showed evidence of tau aggregates. This is not surprising because induction of tau aggregates *in vitro* is nearly impossible, even when neurons are derived from a transgenic mouse line that spontaneously forms tau fibrils *in vivo*.

It remains unclear if repeated stretch injuries, spaced apart by 24 hours, can recreate tau fibrils *in vitro*. Furthermore, it is unclear if changes in tau phosphorylation and microtubule destabilization adversely affects neuronal networks. Additionally, we noted varying degree of tau phosphorylation in individual neurons. Combined calcium imaging and tau immunocytochemistry may reveal a possible relationship between the connectivity of individual neurons and the extent of tau phosphorylation, providing nodal biomarkers of injury.

Repairing an injured circuit

In this dissertation, we examined the integration of individual neurons within the microcircuit and identified some common features that determine whether a neuron is likely to de-integrate, remain integrated or show enhanced integration following injury. In the follow-up studies outlined above, it will become apparent whether there are additional nodal biomarkers, such as the level of NaCh breakdown or the level of tau phosphorylation, that are associated with node loss or remodeling. With this knowledge, it may be possible to identify subsets of neurons that are the most "damaging" to the network, or alternative, if there are sets of neurons that promote synchronous activity. Passive calcium imaging can aid in identifying the functional network connectivity. Active manipulation of individual neurons may be a strategy for repairing an injured circuit. For example, we already identified that neurons with high NR2B content are likely to be affected more adversely than those with high NR2A content. These NR2B-rich neurons contribute to asynchronous oscillations and disrupt the rhythms of the entire network. An optogenetic inhibition of these select neurons may be enough to restore the activity patterns of an injured circuit.

Towards this goal, we already began to combine optogenetics with calcium imaging. We first investigated whether the calcium activity of specific neurons could be silenced with ArchT, a light driven proton pump that hyperpolarizes the membrane potential (Han et al., 2011). We expressed GFP-tagged ArchT in excitatory neurons through the CaMKII promoter (AAV2/1.CaMKII.ArchT.GFP.WPRE.SV40, University

of Pennsylvania Vector Core). We transduced cortical cultures at DIV 10 (1.28×10^9 GC) and found strong ArchT-GFP expression by 1 week (Figure 6. 6 A). In order to simultaneously measure calcium activity *and* inhibit selected neurons, we could not use the traditional green-channel calcium indicators such as fluo-4, GCaMP or Oregon Green because ArchT was tagged with GFP. Additionally, ArchT is maximally activated at 559 nm, precluding the use of red-shifted calcium indicators such as X-rhod1. Instead, we loaded cells with the ratiometric calcium indicator dye fura-2. Fura-2 excites at 340 nm and 380 nm and the ratio of emissions at these two wavelengths at $\lambda_{em} = 510$ nm is correlated to intracellular calcium. We used two-photon excitation of fura-2 at $\lambda_{ex} = 800$ nm obtain maximal spectral separation; this wavelength excites the 380 nm species so rather than a rise in fluorescence with an increase in $[Ca^{2+}]_i$, we observe a decrease in fluorescence. To summarize, ArchT expression was determined in a field of view with GFP ($\lambda_{ex} = 488$ nm). Spontaneous calcium activity was monitored with fura-2 under 2P excitation ($\lambda_{ex} = 800$ nm). Selected neurons that expressed ArchT were then excited with ($\lambda_{ex} = 561$ nm), while simultaneously measuring changes in $[Ca^{2+}]_i$ of the network with fura-2. We observed synchronized Ca^{2+} oscillations with bicuculline (Figure 6. 6 B, C) that could be blocked in specific neurons by selective activation of ArchT (Figure 6. 6 D). Activity continued uninterrupted in rest of the network when only 2 neurons were silenced. This method could be useful to determine the minimum number of neurons that need to be silenced in order to stop network activity, providing an independent estimate of functional connectivity. Separately, we could specifically silence neurons that are

most desynchronized from the rest of the population to bring back synchrony. Similarly, we could also activate select driver nodes with channelrhodopsin-2 to cause a more permanent change in the activity patterns.

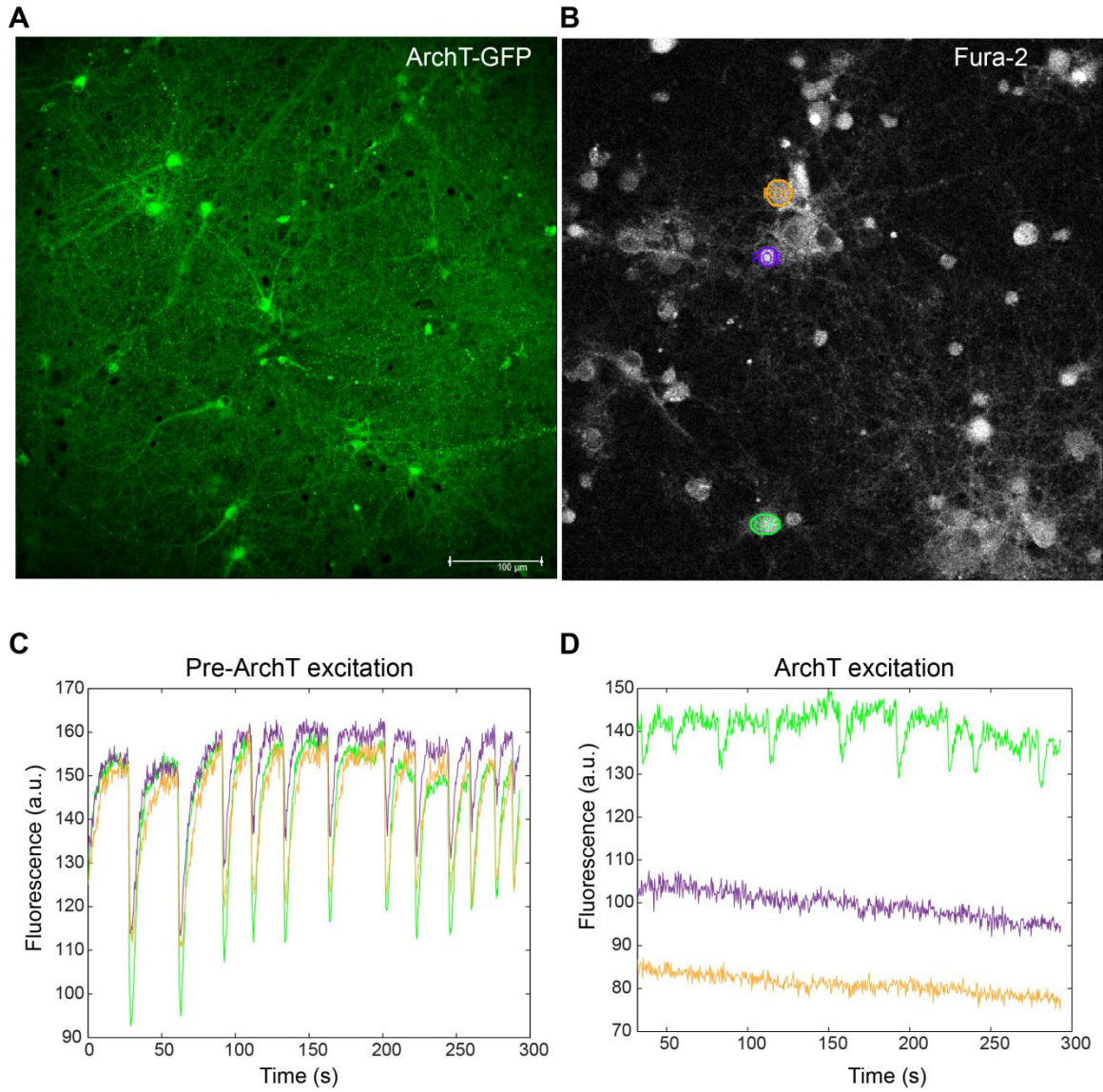


Figure 6. 6: Selective silencing of calcium activity with ArchT *in vitro*. GFP-tagged ArchT was expressed in excitatory neurons under CaMKII promoter (A). The calcium activity of the

excitatory network was monitored with the fluorescent calcium indicator fura-2 under 2P excitation (λ_{ex} 800nm) (B). The network displayed spontaneous synchronized calcium oscillation (fluorescence trace of 3 highlighted ROIs shown in C). Of the 3 highlighted neurons, 2 neurons indicated by purple and orange ROIs expressed ArchT while the green ROI did not. Selective ArchT excitation of these three ROIs ($\lambda_{\text{ex}} = 561\text{nm}$) completely stopped calcium oscillations in the two neurons that expressed ArchT while oscillations continued uninterrupted in the other neurons (C).

Glial modulation of neuronal networks

In this dissertation, we focused on identifying the mechanisms of network dysfunction caused by mechanical stretch injury. The brain is, however, an inhomogenous and irregularly-shaped viscoelastic organ. This means that TBI is likely to create local areas of high deformation, surrounded by regions of little or no deformation. The mechanisms of injury propagation from the site of impact to the mechanical penumbra should be the focus of future investigation. Already previous work from our lab has shown that astrocytes are one of the key players that carry the injury response beyond the initial site of injury both *in vitro* and *in vivo* in the form of propagating intracellular calcium waves (Choo et al., 2013). We replicated those results and found that mechanical injury causes intracellular calcium waves in the penumbra (Figure 6. 7A time-lapse images of calcium wave propagation into the mechanical penumbra; site of injury was one field of view below; fluorescence trace of 4 highlighted astrocytes located in the mechanical penumbra before and after stretch injury, B, C). Our new findings include a chronic enhancement in astrocytic calcium oscillations that persist for several

days following mechanical injury (Figure 6. 7 D). Calcium activity within the astrocyte network was significantly attenuated with the ATP degrading enzyme, apyrase and completely blocked with the calcium chelator BAPTA (Figure 6. 7 E-G).

Astrocytic modulation of neuronal network activity is a debated topic. Although, mounting evidence suggests that astrocytes release glutamate and ATP following a rise in intracellular Ca^{2+} . Astrocytic glutamate may activate either presynaptic NR2B-NMDA receptors, changing the probability of vesicular release or extrasynaptic NR2B receptors and influence post-synaptic currents. Additionally, astrocytic ATP can suppress neuronal activity via activation of purinergic receptors. Thus, we tested whether intracellular calcium waves within astrocytes of the mechanical penumbra influence the activity of neuronal networks. After mechanical injury, astrocyte intercellular calcium waves appeared in the mechanical penumbra (Figure 6. 8 A), and both the frequency of neuronal calcium activity and the temporal coordination of activity decreased significantly with the onset of intercellular wave ($p < 0.01$; Figure 6. 8 B versus C, G and H). Mixed cultures pretreated with either BAPTA-AM, PPADS or apyrase blocked the calcium wave from appearing in astrocytes within the mechanical penumbra (Figure 6. 8 D) and maintained post-traumatic neuronal activity at a level similar to pre-injury values (Figure 6. 8 E versus F, G and H; for both metrics: $p > 0.2$ when treated with BAPTA-AM; $p > 0.1$ when treated with PPADS+apyrase).

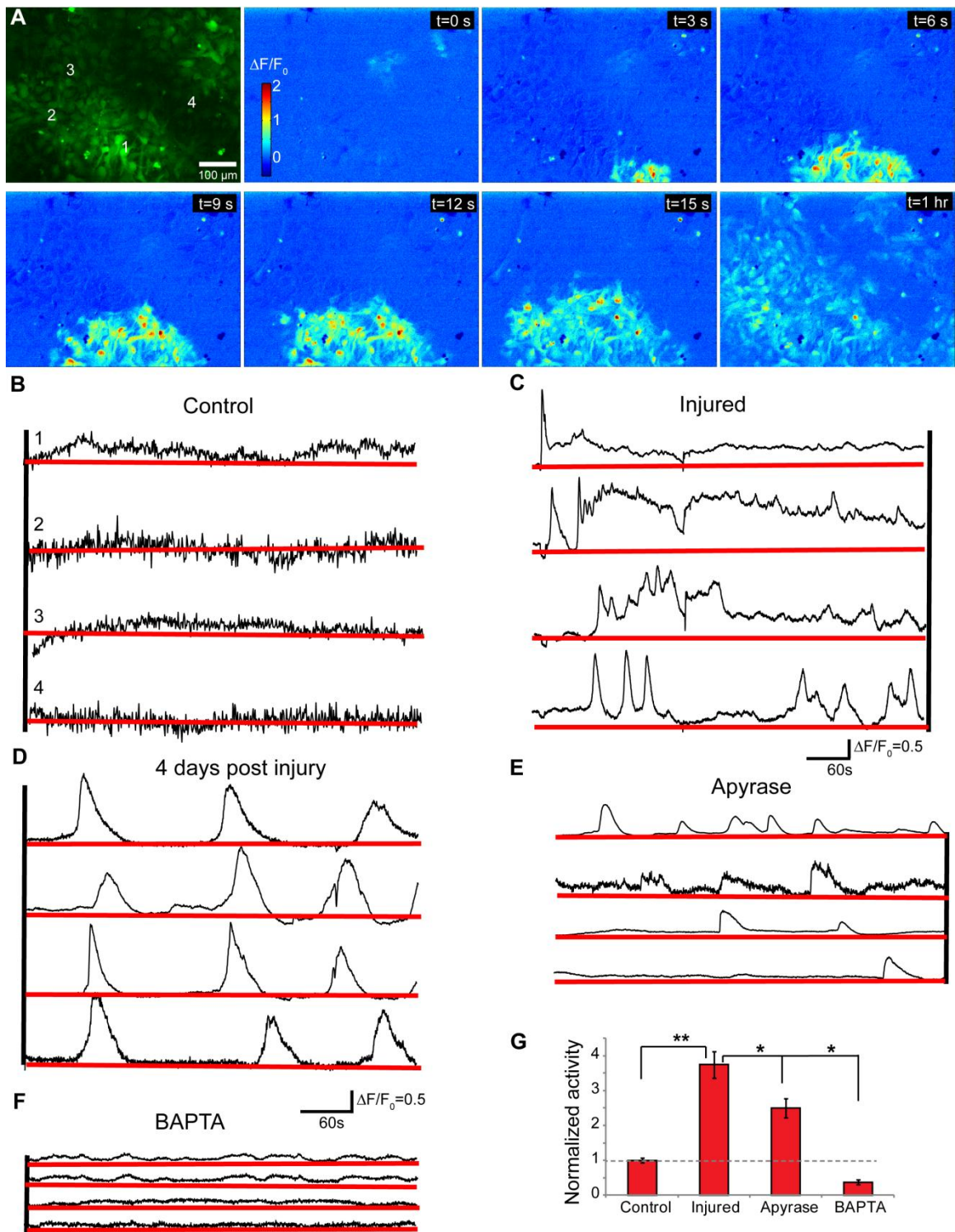


Figure 6. 7: Injury causes long-lasting increase in astrocytic calcium activity in the mechanical penumbra. **A:** Time-lapse images of intracellular Ca^{2+} fluorescence within astrocytes of the mechanical penumbra show a propagating calcium wave following mechanical injury (site of injury was one field of view below). Intracellular calcium activity remained elevated up to 4 days post-injury. Representative fluorescence trace of 4 highlighted astrocytes, located in the mechanical penumbra, before **(B)**, immediately after **(C)**, and 4 days following injury **(D)**. Astrocytic Ca^{2+} oscillations were significantly reduced with apyrase **(E)** and completely abolished with the calcium chelator BAPTA **(F)**. $n=125$ astrocytes, $N = 4$ wells, $**p<0.01$, $*p<0.05$.

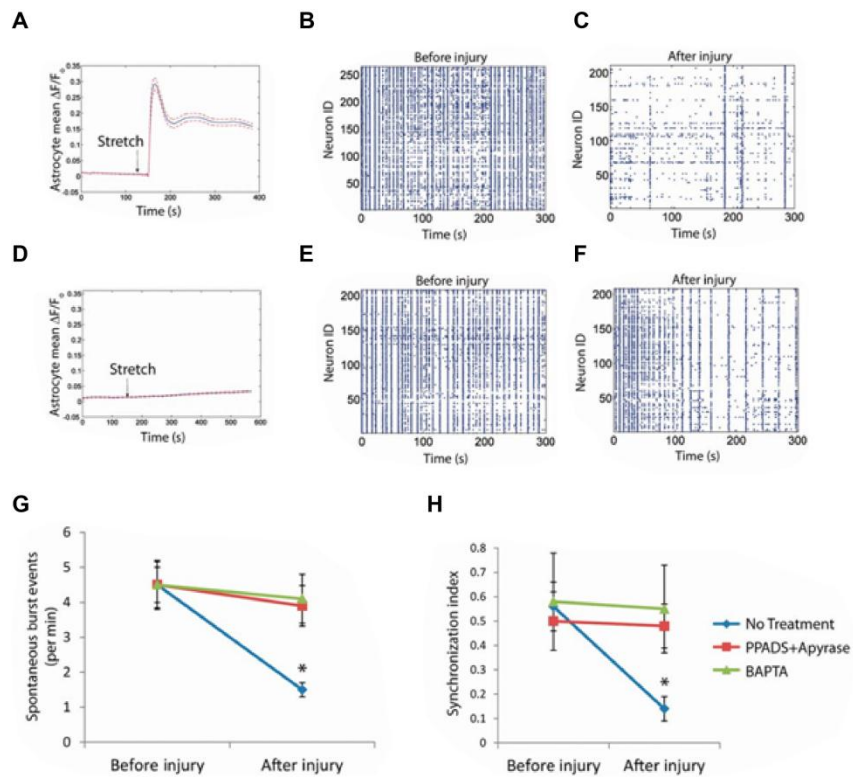


Figure 6. 8: The activity of in vitro neuronal networks in the mechanical penumbra is influenced by intercellular waves in astrocytes and purinergic signaling. Mechanical injury

triggered a calcium transient in astrocytes of the mechanical penumbra within 30 s of injury (**A**). Spontaneous activity in neurons located in the mechanical penumbra decreased after injury (**B** before injury versus **C**-recording period beginning 80 s after injury when calcium wave has passed through). Pretreating mixed cultures with BAPTA-AM or a combination of PPADS and apyrase blocked the calcium wave from propagating into the mechanical penumbra (**D**) and reduced post-traumatic changes in neural activity patterns (**E** versus **F**). Both spontaneous burst events and the synchronized activity were decreased in the penumbra after injury, and these changes were blocked with PPADS + apyrase or BAPTA-AM treatment (**G** and **H**). $n = 4/\text{group}$.

These preliminary results suggest that astrocytes play a potentially important role in spreading the influence of the mechanical injury to neuronal networks outside the area of initial injury. It is unclear, however, whether this is a one-time event or whether reactive changes in astrocytes continue to disrupt neuronal networks over time. Furthermore, since astrocytic calcium oscillations were attenuated with the broad spectrum purinergic receptor antagonist PPADS, it will be important to identify specific purinergic receptor subtypes that can modulate astrocytic activity and thereby modulate neuronal networks. However, since cortical neurons also express purinergic receptors, it may be difficult to ascribe possible improvements in neuronal network activity to inhibition of gliotransmission. For a more direct answer, one could culture cortical neurons from dnSNARE transgenic animals where a dominant-negative expression of the SNARE protein in astrocytes blocks vesicular release. Alternatively, recently developed fluorescent glutamate sensor could be selective expressed in astrocytes and the calcium activity in neuronal networks as well as astrocytic glutamate-release could be monitored

simultaneously. These experiments in vitro will provide a mechanism for network disruption in the mechanical penumbra and identify a therapeutic window. The results from these studies will inform animal studies and potentially lead to a new class of targets for treating TBI - drugs that are glio-centric rather than neuro-centric.

BIBLIOGRAPHY

- Akerboom, J., Rivera, J.D., Guilbe, M.M., Malave, E.C., Hernandez, H.H., Tian, L., Hires, S.A., Marvin, J.S., Looger, L.L., and Schreier, E.R. (2009). Crystal structures of the GCaMP calcium sensor reveal the mechanism of fluorescence signal change and aid rational design. *J Biol Chem* 284, 6455-6464.
- Al-Mubarak, B., Soriano, F.X., and Hardingham, G.E. (2009). Synaptic NMDAR activity suppresses FOXO1 expression via a cis-acting FOXO binding site: FOXO1 is a FOXO target gene. *Channels (Austin)* 3, 233-238.
- Alexander, M.P. (1995). Mild traumatic brain injury: pathophysiology, natural history, and clinical management. *Neurology* 45, 1253-1260.
- Allefeld C, M.M., Kurths J (2007). Eigenvalue decomposition as a generalized synchronization cluster analysis. *International Journal of Bifurcation and Chaos* 17, 3493-3497.
- Amit, D.J., and Brunel, N. (1997). Model of global spontaneous activity and local structured activity during delay periods in the cerebral cortex. *Cereb Cortex* 7, 237-252.
- Andriessen, T.M., Jacobs, B., and Vos, P.E. (2010). Clinical characteristics and pathophysiological mechanisms of focal and diffuse traumatic brain injury. *J Cell Mol Med* 14, 2381-2392.
- Arnold, F.J., Hofmann, F., Bengtson, C.P., Wittmann, M., Vanhoutte, P., and Bading, H. (2005). Microelectrode array recordings of cultured hippocampal networks reveal a simple model for transcription and protein synthesis-dependent plasticity. *J Physiol* 564, 3-19.
- Arrondo, G., Alegre, M., Sepulcre, J., Iriarte, J., Artieda, J., and Villoslada, P. (2009). Abnormalities in brain synchronization are correlated with cognitive impairment in multiple sclerosis. *Mult Scler* 15, 509-516.
- Arundine, M., and Tymianski, M. (2003). Molecular mechanisms of calcium-dependent neurodegeneration in excitotoxicity. *Cell Calcium* 34, 325-337.
- Babiloni, C., Ferri, R., Moretti, D.V., Strambi, A., Binetti, G., Dal Forno, G., Ferreri, F., Lanuzza, B., Bonato, C., Nobili, F., *et al.* (2004). Abnormal fronto-parietal coupling of brain rhythms in mild Alzheimer's disease: a multicentric EEG study. *Eur J Neurosci* 19, 2583-2590.
- Balderas, I., Rodriguez-Ortiz, C.J., Salgado-Tonda, P., Chavez-Hurtado, J., McGaugh, J.L., and Bermudez-Rattoni, F. (2008). The consolidation of object and context recognition memory involve different regions of the temporal lobe. *Learn Mem* 15, 618-624.
- Barker, G.R., and Warburton, E.C. (2011). When is the hippocampus involved in recognition memory? *J Neurosci* 31, 10721-10731.
- Barrett, L.E., Sul, J.Y., Takano, H., Van Bockstaele, E.J., Haydon, P.G., and Eberwine, J.H. (2006). Region-directed phototransfection reveals the functional significance of a dendritically synthesized transcription factor. *Nat Methods* 3, 455-460.

- Bartlett, T.E., Bannister, N.J., Collett, V.J., Dargan, S.L., Massey, P.V., Bortolotto, Z.A., Fitzjohn, S.M., Bashir, Z.I., Collingridge, G.L., and Lodge, D. (2007). Differential roles of NR2A and NR2B-containing NMDA receptors in LTP and LTD in the CA1 region of two-week old rat hippocampus. *Neuropharmacology* 52, 60-70.
- Bass, C.R., Panzer, M.B., Rafaeels, K.A., Wood, G., Shridharani, J., and Capehart, B. (2012). Brain injuries from blast. *Ann Biomed Eng* 40, 185-202.
- Ben-Ari, Y. (2002). Excitatory actions of gaba during development: the nature of the nurture. *Nat Rev Neurosci* 3, 728-739.
- Ben-Ari, Y., Khazipov, R., Leinekugel, X., Caillard, O., and Gaiarsa, J.L. (1997). GABAA, NMDA and AMPA receptors: a developmentally regulated 'menage a trois'. *Trends Neurosci* 20, 523-529.
- Besnard, A., Galan-Rodriguez, B., Vanhoutte, P., and Caboche, J. (2011). Elk-1 a transcription factor with multiple facets in the brain. *Front Neurosci* 5, 35.
- Bialonski, S., and Lehnertz, K. (2006). Identifying phase synchronization clusters in spatially extended dynamical systems. *Phys Rev E Stat Nonlin Soft Matter Phys* 74, 051909.
- Biasca, N., and Maxwell, W.L. (2007). Minor traumatic brain injury in sports: a review in order to prevent neurological sequelae. *Prog Brain Res* 161, 263-291.
- Bonasera, S.J., Schenk, A.K., Luxenberg, E.J., and Tecott, L.H. (2008). A novel method for automatic quantification of psychostimulant-evoked route-tracing stereotypy: application to *Mus musculus*. *Psychopharmacology (Berl)* 196, 591-602.
- Bonnelle, V., Ham, T.E., Leech, R., Kinnunen, K.M., Mehta, M.A., Greenwood, R.J., and Sharp, D.J. (2012). Salience network integrity predicts default mode network function after traumatic brain injury. *Proc Natl Acad Sci U S A* 109, 4690-4695.
- Bonnelle, V., Leech, R., Kinnunen, K.M., Ham, T.E., Beckmann, C.F., De Boissezon, X., Greenwood, R.J., and Sharp, D.J. (2011). Default mode network connectivity predicts sustained attention deficits after traumatic brain injury. *J Neurosci* 31, 13442-13451.
- Breskin, I., Soriano, J., Moses, E., and Tlusty, T. (2006). Percolation in Living Neural Networks. *Physical Review Letters* 97.
- Broadbent, N.J., Squire, L.R., and Clark, R.E. (2004). Spatial memory, recognition memory, and the hippocampus. *Proc Natl Acad Sci U S A* 101, 14515-14520.
- Browne, K.D., Chen, X.H., Meaney, D., and Smith, D.H. (2011). Mild Traumatic Brain Injury and Diffuse Axonal Injury in Swine. *J Neurotrauma*.
- Buki, A., and Povlishock, J.T. (2006). All roads lead to disconnection?--Traumatic axonal injury revisited. *Acta Neurochir (Wien)* 148, 181-193; discussion 193-184.
- Bullmore, E., and Sporns, O. (2009). Complex brain networks: graph theoretical analysis of structural and functional systems. *Nature reviews. Neuroscience* 10, 186-198.
- Burre, J., Sharma, M., Tsetsenis, T., Buchman, V., Etherton, M.R., and Sudhof, T.C. (2010). Alpha-synuclein promotes SNARE-complex assembly in vivo and in vitro. *Science* 329, 1663-1667.
- Buzsaki, G., and Draguhn, A. (2004). Neuronal oscillations in cortical networks. *Science* 304, 1926-1929.

- Cao, C., and Slobounov, S. (2010). Alteration of cortical functional connectivity as a result of traumatic brain injury revealed by graph theory, ICA, and sLORETA analyses of EEG signals. *IEEE Trans Neural Syst Rehabil Eng* 18, 11-19.
- Carbonell, W.S., and Mandell, J.W. (2003). Transient neuronal but persistent astroglial activation of ERK/MAP kinase after focal brain injury in mice. *J Neurotrauma* 20, 327-336.
- Carmignoto, G., and Vicini, S. (1992). Activity-dependent decrease in NMDA receptor responses during development of the visual cortex. *Science* 258, 1007-1011.
- Casadesus, G., Shukitt-Hale, B., and Joseph, J.A. (2001). Automated measurement of age-related changes in the locomotor response to environmental novelty and home-cage activity. *Mech Ageing Dev* 122, 1887-1897.
- Cesari, F., Rennekampff, V., Vintersten, K., Vuong, L.G., Seibler, J., Bode, J., Wiebel, F.F., and Nordheim, A. (2004). Elk-1 knock-out mice engineered by Flp recombinase-mediated cassette exchange. *Genesis* 38, 87-92.
- Chandra, S., Gallardo, G., Fernandez-Chacon, R., Schluter, O.M., and Sudhof, T.C. (2005). Alpha-synuclein cooperates with CSPalpha in preventing neurodegeneration. *Cell* 123, 383-396.
- Chen, H., and Chan, D.C. (2006). Critical dependence of neurons on mitochondrial dynamics. *Curr Opin Cell Biol* 18, 453-459.
- Chen, S.A., O'Dell, L.E., Hofer, M.E., Greenwell, T.N., Zorrilla, E.P., and Koob, G.F. (2006). Unlimited access to heroin self-administration: independent motivational markers of opiate dependence. *Neuropsychopharmacology* 31, 2692-2707.
- Chihara, T., Luginbuhl, D., and Luo, L. (2007). Cytoplasmic and mitochondrial protein translation in axonal and dendritic terminal arborization. *Nat Neurosci* 10, 828-837.
- Cho, D.H., Nakamura, T., and Lipton, S.A. (2010). Mitochondrial dynamics in cell death and neurodegeneration. *Cell Mol Life Sci* 67, 3435-3447.
- Choleris, E., Thomas, A.W., Kavaliers, M., and Prato, F.S. (2001). A detailed ethological analysis of the mouse open field test: effects of diazepam, chlordiazepoxide and an extremely low frequency pulsed magnetic field. *Neurosci Biobehav Rev* 25, 235-260.
- Choo, A.M., Geddes-Klein, D.M., Hockenberry, A., Scarsella, D., Mesfin, M.N., Singh, P., Patel, T.P., and Meaney, D.F. (2012). NR2A and NR2B subunits differentially mediate MAP kinase signaling and mitochondrial morphology following excitotoxic insult. *Neurochem Int* 60, 506-516.
- Choo, A.M., Miller, W.J., Chen, Y.C., Nibley, P., Patel, T.P., Goletiani, C., Morrison, B., 3rd, Kutzing, M.K., Firestein, B.L., Sul, J.Y., *et al.* (2013). Antagonism of purinergic signalling improves recovery from traumatic brain injury. *Brain* 136, 65-80.
- Clavaguera, F., Bolmont, T., Crowther, R.A., Abramowski, D., Frank, S., Probst, A., Fraser, G., Stalder, A.K., Beibel, M., Staufenbiel, M., *et al.* (2009). Transmission and spreading of tauopathy in transgenic mouse brain. *Nat Cell Biol* 11, 909-913.
- Clifford, S., Young, R., and Williamson, P. (2007). Assessing the early characteristics of autistic disorder using video analysis. *J Autism Dev Disord* 37, 301-313.

- Compte, A., Sanchez-Vives, M.V., McCormick, D.A., and Wang, X.J. (2003). Cellular and network mechanisms of slow oscillatory activity (<1 Hz) and wave propagations in a cortical network model. *J Neurophysiol* 89, 2707-2725.
- Conway, K.A., Lee, S.J., Rochet, J.C., Ding, T.T., Williamson, R.E., and Lansbury, P.T., Jr. (2000). Acceleration of oligomerization, not fibrillization, is a shared property of both alpha-synuclein mutations linked to early-onset Parkinson's disease: implications for pathogenesis and therapy. *Proc Natl Acad Sci U S A* 97, 571-576.
- Cossart, R., Aronov, D., and Yuste, R. (2003). Attractor dynamics of network UP states in the neocortex. *Nature* 423, 283-288.
- Cox, R.W. (1996). AFNI: software for analysis and visualization of functional magnetic resonance neuroimages. *Comput Biomed Res* 29, 162-173.
- Cryan, J.F., and Holmes, A. (2005). The ascent of mouse: advances in modelling human depression and anxiety. *Nat Rev Drug Discov* 4, 775-790.
- Cucchiara, R., Grana, C., Piccardi, M., and Prati, A. (2003). Detecting moving objects, ghosts, and shadows in video streams. *Pattern Analysis and Machine Intelligence, IEEE Transactions on* 25, 1337-1342.
- Cui, J., Xu, L., Bressler, S.L., Ding, M., and Liang, H. (2008). BSMART: a Matlab/C toolbox for analysis of multichannel neural time series. *Neural Netw* 21, 1094-1104.
- Cui, Z., Feng, R., Jacobs, S., Duan, Y., Wang, H., Cao, X., and Tsien, J.Z. (2013). Increased NR2A:NR2B ratio compresses long-term depression range and constrains long-term memory. *Sci Rep* 3, 1036.
- Cull-Candy, S.G., and Leszkiewicz, D.N. (2004). Role of distinct NMDA receptor subtypes at central synapses. *Sci STKE* 2004, re16.
- Cullen, D.K., Lessing, M.C., and LaPlaca, M.C. (2007). Collagen-dependent neurite outgrowth and response to dynamic deformation in three-dimensional neuronal cultures. *Ann Biomed Eng* 35, 835-846.
- Damschroder-Williams, P., Irwin, R.P., Lin, S.Z., and Paul, S.M. (1995). Characterization of the excitoprotective actions of N-methyl-D-aspartate in cultured cerebellar granule neurons. *J Neurochem* 65, 1069-1076.
- Davenport, N.D., Lim, K.O., Armstrong, M.T., and Sponheim, S.R. (2012). Diffuse and spatially variable white matter disruptions are associated with blast-related mild traumatic brain injury. *NeuroImage* 59, 2017-2024.
- De Kruijk, J.R., Twijnstra, A., and Leffers, P. (2001). Diagnostic criteria and differential diagnosis of mild traumatic brain injury. *Brain Inj* 15, 99-106.
- Defensor, E.B., Pearson, B.L., Pobbe, R.L., Bolivar, V.J., Blanchard, D.C., and Blanchard, R.J. (2011). A novel social proximity test suggests patterns of social avoidance and gaze aversion-like behavior in BTBR T+ tf/J mice. *Behav Brain Res* 217, 302-308.
- Delorme, A., and Makeig, S. (2004). EEGLAB: an open source toolbox for analysis of single-trial EEG dynamics including independent component analysis. *J Neurosci Methods* 134, 9-21.

- Desplats, P., Lee, H.J., Bae, E.J., Patrick, C., Rockenstein, E., Crews, L., Spencer, B., Masliah, E., and Lee, S.J. (2009). Inclusion formation and neuronal cell death through neuron-to-neuron transmission of alpha-synuclein. *Proc Natl Acad Sci U S A* *106*, 13010-13015.
- Dev, K.K., Petersen, V., Honore, T., and Henley, J.M. (1996). Pharmacology and regional distribution of the binding of 6-[3H]nitro-7-sulphamoylbenzo[f]-quinoxaline-2,3-dione to rat brain. *J Neurochem* *67*, 2609-2612.
- Difiori, J.P., and Giza, C.C. (2010). New techniques in concussion imaging. *Curr Sports Med Rep* *9*, 35-39.
- Doble, A. (1999). The role of excitotoxicity in neurodegenerative disease: Implications for therapy. *Pharmacology & Therapeutics* *81*, 163-221.
- Dombeck, D.A., Harvey, C.D., Tian, L., Looger, L.L., and Tank, D.W. (2010). Functional imaging of hippocampal place cells at cellular resolution during virtual navigation. *Nat Neurosci* *13*, 1433-1440.
- Dombeck, D.A., Khabbaz, A.N., Collman, F., Adelman, T.L., and Tank, D.W. (2007). Imaging large-scale neural activity with cellular resolution in awake, mobile mice. *Neuron* *56*, 43-57.
- Duann, J.R., Jung, T.P., Kuo, W.J., Yeh, T.C., Makeig, S., Hsieh, J.C., and Sejnowski, T.J. (2002). Single-trial variability in event-related BOLD signals. *NeuroImage* *15*, 823-835.
- Effgen, G.B., Hue, C.D., Vogel, E., 3rd, Panzer, M.B., Meaney, D.F., Bass, C.R., and Morrison, B., 3rd (2012). A Multiscale Approach to Blast Neurotrauma Modeling: Part II: Methodology for Inducing Blast Injury to in vitro Models. *Front Neurol* *3*, 23.
- Erreger, K., Dravid, S.M., Banke, T.G., Wyllie, D.J., and Traynelis, S.F. (2005). Subunit-specific gating controls rat NR1/NR2A and NR1/NR2B NMDA channel kinetics and synaptic signalling profiles. *J Physiol* *563*, 345-358.
- Farkas, O., and Povlishock, J.T. (2007). Cellular and subcellular change evoked by diffuse traumatic brain injury: a complex web of change extending far beyond focal damage. *Prog Brain Res* *161*, 43-59.
- Fetcho, J.R., Cox, K.J., and O'Malley, D.M. (1998). Monitoring activity in neuronal populations with single-cell resolution in a behaving vertebrate. *Histochem J* *30*, 153-167.
- Foster, K.A., McLaughlin, N., Edbauer, D., Phillips, M., Bolton, A., Constantine-Paton, M., and Sheng, M. (2010). Distinct roles of NR2A and NR2B cytoplasmic tails in long-term potentiation. *J Neurosci* *30*, 2676-2685.
- French, D.A., and Gruenstein, E.I. (2006). An integrate-and-fire model for synchronized bursting in a network of cultured cortical neurons. *Journal of computational neuroscience* *21*, 227-241.
- Frick, A., Magee, J., and Johnston, D. (2004). LTP is accompanied by an enhanced local excitability of pyramidal neuron dendrites. *Nat Neurosci* *7*, 126-135.
- Fries, P. (2005). A mechanism for cognitive dynamics: neuronal communication through neuronal coherence. *Trends Cogn Sci* *9*, 474-480.

- Friston, K.J. (2011). Functional and effective connectivity: a review. *Brain Connect* 1, 13-36.
- Frost, B., Jacks, R.L., and Diamond, M.I. (2009). Propagation of tau misfolding from the outside to the inside of a cell. *J Biol Chem* 284, 12845-12852.
- Fukuda, A., Muramatsu, K., Okabe, A., Shimano, Y., Hida, H., Fujimoto, I., and Nishino, H. (1998). Changes in intracellular Ca²⁺ induced by GABAA receptor activation and reduction in Cl⁻ gradient in neonatal rat neocortex. *J Neurophysiol* 79, 439-446.
- Furukawa, Y., Okada, M., Akaike, N., Hayashi, T., and Nabekura, J. (2000). Reduction of voltage-dependent magnesium block of N-methyl-D-aspartate receptor-mediated current by in vivo axonal injury. *Neuroscience* 96, 385-392.
- Ganguly, K., Schinder, A.F., Wong, S.T., and Poo, M. (2001). GABA itself promotes the developmental switch of neuronal GABAergic responses from excitation to inhibition. *Cell* 105, 521-532.
- Garaschuk, O., Milos, R.I., and Konnerth, A. (2006). Targeted bulk-loading of fluorescent indicators for two-photon brain imaging in vivo. *Nat Protoc* 1, 380-386.
- Garofalo, M., Nieuwenhuis, T., Massobrio, P., and Martinoia, S. (2009). Evaluation of the Performance of Information Theory-Based Methods and Cross-Correlation to Estimate the Functional Connectivity in Cortical Networks. *PLoS ONE* 4, -.
- Goforth, P.B., Ren, J., Schwartz, B.S., and Satin, L.S. (2011). Excitatory synaptic transmission and network activity are depressed following mechanical injury in cortical neurons. *J Neurophysiol* 105, 2350-2363.
- Goldstein, L.E., Fisher, A.M., Tagge, C.A., Zhang, X.L., Velisek, L., Sullivan, J.A., Upreti, C., Kracht, J.M., Ericsson, M., Wojnarowicz, M.W., *et al.* (2012). Chronic traumatic encephalopathy in blast-exposed military veterans and a blast neurotrauma mouse model. *Sci Transl Med* 4, 134ra160.
- Goulding, E.H., Schenk, A.K., Juneja, P., MacKay, A.W., Wade, J.M., and Tecott, L.H. (2008). A robust automated system elucidates mouse home cage behavioral structure. *Proc Natl Acad Sci U S A* 105, 20575-20582.
- Greenberg, D.S., Houweling, A.R., and Kerr, J.N. (2008). Population imaging of ongoing neuronal activity in the visual cortex of awake rats. *Nat Neurosci* 11, 749-751.
- Guo, J.L., and Lee, V.M. (2011). Seeding of normal Tau by pathological Tau conformers drives pathogenesis of Alzheimer-like tangles. *J Biol Chem* 286, 15317-15331.
- Hall, R.C., and Chapman, M.J. (2005). Definition, diagnosis, and forensic implications of postconcussional syndrome. *Psychosomatics* 46, 195-202.
- Hammond, C., Bergman, H., and Brown, P. (2007). Pathological synchronization in Parkinson's disease: networks, models and treatments. *Trends Neurosci* 30, 357-364.
- Han, X., Chow, B.Y., Zhou, H., Klapoetke, N.C., Chuong, A., Rajimehr, R., Yang, A., Baratta, M.V., Winkle, J., Desimone, R., and Boyden, E.S. (2011). A high-light sensitivity optical neural silencer: development and application to optogenetic control of non-human primate cortex. *Front Syst Neurosci* 5, 18.

- Hardingham, G.E., Arnold, F.J., and Bading, H. (2001). Nuclear calcium signaling controls CREB-mediated gene expression triggered by synaptic activity. *Nat Neurosci* 4, 261-267.
- Hardingham, G.E., and Bading, H. (2002). Coupling of extrasynaptic NMDA receptors to a CREB shut-off pathway is developmentally regulated. *Biochim Biophys Acta* 1600, 148-153.
- Hardingham, G.E., and Bading, H. (2010). Synaptic versus extrasynaptic NMDA receptor signalling: implications for neurodegenerative disorders. *Nat Rev Neurosci* 11, 682-696.
- Hardmeier, M., Schoonheim, M.M., Geurts, J.J., Hillebrand, A., Polman, C.H., Barkhof, F., and Stam, C.J. (2012). Cognitive dysfunction in early multiple sclerosis: altered centrality derived from resting-state functional connectivity using magnetoencephalography. *PLoS ONE* 7, e42087.
- Hertz, L. (1979). Functional interactions between neurons and astrocytes I. Turnover and metabolism of putative amino acid transmitters. *Prog Neurobiol* 13, 277-323.
- Hestrin, S. (1992). Developmental regulation of NMDA receptor-mediated synaptic currents at a central synapse. *Nature* 357, 686-689.
- Hillary, F.G., Slocomb, J., Hills, E.C., Fitzpatrick, N.M., Medaglia, J.D., Wang, J., Good, D.C., and Wylie, G.R. (2011). Changes in resting connectivity during recovery from severe traumatic brain injury. *Int J Psychophysiol* 82, 115-123.
- Hoyt, K.R., McLaughlin, B.A., Higgins, D.S., Jr., and Reynolds, I.J. (2000). Inhibition of glutamate-induced mitochondrial depolarization by tamoxifen in cultured neurons. *J Pharmacol Exp Ther* 293, 480-486.
- Ingebrigtsen, T., Romner, B., Marup-Jensen, S., Dons, M., Lundqvist, C., Bellner, J., Alling, C., and Borgesen, S.E. (2000). The clinical value of serum S-100 protein measurements in minor head injury: a Scandinavian multicentre study. *Brain Inj* 14, 1047-1055.
- Isomura, Y., Fujiwara-Tsukamoto, Y., and Takada, M. (2008). A network mechanism underlying hippocampal seizure-like synchronous oscillations. *Neurosci Res* 61, 227-233.
- Jacobson, L.H., Bettler, B., Kaupmann, K., and Cryan, J.F. (2007). Behavioral evaluation of mice deficient in GABA(B(1)) receptor isoforms in tests of unconditioned anxiety. *Psychopharmacology (Berl)* 190, 541-553.
- Jhuang, H., Garrote, E., Mutch, J., Yu, X., Khilnani, V., Poggio, T., Steele, A.D., and Serre, T. (2010). Automated home-cage behavioural phenotyping of mice. *Nat Commun* 1, 68.
- Jin, S.X., and Feig, L.A. (2010). Long-term potentiation in the CA1 hippocampus induced by NR2A subunit-containing NMDA glutamate receptors is mediated by Ras-GRF2/Erk map kinase signaling. *PLoS ONE* 5, e11732.
- Joachims, T. (1999). Making large-scale support vector machine learning practical. In *Advances in kernel methods* (Cambridge: MIT Press), pp. 169-184.

- Johnson, V.E., Stewart, W., and Smith, D.H. (2012). Axonal pathology in traumatic brain injury. *Exp Neurol*.
- Jonas, W., Lin, Y., and Tortella, F. (2001). Neuroprotection from glutamate toxicity with ultra-low dose glutamate. *Neuroreport* *12*, 335-339.
- Kabra, M., Robie, A.A., Rivera-Alba, M., Branson, S., and Branson, K. (2013). JAABA: interactive machine learning for automatic annotation of animal behavior. *Nat Methods* *10*, 64-67.
- Kamioka, H., Maeda, E., Jimbo, Y., Robinson, H.P., and Kawana, A. (1996). Spontaneous periodic synchronized bursting during formation of mature patterns of connections in cortical cultures. *Neurosci Lett* *206*, 109-112.
- Karlsson, R.M., Holmes, A., Heilig, M., and Crawley, J.N. (2005). Anxiolytic-like actions of centrally-administered neuropeptide Y, but not galanin, in C57BL/6J mice. *Pharmacol Biochem Behav* *80*, 427-436.
- Kerr, J.N., de Kock, C.P., Greenberg, D.S., Bruno, R.M., Sakmann, B., and Helmchen, F. (2007). Spatial organization of neuronal population responses in layer 2/3 of rat barrel cortex. *J Neurosci* *27*, 13316-13328.
- Kerr, J.N., Greenberg, D., and Helmchen, F. (2005). Imaging input and output of neocortical networks in vivo. *Proc Natl Acad Sci U S A* *102*, 14063-14068.
- Kew, J.N., Richards, J.G., Mutel, V., and Kemp, J.A. (1998). Developmental changes in NMDA receptor glycine affinity and ifenprodil sensitivity reveal three distinct populations of NMDA receptors in individual rat cortical neurons. *J Neurosci* *18*, 1935-1943.
- Kinney, J.W., Davis, C.N., Tabarean, I., Conti, B., Bartfai, T., and Behrens, M.M. (2006). A specific role for NR2A-containing NMDA receptors in the maintenance of parvalbumin and GAD67 immunoreactivity in cultured interneurons. *J Neurosci* *26*, 1604-1615.
- Kitagawa, K., Matsumoto, M., Kuwabara, K., Tagaya, M., Ohtsuki, T., Hata, R., Ueda, H., Handa, N., Kimura, K., and Kamada, T. (1991). 'Ischemic tolerance' phenomenon detected in various brain regions. *Brain Res* *561*, 203-211.
- Kohr, G. (2006). NMDA receptor function: subunit composition versus spatial distribution. *Cell Tissue Res* *326*, 439-446.
- Korotkova, T., Fuchs, E.C., Ponomarenko, A., von Engelhardt, J., and Monyer, H. (2010). NMDA receptor ablation on parvalbumin-positive interneurons impairs hippocampal synchrony, spatial representations, and working memory. *Neuron* *68*, 557-569.
- Kraus, J.F., and Nourjah, P. (1988). The epidemiology of mild, uncomplicated brain injury. *J Trauma* *28*, 1637-1643.
- Kuner, T., and Schoepfer, R. (1996). Multiple structural elements determine subunit specificity of Mg²⁺ block in NMDA receptor channels. *J Neurosci* *16*, 3549-3558.
- Kushner, D. (1998). Mild traumatic brain injury: Toward understanding manifestations and treatment. *Archives of Internal Medicine* *158*, 1617-1624.

- Langer, D., and Helmchen, F. (2012). Post hoc immunostaining of GABAergic neuronal subtypes following in vivo two-photon calcium imaging in mouse neocortex. *Pflugers Arch* 463, 339-354.
- LaPlaca, M.C., Prado, G.R., Cullen, D.K., and Irons, H.R. (2006). High rate shear insult delivered to cortical neurons produces heterogeneous membrane permeability alterations. *Conf Proc IEEE Eng Med Biol Soc* 1, 2384-2387.
- Lee, S.H., Liu, L., Wang, Y.T., and Sheng, M. (2002). Clathrin adaptor AP2 and NSF interact with overlapping sites of GluR2 and play distinct roles in AMPA receptor trafficking and hippocampal LTD. *Neuron* 36, 661-674.
- Lesuisse, C., and Martin, L.J. (2002). Long-term culture of mouse cortical neurons as a model for neuronal development, aging, and death. *J Neurobiol* 51, 9-23.
- Levin, H.S., Wilde, E., Troyanskaya, M., Petersen, N.J., Scheibel, R., Newsome, M., Radaideh, M., Wu, T., Yallampalli, R., Chu, Z., and Li, X. (2010). Diffusion tensor imaging of mild to moderate blast-related traumatic brain injury and its sequelae. *J Neurotrauma* 27, 683-694.
- Li, X., Ouyang, G., Usami, A., Ikegaya, Y., and Sik, A. (2010a). Scale-free topology of the CA3 hippocampal network: a novel method to analyze functional neuronal assemblies. *Biophys J* 98, 1733-1741.
- Li, Z., Jo, J., Jia, J.M., Lo, S.C., Whitcomb, D.J., Jiao, S., Cho, K., and Sheng, M. (2010b). Caspase-3 Activation via Mitochondria Is Required for Long-Term Depression and AMPA Receptor Internalization. *Cell* 141, 859-871.
- Li, Z., Jo, J., Jia, J.M., Lo, S.C., Whitcomb, D.J., Jiao, S., Cho, K., and Sheng, M. (2010c). Caspase-3 activation via mitochondria is required for long-term depression and AMPA receptor internalization. *Cell* 141, 859-871.
- Lin, Y.C., Huang, Z.H., Jan, I.S., Yeh, C.C., Wu, H.J., Chou, Y.C., and Chang, Y.C. (2002). Development of excitatory synapses in cultured neurons dissociated from the cortices of rat embryos and rat pups at birth. *J Neurosci Res* 67, 484-493.
- Liu, L., Wong, T.P., Pozza, M.F., Lingenhoehl, K., Wang, Y., Sheng, M., Auberson, Y.P., and Wang, Y.T. (2004). Role of NMDA receptor subtypes in governing the direction of hippocampal synaptic plasticity. *Science* 304, 1021-1024.
- Liu, Y.Y., Slotine, J.J., and Barabasi, A.L. (2011). Controllability of complex networks. *Nature* 473, 167-173.
- Luk, K.C., Song, C., O'Brien, P., Stieber, A., Branch, J.R., Brunden, K.R., Trojanowski, J.Q., and Lee, V.M. (2009). Exogenous alpha-synuclein fibrils seed the formation of Lewy body-like intracellular inclusions in cultured cells. *Proc Natl Acad Sci U S A* 106, 20051-20056.
- Lusardi, T.A., Rangan, J., Sun, D., Smith, D.H., and Meaney, D.F. (2004a). A device to study the initiation and propagation of calcium transients in cultured neurons after mechanical stretch. *Ann Biomed Eng* 32, 1546-1558.
- Lusardi, T.A., Wolf, J.A., Putt, M.E., Smith, D.H., and Meaney, D.F. (2004b). Effect of acute calcium influx after mechanical stretch injury in vitro on the viability of hippocampal neurons. *Journal of neurotrauma* 21, 61-72.

- Mac Donald, C., Johnson, A., Cooper, D., Malone, T., Sorrell, J., Shimony, J., Parsons, M., Snyder, A., Raichle, M., Fang, R., *et al.* (2013). Cerebellar White Matter Abnormalities following Primary Blast Injury in US Military Personnel. *PLoS ONE* 8, e55823.
- Magnuson, J., Leonessa, F., and Ling, G.S. (2012). Neuropathology of explosive blast traumatic brain injury. *Curr Neurol Neurosci Rep* 12, 570-579.
- Marquez de la Plata, C.D., Garces, J., Shokri Kojori, E., Grinnan, J., Krishnan, K., Pidikiti, R., Spence, J., Devous, M.D., Sr., Moore, C., McColl, R., *et al.* (2011). Deficits in functional connectivity of hippocampal and frontal lobe circuits after traumatic axonal injury. *Arch Neurol* 68, 74-84.
- Matthews, P.M., Honey, G.D., and Bullmore, E.T. (2006). Applications of fMRI in translational medicine and clinical practice. *Nat Rev Neurosci* 7, 732-744.
- Mattson, M.P., and Partin, J. (1999). Evidence for mitochondrial control of neuronal polarity. *J Neurosci Res* 56, 8-20.
- Mbye, L.H., Singh, I.N., Carrico, K.M., Saatman, K.E., and Hall, E.D. (2009). Comparative neuroprotective effects of cyclosporin A and NIM811, a nonimmunosuppressive cyclosporin A analog, following traumatic brain injury. *Journal of Cerebral Blood Flow and Metabolism* 29, 87-97.
- Meaney, D.F., and Smith, D.H. (2011). Biomechanics of concussion. *Clin Sports Med* 30, 19-31, vii.
- Meaney, D.F., Smith, D.H., Shreiber, D.I., Bain, A.C., Miller, R.T., Ross, D.T., and Gennarelli, T.A. (1995). Biomechanical analysis of experimental diffuse axonal injury. *J Neurotrauma* 12, 689-694.
- Meier, R., Egert, U., Aertsen, A., and Nawrot, M.P. (2008). FIND--a unified framework for neural data analysis. *Neural Netw* 21, 1085-1093.
- Millecamps, M., Jourdan, D., Leger, S., Etienne, M., Eschaliere, A., and Ardid, D. (2005). Circadian pattern of spontaneous behavior in monarthritic rats: a novel global approach to evaluation of chronic pain and treatment effectiveness. *Arthritis Rheum* 52, 3470-3478.
- Mittmann, W., Wallace, D.J., Czubayko, U., Herb, J.T., Schaefer, A.T., Looger, L.L., Denk, W., and Kerr, J.N. (2011). Two-photon calcium imaging of evoked activity from L5 somatosensory neurons in vivo. *Nat Neurosci*.
- Miyashita, T., Oda, Y., Horiuchi, J., Yin, J.C., Morimoto, T., and Saitoe, M. (2012). Mg(2+) block of Drosophila NMDA receptors is required for long-term memory formation and CREB-dependent gene expression. *Neuron* 74, 887-898.
- Monyer, H., Burnashev, N., Laurie, D.J., Sakmann, B., and Seeburg, P.H. (1994). Developmental and regional expression in the rat brain and functional properties of four NMDA receptors. *Neuron* 12, 529-540.
- Morishita, W., Lu, W., Smith, G.B., Nicoll, R.A., Bear, M.F., and Malenka, R.C. (2007). Activation of NR2B-containing NMDA receptors is not required for NMDA receptor-dependent long-term depression. *Neuropharmacology* 52, 71-76.

- Morris, J.F., Sul, J.Y., Kim, M.S., Klein-Szanto, A.J., Schochet, T., Rustgi, A., and Eberwine, J.H. (2012). Elk-1 phosphorylated at threonine-417 is present in diverse cancers and correlates with differentiation grade of colonic adenocarcinoma. *Hum Pathol*.
- Mukamel, E.A., Nimmerjahn, A., and Schnitzer, M.J. (2009). Automated analysis of cellular signals from large-scale calcium imaging data. *Neuron* 63, 747-760.
- Nakanishi, K., and Kukita, F. (1998). Functional synapses in synchronized bursting of neocortical neurons in culture. *Brain Res* 795, 137-146.
- Nakayama, K., Kiyosue, K., and Taguchi, T. (2005). Diminished neuronal activity increases neuron-neuron connectivity underlying silent synapse formation and the rapid conversion of silent to functional synapses. *J Neurosci* 25, 4040-4051.
- Nenadic, Z., and Burdick, J.W. (2005). Spike detection using the continuous wavelet transform. *IEEE transactions on bio-medical engineering* 52, 74-87.
- Newman, M.E. (2006). Modularity and community structure in networks. *Proc Natl Acad Sci U S A* 103, 8577-8582.
- Oliver, N.M., Rosario, B., and Pentland, A.P. (2000). A Bayesian computer vision system for modeling human interactions. *Pattern Analysis and Machine Intelligence, IEEE Transactions on* 22, 831-843.
- Ommaya, A.K., and Gennarelli, T.A. (1974). Cerebral concussion and traumatic unconsciousness. Correlation of experimental and clinical observations of blunt head injuries. *Brain* 97, 633-654.
- Otani, N., Nawashiro, H., Fukui, S., Nomura, N., and Shima, K. (2002). Temporal and spatial profile of phosphorylated mitogen-activated protein kinase pathways after lateral fluid percussion injury in the cortex of the rat brain. *J Neurotrauma* 19, 1587-1596.
- Ozden, I., Lee, H.M., Sullivan, M.R., and Wang, S.S. (2008). Identification and clustering of event patterns from in vivo multiphoton optical recordings of neuronal ensembles. *J Neurophysiol* 100, 495-503.
- Pagliari, P., Gattullo, D., Rastaldo, R., and Losano, G. (2001). Ischemic preconditioning: from the first to the second window of protection. *Life Sci* 69, 1-15.
- Palmer, A.M., Marion, D.W., Botscheller, M.L., Swedlow, P.E., Styren, S.D., and DeKosky, S.T. (1993). Traumatic brain injury-induced excitotoxicity assessed in a controlled cortical impact model. *J Neurochem* 61, 2015-2024.
- Panzer, M.B., Matthews, K.A., Yu, A.W., Morrison, B., 3rd, Meaney, D.F., and Bass, C.R. (2012). A Multiscale Approach to Blast Neurotrauma Modeling: Part I - Development of Novel Test Devices for in vivo and in vitro Blast Injury Models. *Front Neurol* 3, 46.
- Paoletti, P., and Ascher, P. (1994). Mechanosensitivity of NMDA receptors in cultured mouse central neurons. *Neuron* 13, 645-655.
- Papadia, S., Soriano, F.X., Léveillé, F., Martel, M.-A., Dakin, K.A., Hansen, H.H., Kaindl, A., Sifringer, M., Fowler, J., Stefovská, V., *et al.* (2008). Synaptic NMDA

- receptor activity boosts intrinsic antioxidant defenses. *Nature neuroscience* *11*, 476-487.
- Parga, N., and Abbott, L.F. (2007). Network model of spontaneous activity exhibiting synchronous transitions between up and down States. *Front Neurosci* *1*, 57-66.
- Park, E., Eisen, R., Kinio, A., and Baker, A.J. (2013). Electrophysiological white matter dysfunction and association with neurobehavioral deficits following low-level primary blast trauma. *Neurobiol Dis* *52*, 150-159.
- Passafaro, M., Nakagawa, T., Sala, C., and Sheng, M. (2003). Induction of dendritic spines by an extracellular domain of AMPA receptor subunit GluR2. *Nature* *424*, 677-681.
- Patel, T.P., Ventre, S.C., and Meaney, D.F. (2012). Dynamic changes in neural circuit topology following mild mechanical injury in vitro. *Ann Biomed Eng* *40*, 23-36.
- Peng, T.I., and Greenamyre, J.T. (1998). Privileged access to mitochondria of calcium influx through N-methyl-D-aspartate receptors. *Mol Pharmacol* *53*, 974-980.
- Petersen, C.C. (2007). The functional organization of the barrel cortex. *Neuron* *56*, 339-355.
- Phillips, R.G., and LeDoux, J.E. (1992). Differential contribution of amygdala and hippocampus to cued and contextual fear conditioning. *Behav Neurosci* *106*, 274-285.
- Pilling, A.D., Horiuchi, D., Lively, C.M., and Saxton, W.M. (2006). Kinesin-1 and Dynein are the primary motors for fast transport of mitochondria in *Drosophila* motor axons. *Mol Biol Cell* *17*, 2057-2068.
- Prut, L., and Belzung, C. (2003). The open field as a paradigm to measure the effects of drugs on anxiety-like behaviors: a review. *Eur J Pharmacol* *463*, 3-33.
- Qin, W., and Yaonan, W. (2008). Background subtraction based on adaptive non-parametric model. In *Intelligent Control and Automation, 2008. WCICA 2008. 7th World Congress on*, pp. 5960-5965.
- Quiroga, R.Q., Nadasdy, Z., and Ben-Shaul, Y. (2004). Unsupervised spike detection and sorting with wavelets and superparamagnetic clustering. *Neural Comput* *16*, 1661-1687.
- Raghupathi, R., Muir, J.K., Fulp, C.T., Pittman, R.N., and McIntosh, T.K. (2003). Acute activation of mitogen-activated protein kinases following traumatic brain injury in the rat: implications for posttraumatic cell death. *Exp Neurol* *183*, 438-448.
- Readnower, R.D., Pandya, J.D., McEwen, M.L., Pauly, J.R., Springer, J.E., and Sullivan, P.G. (2011). Post-injury administration of the mitochondrial permeability transition pore inhibitor, NIM811, is neuroprotective and improves cognition after traumatic brain injury in rats. *J Neurotrauma* *28*, 1845-1853.
- Reeves, T.M., Lyeth, B.G., and Povlishock, J.T. (1995). Long-term potentiation deficits and excitability changes following traumatic brain injury. *Exp Brain Res* *106*, 248-256.
- Rego, A.C., and Oliveira, C.R. (2003). Mitochondrial dysfunction and reactive oxygen species in excitotoxicity and apoptosis: Implications for the pathogenesis of neurodegenerative diseases. *Neurochemical Research* *28*, 1563-1574.

- Richter, S.H., Garner, J.P., and Wurbel, H. (2009). Environmental standardization: cure or cause of poor reproducibility in animal experiments? *Nat Methods* 6, 257-261.
- Rintoul, G.L., Filiano, A.J., Brocard, J.B., Kress, G.J., and Reynolds, I.J. (2003). Glutamate decreases mitochondrial size and movement in primary forebrain neurons. *J Neurosci* 23, 7881-7888.
- Rivera, C., Voipio, J., Payne, J.A., Ruusuvuori, E., Lahtinen, H., Lamsa, K., Pirvola, U., Saarma, M., and Kaila, K. (1999). The K⁺/Cl⁻ co-transporter KCC2 renders GABA hyperpolarizing during neuronal maturation. *Nature* 397, 251-255.
- Roberts, E.B., and Ramoa, A.S. (1999). Enhanced NR2A subunit expression and decreased NMDA receptor decay time at the onset of ocular dominance plasticity in the ferret. *J Neurophysiol* 81, 2587-2591.
- Rocher, A.B., Crimins, J.L., Amatrudo, J.M., Kinson, M.S., Todd-Brown, M.A., Lewis, J., and Luebke, J.I. (2010). Structural and functional changes in tau mutant mice neurons are not linked to the presence of NFTs. *Exp Neurol* 223, 385-393.
- Rubinov, M., and Sporns, O. (2010). Complex network measures of brain connectivity: uses and interpretations. *NeuroImage* 52, 1059-1069.
- Rutten, K., Reneerkens, O.A., Hamers, H., Sik, A., McGregor, I.S., Prickaerts, J., and Blokland, A. (2008). Automated scoring of novel object recognition in rats. *J Neurosci Methods* 171, 72-77.
- Sasahira, M., Lowry, T., Simon, R.P., and Greenberg, D.A. (1995). Epileptic tolerance: prior seizures protect against seizure-induced neuronal injury. *Neurosci Lett* 185, 95-98.
- Sato, T.R., Gray, N.W., Mainen, Z.F., and Svoboda, K. (2007). The functional microarchitecture of the mouse barrel cortex. *PLoS Biol* 5, e189.
- Sattler, R., and Tymianski, M. (2000). Molecular mechanisms of calcium-dependent excitotoxicity. *J Mol Med* 78, 3-13.
- Schwarzbach, E., Bonislawski, D.P., Xiong, G., and Cohen, A.S. (2006). Mechanisms underlying the inability to induce area CA1 LTP in the mouse after traumatic brain injury. *Hippocampus* 16, 541-550.
- Shalbuyeva, N., Brustovetsky, T., Bolshakov, A., and Brustovetsky, N. (2006). Calcium-dependent spontaneously reversible remodeling of brain mitochondria. *J Biol Chem* 281, 37547-37558.
- Sharma, A., Callahan, L.M., Sul, J.Y., Kim, T.K., Barrett, L., Kim, M., Powers, J.M., Federoff, H., and Eberwine, J. (2010). A neurotoxic phosphoform of Elk-1 associates with inclusions from multiple neurodegenerative diseases. *PLoS ONE* 5, e9002.
- Sharp, D.J., Beckmann, C.F., Greenwood, R., Kinnunen, K.M., Bonnelle, V., De Boissezon, X., Powell, J.H., Counsell, S.J., Patel, M.C., and Leech, R. (2011). Default mode network functional and structural connectivity after traumatic brain injury. *Brain* 134, 2233-2247.
- Sharp, D.J., and Ham, T.E. (2011). Investigating white matter injury after mild traumatic brain injury. *Curr Opin Neurol* 24, 558-563.

- Sick, T.J., Perez-Pinzon, M.A., and Feng, Z.Z. (1998). Impaired expression of long-term potentiation in hippocampal slices 4 and 48 h following mild fluid-percussion brain injury in vivo. *Brain Res* 785, 287-292.
- Simon, P., Dupuis, R., and Costentin, J. (1994). Thigmotaxis as an index of anxiety in mice. Influence of dopaminergic transmissions. *Behav Brain Res* 61, 59-64.
- Singer, W. (1993). Synchronization of cortical activity and its putative role in information processing and learning. *Annu Rev Physiol* 55, 349-374.
- Singh, P., Doshi, S., Spaethling, J.M., Hockenberry, A.J., Patel, T.P., Geddes-Klein, D.M., Lynch, D.R., and Meaney, D.F. (2012). N-methyl-D-aspartate receptor mechanosensitivity is governed by C terminus of NR2B subunit. *J Biol Chem* 287, 4348-4359.
- Singh, P., Hockenberry, A.J., Tiruvadi, V.R., and Meaney, D.F. (2011). Computational Investigation of the Changing Patterns of Subtype Specific NMDA Receptor Activation during Physiological Glutamatergic Neurotransmission. *PLoS Comput Biol* 7, e1002106.
- Smith, D.H., Nonaka, M., Miller, R., Leoni, M., Chen, X.H., Alsop, D., and Meaney, D.F. (2000). Immediate coma following inertial brain injury dependent on axonal damage in the brainstem. *J Neurosurg* 93, 315-322.
- Sorbara, C., Misgeld, T., and Kerschensteiner, M. (2012). In vivo imaging of the diseased nervous system: an update. *Curr Pharm Des* 18, 4465-4470.
- Soriano, F.X., Papadia, S., Hofmann, F., Hardingham, N.R., Bading, H., and Hardingham, G.E. (2006). Preconditioning doses of NMDA promote neuroprotection by enhancing neuronal excitability. *J Neurosci* 26, 4509-4518.
- Spacek, M., Blanche, T., and Swindale, N. (2008). Python for large-scale electrophysiology. *Front Neuroinform* 2, 9.
- Sponheim, S.R., McGuire, K.A., Kang, S.S., Davenport, N.D., Aviyente, S., Bernat, E.M., and Lim, K.O. (2011). Evidence of disrupted functional connectivity in the brain after combat-related blast injury. *NeuroImage* 54 Suppl 1, S21-29.
- Spruston, N., Schiller, Y., Stuart, G., and Sakmann, B. (1995). Activity-dependent action potential invasion and calcium influx into hippocampal CA1 dendrites. *Science* 268, 297-300.
- Stam, C.J., and Reijneveld, J.C. (2007). Graph theoretical analysis of complex networks in the brain. *Nonlinear Biomed Phys* 1, 3.
- Stam, C.J., van der Made, Y., Pijnenburg, Y.A., and Scheltens, P. (2003). EEG synchronization in mild cognitive impairment and Alzheimer's disease. *Acta Neurol Scand* 108, 90-96.
- Stanika, R.I., Pivovarova, N.B., Brantner, C.A., Watts, C.A., Winters, C.A., and Andrews, S.B. (2009). Coupling diverse routes of calcium entry to mitochondrial dysfunction and glutamate excitotoxicity. *Proceedings of the National Academy of Sciences of the United States of America* 106, 9854-9859.

- Stauffer, C., and Grimson, W.E.L. (1999). Adaptive background mixture models for real-time tracking. In *Computer Vision and Pattern Recognition, 1999. IEEE Computer Society Conference on.*, p. 252 Vol. 252.
- Steele, A.D., Jackson, W.S., King, O.D., and Lindquist, S. (2007). The power of automated high-resolution behavior analysis revealed by its application to mouse models of Huntington's and prion diseases. *Proc Natl Acad Sci U S A* *104*, 1983-1988.
- Stern, R.A., Riley, D.O., Daneshvar, D.H., Nowinski, C.J., Cantu, R.C., and McKee, A.C. (2011). Long-term consequences of repetitive brain trauma: chronic traumatic encephalopathy. *PM R* *3*, S460-467.
- Stocca, G., and Vicini, S. (1998). Increased contribution of NR2A subunit to synaptic NMDA receptors in developing rat cortical neurons. *J Physiol* *507 (Pt 1)*, 13-24.
- Stosiek, C., Garaschuk, O., Holthoff, K., and Konnerth, A. (2003). In vivo two-photon calcium imaging of neuronal networks. *Proc Natl Acad Sci U S A* *100*, 7319-7324.
- Takahashi, N., Sasaki, T., Usami, A., Matsuki, N., and Ikegaya, Y. (2007). Watching neuronal circuit dynamics through functional multineuron calcium imaging (fMCI). *Neurosci Res* *58*, 219-225.
- Tamborini, P., Sigg, H., and Zbinden, G. (1989). Quantitative analysis of rat activity in the home cage by infrared monitoring. Application to the acute toxicity testing of acetanilide and phenylmercuric acetate. *Arch Toxicol* *63*, 85-96.
- Tang, X., Orchard, S.M., and Sanford, L.D. (2002). Home cage activity and behavioral performance in inbred and hybrid mice. *Behav Brain Res* *136*, 555-569.
- Tang, X., and Sanford, L.D. (2005). Home cage activity and activity-based measures of anxiety in 129P3/J, 129X1/SvJ and C57BL/6J mice. *Physiol Behav* *84*, 105-115.
- Tetzlaff, C., Okujeni, S., Egert, U., Worgotter, F., and Butz, M. (2010). Self-organized criticality in developing neuronal networks. *PLoS Comput Biol* *6*, e1001013.
- Thomas, C.G., Miller, A.J., and Westbrook, G.L. (2006). Synaptic and extrasynaptic NMDA receptor NR2 subunits in cultured hippocampal neurons. *J Neurophysiol* *95*, 1727-1734.
- Tian, L., Hires, S.A., Mao, T., Huber, D., Chiappe, M.E., Chalasani, S.H., Petreanu, L., Akerboom, J., McKinney, S.A., Schreiter, E.R., *et al.* (2009). Imaging neural activity in worms, flies and mice with improved GCaMP calcium indicators. *Nat Methods* *6*, 875-881.
- Toga, A.W., Thompson, P.M., Mori, S., Amunts, K., and Zilles, K. (2006). Towards multimodal atlases of the human brain. *Nat Rev Neurosci* *7*, 952-966.
- Tomek, J., Novak, O., and Syka, J. (2013). Two-Photon Processor and SeNeCA - A freely available software package to process data from two-photon calcium imaging at speeds down to several ms per frame. *J Neurophysiol*.
- Tovar, K.R., and Westbrook, G.L. (1999). The incorporation of NMDA receptors with a distinct subunit composition at nascent hippocampal synapses in vitro. *J Neurosci* *19*, 4180-4188.

- Uhlhaas, P.J., Haenschel, C., Nikolic, D., and Singer, W. (2008). The role of oscillations and synchrony in cortical networks and their putative relevance for the pathophysiology of schizophrenia. *Schizophr Bull* 34, 927-943.
- Uhlhaas, P.J., and Singer, W. (2006). Neural synchrony in brain disorders: relevance for cognitive dysfunctions and pathophysiology. *Neuron* 52, 155-168.
- Uversky, V.N., Li, J., and Fink, A.L. (2001). Evidence for a partially folded intermediate in alpha-synuclein fibril formation. *J Biol Chem* 276, 10737-10744.
- van den Heuvel, M.P., Stam, C.J., Boersma, M., and Hulshoff Pol, H.E. (2008). Small-world and scale-free organization of voxel-based resting-state functional connectivity in the human brain. *NeuroImage* 43, 528-539.
- van Horssen, J., Witte, M.E., and Ciccarelli, O. (2012). The role of mitochondria in axonal degeneration and tissue repair in MS. *Mult Scler* 18, 1058-1067.
- van Vreeswijk, C., and Sompolinsky, H. (1996). Chaos in neuronal networks with balanced excitatory and inhibitory activity. *Science* 274, 1724-1726.
- Vianna, M.R., Alonso, M., Viola, H., Quevedo, J., de Paris, F., Furman, M., de Stein, M.L., Medina, J.H., and Izquierdo, I. (2000). Role of hippocampal signaling pathways in long-term memory formation of a nonassociative learning task in the rat. *Learn Mem* 7, 333-340.
- Voigt, T., Opitz, T., and de Lima, A.D. (2005). Activation of early silent synapses by spontaneous synchronous network activity limits the range of neocortical connections. *J Neurosci* 25, 4605-4615.
- Volpicelli-Daley, L.A., Luk, K.C., Patel, T.P., Tanik, S.A., Riddle, D.M., Stieber, A., Meaney, D.F., Trojanowski, J.Q., and Lee, V.M. (2011). Exogenous alpha-synuclein fibrils induce Lewy body pathology leading to synaptic dysfunction and neuron death. *Neuron* 72, 57-71.
- von Engelhardt, J., Doganci, B., Seeburg, P.H., and Monyer, H. (2009). Synaptic NR2A- but not NR2B-Containing NMDA Receptors Increase with Blockade of Ionotropic Glutamate Receptors. *Front Mol Neurosci* 2, 19.
- von Reyn, C.R., Spaethling, J.M., Mesfin, M.N., Ma, M., Neumar, R.W., Smith, D.H., Siman, R., and Meaney, D.F. (2009). Calpain mediates proteolysis of the voltage-gated sodium channel alpha-subunit. *J Neurosci* 29, 10350-10356.
- White, R.J., and Reynolds, I.J. (1996). Mitochondrial depolarization in glutamate-stimulated neurons: an early signal specific to excitotoxin exposure. *J Neurosci* 16, 5688-5697.
- Witt, S.T., Lovejoy, D.W., Pearlson, G.D., and Stevens, M.C. (2010). Decreased prefrontal cortex activity in mild traumatic brain injury during performance of an auditory oddball task. *Brain Imaging Behav* 4, 232-247.
- Womelsdorf, T., Schoffelen, J.M., Oostenveld, R., Singer, W., Desimone, R., Engel, A.K., and Fries, P. (2007). Modulation of neuronal interactions through neuronal synchronization. *Science* 316, 1609-1612.

- Wood-Kaczmar, A., Deas, E., Wood, N.W., and Abramov, A.Y. (2013). The role of the mitochondrial NCX in the mechanism of neurodegeneration in Parkinson's disease. *Adv Exp Med Biol* 961, 241-249.
- Yaksi, E., and Friedrich, R.W. (2006). Reconstruction of firing rate changes across neuronal populations by temporally deconvolved Ca²⁺ imaging. *Nature methods* 3, 377-383.
- Yamada, J., Okabe, A., Toyoda, H., Kilb, W., Luhmann, H.J., and Fukuda, A. (2004). Cl⁻ uptake promoting depolarizing GABA actions in immature rat neocortical neurones is mediated by NKCC1. *J Physiol* 557, 829-841.
- Yang, S.H., Bumpass, D.C., Perkins, N.D., and Sharrocks, A.D. (2002). The ETS domain transcription factor Elk-1 contains a novel class of repression domain. *Mol Cell Biol* 22, 5036-5046.
- Yoshiyama, Y., Higuchi, M., Zhang, B., Huang, S.M., Iwata, N., Saido, T.C., Maeda, J., Suhara, T., Trojanowski, J.Q., and Lee, V.M. (2007). Synapse loss and microglial activation precede tangles in a P301S tauopathy mouse model. *Neuron* 53, 337-351.
- Yu, Z., and Morrison, B., 3rd (2010). Experimental mild traumatic brain injury induces functional alteration of the developing hippocampus. *J Neurophysiol* 103, 499-510.
- Yuste, R., Peinado, A., and Katz, L.C. (1992). Neuronal domains in developing neocortex. *Science* 257, 665-669.
- Zhang, L., Rzigalinski, B.A., Ellis, E.F., and Satin, L.S. (1996). Reduction of voltage-dependent Mg²⁺ blockade of NMDA current in mechanically injured neurons. *Science* 274, 1921-1923.